UNIVERSITÀ DEGLI STUDI DI PARMA

Dottorato di Ricerca in Ingegneria Civile e Architettura

Ciclo XXXVII

Analysis and assessment of vegetation's contribution to the prevention of risks associated with the triggering and development of rainfall induced shallow landslides (soil slips)

Coordinator:

Chiar.mo Prof. Andrea Spagnoli

Tutor:

Chiar.ma Prof.ssa Lorella Montrasio

Co-Tutor:

Dott. Ing. Michele Placido Antonio Gatto

PhD Candidate: Salvatore Misiano

Academic Years 2021/2022 – 2024/2025

Per migliorare, bisogna imparare dagli errori…

ACKNOWLEDGEMENTS

There are so many people I should thank, so I hope I do not forget anyone.

First of all, the person I should thank the most is myself, for dedicating myself fully to this project with hard work and perseverance.

Next, I would like to thank the people who have been closest to me during this journey or who have contributed to this study, taking part in this period of my life:

To Chiara, who is always waiting for me and fills me with love. You are an endless resource, and I thank you for allowing me to live and share life with you.

To Michele, who puts up with me every day and has enlightened me in moments when my research seemed to wander into emptiness.

To Professor Montrasio, who gave me the opportunity to embark on this long journey and allowed me the freedom to follow my intuition, creating a path together and guiding me through the most critical aspects.

To the company TENAX, which gave me the opportunity to work on an experimental prototype of biodegradable erosion control netting.

To Professor Spagnoli, coordinator of the PhD program DIA in Parma, who has always been available for any need.

To Peter, a brilliant Senior Scientist at ETH, who supported me during a crucial period of my life in Zurich, providing me with solid foundations, inspiring me, and improving many aspects of my professional profile.

To the entire team at the Physics of Soil and Terrestrial Ecosystems at ETH, led by the ever-friendly Andrea, who welcomed me as a full member and helped me grow.

To Daniela and Miriam, two incredibly generous and remarkable people who helped me during my time in Zurich. Thank you for the interesting insights and deep discussions we had!

To my parents, who always support me in any choice I make, without judgment, and always rowing in the same direction as me.

To Luca and Giusy, who have become my second family and offer so much without ever asking for anything in return.

To all my friends, who make me laugh and create unforgettable moments, making it possible for me to disconnect when needed.

To all the people who have not been mentioned but who have contributed to all of this, a heartfelt thank you!

OBJECTIVE

The aim of this study is to analyse the potential causes and contributing factors that lead to the occurrence of rainfall-induced shallow landslides, with a focus on quantifying the role of vegetation in such processes and exploring how bioengineering techniques employing specific plant species can be implemented to mitigate risks. To achieve this, a platform was developed to facilitate predictive analyses, incorporating the contribution of vegetation from multiple perspectives.

Two predictive models were designed: LEP-AI and PIP-AI. These models enable instability analyses over extensive study areas at varying scales, including the effects of vegetation. Additionally, a hybrid model combining SLIP, a physically-based predictive model, with PIP-AI, the artificial intelligence-based predictive model, was developed. The results indicate the need for further refinement of the LEP-AI model, while PIP-AI demonstrated high predictive capabilities, particularly when integrated with SLIP.

Complementary to these efforts, a biodegradable net was designed to reduce soil erosion during vegetation planting on slopes. Furthermore, a simplified model was developed to identify potential landslide paths and quantify the kinematic and dynamic aspects of landslide motion.

ABSTRACT

In recent decades, the frequency and intensity of extreme rainfall events have increased significantly, a phenomenon closely linked to global climate change. These events, exacerbated by rising global temperatures and increased atmospheric moisture capacity, play a critical role in triggering shallow landslides in susceptible areas. Shallow landslides, often involving the surface soil layer, can evolve into debris flows, posing substantial risks to infrastructure, ecosystems, and human lives. The increasing vulnerability of previously stable regions necessitates reevaluating hazard assessments and mitigation strategies to address these evolving risks.

Vegetation emerges as a crucial factor in mitigating landslide susceptibility by influencing soil's mechanical and hydraulic properties, such as cohesion, water retention, and surface runoff. Eco-sustainable solutions involving vegetation offer a promising alternative to conventional engineering approaches, which are often environmentally intrusive and economically demanding. Understanding the complex interplay among rainfall, soil, and vegetation is essential for developing effective land management strategies and climate change adaptation measures.

This study will be structured into several sections, with the intent to: (i) investigate historical landslide events and their possible causes; (ii) analyse the state of the art on shallow landslide susceptibility and root reinforcement; (iii) assess the role of vegetation in slope stability across species; (iv) develop predictive models to identify high-susceptibility areas (LEP-AI and PIP-AI) and simulate landslide flow paths (GPE); (v) design eco-friendly stabilization measures and create a fast geo-spatial platform for landslide management (X-SLIP); (vi) study a real case application of the designed models on a wide area of Emilia-Romagna region;

Specifically, this research integrates physically-based models and advanced machine learning techniques to enhance the understanding and prediction of rainfall-induced shallow landslides, coupled with vegetation. Specifically, the Shallow Landslide Instability Predictor (SLIP) model is employed for its balance between computational efficiency and accuracy, while machine learning approaches, including neural networks and ensemble methods, address the dynamic and non-linear nature of landslide processes. Two machine learning model prototypes are developed: a rapid macro-scale model for filtering susceptible areas based on rainfall events (LEP-AI) and a detailed micro-scale model for pixel-by-pixel slope

stability assessment (PIP-AI). The first model, LEP-AI, shows fluctuating results at just a sufficient level, but substantial improvements are needed. The second model, PIP-AI, demonstrates high and consistent performance, which can be further refined when coupled with a physically-based model such as SLIP. Both models exhibit excellent analysis timing, with LEP-AI taking 0.06 seconds for the analysis of 40 municipalities, and PIP-AI taking 1.2 seconds for 4 municipalities with a 15x15 resolution.

By bridging classical soil mechanics and data-driven machine learning methodologies, this research establishes a robust framework for landslide prediction and mitigation, advancing the field's capacity to address climate-driven geohazards effectively.

CONTENTS

LIST OF FIGURES

LIST OF FIGURES

LIST OF FIGURES

LIST OF TABLES

INTRODUCTION

In recent decades, a marked increase in frequency and intensity of extreme rainfall events was observed. The scientific community believes that this phenomenon can be attributed to global climate change, the issue of the 21st century. In fact, since global temperatures continue to rise, the atmosphere's capacity to hold moisture increases, leading to more frequent and intense rainfall events (Burt et al., 2016; Guhathakurta et al., 2011; Lavell et al., 2012; Martel et al., 2021).

One of the relevant aspects of intense and prolonged rainfall is their potential to trigger shallow landslides in susceptible areas. Shallow landslides involve commonly a thin layer of the top-soil, i.e., the surface layer, and may evolve into debris flows or avalanches. Thus, shallow landslides represent a substantial risk to infrastructure, ecosystems, and oftentimes human lives, making their study of paramount importance in the fields of geohazards, environmental science, and civil engineering. Consequently, areas that were previously considered stable, may now face unprecedented risk of landslides, necessitating a re-evaluation of hazard assessments and mitigation strategies (Alvioli et al., 2018; Crozier, 2010; Gariano & Guzzetti, 2016; Jakob & Owen, 2021; Jemec Auflič et al., 2023; Tiranti & Ronchi, 2023).

Within this context, the role of vegetation in slope stability emerges as a crucial factor (Abe & Ziemer, 1991; Ali, 2010; Cecconi et al., 2012; Kokutse et al., 2016; Lehmann et al., 2019; Murgia et al., 2022; Nilaweera & Nutalaya, 1999; Operstein & Frydman, 2000; Schwarz, Lehmann, et al., 2010; Von Ruette et al., 2018; Ziemer, 1981a). As a matter of fact, vegetation influences mechanical and hydraulic soil parameters, such as cohesion, water uptake, and surface runoff. Consequently, vegetation could potentially mitigate landslides risk, representing an innovative and eco-sustainable solution, as an alternative to common engineering practices, which could be too impactful on environment and, not to mention, also expensive. Therefore, understanding these complex interactions between rainfall, soil, and vegetation, is essential for developing effective land management approaches and adaptation strategies in the face of climate change.

In addressing these complex challenges, various approaches to study and predict shallow landslides have been developed in the past years. These approaches can be broadly categorized into three main groups: statistical methods, physically-based models, and machine learning techniques.

Statistical methods have been employed in landslide susceptibility mapping for years (Brunetti et al., 2010; Budimir et al., 2015; Frattini et al., 2009; Guzzetti et al., 2007; S. He et al., 2020; Huang et al., 2022; C. T. Lee et al., 2008b; Martelloni et al., 2012; Peruccacci et al., 2017; Reichenbach et al., 2018; Rosi et al., 2016; J. Schmidt et al., 2008; Segoni, Piciullo, et al., 2018). These methods analyse the historical relationship between landslide occurrences and just rainfall patterns, identifying rainfall thresholds that, once exceeded, should indicate the possible triggering of landslides. For instance, techniques like logistic regression (C. Y. J. Peng et al., 2002), discriminant analysis, and frequency ratio models (L. Li et al., 2017) fall under this category. While these methods can provide valuable insights into landslide-prone areas, they often struggle to account for the dynamic nature of triggering factors. Another point against these models is that they are also site-specific, which means that a new model should be built every time a new area is studied, making them not scalable (Chung et al., 2017; Crosta, 1998; Gariano et al., 2015; Saito et al., 2010). In this study, these types of models are not taken into account, since literature has extensively explored them, and they would not represent an element of novelty for research purposes.

In contrast, physically-based models attempt to simulate the actual physical processes leading to slope instability. These models integrate all the geotechnical, hydrological, and mechanical principles in a simplified manner, to assess slope stability. They typically incorporate factors such as morphological and mechanical soil properties, groundwater dynamics, and in some cases also root reinforcement. The infinite slope model or more complex 3D models are some examples of this approach, but generally, depending on the degree of simplification, various models are present in the literature (Baum & Godt, 2010; Bishop, 1955; Bishop & Morgenstern, 1960; Borga et al., 1998; Formetta et al., 2016; Medina et al., 2021; Montgomery & Dietrich, 1994; Montrasio, 2000; Pack, 1998; G. Rossi et al., 2013; Salvatici et al., 2018; Vieira et al., 2010; von Ruette et al., 2017). However, such types of models offer the advantage of being able to translate well in different scenarios, beyond those for which they were originally designed, but they often require detailed input data, which can be challenging to obtain over large areas. The physically-based approach used in this work is SLIP (Shallow Landslide Instability Predictor) (Montrasio, 2000; Montrasio et al., 2011, 2013, 2014, 2018; Montrasio & Valentino, 2007, 2016a, 2016b), which leverages the limit equilibrium method coupled with simple and basic conceptualizations, like the infinite slope scheme and a simplified and homogenised water infiltration process, as well as the uniformization of roots in a single shear strength term. Based on these assumptions, SLIP is one of the best compromises between efficiency and quality, which means that it can be applied over large areas (challenging for elaborate models) within reasonable analysis timing, providing good space predictions, as demonstrated in different past studies (Gatto et al., 2023a; Misiano et al., 2023; Montrasio et al., 2009, 2010, 2012, 2015; Schilirò et al., 2015, 2016).

A new trend of recent years is instead machine learning, emerged as a powerful tool in various fields (Abiodun et al., 2018; Alzubaidi et al., 2021; Berahmand et al., 2024; Butler et al., 2018; Gardner & Dorling, 1998; Mountrakis et al., 2011; Otter et al., 2021; Sarker, 2021; Sze et al., 2017; Y. Yu et al., 2019), including landslide prediction and susceptibility mapping. Techniques such as artificial neural networks, support vector machines, and tree ensembles, like random forests (Breiman, 2001) or adaptive boosting (Schapire, 1999), can identify complex and non-linear relationships between landslide occurrence and predictor variables. In literature, the contributions of these types of approaches for shallow landslides prediction are various and increasing (Kadavi et al., 2018; Z. Liu et al., 2021; Ma et al., 2021; Merghadi et al., 2020; Nefeslioglu et al., 2008; Nhu et al., 2020; Nocentini et al., 2023; Tien Bui et al., 2016; H. Xu et al., 2023). These methods excel at pattern recognition and can integrate diverse datasets to make them interact, including remote sensing data. Such types of models often give high predictive accuracy with large and multidimensional data, as well as an astonishing speed and efficiency in terms of numerical processing, once trained. On the other hand, they may lack the explicit physical basis of the problem to analyse and be sensitive to the quality and representativeness of data used to train them. Particularly, the machine learning techniques adopted in this paper are random forests, adaptive boosting, adaptive logistic regression (Friedman et al., 2000), robust boosting (Freund, 2009), and finally neural networks (Cross et al., 1995; Kalhor, 2020; Merceron & Tato, 2020; Montavon, 2020; Svozil et al., 1997), which are a subset of machine learning, called deep learning. All these techniques are employed to create two possible model prototypes. The first one is a swift model that act like an advanced rainfall-threshold, to determine which areas could be susceptible for a specific rainfall event. In other words, a model that behaves as a filter for macro-areas. The second one is a detailed pixel-by-pixel model that analyses each cell of a given digital terrain model, i.e., a model that acts like a physically based approach on small scale.

This thesis aims to investigate the intricate relationships between rainfall-induced shallow landslides and vegetation cover, to use the acquired knowledge for civil protection purposes, i.e., to prevent landslides triggering or to control damage. By employing a combination of physically-based models and advanced artificial intelligence techniques, specifically neural networks, this research seeks to enhance our predictive capabilities and deepen the understanding of such type of geohazards. In fact, by combining a deterministic understanding of slope stability processes, derived by physically-based approaches, with pattern recognitions capabilities, entrusted to neural networks, a robust and comprehensive framework for assessing shallow landslide risk is developed and made available as a starting point for further studies in this direction. Hence, through this multifaceted approach, we seek to advance the field of landslide prediction and contribute to more effective strategies for mitigating the impacts of these hazards in a climate change, following a linear, natural, and step-by-step path.

More precisely, this study will be targeted and focused on:

- Investigating some historical events occurred in the past, analysing causes and consequences of triggering.
- Providing a comprehensive view of the state of the art on shallow landslide susceptibility and root reinforcement.
- Analysing the impact of rainfall patterns on shallow landslide occurrence.
- Evaluating the role and impact of vegetation in slope stability, considering differences between species.
- Developing and validating different predictive models, to identify high-risk areas and assess the stability at different scales, starting from macro to micro.
- Creating and developing a fast geo-spatial platform to specifically handle rainfall-induced shallow landslides, implementing various and numerous tools and models.
- Designing and modelling appropriate naturalistic support measures intended to stabilize possible susceptible slopes.
- Developing a simple and efficient landslide flow-path predictor, considering the physical and geomorphological aspects, as well as the dampening of vegetation.

In pursuit of these objectives, the work will be structured into chapters: Chapter I contains a general introduction and dissertation about shallow landslides, showing an overview of past occurrences, explaining the underlying dynamics of this complex problem, and discussing widely the main methodologies at our disposal and currently applied, taking into consideration the limitations as well. Chapter II illustrates the intricated problem of the vegetation in the context of slope stability, following a summary of the evolution of literature in this regard, highlighting recent discoveries and adopted techniques, but also clarifying the actual confines and future work to be undertaken in this field. Chapter III reveals all the techniques and theory employed particularly in this work, regarding both the physically-based and machine learning approach types. Chapter IV expounds the ad hoc built MATLAB platform (X-SLIP), describing the main founding principles, the structuring, functioning, and the potential, as well as possible improvements and future development directions. Chapter V shows some applications and results of the above-mentioned platform and models. Chapter VI analyses certain extra aspects of the shallow landslides problem, coupled with vegetation, introducing an eco-friendly solution to allow or facilitate vegetation growth in areas that would need those types of stabilization interventions and defining a simplified approach to simulate possible evolutions of flow-paths of landslides once triggered.

To conclude, the findings of this research can have significant implications for land use planning, landslide risk reduction, and climate change adaptation strategies. Furthermore, by reducing the gap between classic soil mechanics and data science, this study contributes to the broader goal and challenge of connecting two diametrically opposed ways of doing

science: starting from intuition and hypothesis to create models, achieve results, and explain the evidence, or starting from the model and the results to obtain answers from the evidence.

In other words, from the perspective of the writer, the paradigm of soil mechanics is to start from the bottom to end with a model based on specific physical laws that tries to reflect the reality. Certainly, a robust way to solve problems, which nevertheless is very difficult to implement with complex problems as shallow landslides, which have a lot of covariables and factors. In contrast, the paradigm of machine learning is to start from the top, i.e., the model is already built and gives results, hence the scientist task is to interpret it and understand its dynamics. This is a smart way of modelling a given problem, which, however, can lead to errors and drift away from the objective reality, especially with noisy or incorrect data. Connecting the two worlds means leveraging the benefits of both, so that, if desired, a certain physic law or property could be implemented during the building of a machine learning model, or alternatively, a pure machine learning model could be used as support to understand and then create a simplified classical physical model.

I SHALLOW LANDSLIDES

Shallow landslides, also called soil slips, are rapid and sudden mass movements of soil or organic matter, which typically occur within the upper layers of the surface, usually from 1 to 2 meters of depth. These events may evolve often into possible and subsequent debris flows or mud flows, depending on the initial composition and geomorphological aspects. Essentially, shallow landslides differ from deep-seated landslides in several key aspects: depth, speed, water content, triggering mechanisms, slip surface.

The depth, as above-mentioned, is confined to the near-surface soil layers, in contrast to deep-seated landslides, which may extend several meters or even tens of meters into the ground (Dou et al., 2015; Shou & Chen, 2021), like deep-seated gravitational slope deformations (DGSD).

The speed of shallow landslides could be very rapid, reaching in certain conditions also 10-20 m/s (Iverson, 1997; Marinelli et al., 2022; Rickenmann, 1999). This speed refers to the evolution of motion, which compared to deep-seated landslides as DGSV is impressively high. In fact, for instance, a common range of speed for DGSD is 1 to 100 mm/yr (Cignetti et al., 2023). Thus, the high speed of shallow landslides, coupled with the involved masses and volumes, which typically ranges from 10 to 10,000 m^3 (Bainbridge et al., 2022; H. Jiang et al., 2023; X. Liu et al., 2022), carry with them also a high disruptive power, as well documented by history, reviewed in the following sections.

The water content is a crucial aspect of rainfall-induced shallow landslides, because as suggested by the name, the main cause factor is the water originating from rainfall, which is retained in the pores of soil. Specifically, pore water is responsible for the reduction of cohesion in soils (consequently lowering the stabilizing shear forces and generating an eventual slope instability), but it also contributes to the fluid-like behaviour during motion.

The triggering mechanisms of shallow landslides are a combination of predisposing factors and immediate causes, generally and mainly related to short-term environmental changes. More in depth, the main causes are commonly intense rainfall events, but even other minor factors can contribute to the occurrence, as for instance: rapid snowmelts, which would mimic intense rainfalls; human activities like deforestation (García-Ruiz et al., 2017; Gatto et al., 2023b; Lehmann et al., 2019), changes in land use, construction activities, and improper drainage management; earthquakes (Hasegawa et al., 2009; C. T. Lee et al., 2008a), albeit more rarely. In contrast, deep-seated landslides may be caused also by geological

alterations, erosion at the base of the slopes, slope overloads, thermal variations (that would fracture rocks), and tectonic movements.

The failure surface, or slip surface, is in most cases parallel to the ground surface for shallow landslides. This characteristic is primarily due to the nature of the triggering mechanisms, above discussed. Indeed, as water infiltrates the soil, it creates a zone of saturation that moves downward, generating an interface between it and the underlying, less permeable, soil or bedrock. Consequently, the latter interface becomes the locus of failure. However, regardless of the type of landslide, the shape of the failure surface can vary depending on local conditions and could be planar, curved, or stepped. The planar failure is commonly seen in shallow landslides, especially when the soil type is colluvial and with an underlying bedrock. Curved, or "spoon-shaped" failure may also be seen in shallow landslides, when the soil is cohesive, or whenever there is a gradual transition in soil properties, but it is more commonly attributed to deep-seated landslides. Finally, stepped failure can be observed when different soil layers, or a series of weak interfaces, are present. In those cases, failure surface may follow a stepped pattern, moving along some predetermined lines or weak zones. Nevertheless, stepped failure represents a quite rare eventuality for shallow landslides, but more likely for deep ones, since they usually reach depths of several meters, increasing the probability of intersect different layers.

In other words, it could be briefly stated that shallow landslides failures are characterized in their own nature by:

- rapid response, because they can be triggered very quickly in response to rainfall events, often within hours or even minutes of intense precipitation.
- higher mobility, because the relatively thin mass, combined with high water content, often results in a great mobility and flow-like behaviour.
- sensitivity to surface conditions, because they rely on near-surface conditions such as vegetation cover, soil structure, and micro-topography.
- cyclical nature, because areas prone to shallow landslides may experience repeated failures over time, as the shallow soil mantle is replenished. Conversely, deep-seated landslides often involve larger, not replenishable, one-time movements.

On the other hand, regarding statistics, as can be guessed the incidence of shallow landslides varies greatly depending on geographical, geological, and climatic contexts. Several studies have attempted to quantify their occurrence and impact in our society, some of them invoking climate change (Alvioli et al., 2018; Crozier, 2010; Gariano & Guzzetti, 2016; Geertsema et al., 2009; Guzzetti, 2000; Jakob & Owen, 2021; Jemec Auflič et al., 2023; H. Y. Luo et al., 2023; Pourghasemi et al., 2018; Tiranti & Ronchi, 2023; Trezzini et al., 2013; Turner, 2018).

From a global point of view, a comprehensive study by Froude and Petley (Froude & Petley, 2018) analysed global landslide data from 2004 to 2016 and found that rainfall-triggered landslides, many of which were shallow landslides, caused over 55,997 fatalities worldwide during this period. The total number of landslide events considered was 4862. Another study by Dowling and Santi (Dowling & Santi, 2014), analysed debris flows from 1950 to 2011 and estimated that 213 landslides occurred, with 77,779 fatalities recorded. 143 of 213 debris flows were rainfall triggered landslides and their median number of human losses is equal to 9, which is a significant amount, especially considering that the evidence suggests a rise in occurrences of such events.

From a regional point of view, certain regions are particularly prone to shallow landslides. For instance, in Italy, shallow landslides account for approximately 50% of all landslide events, which are around 650,000 according to the historical inventories, updated to 2021, and 94% of Italian municipalities are at risk of landslides (Trigila et al., 2021). As a matter of fact, Italy is one of the countries most affected by this issue, counting a frequency of 8.52 fatal landslides per year, as suggested by Guzzetti in a study that analysed data from 1900 to 2002 (Guzzetti, 2000; Guzzetti et al., 2005). In other parts of the world, like for instance in the western United States, post-wildfire debris flows, often classified as shallow landslides and caused by climate change, have caused significant damage and loss of life in different historical events. Just to name a few, some memorable events are the Storm King Mountain (1994) and the Missionary Ridge Fire (2002), both in Colorado, or the Old e Grand Prix Fires and the Camp St. Sophia (2003) in California (Cannon & DeGraff, 2009). At the same time, in tropical regions like Southeast Asia, shallow landslides represent a recurring hazard during monsoon seasons (Burrows et al., 2023; Hao et al., 2020; Jones et al., 2021; Marc et al., 2019; Nagarajan et al., 2000).

Another significant aspect of shallow landslides to consider is their economic impact. Although the estimation of costs could be very difficult to quantify, even more so for specific hazards like shallow landslides, in this regard, the World Bank estimated that the global economic losses from landslides (including shallow landslides) exceed $20 billion annually (Crovelli, 2000; Fleming & Taylor, 1980; Galve et al., 2016; Hallegatte et al., 2019; H. G. Kim et al., 2018; Qi et al., 2023; UNDRR & CRED, 2020), and this is not the end. In fact, several studies suggest an increasing trend in the frequency of shallow landslides due to climate change (Alvioli et al., 2018; Burt et al., 2016; Cannon & DeGraff, 2009; Crozier, 2010; Guhathakurta et al., 2011; Jakob & Owen, 2021; Jemec Auflič et al., 2023; Lavell et al., 2012; Tiranti & Ronchi, 2023), particularly in mountainous regions. Instead, in Italy, the estimates are more uncertain but are close to 3 billion of economic loss per year, considering both landslides and flood (Lawrence, 2024; ‘Quanto Costa All’Italia La Crisi Climatica?’, 2021; ‘World Landslides Forum: Each Year, Landslides Cause Damage to 6 Billion Euros’, 2023; Trezzini et al., 2013).

Regarding possible solutions, nowadays, prevention and mitigation techniques for shallow landslides are different and may consist of a combination of engineering, land management, and technological solutions. Specifically, these techniques might include one or a combination of some of the following points: monitoring and early warning systems; nature-based solutions and soil bioengineering; structural measures; advanced numerical modelling; land-use planning and policy; public education and community awareness.

Monitoring and early warning systems (Baum & Godt, 2010; Guzzetti et al., 2020; Piciullo et al., 2017; Tarolli et al., 2021) rely on advanced remote sensing techniques using satellite imagery and LiDAR to detect slope deformations, real-time monitoring of rainfall and soil moisture using networks of sensors, and development of machine learning algorithms for improved prediction of possible landslide occurrence, based on multiple parameters, also called features.

Nature-based solutions and soil bioengineering (Abe & Ziemer, 1991; Ali, 2010; Bordoloi & Ng, 2020; Burylo et al., 2011; Cazzuffi et al., 2016; Cecconi et al., 2012; H. Jiang et al., 2023; Kokutse et al., 2016; Mickovski & van Beek, 2009; Misiano et al., 2023; Murgia et al., 2022; Nilaweera & Nutalaya, 1999; Phillips et al., 2021; Waldron & Dakessian, 1981; X. Wang et al., 2020; Ziemer, 1981a) may consist of strategic planting of deep-rooted vegetation, which increases soil cohesion and enhances slope stability; use of natural materials like jute netting or biodegradable nets for temporary slope reinforcement, while vegetation establishes; restoration of natural ecosystems, such as forests and wetlands, to enhance natural slope stability; implementation of sustainable urban drainage systems, to manage the runoff and reduce the pore water pressure in developed areas.

Structural measures (Z. Chen et al., 2016; Cheng et al., 2013; Kamchoom & Leung, 2018; Y. J. Kim et al., 2019; J. Liu et al., 2019; Nurtjahjaningtyas et al., 2023; Salimi & Ghazavi, 2021; H. Wu et al., 2020; G. Zhang et al., 2017) include the construction of retaining walls, soil nailing, live poles, and anchoring systems, to mechanically stabilize slopes; implementation of surface and subsurface drainage systems, to manage the water content in susceptible and landslide-prone slopes; use of geotextiles, geomembranes, and geocells both for soil reinforcement and pore water management.

Advanced numerical modelling means to make use of physically-based models (Alvioli et al., 2014; Borga et al., 1998; Dupuy et al., 2005; Dyson et al., 2023; Gatto & Montrasio, 2023; Kokutse et al., 2016; Medina et al., 2021; Misiano et al., 2023; Montgomery & Dietrich, 1994; Montrasio & Valentino, 2007, 2016a, 2016b; G. Rossi et al., 2013; Salvatici et al., 2018; Schilirò et al., 2015; Thomas & Pollen-Bankhead, 2010; Vieira et al., 2010; von Ruette et al., 2017) that would incorporate hydrological and geotechnical parameters for more accurate prediction of landslide susceptibility, but considering and integrating climate change scenarios into long-term landslide risk assessments. Obviously, the latter is a complex challenge and oftentimes prevented by the current limits in numerical computation of machines.

Land-use planning and policy involves the development of comprehensive landslide hazard maps (Cardinali et al., 2006; Gatto et al., 2023a; Guzzetti, 2000; Guzzetti et al., 2005; Kadavi et al., 2018; X. Li et al., 2023; Nagarajan et al., 2000; Notti et al., 2023; Puglisi et al., 2013) to inform about landslide risk zoning, the implementation of stricter building codes and laws, but also restricting the development in high-risk zones, identified as a result of geological and geotechnical assessments.

Public education and community awareness may be based on campaigns to educate residents about landslide risks and warning signs, a development of community-based early warning systems and evacuation plans, or also training programs for local authorities and emergency responders.

Despite these advancements, the management of shallow landslide risks remains challenging, particularly in the context of climate change. The increasing frequency and intensity of extreme weather events, coupled with ongoing land-use changes in many regions, underscore the need for continued research, innovation, and interdisciplinary collaboration in this field. Future directions of studies may include the development of more sophisticated artificial intelligence data-driven prediction models, supported by physical modelling or laws, the integration of real-time monitoring data with automated early warning systems, and the exploration of some novel, sustainable materials for slope stabilization.

In the following sections, first and foremost, an overview of the possible types of shallow landslides is given. Following this, an analysis of the past historical evidence is summarized. Additionally, some statistics and relevance of Emilia-Romagna region in shallow landslides are discussed, and some common issues of the current landslide inventories are outlined. Finally, the current state of the art is shown and commented.

1.1 Shallow Landslide Types

David J. Varnes proposed in 1978 the first landslide classification system (Varnes, 1978), later refined and updated (Cruden & Varnes, 1996; Hungr et al., 2014). The afore-mentioned studies remain a fundamental framework for categorizing landslides and continue to be pertinent today, especially for shallow landslides. Within this system, shallow landslides can be primarily classified based on the type of movement and the material involved. Particularly, the main types of shallow landslides include shallow translational, shallow rotational, and complex landslides, but also flows, which could be essentially debris, earth, or mud flows, and finally avalanches, which are extremely rapid mass movements.

a. Shallow translational landslides involve the movement of a relatively thin layer of soil or rock along a planar or undulating surface. They are characterized by a length-to-depth ratio typically greater than 10:1 and often occur parallel to the slope surface. These slides are common in colluvial soils and are frequently triggered by intense rainfall events.

b. Shallow rotational landslides are less common than translational slides in shallow contexts. They involve the rotation of a soil or rock mass around an axis parallel to the slope contour. In shallow settings, they may occur in homogeneous, cohesive soils or weak rock masses.
c. Complex and compound landslides are landslides that exhibit characteristics of multiple movement types, either simultaneously (complex) or sequentially (compound). For instance, a shallow translational slide may evolve into a debris flow as it moves downslope.
d. Debris flows are rapid mass movements of fully saturated and unconsolidated debris that behave like viscous fluids. They are particularly relevant to shallow landslide studies as they often initiate as shallow slides before transforming into flows due to increased water content and loss of internal structure.
e. Earth flows are movements similar to debris flows but composed primarily of fine-grained materials (predominantly smaller than sand size), these can occur as shallow phenomena in certain geological contexts.
f. Mud flows are distinguished from earth flows by their higher water content and lower viscosity. They are characterized by very rapid to extremely rapid flow of saturated plastic clay or silt. In the context of shallow landslides, mud flows can originate from the liquefaction of fine-grained surface deposits during intense rainfall events.
g. Debris avalanches category refers to very rapid to extremely rapid shallow flows of partially or fully saturated debris on a steep slope. They are distinguished from debris flows by their lack of confinement in an established channel. Debris avalanches are particularly relevant to shallow landslide studies in mountainous terrain.

The material composition of shallow landslides is typically categorized as either "debris" (coarse material) or "earth" (fine material), with the distinction based on the percentage of coarse grain sizes in the displaced mass. Moreover, the Hungr classification (Hungr et al., 2014) also emphasizes the role of different factors in determining landslide behaviour, as the importance of water content, material plasticity, and the rate of movement, which can range from slow (fearth flows) to extremely rapid (debris flows and avalanches).

To conclude, the updated landslide classification system provides a comprehensive framework for understanding the mechanics, behaviour, and potential impacts of different types of shallow landslides. It serves both for research methodologies and risk management strategies in landslide-prone areas, offering a nuanced approach to categorizing and analysing these complex geomorphological phenomena.

1.2 Historical Evidence Of Shallow Landslides

The occurrence of shallow landslides has been well documented throughout human history, with evidence found in geological inventories, historical accounts, and also archaeological findings. Actually, some of the notable historical references date back to Ancient Roman period, with some writings, such as those by the Roman author Gaius Plinius Secundus, also called Pliny the Elder (23-79 AD), which described landslide events that would be now classified as shallow, based on his description. Another instance is the one of Leonardo da Vinci's notebooks (15th-16th century), which contain observations on the movement of earth and water that resemble shallow landslide processes. To finally reach more recent times, with the Vajont Dam disaster in Italy (1963), which, though not a shallow landslide itself, brought particular attention towards the study of various landslide types, including shallow ones. In fact, shortly thereafter Vernes would publish his findings in his groundbreaking research on the subject: Slope Movement Types and Processes (Varnes, 1978) and Landslide types and processes (Cruden & Varnes, 1996).

However, it can be said that systematic scientific study of shallow landslides began even earlier, in the first half of the 20th century. Some pioneering work that could be cited are by geologists and engineers such as Karl Terzaghi (Terzaghi, 1943), which laid the foundation for modern soil mechanics and slope stability analysis. Subsequently, the development of technologies like aerial photography and later satellite imagery, in the second half of the 20th century, significantly advanced the ability to study and map shallow landslides on a larger and macro scale.

In the following paragraphs, a chronological and brief summary of some past, major, and memorable shallow landslide events is reported, to emphasize the problematic and catastrophic nature of such phenomena.

1.2.1 Sarno e Quindici, Campania (1998)

The Sarno and Quindici disaster of May 1998 stands as one of the most catastrophic shallow landslide events in recent Italian history, providing a stark illustration of the devastating potential of these geohazards. This case study offered valuable insights into the triggering mechanisms, progression, and consequences of rainfall-induced shallow landslides in urbanized mountainous terrain.

On May 5-6, 1998, an exceptional precipitation event occurred in the Campania region of southern Italy, primarily affecting the Sarno area, near Naples. Meteorological records indicate that over a 72-hour period, rainfall accumulation exceeded 240-300 mm, far surpassing typical values of Campania. This intense and prolonged rainfall event served as the primary trigger cause for a series of violent mass movements.

Water infiltration led to the initiation of numerous soil slips on the slopes of Mount Pizzo d'Alvano. These initial failures rapidly evolved into debris flows, which proceeded downslope,

with a powerful kinetic energy and devastating effect. The impact was particularly severe in the surrounding urban areas, including a direct hit on the 'Villa Malta' Hospital in Sarno. Concurrent with the events in Sarno, approximately ten additional landslide events occurred on the eastern mountain slopes of Avellino province. Two of these events were especially significant, affecting the towns of Quindici, Siano, Bracigliano, and San Felice a Cancello.

The consequences of all these disasters were profound and tragic, placing this among the most catastrophic events recorded in Italy. In fact, the final toll included:

- fatalities - 161 deaths, most of which (137) occurred in Sarno, followed by 11 in Quindici, and 5 in Siano.
- injuries - approximately 350 people were wounded.
- infrastructure damage - entire sections of affected towns were obliterated, most notably the Episcopio district of Sarno, which was completely destroyed.
- displacement - an estimate of 3,000 citizens were displaced from their homes.

The Sarno and Quindici disaster underscores several critical aspects of shallow landslide hazards. To begin with, the rapid onset, since the swift transition from intense rainfall to catastrophic mass movements highlights the potential for rapid initiation of shallow landslides. Moreover, urban vulnerability, given that the severe impact on populated areas, including critical infrastructure such as the hospital, demonstrates the heightened risk in urbanized mountainous regions. Additionally, the multi-hazard nature, because the event illustrates how multiple landslides can occur simultaneously across a region during extreme weather events, complicating emergency response efforts. To conclude, the role of the geomorphological context, as the disaster emphasizes the importance of understanding local geomorphology, since the local mountainous terrain contributed significantly to the destructive power of the various debris flows occurred.

In conclusion, this event served as a catalyst for enhanced research into shallow landslide processes and revealed the necessity to develop more robust early warning systems in Italy. It also highlighted the critical need for improved land-use planning and risk management strategies in areas prone to such hazards. Thus, the Sarno and Quindici disaster remains a seminal case study in the field of landslide hazard assessment and management, offering valuable lessons for researchers and practitioners who are working to mitigate the risks associated with rainfall-induced shallow landslides, in populated mountainous regions worldwide, and beyond.

Figure I-1: The Sarno landslide event, May 5-6, 1998

1.2.2 MESSINA, SICILIA (2009)

The Messina disaster of October 1-2, 2009, represents another significant case study in the field of rainfall-induced shallow landslides, illustrating once again the destructive potential of these geohazards in densely populated coastal regions. This event, which occurred in northeastern Sicily, provides valuable insights into the dynamics of rapid-onset shallow landslides triggered, but this time, in contrast to Sarno, by intense and short-duration rainfall.

On the evening of October 1, 2009, extending into the early hours of October 2, the northeastern coast of Sicily experienced an exceptionally intense, albeit brief, precipitation event. The area most severely affected was the Ionian coastal region immediately south of Messina city. Meteorological data indicate that approximately 220-230 mm of rainfall was recorded within a mere 8-hour period (between 15:00 and 23:00), with some localities experiencing even higher precipitation peaks. This extreme rainfall intensity far exceeded the soil's water retention capacity, rapidly saturating the shallow subsurface, lowering stabilizing forces, and triggering numerous soil slips.

The most severely impacted areas included: Scaletta Marina, in the municipality of Scaletta Zanclea, where debris flows inundated approximately 700 meters of the town; several localities within the Messina municipality, i.e., Giampilieri Superiore, Giampilieri Marina, Altolia, Molino, Santo Stefano di Briga, Briga Superiore, and Pezzolo; Guidomandri district, which reported significant damage; other areas within Scaletta Zanclea and Itala municipalities.

The consequences of this disaster were severe and multifaceted. In fact, the final toll included:

- fatalities - 37 deaths were recorded.
- injuries - 29 individuals required hospitalization.

- infrastructure damage - critical transportation arteries were severely impacted, including the Strada Statale 114 Orientale Sicula (a major highway), the A18 motorway, and the Messina-Catania railway line.
- displacement - 564 people were evacuated from their homes.

The disruption to these key transportation routes resulted in the complete isolation of numerous towns and districts, and various forms of communication were also severed at the same time. The most catastrophic impacts on infrastructure were observed in Giampilieri (Messina), where rapid debris flows caused extensive destruction.

This event, like the event of Sarno, highlights roughly the same critical aspects of shallow landslide hazards: the rapid onset, in this case more pronounced, due to the shorter rainfall time window, which left too little time for warning or evacuation; the spatial distribution, because especially in this instance, the widespread occurrences, across multiple municipalities, illustrates the potential for simultaneous, geographically dispersed events during extreme rainfall episodes; the infrastructure vulnerability and the urban risk, since there were no other alternative or emergency communication routes; the hydrological trigger, as the event provides a clear example of how short-duration and high-intensity rainfall can be the main cause of shallow landslides, particularly in steep slope areas with susceptible geology.

To conclude, also the 2009 Messina disaster serves as a crucial case study for researchers and practitioners in the field of landslide hazard assessment and management, highlighting the same needs identified from the Sarno case study, that is to have improved early warning systems, as well as the integration of landslide risk into urban planning and infrastructure design for susceptible coastal and mountainous regions. Furthermore, this event underscored and reinforced, 11 years after the Sarno event, the necessity of comprehensive and multi-hazard approaches.

Figure I-2: The Messina landslide event, October 1-2, 2009

1.2.3 Genova - La Spezia - Massa-Carrara, Liguria and Toscana (2011)

The autumn of 2011 saw a series of devastating shallow landslide events in the regions of Liguria and Tuscany, Italy, providing multiple case studies and highlighting the destructive potential of these geohazards when triggered by extreme rainfall events. This section examines three significant episodes that occurred in La Spezia and Massa-Carrara on October 25, and in Genoa on November 4, 2011.

La Spezia (Liguria) and Massa-Carrara (Tuscany) refer to a single event, occurred on October 25, 2011, due to an exceptionally intense rainfall event, as the previous case studies. Within a mere 6-hour period, cumulative rainfall reached a staggering amount of 542 mm. This extreme rainfall triggered numerous soil slips, resulting in catastrophic consequences for the affected areas. The impact of this event was severe and counted:

- fatalities - 13 lives were lost.
- economic losses - the total estimated damages amounted to 116,213,535 €.
- infrastructure damage - significant damage to transport networks occurred, including the collapse of a section of the A12 motorway.
- displacement - 1,183 individuals were evacuated from their homes.

Moreover, a notable aspect of this event was the correlation between land use changes and landslide occurrence. Analysis of 88 landslide cases revealed a statistically significant relationship between agricultural land abandonment and landslide incidents. In this case study, 92.05% (81 cases) showed evidence of land abandonment, and only 7.95% (7 cases) occurred in areas without signs of abandonment, with 5 of these in actively cultivated areas and 2 in recently deforested zones. This finding highlights the potential role of land management practices in mitigating shallow landslide risks.

Another catastrophic event, like the La Spezia and Massa-Carrara, is the Genoa event, occurred on November 4, 2011, just over a week later. In a matter of hours, approximately 500 mm of rainfall was recorded, triggering numerous shallow landslides throughout the urban and peri-urban areas. The consequences of this event were equally severe, albeit less serious than La Spezia and Massa-Carrara:

- fatalities - 6 lives were lost.
- injuries - 13 people were injured.
- displacement - 120 residents were evacuated from their homes.

Both the La Spezia Massa-Carrara and the Genoa events, occurring in close geographical and temporal proximity, provide valuable insights into the nature and impact of shallow landslides in the Liguria and Tuscany regions. Specifically, both events were characterized by extremely high rainfall intensities over short durations, i.e., around 500 mm in 6 hours or less, far exceeding the infiltration capacity of the soil and rapidly triggering multiple landslides.

The affected areas were both coastal (Genoa, La Spezia) and inland (Massa-Carrara), demonstrating the widespread vulnerability of this region to such events. Both the events highlighted a particular vulnerability of urban and peri-urban areas, where the consequences of landslides were amplified due to high population density and inadequate infrastructure. The strong correlation between land abandonment and landslide occurrence in the La Spezia and Massa-Carrara event denote the importance of land management practices in landslide risk mitigation. The substantial financial damages reported (over €116 million for the La Spezia and Massa-Carrara event alone) highlight the significant economic impact of these disasters. The damage to major transportation networks, including highways and local roads, demonstrates the potential for shallow landslides to cause widespread disruption to critical infrastructure.

As reported in the previous case studies, these events collectively emphasize the need for an improved early warning system and an enhanced land use planning and management, particularly in areas prone to abandonment.

To conclude, the 2011 Liguria and Tuscany shallow landslide events add to the others, previously treated, thus they equally serve as critical case studies for researchers and practitioners in the field of shallow landslides.

Figure I-3: The La Spezia and Massa-Carrara landslide event, October 25, 2011

1.2.4 VARGAS, VENEZUELA (1999)

The Vargas disaster of December 1999 stands as one of the most, if not the primary, catastrophic shallow landslides. This event, occurred in Vargas State, Venezuela, on December 15, 1999, is comparable to the Sarno event in Italy, but on a larger scale and with markedly more serious consequences.

Particularly, between December 14-16, 1999, Vargas State experienced an extraordinary period of torrential rainfall. Rainfall amount over this three-day period reached 911 mm, with a remarkable peak intensity of 72 mm, recorded just in a single hour. This extreme rainfall

was attributed to a stationary cold front interacting with tropical moisture, creating ideal conditions for sustained and intense precipitation.

The prolonged, high-intensity rainfall led to a widespread increase of saturation in the thin mantle of the soil that overlay the steep, characterized by metamorphic bedrock of the Coastal Cordillera mountains. The high level of saturation triggered thousands of shallow landslides, which rapidly evolved into massive and hyper concentrated debris flows as they moved downslope. The mountainous topography, characterized by short, steep watersheds, facilitated the swift movement of these flows towards the densely populated coastal areas. As a result, the final scale and the intensity of this disaster were unprecedented in Venezuela's recent history:

- fatalities - estimates suggest that approximately 30,000 people lost their lives, representing nearly 10% of Vargas State's population at the time, thus a huge and impressive number in the history. This high mortality rate underscores the extreme rapidity and destructive power of the shallow landslides, evolving into debris flows.
- infrastructure damage - entire communities were obliterated by the landslides and debris flows. Some examples that can be cited are Los Corales, a neighbourhood buried under 3 meters of debris, or Cerro Grande and Carmen de Uria, two towns that were completely razed and effectively ceased to exist post-disaster.
- economic losses - while precise figures are challenging to ascertain, the economic losses were substantial, including destruction of homes, businesses, roads, and other critical infrastructure, without counting the potential productivity that the totally or partially abandoned cities would have had in the future.
- geomorphological changes - the event significantly altered the coastal landscape, with massive sediment deposition creating new alluvial fans and modifying existing drainage patterns.
- displacement – around 190,000 people were evacuated, and moreover thousands of survivors were permanently displaced.

The same critical aspect, highlighted in the previously mentioned case studies, can be reported also for the Vargas disaster. Once more, the disaster clearly illustrated the intrinsic risk of shallow landslides, namely the potential to trigger a cascade of secondary hazards, more impactful than simple sliding of soil on a surface, like debris flows, flash floods, and coastal sedimentation.

The needs that emerged from this event, as previously discussed, are an efficient and improved early warning system, an enhanced land use planning and management, and comprehensive multi-hazard approaches.

Ultimately, the 1999 Vargas disaster remains a seminal case study in the field of shallow landslide research and disaster risk management. Its unprecedented scale and impact

continue to inform scientific understanding of extreme rainfall-induced landslide events and shape approaches to risk mitigation in similarly vulnerable regions worldwide.

Figure I-4: The Vargas landslide event, December 15, 1999

1.2.5 Southern Leyte, Philippines (2006)

The Southern Leyte landslide of February 17, 2006, represents a significant case study in the field of shallow landslide research, slightly different from the previously treated, since it illustrates the complex interplay between prolonged rainfall, local geology, but also seismic activity in triggering catastrophic mass movements.

The landslide event was preceded by a period of intense and sustained precipitation. In fact, between February 4 and February 14, 2006, the region experienced approximately 1200 mm of rainfall. This prolonged period of heavy precipitation led to significant soil saturation and increased pore water pressure within the slope materials.

Compounding the effects of the rainfall, the area experienced a minor seismic event on February 17. Although relatively small, with a magnitude of 2.6 on the Richter scale, this earthquake may have played a crucial role in the final destabilization of the already saturated slope. As a matter of fact, quick loads as seismic waves may suddenly increase the pore water pressure and nullify stabilizing forces, especially with clayey soils, because the drainage of water from the pores is prevented by the soil itself, considering that water release would require more time, depending on the soil particle size distribution.

The resulting landslide was characterized as a shallow, rapid earth movement, primarily involving the upper layers of soil and weathered rock. The combination of saturated conditions and seismic perturbation led to a catastrophic failure, generating a fast-moving debris flow that engulfed significant portions of inhabited areas. Despite the inhabited areas, severe impacts and consequences were experienced also in urban zones:

- fatalities - the event claimed 1,126 lives plus 246 people declared missing, marking it as one of the deadliest landslides in recent Philippine history.

- infrastructure damage - extensive destruction of residential areas, agricultural land, and local infrastructure occurred within the path of the debris flow.
- economic losses - no precise figures are available, due to the challenging nature. However, the economic impact was substantial, encompassing direct damage to property and long-term disruption of local livelihoods.
- displacement – around 19,000 people were displaced.

The magnitude of the disaster prompted a significant international emergency response. Multiple nations contributed to relief efforts, with substantial financial resources mobilized to support immediate rescue operations and subsequent recovery initiatives.

The Southern Leyte disaster highlighted a new possible critical aspect of shallow landslides, that is the seismic influence. Specifically, the role of the minor earthquake in potentially triggering the landslide emphasizes the need to consider even low-magnitude seismic events in landslide susceptibility assessments, especially in areas already destabilized by prior heavy rainfall.

In summary, the 2006 Southern Leyte landslide stands as a poignant example of the complex and often unpredictable nature of shallow landslide hazards in tropical, mountainous environments. The devastating impact of this event continues to inform scientific understanding of the interaction between rainfall, seismic activity, and slope stability. The lessons learned from this event are crucial for improving landslide risk assessment, early warning systems, and disaster preparedness strategies.

Figure I-5: The Southern Leyte landslide event, February 17, 2006

1.2.6 RIO DE JANEIRO, BRASILE (2011)

The Rio de Janeiro landslide disaster of January 2011 is one of the most devastating shallow landslide events in Brazil. Particularly, during January 2011, the mountainous region north of Rio de Janeiro experienced an exceptional period of intense rainfall. On January 11 and 12, precipitation totals in some areas exceeded 280 mm in a 24-hour period, with some locations recording over 100 mm in a single hour. This extreme rainfall event was attributed to the

South Atlantic Convergence Zone, a meteorological phenomenon known for producing intense summer rainfall in southeastern Brazil.

The prolonged and high-intensity rainfall led to widespread high saturation of the thin soil mantle overlying the crystalline bedrock, typical of the region. This saturation, combined with the steep topography of the Serra do Mar mountain range, triggered thousands of shallow landslides. Many of these rapidly evolved into destructive debris flows and mudflows as they moved downslope towards populated areas. Consequently, the scale and intensity of the disaster were unprecedented, considering the region's history:

- fatalities - official reports indicated that over 900 people lost their lives, but some estimates exceeded 1,000 fatalities.
- infrastructure damage - extensive destruction occurred across several municipalities, including Nova Friburgo, Teresópolis, and Petrópolis. Numerous buildings, roads, and bridges were destroyed or severely damaged.
- economic losses - the economic losses were substantial, estimated to be in the hundreds of millions of dollars.
- environmental consequences - the event caused significant environmental damage, including alterations to local river systems and destruction of natural habitats.
- displacement - approximately 35,000 people were displaced, many losing their homes entirely.

In closing, the 2011 Rio de Janeiro landslide disaster remains a seminal case study in the field of urban landslide risk management. As urbanization continues to expand into hazardous terrain in many parts of the world, the insights gained from the Rio de Janeiro disaster become ever more relevant for global efforts in landslide risk mitigation and sustainable urban development.

Figure I-6: The Rio de Janeiro landslide event, January 11, 2011

1.2.7 UTTARAKHAND, INDIA (2013)

The Uttarakhand disaster of June 2013 stands as one of the most severe natural calamities in India's recent history, second only to the 2004 Indian Ocean tsunami in terms of its devastating impact. This event provides a critical case study for understanding the complex interplay between extreme meteorological conditions, fragile Himalayan ecology, and anthropogenic factors in triggering catastrophic shallow landslides and associated hazards.

During the 16-17th of June 2013, the state of Uttarakhand experienced unprecedented rainfall, far exceeding typical monsoon patterns for the region. The India Meteorological Department reported that some areas received rainfall up to 375% above the normal June average. Precisely, some rain gauges recorded around 400 mm in just 24 hours. This extreme precipitation was attributed to the unusually early arrival and intensity of the monsoon, combined with a weather system that remained stationary over the region.

As commonly happens, the prolonged and high-intensity rainfall led to widespread saturation of the soil mantle in the geologically young and fragile Himalayan terrain. Consequently, this saturation triggered numerous shallow landslides across the region. The disaster was further exacerbated by the cascading nature of the hazards. In fact, multiple landslides blocked river channels, creating temporary dams. Subsequently, the breach of these landslide dams resulted in flash floods and debris flows, and as a result, river channels, swollen with rainfall and debris, overflowed their banks, causing extensive flooding in downstream areas. Severe impacts and consequences were experienced after this unprecedented disaster:

- fatalities - official reports indicated 5,748 lives were lost.
- infrastructure damage: an astounding number of 4,550 villages were severely affected or destroyed, highlighting the widespread nature of the disaster.
- economic impact - precise figures are challenging to ascertain, but the economic losses were substantial, estimated to be in billions of dollars. This included damage to homes, infrastructure, agricultural land, and the tourism industry, a key economic driver in the region.
- environmental consequences - the event caused significant alterations to the local landscape, including changes in river courses, destruction of forested areas, and destabilization of slopes, hence, potentially increasing future landslide risks.
- displacement: tens of thousands of people were displaced, with many losing their homes and livelihoods.

In conclusion, the 2013 Uttarakhand disaster remains a seminal case study in the field of mountain hazard management. Its unprecedented scale and impact continue to inform scientific understanding of extreme weather-induced landslide events in the Himalayas and other mountain regions globally. Furthermore, as climate change continues to alter

precipitation patterns and exacerbate extreme weather events, the insights gained from the Uttarakhand disaster become increasingly relevant for global efforts in landslide risk mitigation and sustainable mountain development.

Figure I-7: The Uttarakhand landslide event, June 16, 2013

1.2.8 Freetown, Sierra Leone (2017)

The Freetown landslide of August 14, 2017, stands as the most devastating natural disasters in Sierra Leone's recent history. This event provides a critical case study for understanding the complex interplay between extreme rainfall, rapid urbanization, and environmental degradation in triggering catastrophic shallow landslides in tropical urban settings.

In the early hours of August 14, 2017, Freetown, the capital city of Sierra Leone, experienced the most intense rainfall event. Particularly, the Freetown meteorological station recorded approximately 400 mm of rain within a 24-hour period, of which 264 mm just in 6 hours, from 3 to 9 am. Such a volume is nearly three times the average of August rainfall for the area. This extreme precipitation was attributed to a combination of factors, including the intensification of the West African monsoon and local topographic effects.

The intense rainfall led to rapid saturation of the soil mantle on the steep slopes of Sugar Loaf mountain, in the Regent area of Freetown. At approximately 6:00 am local time, a massive shallow landslide was triggered. The initial slope failure rapidly evolved into a debris flow, incorporating large volumes of soil, rock, and vegetation while it moved downslope towards densely populated areas. The scale and intensity of the disaster were unprecedented in Sierra Leone, revealing severe impacts and consequences:

- fatalities - official reports indicated that over 1,100 people lost their lives, with some estimates suggesting the death toll may have been even higher. Many victims were buried alive as the debris flow engulfed homes and informal settlements.
- infrastructure damage - extensive destruction occurred in the affected areas, with hundreds of buildings destroyed or severely damaged. Critical infrastructure, including roads and bridges, was also impacted.

- economic impact - no precise figures are available, but the economic losses were substantial for a country already facing significant economic challenges.
- health consequences - in the aftermath of the landslide, there were serious concerns about the spread of waterborne diseases, particularly cholera, due to contaminated water sources and disrupted sanitation systems.
- displacement - approximately 3,000 people were rendered homeless, with many losing all their possessions in the disaster.

To conclude, the 2017 Freetown landslide disaster, as all the other treated, remains a seminal case study in the field of urban landslide risk management in developing countries. As urbanization continues to accelerate in many parts of the Global South, the insights gained from the Freetown disaster become ever more relevant for global efforts in landslide risk mitigation and sustainable urban development in vulnerable regions.

Figure I-8: The Freetown landslide event, August 14, 2017

1.3 EMILIA ROMAGNA IN THE CONTEXT OF SHALLOW LANDSLIDES

Emilia-Romagna is one of the 20 Italian regions and stands out as one of the most significant and interesting for shallow landslide phenomena within the country, presenting a complex interplay of geological, meteorological, and anthropogenic factors that contribute to its high susceptibility to this type of hazards.

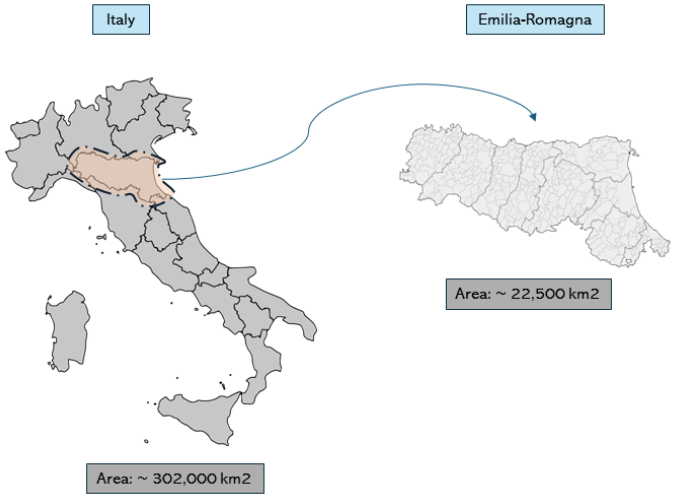

Figure I-9: Geolocation of the Emilia-Romagna region

According to the Italian Superior Institute for Environmental Protection and Research (ISPRA), Emilia-Romagna is one of the most landslide-prone regions in Italy. Approximately 11.4% of its territory is classified as having "very high" or "high" landslide hazard (Trigila et al., 2021). The Regional Agency for Prevention, Environment and Energy of Emilia-Romagna (ARPAE) reports that the region hosts about 80,000 landslides, covering an area of nearly 2,510 km^2, which constitutes about 11.4% of the region's mountainous and hilly territory (Pavan et al., 2021; Trigila et al., 2018, 2021). By way of example, a recent intense and prolonged rainfall event, occurred on May 15-17, 2023, following another previous event occurred between 1st and 4th of May 2023, underscored the ongoing vulnerability of Emilia-Romagna to shallow landslides, causing several damage and disruption. In fact, during this events, respectively 210 mm (May 1-4) and 240 mm (May 15-17) of cumulative rainfall were reached, triggering around 300 landslides, most of these interfering with infrastructure like highways and railroads, resulting in millions of euros worth of economic damage. Additionally, it should be noted that the vast majority of landslides were debris and earth flows, or also translational soil slips, with a trigger area less than 1,000 m2 observed in 72% of total cases, thus very likely shallow landslides (Brath et al., 2023; ISPRA, 2023).

Figure I-10: The Emilia-Romagna landslide event of May 2023

The susceptibility of Emilia-Romagna region to shallow landslides is attributed to its complex geological setting. Specifically, Emilia-Romagna Apennines are characterized by weak and clay-rich formations that are particularly prone to full saturation and consequently to instability. Furthermore, the topography of Emilia-Romagna plays a crucial role in landslide occurrence. The transition from the Po Plain to the Apennine chain creates steep gradients and complex slope geometries that are conducive to shallow landslide initiation. Thus, topographic setting, combined with the weak lithological units, creates a naturally susceptible environment for mass movements.

Another crucial issue is the climate of this region, characterized by distinct wet seasons and the potential for intense rainfall events, which further exacerbates the landslide risk. Various researchers developed rainfall thresholds and physical models for the initiation of landslides in this region (Bardi et al., 2017; Berti et al., 2012; Bertolini et al., 2005; Ferrario & Livio, 2024; Martelloni et al., 2012; Montrasio et al., 2009, 2011, 2012; Montrasio & Valentino, 2008a, 2008b; M. Rossi et al., 2010; Segoni et al., 2015; Segoni, Rosi, et al., 2018; Zhao et al., 2019), demonstrating the strong correlation between intense or prolonged rainfall and shallow landslide occurrence. Besides, climate change projections are suggesting an increase in extreme precipitation events for the Mediterranean region (including northern Italy) indicate a potential for increased shallow landslide activity in the future.

In addition to the factors above cited, also human activities have significantly influenced landslide susceptibility in Emilia-Romagna. Land-use changes, particularly deforestation and urbanization in hilly and mountainous areas, have altered slope hydrology and stability. Additionally, the expansion of infrastructure and urban areas into landslide-prone zones has increased the potential consequences of shallow landslide events. This is particularly

concerning given the high population density and economic importance of many areas within the Emilia-Romagna region.

In the national context of Italy, Emilia-Romagna ranks third among Italian regions for the number of municipalities affected by landslide risk, with 307 out of 328 municipalities (93.6%) exposed to some degree of landslide hazard (Trigila et al., 2018, 2021). This high level of exposure, combined with the region's significant population density and economic importance, makes Emilia-Romagna one of the first critical areas for shallow landslide risk in Italy. Actually, this region has been and still is at the forefront of developing landslide risk management strategies. The Emilia-Romagna Geological Survey has implemented advanced landslide monitoring systems and early warning protocols, particularly for shallow, rapid-moving landslides. These efforts include the use of satellite-based InSAR techniques for regional-scale landslide detection and monitoring (Bayer et al., 2017).

Looking forward, the challenge of managing shallow landslide risk in Emilia-Romagna is likely to grow. Factors such as climate change, ongoing urbanization, and the aging of existing infrastructure will necessitate continued investment in research, monitoring, and mitigation efforts. The development of more sophisticated early warning systems, improved land-use planning, and the implementation of nature-based solutions for slope stabilization are areas of active research and policy development in this region.

Therefore, the high susceptibility of Emilia-Romagna to shallow landslides, combined with its demographic and economic significance, makes it a critical case study for understanding and managing these hazards in Italy and beyond. In fact, the region's experience offers valuable lessons for other areas facing similar challenges, particularly in the context of climate change and increasing human pressure on marginal lands. Continued research and innovation in landslide risk management in Emilia-Romagna will be crucial for enhancing resilience and reducing the impacts of these hazards on communities and infrastructure in the coming decades. These are some of the reasons why different case studies of this work, shown in following sections, take place in Emilia-Romagna.

1.4 Current Landslide Inventories, Problem And Solution

Landslide inventories and databases are the cornerstone in risk assessment and management strategies, serving as crucial resources to understand the spatial and temporal distribution of mass movements. These repositories are typically compiled through a combination of diverse methods, each one with its own pros and cons.

Some examples of standard techniques to create landslide datasets are field surveys, aerial photography, or satellite imagery. Field surveys, while providing detailed ground-truth data, are often time-consuming and may be limited in scope due to accessibility issues. Aerial photograph interpretation allows for historical analysis and covers large areas but may miss smaller landslides, which commonly are shallow, or those obscured by vegetation. Satellite

imagery analysis offers wide coverage and frequent updates but may have limitations on resolution which could not allow to detect smaller landslides, typically shallow.

In recent years, more advanced technologies are increasingly being employed to enhance the accuracy and comprehensiveness of landslide inventories. These technologies refer to LiDAR and InSAR. LiDAR (Light Detection and Ranging) provides high-resolution and 3D topographic data, useful for detecting subtle landslide features, but it can become in some cases very expensive and requires specialized processing. Instead, InSAR (Interferometric Synthetic Aperture Radar) excels at detecting slow-moving landslides and measuring ground deformation over time, though it can be affected by vegetation and rapid ground changes. However, the latter technique is not recommended for shallow landslides.

Simultaneously, emerging innovative techniques are also being integrated into the landslide mapping toolkit. In fact, it is possible to employ new instruments like drones and GPS, as well as using seismic data, or exploiting citizen alerts via smartphones. Drone-based photogrammetry offers high-resolution imagery and 3D models of landslide areas, particularly useful for terrains that would have been inaccessible. GPS surveying, instead, is similar to field surveys and aligns closely with it, but additionally provides precise positional data for landslide features, enhancing the spatial accuracy of inventories. Seismic data analysis can help in identifying landslide events, especially in remote areas, since the principle of a landslide is the same of an earthquake: it consists of a movement of the earth, that emits waves with a certain energy. Citizen science initiatives, leveraging new mobile technologies, are emerging as a promising avenue for supplementing professional data collection efforts, particularly in remote or understudied areas, and possibly through specific smartphone apps which require data gathering to adhere to certain standards.

Despite these varied approaches, the creation and maintenance of comprehensive landslide inventories face several significant challenges. Firstly, as just mentioned, the inconsistency in data collection methodologies across different regions or time periods, which can lead to heterogeneous datasets, complicating comparative analyses. In addition, the dynamic nature of landscapes, which means that inventories may quickly become outdated, particularly in areas experiencing rapid geomorphological change. Finally, the strong bias towards recording just larger, more visible events, which may potentially underrepresent the real frequency and impact of also smaller landslides, i.e., shallow ones.

To address these issues, several innovative solutions, which take advantage of the new internet era and cloud data, are being explored. Some prime examples of that are remote sensing and machine learning. On one side, the integration of remote sensing technologies, growing in popularity and affordability, offers opportunities for more frequent and accurate updating of inventories. On the other hand, machine learning algorithms are being developed to automate the detection and classification of landslides from satellite imagery, to potentially reduce human error and increase the efficiency behind the creation of inventories and

datasets. As a matter of fact, these AI-based approaches are showing promising potential in processing of large volumes of data and identifying subtle landslide features, that might be missed by traditional methods.

Furthermore, the establishment of standardized protocols for data collection and reporting could enhance the consistency and interoperability of landslide databases across different regions. Such a standardization is crucial to create global or large-scale regional landslide inventories that can be used more effectively for comprehensive risk assessments and climate change impact studies.

By addressing these challenges and implementing innovative solutions, the scientific community aims to develop more comprehensive, up-to-date, and reliable landslide inventories. These improved datasets will ultimately enhance our ability to predict and mitigate landslide hazards, particularly regarding the efficient application of the above cited machine learning techniques.

1.5 The State Of The Art In Shallow Landslides Prediction

Shallow landslides pose significant risks to infrastructure, human life, and the environment. Therefore, the ability to accurately model and predict these events is crucial for effective risk management and mitigation strategies. The purpose of this chapter is to present a comprehensive review of the current state of the art in shallow landslide modelling and prediction, focusing on the three main categories of approach: statistical (threshold-based), physically-based, and machine learning models.

1.5.1 Statistical Models

Statistical models, which are commonly based on rainfall thresholds, have been widely used in landslide prediction due to their relative simplicity and effectiveness, especially in regional-scale applications. In fact, threshold-based models are based on simple correlation principles, typically establishing a relationship between landslide occurrence and triggering factors, which most commonly are rainfall intensity and duration (Berti et al., 2012; Brunetti et al., 2010; Chung et al., 2017; Crosta, 1998; Frattini et al., 2009; Gariano et al., 2015; Guzzetti et al., 2007; S. He et al., 2020; Huang et al., 2022; C. T. Lee et al., 2008b; Martelloni et al., 2012; Melillo et al., 2018; Peruccacci et al., 2017; Piciullo et al., 2017; Reichenbach et al., 2018; Rosi et al., 2016; Saito et al., 2010; Segoni et al., 2015; Segoni, Piciullo, et al., 2018; Vennari et al., 2014; Zhao et al., 2019). These models are derived from historical data, which is essential, and aim to define critical conditions above which landslides are likely to occur, depending on the analysed area. As a matter of fact, such type of models must be calibrated for each specific study area, making them site-specific. Therefore, statistical models typically outline site-thresholds on few triggering factors, dividing possible stability from possible instability state.

Applications of statistical models vary and may include early warning systems for landslide hazards, regional susceptibility mapping, and rainfall-induced landslide forecasting.

The key advantages of statistically-based models are different, and among these are:

- simplicity and ease of implementation
- effectiveness in regional-scale applications
- minimal data requirements compared to other approaches
- ability to incorporate uncertainty through probabilistic thresholds

Nonetheless, these methods also present various weaknesses, as:

- limited consideration of complex physical processes
- potential oversimplification of the landslide triggering process
- dependence on past historical data, which may not capture future climate scenarios and may lead to incorrect assumptions, if reports contain many errors
- difficulty in transferring thresholds between different geographic areas

1.5.2 Physically-Based Models

Physically-based models attempt to simplify and simulate the underlying mechanics of shallow landslides by incorporating geotechnical, hydrological, and topographical factors. These models typically combine infinite slope stability and limit equilibrium analysis with hydrological models to assess the factor of safety across a landscape. They often incorporate several variables, commonly related to topology, such as slope inclination and curvature; soil mechanics, such as cohesion, friction angle, and over consolidation; soil hydraulics, such as degree of saturation, suction, and soil permeability coefficient; and finally vegetation, such as root cohesion reinforcement, evapotranspiration coefficient, and runoff (Alvioli et al., 2014; Baum & Godt, 2010; Bishop, 1955; Bishop & Morgenstern, 1960; Borga et al., 1998; Formetta et al., 2016; Lehmann et al., 2019; Medina et al., 2021; Misiano et al., 2023; Montgomery & Dietrich, 1994; Montrasio, 2000; Montrasio & Valentino, 2016a, 2016b; Pack, 1998; G. Rossi et al., 2013; Salvatici et al., 2018; Schilirò et al., 2015; Vieira et al., 2010).

Applications of physically-based models include different areas, like detailed slope stability assessment, scenario analysis for land-use changes or climate change impacts, spatial and temporal prediction of landslide occurrence both for back analyses and forecasting purposes, or ultimately assessment of vegetation effects on slope stability.

The key advantages of physically-based models are different and could be:

- robust theoretical foundation based on physical processes
- ability to incorporate multiple factors affecting slope stability
- capability to simulate scenarios without historical precedent
- potential for high spatial and temporal resolution predictions

Despite all, these methods may present also various weaknesses, as:

- high data requirements, often including detailed soil and hydrological parameters
- computationally demanding, especially for large areas or fine resolutions
- uncertainty in parameter estimation and model structure
- difficulty in capturing some complex processes that involve several variables (e.g., preferential flow paths)

1.5.3 Machine Learning Models

Machine learning approaches have gained significant traction in recent years, offering new possibilities for landslide prediction and susceptibility mapping. Such a type of models in landslide studies encompass a wide range of techniques, including support vector machines, ensembles, and artificial neural networks. Please see Appendices Chapter for more information on the just mentioned approaches. The core principle behind these models is quite simple and consists in learning patterns from training data to predict outcomes, which may involve classification or numerical regression. According to the architecture and algorithms applied, different models can be obtained and various tasks can be completed, achieving varying levels of quality, depending on the context and requirements (Bui et al., 2019; Di Napoli et al., 2021; Dou et al., 2015; Kadavi et al., 2018; Kikuchi et al., 2023; Z. Liu et al., 2021; X. Luo et al., 2019; Ma et al., 2021; Merghadi et al., 2020; Mountrakis et al., 2011; Nhu et al., 2020; Nocentini et al., 2023; Tien Bui et al., 2016; H. Xu et al., 2023).

Some of the main applications of machine learning models in shallow landslides include landslide susceptibility mapping, real-time prediction of landslide occurrence, feature importance analysis for landslide conditioning factors, and integration with physically-based models, with the aim to improve predictions.

The key advantages of machine learning models are various, but can primarily be summarized as:

- ability to capture complex, non-linear relationships between variables
- capacity to handle very large datasets and multiple input variables
- potential for high predictive accuracy, when properly trained
- flexibility in incorporating diverse data types (e.g., remote sensing, geophysical data)

Of course, these methods also have potential weaknesses, as:

- dependence on the quality and quantity of training data
- potential for overfitting, especially with limited data
- lack of explicit physical process representation ("black box" nature)
- challenges in extrapolating beyond the range of training data in certain use cases

1.5.4 Comparative Analysis and Future Directions

Each type of modelling approach previously discussed offers distinct advantages but faces the same unique challenge in the context of shallow landslide prediction. In summary, statistical models provide simplicity and broad applicability but with the need for a calibration on each new area and with an oversimplification of complex processes. Instead, physically-based models offer a robust theoretical foundation and a great scalability but present some shortcomings mainly related to parameter estimation and computational demands. Lastly, machine learning approaches show promise in capturing very complex relationships with good results but require careful handling and knowledge to ensure physical plausibility and generalizability, in addition to the "black box" intrinsic nature.

At the current state of affairs, the majority of Italian regions, and not only, make use of statistical models for civil alert purposes, due to their easy and rapid applicability (Pizziolo et al., 2008; Protezione Civile Nazionale, 2016; Regione Autonoma della Sardegna, 2018; Soglie Pluviometriche, 2004). In contrast, physically-based models tend not to be considered for alerts but only in reinforcement, redevelopment works, or back analyses (Borga et al., 1998; Gatto et al., 2023a; Gatto & Montrasio, 2023; Lehmann et al., 2019; Medina et al., 2021; Misiano et al., 2023; Montrasio et al., 2010; Montrasio & Valentino, 2016a, 2016b; G. Rossi et al., 2013; Salvatici et al., 2018; Schilirò et al., 2015, 2016). Finally, regarding machine learning models, just few documented applications for alert and monitoring purposes are present over the world (Ma et al., 2021; Mountrakis et al., 2011; H. Wang et al., 2021; Xiao et al., 2022). The reason behind this poor adoption is that we are in the middle of an experimental era for these types of approaches, applied on shallow landslides. Primarily, at present, many comparative analyses are being conducted with robust and widely applied physical or statistical models, showing a good potential, especially on risk mapping (K. T. Chang et al., 2019; Kadavi et al., 2018; Merghadi et al., 2020; Nhu et al., 2020; Tien Bui et al., 2016).

However, the future of shallow landslide modelling appears to rely on hybrid approaches that leverage the strengths of multiple model types (Bui et al., 2019; W. Chen et al., 2020; Degen et al., 2023; Di Napoli et al., 2021; Hong, 2023; Misiano et al., 2023; V. V. Nguyen et al., 2019; Pham et al., 2019; Xie et al., 2021; Zhou et al., 2021), as it is concurrently occurring in many other areas of study (Ahmed et al., 2024; W. Chen et al., 2021; Jirasek & Hasse, 2023; Jorner et al., 2021; Khan et al., 2022; Kraft et al., 2022; Lu et al., 2021; Mao et al., 2020; B. Q. V. Nguyen et al., 2022; Rai & Sahu, 2020; Raissi et al., 2019; Samaniego et al., 2020; Shang et al., 2023; Sharma et al., 2023; Sun et al., 2020; H. Tu et al., 2023; Y. Xu et al., 2023). For instance, machine learning techniques could be used to optimize parameter selection in physically-based models, or physical constraints could be incorporated into machine learning frameworks to ensure consistency with known processes.

Parallelly, new emerging areas of research include the integration of real-time monitoring data with more refined predictive models than rainfall-thresholds, the

incorporation of climate change scenarios into long-term landslide risk assessment, the development of multi-hazard models that consider landslides in conjunction with other natural disasters, and the improvement of model uncertainty quantification and communication.

In conclusion, while significant progress has been made in shallow landslide modelling and prediction with statistical and physically-based models, challenges remain in balancing the real model complexity, data requirements, and predictive accuracy, especially leveraging the possible help of machine learning techniques. Thus, continued research and integration of variegate modelling approaches will be crucial in advancing our ability to mitigate landslide risks in a changing environment for the coming years.

II VEGETATION

The understanding of the influence of vegetation on slope stability has been a subject of increasing interest in geotechnical and ecological engineering over the past several decades. The complex interactions between plants and soil have large implications for landslide prevention, erosion control, and ecosystem management in mountainous and hillslope environments. This interdisciplinary field has evolved significantly over the years, connecting and integrating knowledge from soil science, hydrology, plant biology, and geotechnical engineering, in order to provide a comprehensive insight into how vegetation affects slope dynamics and consequent stability.

The study of vegetation's role in slope stability began in earnest in the early 20th century, with pioneering work by foresters and researchers such as Zon (1874 - 1956). However, it was not until the 1960s and 1970s that systematic research began to quantify the effects of vegetation on slopes, which can be primarily categorized into mechanical and hydrological effects.

Particularly, from the mechanical point of view, plant roots reinforce soil through tensile strength and increased soil cohesion, a phenomenon often referred to as root reinforcement, through the so-called root cohesion. The increase of soil cohesion by vegetation was first quantified simultaneously by Wu et al. (T. H. Wu, 1976; T. H. Wu et al., 1979) and Waldron (Waldron, 1977). Subsequently, starting from 2005, root cohesion began to be quantified by using the Fiber Bundle Model (*FBM*) (Pollen & Simon, 2005), which has since been refined and expanded (Cohen et al., 2009; Cohen & Schwarz, 2017; Ji et al., 2020; Kun et al., 2006; Meijer, 2021; Pradhan et al., 2010; Schwarz, Cohen, et al., 2010; Schwarz et al., 2013; Schwarz, Lehmann, et al., 2010; Schwarz, Preti, et al., 2010; Thomas & Pollen-Bankhead, 2010). Please see Appendices Chapter for more information on *FBM*. In addition, other side effects of vegetation are also the soil arching between root anchors and the surcharge from vegetation weight, which can be however both beneficial and detrimental, depending on the case.

Instead, from the hydrological point of view, vegetation influences slope stability through several mechanisms, such as interception of rainfall, enhancement of soil infiltration capacity, extraction of soil moisture through transpiration, modification of soil suction, and many other minor effects. The combination of all these possible processes is commonly known in literature as the canopy effect. Regardless, these hydrological effects have been studied constantly through field studies and theoretical works since the second half of the

20th century, initiated by researchers such as Hewlett and Hibbert (Hewlett & Hibbert, 1967) or Sidle and Swanston (Sidle & Swanston, 1982).

However, an important factor to consider is the fact that the contribution of vegetation to slope stability varies significantly depending on the plant species present. This variability presents a great challenge in accurately quantifying root reinforcement effects. In fact, recent research has focused on developing methods to assess and predict species-specific contributions to soil reinforcement (Abdi et al., 2010; Adhikari et al., 2013; Ali, 2010; Bischetti et al., 2005, 2009; Burylo et al., 2011; Comino et al., 2010; Comino & Druetta, 2009; Danjon et al., 2005; De Baets, Poesen, et al., 2008; Docker & Hubble, 2008; Draebing et al., 2023; Esmaiili et al., 2021; Genet et al., 2008; Ghestem, Cao, et al., 2014; Ghestem, Veylon, et al., 2014; Hu et al., 2013; Leung et al., 2015; Mickovski & van Beek, 2009; Miles & Swanson, 1986; Preti & Giadrossich, 2009; Roering et al., 2003; Schmid & Kazda, 2001; Simpson Nyambane & Kinyua Mwea, 2011; Stokes et al., 2009).

More in depth, different plant species exhibit varied root system architectures, which directly influence their effectiveness in soil reinforcement. For instance, tap root systems, which are characterized by a vertical primary root and multiple lateral branches, representative of many tree species, provide deep anchoring but may offer less widespread reinforcement. In contrast, fibrous root systems, representative of many grasses, offer the opposite behaviour, which means a minimal deep reinforcement and extensive shallow reinforcement. Finally, heart root systems, representative of some shrubs, represent a good balance between the two previous types of systems treated, i.e., a compromise between depth and lateral reinforcement. A major study of Stokes et al. (Stokes et al., 2009) provided a comprehensive review of how root architecture influences slope stability across various ecosystems, suggesting the preferable characteristics that vegetation species should have for soil reinforcement.

Moreover, the tensile strength of roots varies not only between different species but also within the same species, depending on factors like root diameter and age of the plant. As a matter of fact, extensive studies on the variability of root tensile strength across different tree species and root diameters in the French Alps were conducted (Genet et al., 2005), noting some significant differences also within the same species.

In any case, several modelling approaches have been developed to account for species-specific root reinforcement. For instance, some of the current main models are: the previously mentioned Fiber Bundle Model (*FBM*), eventually adapted by various researcher to account for species-specific root diameter distributions and tensile strengths (Cohen et al., 2009; Ji et al., 2020; Pollen & Simon, 2005; Thomas & Pollen-Bankhead, 2010); the Root Bundle Model (RBM), which is a modified version of *FBM*, specifically designed to model vegetation roots and consider the progressive failure of them during soil deformation (Schwarz et al., 2013; Schwarz, Lehmann, et al., 2010); various three-dimensional root distribution models, which

attempt to simulate realistic spatial root architecture for different species (De Baets, Torri, et al., 2008; Dupuy et al., 2005; Dyson et al., 2023; Masi et al., 2021; Meijer et al., 2022; Murgia et al., 2022); simplified mono-dimensional models, which quantify the root reinforcement based on few additional parameters, such as root cohesion, introduced in pre-existing slope stability criteria (Greenwood, 2006; Mao et al., 2013; Montrasio et al., 2023; Operstein & Frydman, 2000; L. M. W. Rossi et al., 2017; Stokes et al., 2008; T. H. Wu, 1994a).

The latter models were obtained starting from one or more different scientific processes. In fact, today's methods for studying vegetation's contribution can be broadly categorized into field measurements, laboratory experiments, and modelling approaches. To begin with, field measurements consist of in-situ shear tests to quantify root reinforcement, tensiometer measurements to assess soil suction changes, sap flow measurements to estimate transpiration rates, rainfall interception studies using throughfall and stemflow gauges, and root distribution mapping using trench wall techniques or ground-penetrating radar. Following this, laboratory experiments include direct shear tests on root-permeated soil samples, centrifuge modelling of vegetated slopes, root tensile strength testing, triaxial tests on rooted soil specimens. To conclude, modelling approaches incorporate, finite element analysis incorporating root reinforcement, coupled hydro-mechanical models, probabilistic models assessing vegetation effects on slope reliability, and machine learning techniques for predicting vegetated slope behaviour.

Recent advancements have thus enhanced our ability to study the interactions between vegetation and slope. Technologies such as Light Detection and Ranging (LiDAR) or drone-based photogrammetry now allow for high-resolution 3D mapping of vegetation structure and slope morphology. Ground-penetrating radar (GPR) provides insights into root system architecture without destructive sampling. X-ray computed tomography allows for a detailed analysis of root-soil interactions. Therefore, these tools, combined with advanced computational methods, are expanding the boundaries of our knowledge about vegetated slope systems.

Currently, numerous worldwide interventions have been implemented to stabilize slopes using vegetation. These bioengineering techniques often combine plants with structural elements. Some examples that can be cited could be live staking, that is the insertion of live, woody cuttings into the soil to grow into new plants; brush layering, i.e., placing live branch cuttings between layers of soil on slopes; fascines, which consist of bundles of live branches placed in trenches along the contour of a slope; vegetated geomats, which are erosion control mats seeded with native vegetation; vegetated riprap, that is the incorporation of live plants between or within rock structures; live crib walls, namely wooden structures filled with soil and live cuttings; or, finally, green terraces, i.e., terraced slopes reinforced with vegetation. Some successful examples of the application of these techniques are the use of vetiver grass, succulent plants, or shrubby trees for slope stabilization in

tropical and subtropical regions, but not only. As a matter of fact, in Malaysia and in China, specifically in Yunnan, significant improvements in slope stability were reported, following these implementations on some infrastructure like highway embankments (Ghestem, Cao, et al., 2014; Mohamed et al., 2023). Or again, in Hong Kong, the Geotechnical Engineering Office has extensively used bioengineering techniques in combination with traditional engineering structures to stabilize cut slopes (Choi & Cheung, 2013; Law et al., 2023; Leung et al., 2015; Martin, 2001; S. L. Ng et al., 2011; Patil et al., 2021; Stokes et al., 2010). In addition, just to mention another practical example, in Southern England, a highway cut-slope was reinforced using hawthorn and oak roots (Norris, 2005).

Another relevant evidence of the importance of vegetation is the impact of deforestation on slope stability. Indeed, deforestation has been linked to increased landslide occurrence in numerous studies worldwide, both in tropical and temperate regions (Bruijnzeel, 2004; J. C. Chang & Slaymaker, 2002; Depicker et al., 2021; Dhakal & Sidle, 2003; Forbes et al., 2013; Glade, 2003; Montgomery et al., 2000; Papathoma-Koehle & Glade, 2013; Rmer, 2013; Roder et al., 2016; Saito et al., 2017; Sakals et al., 2006; Schwendtner et al., 2013; H. M. Tu & Chen, 2020; Vanacker et al., 2003; Von Ruette et al., 2018; T. H. Wu & Swanston, 1980). Furthermore, deforestation not only removes mechanical reinforcement of roots in the immediate, but also alters hydrological regimes, having long term consequences, even decades after the initial deforestation event (Jayawickreme et al., 2010; Mango et al., 2011; Mantero et al., 2020; Nasta et al., 2017; Numata et al., 2021; O. et al., 2012; Salemi et al., 2012; Woldesenbet et al., 2017).

Despite the above-discussed advances, significant challenges remain nowadays in characterizing, modelling, and predicting the effects of vegetation on slope stability. The spatial and temporal variability of root systems, the dynamic nature of plant-water interactions, and the complexity of soil-root mechanical behaviour, integrated into an already convoluted three-phase system of soil, continue to present difficulties in developing efficient and universally applicable models. Moreover, the impacts of climate change on vegetation patterns and extreme weather events add a further new layer of complexity to long-term slope stability assessments. Thus, future directions in this field are likely to focus on improving our understanding of root-soil interactions at the microscale, developing more sophisticated coupled hydro-mechanical models that incorporate vegetation dynamics, assessing the long-term impacts of climate change on vegetated slope systems, optimizing vegetation cover for slope stabilization in various climatic and geological settings, and finally integrating remote sensing and machine learning for large-scale assessment of vegetation's impact on slope stability.

In conclusion, the study of the role of vegetation in slope stability represents a vibrant, current, and evolving field of research, with significant implications in various fields, such as landslide risk management, ecological restoration, and sustainable land use practices. As the scientific community continues to unravel the complexities of plant, soil, and water

interactions on slopes, we move closer to more effective, eco-friendly, and environmentally harmonious solutions for slope stabilization in landslide prevention, and not only.

In the following sections, first and foremost, some case studies of the evidence, contained in the History, is given. Following this, a more in-depth overview of the progress in root modelling, and in hydraulic vegetation effects, is reported, relatively to slope stability. Moreover, the current state of the art is presented and commented. To conclude, some practical applications of these type of biocompatible interventions are shown and explained.

2.1 Historical Evidence Of Vegetation's Impacts In Slope Stability

The relationship between vegetation and slope stability has been observed empirically for centuries, but its scientific study, as previously mentioned, can be traced back to the first half of the 20th century, with pioneering work by foresters and researchers such as Zon, a prominent U.S. Forest Service researcher who recognized the importance of forest cover in watershed protection in one of his works (Zon, 1935). However, it was not until the 1960s and 1970s that systematic research began to quantify the effects of vegetation on slope stability. In fact, seminal work by Waldron provided some of the first quantitative assessments of how plant roots contribute to soil reinforcement (Waldron, 1977; Waldron & Dakessian, 1981). Subsequently, pioneering studies by Gray, Leiser, Greenway, and Ziemer (Greenway, 1987; H. Gray & T. Leiser, 1982; Ziemer, 1981b, 1981a) laid the foundation for understanding the complex mechanisms by which plants would influence soil strength and hillslope hydrology, inspiring more specific works by other scientists, such as Wu (T. H. Wu, 1984, 1994a; W. Wu & Sidle, 1995) and Greenwood (Greenwood, 2006; Greenwood et al., 2004, 2007).

Some historical cases supported the assumptions of the above-cited works, revealing an increase in shallow landslide occurrence following deforestation or land-use changes, consequently demonstrating the importance of vegetation for slope stability. For instance, as a result of European settlement and widespread deforestation of the 19th century, New Zealand experienced a dramatic increase in shallow landslides (Glade, 2003). Similarly, in Japan, it was found that the conversion of natural forests to cedar plantations in the early 20th century led to an increase in shallow landslides, particularly during the trees' juvenile stages (Imaizumi et al., 2008). Equally, in the French Alps, historical records showed how deforestation for agriculture and grazing in the 18th and 19th centuries corresponded with increased landslide and erosion events (Delsigne et al., 2001; Lopez Saez et al., 2012). More recently, in Taiwan, it was demonstrated a clear correlation between the clearance of natural forests for agriculture and a subsequent rise in landslide occurrences (J. C. Chang & Slaymaker, 2002; Roder et al., 2016; H. M. Tu & Chen, 2020). In addition, in the Pacific Northwest of the United States, a clear correlation between timber harvesting and increased frequency of shallow landslides was demonstrated (Montgomery et al., 2000). Ultimately,

land-use changes in the Italian Alps, including deforestation, revealed an increase in shallow landslide susceptibility over a 50-year period (Papathoma-Koehle & Glade, 2013; Schwendtner et al., 2013). It is worth to note that the latter aspect, regarding the role of land-use changes in landslide susceptibility, was also exposed in Section 1.2.3 for the La Spezia and Massa-Carrara landslide event, on October 25, 2011.

To summarize, these historical cases, spanning different geographical and climatic regions, have provided compelling evidence for the protective role of vegetation against shallow landslides. They have also underscored the often long-term and far-reaching consequences of land-use changes on slope stability, routing current approaches to a more conservative land management.

In the following paragraphs, a chronological and brief summary of some past and major cases is reported, to highlight the importance of vegetation, and in particular of forests, in slope stability.

2.1.1 The Effects Of Vegetation In The Oregon Case, USA

The forested landscapes of Oregon provide a compelling case study for understanding the relationship between vegetation and shallow landslides. Topography and high annual rainfall of this state create conditions conducive to shallow landslides, particularly in the Coast Range and Cascade Mountains. Various research in this region has demonstrated a strong correlation between forest management practices and landslide frequency (Cronkite-Ratcliff et al., 2022; Miles & Swanson, 1986; Montgomery et al., 2000; Robison et al., 1999; Roering et al., 2003; K. M. Schmidt et al., 2001). In fact, The Oregon state was the subject of an impactful deforestation occurred during the second part of the 20th century.

Particularly, the extensive deforestation in Oregon has its roots in the state's economic history and development. Timber harvesting has been a cornerstone of Oregon's economy since the mid-19th century, driven by several factors. To start with, the economic growth, because the demand for timber surged during the post-World War II building boom, leading to increased harvesting rates. Secondly, technological advancements, thanks to the introduction of chainsaws and logging trucks in the 1940s and 1950s, which made large-scale harvesting more efficient and economically viable. Moreover, the forest management policies, since the U.S. Forest Service's policy of fire suppression, beginning in the early 20th century, led to denser forests, which were then seen as prime for harvesting. To conclude, job creation and revenue for public services were other two factors that contributed to the deforestation, due to the fact that the timber industry was a significant employer in rural Oregon, providing at the same time substantial revenue for counties, funding schools, etc.

Despite the economic benefits, the environmental consequences of extensive deforestation became increasingly apparent and severe. As a matter of fact, Montgomery et al. (2000) found that for a total of 3224 shallow landslide analysed, density in clear-cut areas

was approximatively 3 to 9 times higher than in mature forests, considering the short time scale. Moreover, one of the studies of the Oregon Department of Forestry (Robison et al., 1999), spanning 1984 to 1995, revealed that the landslide rate in industrial forests, which experienced more intensive harvesting, was around 0.16 landslides per square kilometres per year, compared to 0.04 in state forests with less intensive management.

The latter statistics underscore the significant impact of deforestation on slope stability in Oregon. Additionally, it should be noted that the increased landslide risk may persist for several years post-harvest, since the period of highest susceptibility occurs 3-15 years after clear-cutting, which coincide with the decay of tree roots and before new vegetation can establish substantial root systems. These findings, although from research with many years, still have profound implications for forest management policies, in Oregon but not only, leading to the implementation of more sustainable harvesting practices, in addition to the possible establishment of riparian buffer zones with vegetation, to mitigate landslide risks.

Figure II-1: An example of deforestation due to clearcutting of vegetation in Oregon

2.1.2 The Effects Of Vegetation In The Loess Plateau Case, Cina

The Loess Plateau case, in north-central China, offers another distinctive case study for understanding the relationship between vegetation and shallow landslides, especially because of its reforestation. This region, covering approximately 640,000 square kilometres, is characterized by its thick aeolian deposit (fine-grained sand and glacial silt deposits), steep terrain, and semi-arid climate. As a result, this region has a high susceptibility to soil erosion and shallow landslides.

Historically, deforestation and intensive agriculture have significantly impacted the landscape stability. In fact, comprehensive studies by different authors (Guo et al., 2023; L. He et al., 2023; Meng et al., 2021; J. Peng et al., 2019; H. B. Wang et al., 2011; X. Z. Xu et al., 2017; Zhuang et al., 2018) unanimously agree that this region was one of the most landslide-affected regions in China, as in the world, and that the forests play a fundamental role in the stability, considering that during the intensive deforestation period (ended in the early 2000s) it was reached in certain areas an impressively high landslide rate of around 6

landslides per square kilometres. This is the reason why a reforestation initiative, called Grain for Green Programme (Y. Wang et al., 2018), was proposed at the end of the 20th century (1999) and effectively started in the early 21st century, resulting in a marked improvement and raising the percentage of forested areas from around 8.19% to 15.82%. Consequently, a contraction of both erosion and shallow landslides was experienced, with a percentage of reduction (on tonnes of eroded soil) of around 31.5% (Wei et al., 2021). Nevertheless, for the sake of intellectual honesty, it is important to report that some very recent studies have revealed that areas in Loss Plateau which exceeding the 90% of vegetation cover increased the susceptibility of slopes to shallow landslides, instead of reducing it, whenever an extreme rainfall event occurs (Y. Xu et al., 2024; J. Zhang et al., 2022). The authors attributed this unexpected behaviour to the fact that a high density of roots could increase the saturation of soils (roots tend to retain water), which in turn, coupled with the weight of high trees and the low hydraulic conductivity of the underlying loess soils, would increase the pore water pressure, in case of intense rainfall events. Thus, according to the authors of these recent studies, a percentage of vegetation cover below 90% would maintain its beneficial effects on slope stability, reaching the best and ideal conditions at around 70-80%, both for erosion and shallow landslides.

However, extensive land degradation in the Loess Plateau has its roots in long-term human activities and not only. Initially, the historical deforestation, began over 2000 years ago for agriculture purposes but intensified during periods of population growth due to agricultural expansion, and the consequent conversion of steep slopes to cropland. Following this, the overgrazing, which contributed to vegetation loss and soil compaction, that normally would be beneficial, since compaction increases soil's mechanical properties, but it also reduces the hydraulic conductivity, increasing pore water pressure. Finally, the climate change, because the increasing frequency of extreme rainfall events in this region has boosted the susceptibility to shallow landslides.

Therefore, the environmental consequences of all these activities became increasingly apparent in the 20th century, promoting the initiative of the above-mentioned Grain for Green Programme in 1999. Among the key elements of the program, the large-scale afforestation and revegetation; terracing of steep slopes, to reduce soil erosion (caused also by shallow landslides) in treated areas; the implementation of check dams, with the aim to decrease sediment transport in gullies; restrictions on grazing and cultivation on steep slopes, allowing natural vegetation recovery in sensitive areas.

The impact of these measures has been significant. For instance, it was reported a reduction of 90% in sediment load, caused by erosion and shallow landslides, in the Yellow River, from 1980 to 2010. The latter result is largely attributed to the increasing vegetation cover of the 12 main sub-basins of the Yellow River in Loess Plateau, which augmented from 25% in 1980 to 46% in 2010 (S. Wang et al., 2016).

The case study of Loess Plateau demonstrates again the complex interplay between human activities, vegetation cover, and shallow landslide occurrence. It also highlights how large-scale ecological restoration efforts can be significant to mitigate landslide risks, providing valuable insights for sustainable land management in similar environments worldwide.

Figure II-2: Examples of Loess Plateau before (left) and after (right) reforestation

2.1.3 The Effects Of Vegetation In The Southern California Case, USA

Southern California presents a singular case study, due to its Mediterranean climate, which is characterized by long dry summers and short, intense wet seasons. The steep topography of this region, coupled with periodic wildfires and occasional intense rainfall events, creates a dynamic environment prone to landslides. Unlike the Loess Plateau or Oregon case studies, where deforestation for human activities was the primary issue, the landslide risk in Southern California is instead significantly influenced by its natural fire regime and subsequent vegetation changes.

Wildfires play a crucial role in the landslide dynamics of this region. Different studies found that recently burned areas in Southern California could be more likely to produce debris flows during intense rainfall, compared to unburned areas (Abdollahi et al., 2023; Cannon & DeGraff, 2009; Oakley et al., 2017; Parise & Cannon, 2012; Ren & Leslie, 2020; Rengers et al., 2020). For instance, an area burned two times, once with the Morris wildfire of 2009 and the other with San Gabriel Complex fire of 2016, reported a landslide density of 11.6 landslides per square kilometres, in contrast with a density of 0.2 for the unburned near areas (Rengers et al., 2020). This increased susceptibility is caused by the loss of vegetation cover, which no longer provides any hydraulic contribution, and it does not increase

infiltration capacity, but also by changes in soil properties following fires. Particularly, changes in soil properties are related to the fact that plant roots dramatically reduce their contribute with the tensile strength, lowering the initial strength from 25% to 80%, depending on fire intensity (consequently the root cohesion is suddenly lower) but also for the fact that soil water balance changes (the degree of saturation directly affects soil cohesion).

Consequently, vegetation in Southern California has evolved to adapt to periodic fires, with many species exhibiting fire-resistant or fire-dependent traits, but despite this, also human activities have altered natural fire regimes, through factors such as the urban expansion (since human presence tends to led to more frequent ignitions and fire suppression efforts, altering natural vegetation cycles), the introduction of invasive species, the climate change (longer, drier summers have extended the fire season and increased vegetation stress), the fire suppression policies (long-term fire suppression has led to fuel accumulation in some areas, potentially resulting in more severe fires when they do occur).

In response to these challenges, land management strategies in Southern California have evolved during the years. Nowadays, fire mitigation is conducted by means of: vegetation management (controlled burns and mechanical thinning, used to reduce fuel loads, miming natural fire regimes); post-fire treatments (mulch or hydroseeding applied to reduce erosion and promote rapid revegetation after fires); land-use planning (restrictions on development in high-risk fire and landslide zones); native plant restoration.

The effectiveness of these measures varies. A study by Wohlgemuth et al. (2019) found that the post-fire mulching treatments (hydromulch) adopted in Southern California reduced sediment yield and erosion significantly, thanks to the BAER emergency plan, during the first two years after fires (Robichaud, Lewis, et al., 2013; Robichaud, Wagenbrenner, et al., 2013; Wohlgemuth et al., 2007). However, the long-term impact on shallow landslide occurrence requires further study.

Figure II-3: The Montecito mud and debris flows of January 2018, after Thomas Fire (2017-2018)

2.1.4 The Effects Of Vegetation In The Forests Of New Zealand

New Zealand provides another significant case study of the impacts of deforestation on slope stability. The country's mountainous terrain, coupled with its high rainfall, creates conditions that are critical from the beginning, relatively to slope instability. Moreover, historical extensive deforestation for agricultural expansion, grazing, and timber extraction during the 19th and 20th centuries has led to widespread soil degradation and increased incidence of shallow landslides.

Different studies in New Zealand have shown that areas subjected to deforestation exhibit a higher frequency of shallow landslides compared to regions with intact native forest cover (Glade, 2003; Hancox & Wright, 2005; Hughes, 2016; Lehmann et al., 2019; Marden et al., 2005; Marden & Rowan, 2015; Phillips & Marden, 2012). Beyond landslides, deforestation has also been linked to accelerated rates of soil erosion. In fact, the removal of vegetation exposes the soil surface to direct impact from rainfall, which can dislodge soil particles and initiate erosion. This process is exacerbated on steep slopes, which further destabilizes the soil, leading to significant loss of the fertile upper soil layers that would flow downhill and potentially evolve into debris flows.

In response to deforestation, New Zealand has undertaken significant restoration measures. The reintroduction of native tree species, such as poplars, beech, podocarps, willows, or Pinaceae (Basher, 2013; Crozier, 2005; Fernandez, 2017; Phillips et al., 2015; Phillips & Marden, 2005; Satchell, 2018) has been shown to reduce both soil erosion and landslide occurrence. Additionally, policy measures promoting sustainable forestry practices, and the protection of existing native forests, have been implemented to mitigate further environmental degradation. The lessons learned from New Zealand's experience over the past years can inform land management strategies in other regions facing similar challenges, emphasizing the importance of preserving and restoring natural vegetation as a means of mitigating landslide risks.

Figure II-4: Multiple shallow landslides after the storm of February 2004, in Manawatu (left) and the storm of February 2023, in Auckland (right)

2.1.5 The Effects Of Vegetation In The Forests Of Japan

Japan's mountainous topography, coupled with its exposure to intense rainfall events and the high seismic activity, makes it particularly susceptible to shallow landslides. Approximately, 67% of Japan's land area is covered by forests, which play a crucial role in slope stabilization, influencing both hydraulically and mechanically the problem, mainly through the runoff (Gomi et al., 2008; Miyata et al., 2009) and the increase of soil cohesion. Regarding the latter, the contribute of root cohesion can also increase soil shear strength by up to 20 kPa in certain soil types and under certain conditions (Abe & Ziemer, 1991).

However, Japan has experienced significant land-use changes due to urbanization and agricultural expansion. Specifically, between 1900 and 2000, broad-leaved forest cover changed drastically, halving and converting to mixed forests. At the same time, urban areas have tripled compared to the beginning (Himiyama, 1998). This change has been linked to an increase in shallow landslide occurrences and soil erosion, particularly during the first half of the 20th century, in regions with steep slopes and high precipitation rates. For instance, it was found that landslide frequency in deforested areas was up to ten times higher than in forested slopes under similar topographic and geological conditions (Imaizumi et al., 2008; Saito et al., 2017), but also that rainfall thresholds may be halved, making slopes more susceptible, especially if the clear-cut forest was mature (Imaizumi & Sidle, 2012; Lusiana et al., 2024; Shinohara & Kume, 2022). Nevertheless, it must be noted that when the forest is mature and a landslide occurs, a larger volume of driftwood can be involved, significantly increasing the landslide volume and the associated risk. The latter is an open question and will likely be the subject of future studies.

To address the problem of the increasing shallow landslides, both rainfall and earthquake-induced, Japanese authorities have implemented various preventive measures. Specifically, the Sabo projects, initiated around 1930 and continually updated since then, include reforestation as one of the key strategies for landslide mitigation. In fact, these projects have led to the planting of millions of trees, with a focus on deep-rooted species such as Cryptomeria japonica, Chamaecyparis obtusa, or Quercus serrata, known for their soil-binding properties (Sato et al., 2023; Sidle et al., 2006; Yamase et al., 2021). In addition to reforestation, Japan has implemented stricter land-use regulations, such as the 2001 revision of the original Forest Law (1951) strengthened protections for forested areas and introduced more rigorous requirements for land development in mountainous regions (Ota, 2010). These regulatory measures, coupled with ongoing research into the optimal use of vegetation for slope stabilization, form a multi-faceted approach to landslide risk reduction in Japan.

Despite these efforts, challenges remain, since climate change is projected to increase the frequency and intensity of extreme rainfall events in Japan, potentially exacerbating landslide risks (Kawagoe et al., 2010; Shinohara & Kume, 2022; WU et al., 2020). Consequently, the latter issue has led to an increasing focus on developing more resilient

vegetation management strategies, selecting the most appropriate vegetative species (also in view of possible future occurrences, when the forest would be mature), and integrating vegetation-based approaches with other structural and non-structural mitigation measures.

Figure II-5: Landslides induced by the September 2018 earthquake, in Hokkaido Island. Areas with dense and deep-rooted vegetation were not affected by the earthquake.

2.1.6 The Effects Of Vegetation In The Vancouver Island (British Columbia), Canada

The last case study to review is the one concerning Vancouver Island, but generally of its province, the British Columbia, in Canada. The island has a steep topography, maritime climate, and extensive forestry activities. Particularly, Vancouver Island is characterized by its mountainous terrain, with the Vancouver Island Ranges dominating much of its landscape. The island's geology is complex, featuring a mix of volcanic and sedimentary rocks, often overlain by glacial till and colluvium. Moreover, the climate is classified as temperate rainforest, with high annual precipitation, particularly during winter months. This combination of steep slopes, varied geology, and intense rainfall events creates conditions highly prone to shallow landslides.

Historically, Vancouver Island was populated by old-growth temperate rainforests. However, extensive deforestation since the early 20th century have significantly altered the landscape. For instance, it was estimated that the total watershed of Macktush Creek, Artlish River, and Nahwitti River was approximately logged of 50%, 21%, and 23%, respectively, by the turn of the 21st century (Guthrie, 2002). Consequently, numerous are the studies that have documented the relationship between logging activities and increased landslide frequency, in which it was found that landslide density in logged areas was up to around 16 times higher than in undisturbed forests, such as the Nahwitti River (Guthrie, 2002). Instead, the landslide volume can increase by 5-fold after clearcutting (Dhakal & Sidle, 2003) and partial cutting would be highly suggested, since it would maintain both low landslide volume and frequency. Furthermore, this risk would remain elevated for up to 15-20 years post-harvest, due to the

degradation of root strength in fallen trees and the slow renewal of new roots (Jakob, 2000). On the other hand, concerning the mechanical contribution of roots, it was demonstrated that root cohesion of the Vancouver Island forests may fall to 40% of the original pre-cut value, especially during the first years (Sakals & Sidle, 2004; Stevens et al., 2006). At the same time, from the hydrological point of view, clear-cutting would lead to increased soil moisture and higher pore water pressures during rainfall events, further contributing to slope instability.

Recent studies have also deepened the potential impacts of climate change on landslide dynamics on Vancouver Island. Projections suggest that the frequency of extreme rainfall events could increase by up to 35% by the end of the 21st century (Jakob & Owen, 2021), especially during autumn and winter and potentially increasing landslide risks, particularly in areas with compromised vegetation cover. Moreover, landslides frequency could triple and their average volume rise by 50%.

In response to the recognized link between forestry practices and landslide occurrence, British Columbia has implemented various regulations and best practices. For instance, The Forest and Range Practices Act (FRPA), formulated in 2002 and enacted in 2004, requires forest managers to consider terrain stability in their harvesting plans (BC Ministry of Forests, 2002). This has led to more selective logging practices in high-risk areas and the implementation of reforestation strategies designed to accelerate the recovery of root cohesion.

To conclude, the case of Vancouver Island demonstrates the critical role of vegetation in maintaining slope stability in steep, high-precipitation environments. The interplay between forestry activities, rainfall, and climate change provides valuable lessons for future challenges and land management in similar regions worldwide. In fact, as climate change threatens to alter precipitation patterns, the importance of maintaining and restoring robust vegetation cover on Vancouver Island's slopes (and similar) becomes even more crucial.

Figure II-6: A combination of shallow landslides and debris flows near the Williams Lake, during the recent flood of July 2024, in British Columbia. The landslide, triggered by rainfall in a deforested area, dammed the Chilcotin River.

2.2 An Overview Of The Progress In The Interaction Between Plant And Soil

The study of interactions between soil and vegetation, and their impact on slope stability, has undergone a remarkable evolution over the past century, transitioning from rudimentary observations to sophisticated, multi-disciplinary approaches. This progression reflects advancements in technology and computational power, expanding our knowledge about complex natural systems such as soil-vegetation-rainfall.

Early investigations in the early 20th century were largely qualitative, focusing on observational studies of vegetation's role in erosion control and slope stabilization. As discussed in the previous sections, authors such as Cooper, Pearson, Sears, Walford and Zon highlighted the importance of forest cover in watershed management (Walford & Zon, 1942; Zon, 1935; Zon et al., 2017). Subsequently, the 1970-80s marked a turning point with the emergence of quantitative approaches, nut also a rapid expansion in research scope and methodology, due to the work of researchers like Gray, Greenway, Leiser, Ziemer and others (Abe & Ziemer, 1991; Gray & Megahan, 1981; Greenway, 1987; H. Gray & T. Leiser, 1982; Ziemer, 1981b, 1981a). Nevertheless, a significant breakthrough came especially with the work of Waldron et al. (Terwilliger & Waldron, 1990; Waldron, 1977; Waldron & Dakessian, 1981) and Wu et al. (T. H. Wu, 1976, 1984, 1994b, 1994a; T. H. Wu et al., 1979; T. H. Wu & Swanston, 1980), who developed similar models for root reinforcement. In fact, their approach, often referred to as the Wu/Waldron model, became the foundation for much of the subsequent research in the field.

The key concepts of the Wu/Waldron model are: (i) the root analogy, since the model treats roots as equal cylindrical fibres providing additional cohesion to the soil matrix; (ii) the tensile strength, because it assumes that roots mobilize their full tensile strength during soil shear stresses; (iii) the orientation, considering that the model considers an average root orientation angle with respect to the shear plane (Figure II-7).

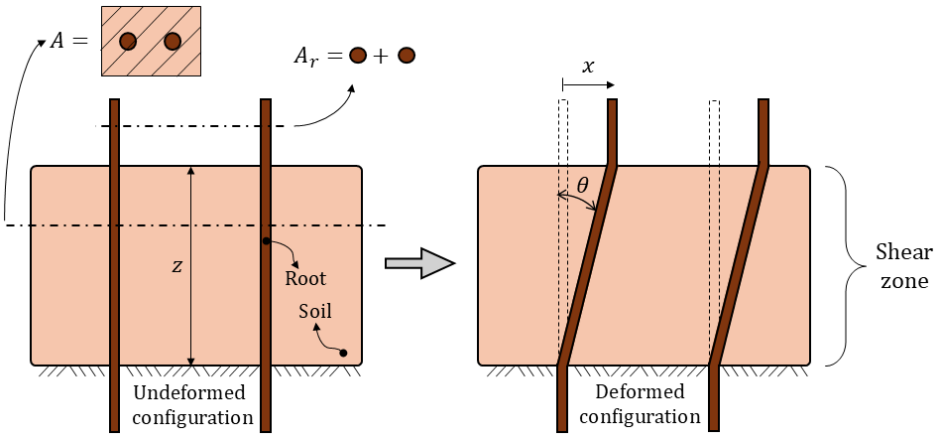

Figure II-7: Example of Wu-Waldron's soil-roots scheme before (left) and after (right) applying shear stress. The roots initial configuration is required to be orthogonal to the shear, slide plane (roots are vertical). After deformation, in the shear zone of height z, the displacement on top is x and a shear angle θ is generated.

The mathematical representation of the additional shear strength (c_r) provided by roots, also referred as root cohesion, is expressed as following:

$$c_r = t_r \cdot a_r \cdot (cos\,\theta \cdot tan\,\varphi + sin\,\theta) \quad (1)$$

where:

- t_r is the average tensile strength of roots
- $a_r = \frac{A_r}{A}$ is the root area ratio (total cross-sectional area of roots per unit area of soil)
- θ is the angle of shear distortion in the shear zone
- φ is the soil friction angle

Wu et al. proposed also a simplified version of Eq. 1:

$$c_r = 1.2 \cdot t_r \cdot a_r \quad (2)$$

This simplification assumes an average angle in the range from 48° to 72° for root orientation and a soil friction angle of 30°. However, both Eq. 1 and Eq. 2 rely on different assumptions and present limitations, such as (i) the simultaneous failure, since the model assumes all roots break simultaneously at their peak strength; (ii) the homogeneity, considering that they treat the root network as homogeneous, not accounting for variability in root sizes and strengths; (iii) the only tensile strength of roots, neglecting compression and bending; (iv) the static condition, because they do not account for dynamic stress distributions during progressive failure; (iv) the vertical inclination of roots, given that roots are supposed to be straight and perpendicular to soil slip plane as initial condition. Despite these limitations and simplifications, the Wu/Waldron model remains a cornerstone in root reinforcement studies, providing a straightforward method for estimating the mechanical contribution of roots to soil strength. Its simplicity has made it widely used in slope stability analyses and has formed the basis for more complex models developed in subsequent years. For instance, Waldron himself, with the help of Dakessian (Waldron & Dakessian, 1981), focused on the aspect of root-soil friction, identifying, in the years following the development of the first model, three types of ultimate conditions, which are respectively breakage, stretching, or pull-out. Specifically, according to Waldron the root is not necessarily stressed along its entire length and depending on where the shear zone is positioned along the root, different values of tensile stress can be reached, with the maximum located on the half of the length involved. As a result, based on the tensile stress (t_n), the tensile strength of the root (t_r), the actual length of the root (L), and the length of the root stressed (l), breakage is achieved when $l < L$ and $t_n > t_r$; stretching occurs when $l < L$ and $t_n < t_r$, thus the root would deform with a linear elastic behaviour, contributing to soil cohesion through c_r; pull-out is obtained when $l > L$ and $t_n < t_r$, since the root would need more than the actual length to perform its function properly.

Afterwards, different studies were aimed at improving and expanding the applications of the Wu/Waldron formula. One mentionable example could be the one from Gray, which studies the same problem but starting from a different initial configuration of roots (Figure II-8), that is when they are not perpendicular to the slip surface but with a pre-existing inclination (i) (Gray & Ohashi, 1983).

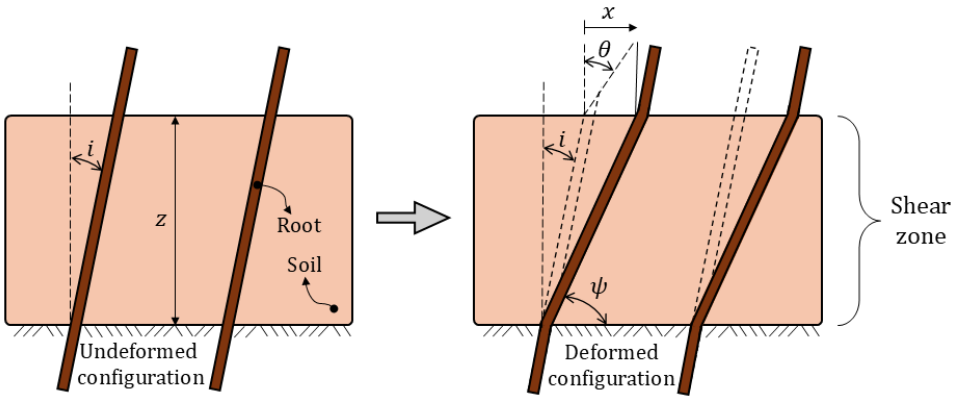

Figure II-8: Example of Gray's soil-roots scheme before (left) and after (right) applying shear stress. The roots initial configuration is not orthogonal to the shear, slide plane ($i > 0°$). After deformation, in the shear zone of height z, the displacement on top is x and a shear angle θ is generated, which should be combined with the initial angle i. The result is a new angle ψ which represents the deformed configuration; i and θ cannot be summed.

In such a case, a new angle (ψ) which includes both i and θ must be introduced:

$$\psi = tan^{-1} \frac{1}{tan\,\theta + (tan\,i)^{-1}} \tag{3}$$

It must be noted that ψ corresponds to the angle formed by the shear plane and the final, deformed root configuration. Hence $90° - \psi$ can be seen as an updated angle of shear distortion, and the contribution of the root cohesion can be now expressed as:

$$c_r = t_r \cdot a_r \cdot [cos(90° - \psi) \cdot tan\,\varphi + sin(90° - \psi)] \tag{4}$$

Regardless, the turn of the millennium brought about significant advancements in modelling approaches and recognition of the Wu/Waldron model's limitations led to the development of more sophisticated techniques. Among these, there are certainly the Fiber Bundle Model (*FBM*) (Pollen & Simon, 2005) and the Root Bundle Model (*RBM*) (Schwarz, Cohen, et al., 2010; Schwarz, Lehmann, et al., 2010), which addressed the limitation of simultaneous root breakage assumption in earlier models. These probabilistic approaches allowed for progressive root failure, providing more realistic estimates of root reinforcement.

The *FBM*, originally developed in materials science, was adapted for the first time to root reinforcement in 2005 (Pollen & Simon, 2005). The key strength of such a model lies in considering, firstly, the progressive failure of roots during soil deformation, and, secondly, the variability of roots. In fact, (i) roots break sequentially, not simultaneously, (ii) when a root

breaks, its load is redistributed among remaining intact roots, and (iii) the model accounts for variations in root diameters and tensile strengths.

The mathematical core concept of the *FBM* is based on the following main equation, which represents the total force (F_{Rt}) supported by a bundle of roots:

$$F_{Rt} = \sum_{i} F_{Ri} \tag{5}$$

where:

- F_{Ri} is the force carried by an intact root of the bundle

Consequently, each root has a breaking threshold, i.e., the root breaks when its load exceeds its strength, when the following condition occurs:

$$F_{Ri} > \pi \cdot \left(\frac{d_{ri}}{2}\right)^2 \cdot t_{ri} \tag{6}$$

where:

- d_{ri} is the diameter of the root i
- t_{ri} is the tensile strength of the root i, given by a Weibull probabilistic approach

After a root breaks, a load redistribution occurs, and the load that was carried by the broken root is then equally redistributed among surviving roots (global load sharing, *GLS*). Therefore, in a stress-controlled model, each fibre suddenly experiences an increase in load:

$$\Delta F_{Ri} = \frac{\sum_b F_{Rb}}{N - n_b} \tag{7}$$

where:

- F_{Rb} is the force carried by a root before breaking
- N is the starting number of roots, before breaking
- n_b is the number of broken roots

It must be noted that once some roots break, an avalanche can be triggered because some of the remaining roots, which suddenly face an increased load, may also hit their thresholds and fail in turn, triggering a cycle that terminates when a new configuration of equilibrium is met. Moreover, the distribution of the tensile strengths (t_{ri}) among the various roots is probabilistic (typically following the Weibull distribution), meaning that some roots would have a greater or smaller strength compared to others, assuming equal geometrical and material conditions.

In contrast, when the process of the *FBM* is strain-controlled, and a fibre breaks, the strain must be the same as the previous time step, since it is fixed. As a result, to maintain the

same strain, but with less intact roots, the total stress applied must decrease, from a macroscopic point of view. In other words, maintaining the deformation and assuming that roots are elastic, the individual contribution of each intact root (F_{Ri}) to the total force (F_{Rt}) is equal to the pre-failure value, but the total number of roots diminished, and consequently the new total force decreases, compared to the former value.

$$\sigma_{Rt} = E_R \cdot \varepsilon(\theta) \tag{8}$$

$$F_{Rt}(\theta_t) = F_{Rt}(\theta_{t-1}) \cdot [1 - P(\sigma_{Rt})] \tag{9}$$

where:

- E_R is the Young 's modulus of the roots in the bundle
- $\varepsilon(\theta)$ is the linear strain of the roots, which is controlled at each time step, and it is a function of the shear angle θ
- $F_{Rt}(\theta_{t-1})$ is the total root's tensile force before the breaking of the roots happened at the time step t
- $[1 - P(\sigma_{Rt})]$ represents the percentage of the remaining roots at the time step t. Specifically, $P(\sigma_{Rt})$ is the percentage of roots that have a tensile strength equal or smaller than σ_{Rt}, which in turn is the tensile stress of the roots at the step t.

Thus, both for stress and strain-controlled conditions, it was demonstrated that the soil-roots combination behaves differently from what was formulated by previous studies. Because there is a progressive failure, the actual contribution of roots in soil shear strength is smaller than what expected with approaches such as Wu/Waldron. In fact, using the *FBM*, root reinforcement (c_r) would change at any given displacement, becoming a function of θ:

$$c_r(\theta) = \frac{F_{Rt}(\theta)}{A} \cdot [cos(90° - \psi) \cdot tan\,\varphi + sin(90° - \psi)] \tag{10}$$

where:

- $F_{Rt}(\theta)$ is the roots' total force, function of θ, which leads to a decrease in strength due to breakage of roots
- A is the total area of the shear plane

Ultimately, the key features of the *FBM* can be summarized as (i) a strain-dependent behaviour, since root reinforcement is a function of soil displacement $\theta \cdot z$, where z is the height of the shear zone; (ii) the grouping of diameter classes, for computational efficiency; (iii) the statistical representation of root properties, both from a mechanical and geometrical perspective. On the other hand, the assumptions of *FBM* may be condensed into equal load sharing, because it assumes that the load is equally distributed among roots of the same diameter class, and no root slippage, since it assumes roots break rather than pull out.

Nevertheless, the *FBM* is also subject to limitations, including the computational intensity, considering its more complex and computationally demanding nature, and data requirements, since detailed root property data is required for accurate and appropriate modelling.

A few years after the first application of the *FBM* to roots, the *RBM* was developed, offering another advancement. Specifically, the *RBM* is an enhanced version of the *FBM*, which is based on the same principles but considers the mechanical properties of different root diameter classes, the interaction between soil and roots (friction at the interface), and the pull-out failure, allowing for a more accurate representation of root system variability. The *RBM* was also later refined and extended in the following years, with versions like *RBMw* (Schwarz et al., 2013), which incorporates the Weibull survival function.

Parallelly to the introduction of the *FBM* for roots' reinforcement, the technological advancements of the early 2000s, such as the integration of remote sensing and GIS technologies, allowed for larger-scale analyses. Particularly, LiDAR data revolutionized the ability to characterize vegetation type and structure over wide areas, allowing for the implementation of root reinforcement at landscape scale, either through derivations of pre-existing models, such as the LAPSUS-LS model (Claessens, Knapen, et al., 2007; Claessens, Schoorl, et al., 2007; L. M. W. Rossi et al., 2017); SHETRAN (Bathurst et al., 2010); IDSSM (Dhakal & Sidle, 2003); SLIP4EX (Greenwood, 2006); SHALSTAB.V (Dietrich et al., 2011); TRIGRS-P (Raia et al., 2014); and many others, or straightforward applications of existing approaches (Casadei et al., 2003; Hales et al., 2009; Rickli & Graf, 2009), including statistical models.

To conclude, after the above discussed advancements, what led us to the current state of art were some emerging areas of research, such as the incorporation of climate change scenarios into long-term slope stability assessments, innovative bioengineering solutions, the availability of large, detailed landslide inventories in forested areas, which has facilitated the introduction of machine learning, and the use of a continuously improved high-resolution, throughout the years, in remote sensing data (e.g., hyperspectral imagery), which enables for detailed vegetation characterization in landslide-prone areas.

2.3 The State Of Art In Plant-Soil Interactions

The integration of vegetation effects into slope stability modelling has seen significant advancements in recent years, as discussed in the previous Section 2.2. These developments span various methodologies, from refined physically based models to innovative machine learning approaches. Nowadays, the state of art in the field of plant-soil interaction for slope stability is exemplified by numerous research efforts (DiBiagio et al., 2024; Y. Li & Duan, 2024; Masi et al., 2021; Murgia et al., 2022; Reichenbach et al., 2018).

2.3.1 Statistical Models (Including Vegetation)

Statistical models are fast and valuable approaches to quantify the effects of vegetation, and among these, Bayesian methods have gained traction in landslide susceptibility mapping. Typically, they include vegetation in the form of a Normalized Difference Vegetation Index (NDVI), and eventually through the Shannon Wiener Index (SWI).

In recent applications, the most employed Bayesian technique is the Binary Logistic Regression (BLR) (Abeysiriwardana & Gomes, 2022; Lombardo & Mai, 2018; Schmaltz et al., 2017; Von Ruette et al., 2011), with the possible integration of techniques to select the co-variables to maintain, like the Least Absolute Shrinkage Selection Operator (LASSO). Other techniques that are applied our days (with vegetation indices) are the Frequency Ratio (FR), the Multiple Linear Regression (MLR), the Information of Value (IV), and the Weight of Evidence (WoF) (Niraj et al., 2023), where IV and WoF are commonly combined with LR to improve the quality of the inputs, rather than being applied individually. However, the result is a susceptibility map but, more important, the ranking of the importance of the co-variables, including the NDVI and SWI. Furthermore, these approaches often allow for the incorporation of uncertainty in both input data and model parameters, providing more robust predictions.

2.3.2 Physically Based Models (Including Vegetation)

Relatively to physically based approaches that includes the effects of vegetation, different models represent the state-of-art. For instance, the SLIP model has been recently updated to include vegetation's contribution. The updated version, G-SLIP (Montrasio et al., 2023), performed very well in different applications, although characterized by a simple, straightforward implementation of a revised version of Wu/Waldron model, coupled with hydrological laws to consider runoff, evapotranspiration, and roots' water uptake. Both in SLIP and G-SLIP, slope stability is assessed by means of the infinite slope model and the limit equilibrium method. Another revised implementation of the Wu/Waldron model can be found in the SPRIn-SL model (Raimondi et al., 2023), which also takes advantage of the infinite slope model.

In contrast, a recent implementation of the alternative paradigm, that is fibre bundle models, could be tRIBS-VEGGIE (Arnone et al., 2016), which is an eco-hydrological model that combines vegetation dynamics with shallow landslide initiation, presented in 2016. tRIBS-VEGGIE is particularly noteworthy for describing root architecture through a so-called Leonardo's rule and for the ability to simulate hydrological effects of roots, considering factors such as root growth, decay, and seasonal variations in transpiration. Summarily, slope stability is assessed by means of the limit equilibrium analysis on the infinite slope model, while root reinforcement, from a mechanical point of view, is estimated by using the *RBM*. Another recent powerful tool that makes use of the *RBM* to evaluate root mechanical

reinforcement is the SOSlope model (Cohen & Schwarz, 2017), which evaluates factors of safety for each point of a bi-dimensional grid and can be used at different scales, ranging from single slopes to entire geographic basins. SOSlope represents a comprehensive framework, applying the discrete element method and integrating both slow and preferential rapid fluxes, macropores pressure, root reinforcement with *RBM*, and soil-roots friction.

Addressing the need for multi-scale approaches, another mentionable model is the VS2DTI, developed in 2019 (Fusco et al., 2019). VS2DTI is a spatially distributed slope stability model that leverages finite difference methods to model hydrological processes, both of soil and vegetation, which contribute to assess potential instability. The model can be applied to determine what are the site-specific rainfall thresholds (intensity/duration) which may led to the instability of slopes.

Finally, further recent studies which uses updated versions of the limit equilibrium, applied to the infinite slope and suitable for slope-scale analyses, were presented over the last few years (Abdollahi et al., 2023; Gonzalez-Ollauri & Mickovski, 2017; Ni et al., 2018; Okada et al., 2023).

2.3.3 Machine Learning Models (Including Vegetation)

Machine learning approaches have emerged as powerful tools to implement the contribution of vegetation in slope stability. Different algorithms are applied in this regard, ranging from support vector machines to ensemble methods (as random forest, adaptive boosting, etc), or artificial neural networks (Achu et al., 2023; Asada & Minagawa, 2023; Azarafza et al., 2021; L. Chen et al., 2024; Md.Sharafat et al., 2024; Misiano et al., 2023; T. Zhang et al., 2022). Particularly, different deep learning techniques have been explored, and the most used structures involve different forms of artificial neural networks, such as Convolutional Neural Networks (CNNs) to read geospatial data (grid maps of elevation, lithology etc), Recurrent Neural Networks (RNNs) to read time-dependent signals (rainfall and temperature patterns), Multi-Layer Perceptrons (MLPs) to learn generic patterns between inputs, or Encoder-Decoder Neural Networks (EDNNs) to compress and expand complex signals and numerical relationships. At times, the afore-mentioned types of neural networks can also be combined to differentiate tasks and optimize the outcome.

Regardless, vegetation is generally considered through various indices, derived from remote sensing data, which can be raw data, such as satellite imagery, or processed data, such as the NDVI, the SWI, the Enhanced Vegetation Index (EVI), and the Soil-Adjusted Vegetation Index (SAVI) mainly.

Results of the predictions in recent studies are often higher in metrics, compared to physically based or statistical models, demonstrating the potential of machine learning in handling complex, non-linear relationships between multiple environmental factors, by

capturing subtle patterns and interactions that might be missed by traditional statistical methods or excessively simplified by physically based approaches.

2.3.4 Combined, Comparative Analysis, And Future Directions

With several approaches available for studying slope stability, incorporating vegetation effects, recent years have seen the emergence of numerous studies comparing different models or integrating and combining them within a unified framework. For instance, machine learning models can be coupled with physically based approaches (Strauch et al., 2018; Yang et al., 2024), or statistic can be incorporated into physically based models, creating probabilistic physically based models (Oliveira et al., 2017; Van Zadelhoff et al., 2022), or again, machine learning can be used as support for pure statistical or empirical models (Spiekermann et al., 2021). Alternatively, with the intent to guide in the development of future, more sophisticated models, comparative studies of the various recent and widely recognized models from the literature have come to the forefront (Fusco et al., 2023; Spiekermann et al., 2023; T. Zhang et al., 2022).

Regardless of the model adopted, it was generally shown that the results can improve substantially when factors related to vegetation are implemented. Despite this, as of the writing of this work, there are no known machine learning approaches in the literature that examine the impact of various plant species on slope stability, in contrast to the findings related to physically based and statistical methods.

Amid all this, advances in remote sensing technology have enabled more accurate and extensive mapping of vegetation parameters relevant to slope stability. Different studies demonstrated the use of multi-temporal satellite imagery techniques to assess vegetation dynamics in a more appropriate way (Gao et al., 2020; Tian et al., 2021; H. Zhang et al., 2020). These approaches would allow for large-scale, long-term, and high-resolution monitoring of vegetation changes and their potential effects on slope stability.

Regarding climate change, recent models and studies have begun to incorporate its long-term scenarios and consequences on vegetation (Gariano & Guzzetti, 2016; Jakob, 2022; Jakob & Owen, 2021; Jemec Auflič et al., 2023; Kalsnes & Capobianco, 2022; Scheidl et al., 2020). Although there are still few studies that incorporate climate change, developing a model that assesses the combined impacts of vegetation and climate change projections on slope stability would be crucial and highly relevant, providing valuable insights into potential future landslide risks under our changing environmental conditions. However, challenges remain. The complexity of these models often requires extensive data inputs, which may not always be available. Additionally, validating these models across diverse environmental conditions remains a significant task.

Consequently, future research is likely to focus on (i) improving the scalability of detailed models for practical application in large-scale risk assessments; (ii) promoting the

integration of real-time monitoring data with predictive models; (iii) developing more robust approaches for modelling the long-term effects of climate change on vegetation-slope interactions; (iv) introducing the possible differences between vegetation species into machine learning models; (v) refining machine learning through explainable and interpretable models, which can provide not just predictions, but also insights into the underlying physical processes of soil coupled with vegetation.

In conclusion, the assessment of the vegetative impact on slope stability modelling has seen remarkable progress since 1976, especially during the last 15 years. Furthermore, the trend towards integrated, multi-disciplinary approaches promises more accurate and comprehensive assessments of landslide risk in vegetated slopes, with significant implications for land management and hazard mitigation strategies.

2.4 Practical Applications Of Vegetation For Slope Stability

Recent advancements in bio-engineering techniques and green mitigation strategies have significantly expanded the toolkit for mitigating shallow landslides, offering eco-friendly and cost-effective alternatives to traditional engineering solutions. As a result, the practical applications of such types of intervention are widely spreading worldwide (Andreu et al., 2008; Anstead & Boar, 2010; Gidon & Sahoo, 2020; J. T. Lee et al., 2020; Mickovski & Thomson, 2017; Polster, 2003; Preti & Giadrossich, 2009; Punetha et al., 2019; Rauch et al., 2022; Smith et al., 2015; Stokes et al., 2014), and a recent study introduced also the possible temporal issue related to these types of techniques (Bischetti et al., 2021).

The most common bio-engineering techniques that are currently applied for slope stabilization consists of direct planting of trees, shrubs, and grass (Figure II-9) with different geometrical configurations.

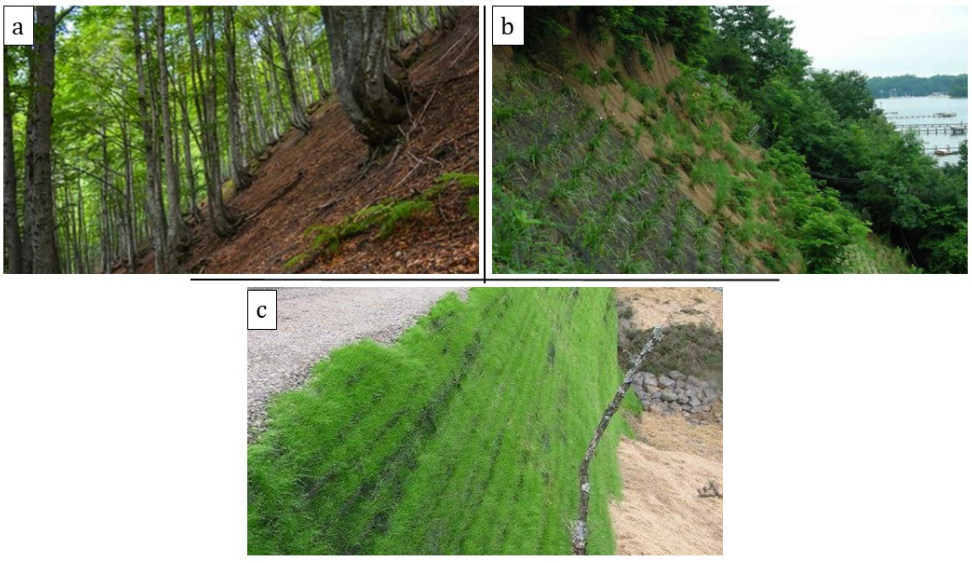

Figure II-9: Examples of direct planting of (a) Trees; (b) Shrubs; (c) Grass to improve slope stability

Alternatively, it is also appropriate to talk about bioengineering when using cuts from trees or shrubs, such as live gully breaks, fascines and wattle fences (with different types of vegetation, like willow revetments), live stakes/poles, live pole drains, vegetated crib walls and gabions, etc, as shown in Figure II-10.

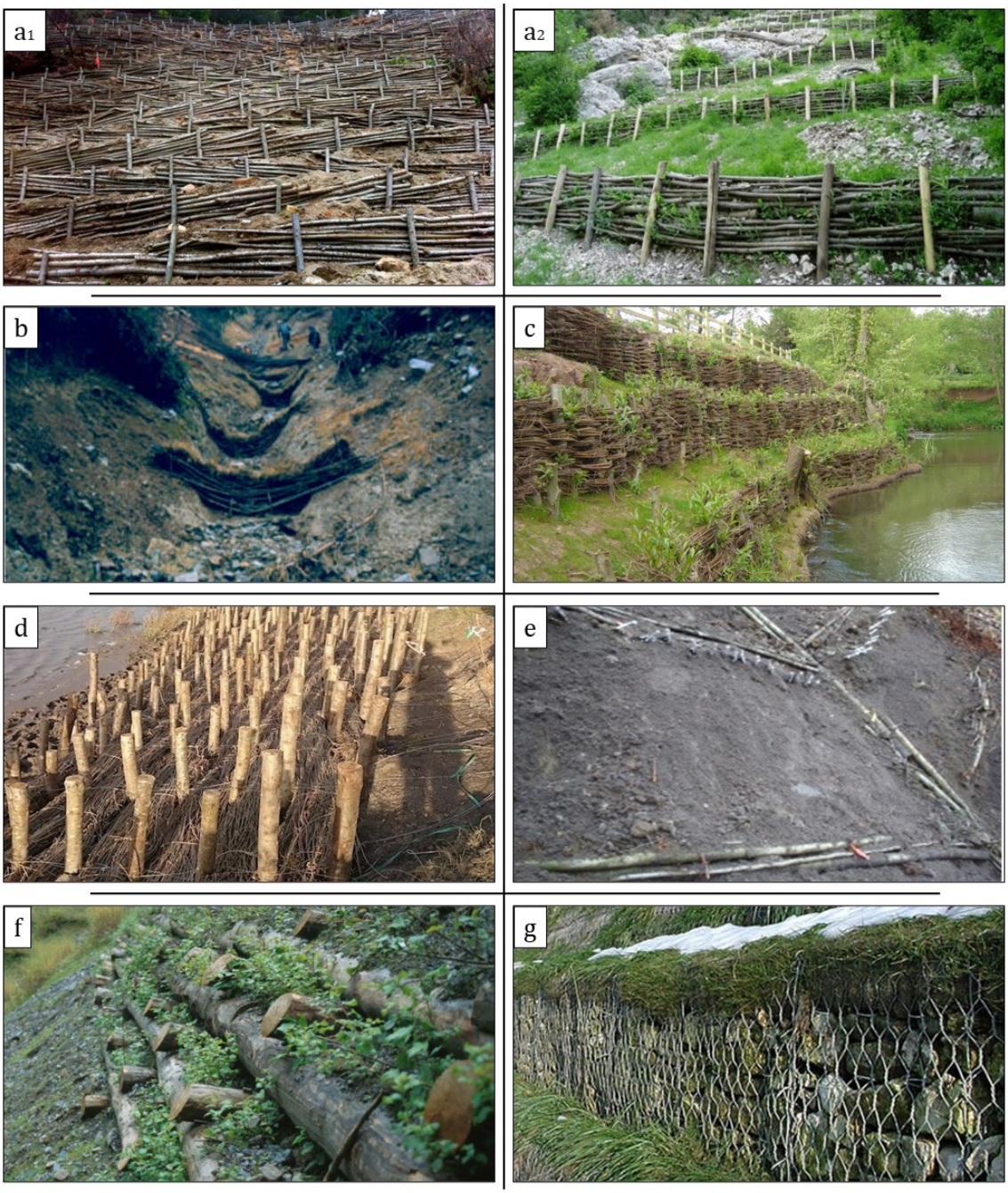

Figure II-10: Examples of bio-engineering techniques utilizing cut and processed trees: (a1, a2) wattle fences; (b) gully breaks; (c) fascines; (d) live poles; (e) live pole drains; (f) vegetated crib walls; (g) vegetated gabions

Finally, bioengineering can be mentioned even when employing materials such as geotextiles, geomembranes, and geocells, coupled with a top layer which contains vegetation and in certain cases using ecological, natural fibres to create the membranes.

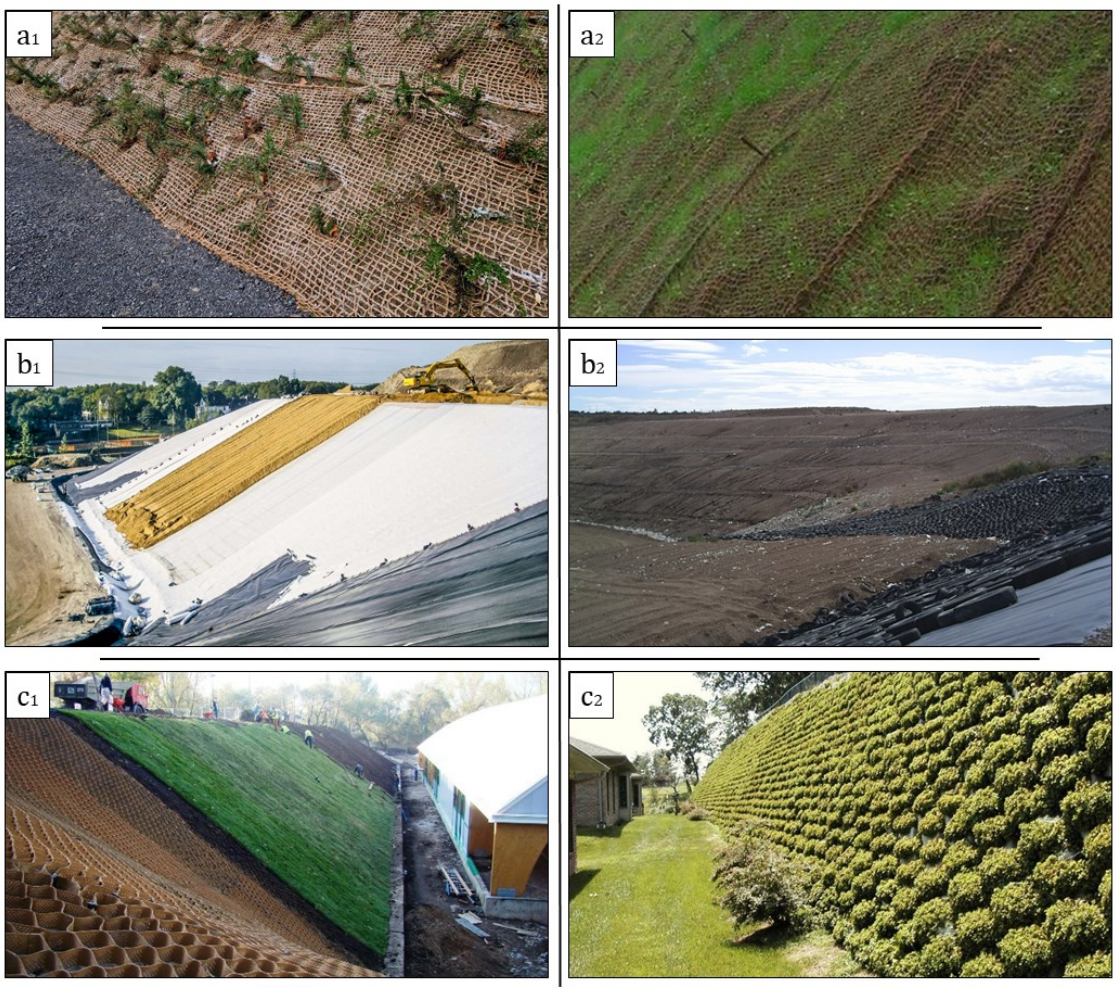

Figure II-11: Examples of ongoing applications of geomaterials: (a1, a2) Geotextiles made of ecological fibres with growing vegetation; (b1, b2) Geomembranes with a top layer made of soil and seeded vegetation; (c1, c2) Geocells incorporating a top layer of vegetated soil

Typically, to maximize the context and allow for the long-term success of bioengineering interventions, native plant species are chosen, as they do not require adaptation to foreign climatic conditions and are readily available on-site. For instance, in the Apennine mountains of central Italy, it was demonstrated the efficacy of combined live fascines and brush layering techniques using native species such as Salix purpurea (purple willow) and Spartium junceum (Spanish broom). This approach not only stabilized slopes affected by shallow landslides but also enhanced biodiversity and landscape aesthetics. In Taiwan and Hong Kong, where typhoon-induced landslides pose a significant threat, it is commonly used the Hibiscus taiwanensis, Macaranga tanarius, Mallotus paniculatus, and more recently, the

Phyllostachys edulis (Moso bamboo), both for slope reinforcement in landslide prone areas and restoration of landslides. Alternatively, as the Geotechnical Engineering Office (GEO) did on several cut slopes, it is used a combination of long-term and short-term native vegetation species. The short-term species can be native grass or small shrubs, to avoid erosion, support the growth of robust vegetation, and improve hydraulic characteristics immediately. Anyway, these methods proved particularly valuable in remote areas where conventional engineering interventions were logistically challenging or prohibitively expensive. Moreover, in case of bamboo, its rapid growth rate (up to 1 meter per day) allows for quick establishment of vegetative cover, providing almost immediate benefits. Other examples can be found in Scotland, where it was developed an innovative hybrid solution, combining willow spiling with recycled materials to stabilize riverbanks along rivers. This method, which involved weaving living willow branches through vertical posts made from recycled plastic demonstrated remarkable resilience during flood events. The approach was chosen for its ability to self-repair and strengthen over time as the willow roots developed, offering a dynamic solution that traditional static structures may not match. Additionally, a sustainability assessment framework was designed, based on a study case from Scotland at Bervie Braes, where soil nails were used with an innovative head assembly, made of pre-seeded biodegradable bags. The latter framework returns a set of key performance indicators to help in the evaluation of pros and cons in adopting such types of techniques. The rest of the UK also adopted approaches like Scotland, with native vegetation, to stabilize different slopes vulnerable to shallow landslides or exposed to continuous erosion.

These diverse examples underscore the growing recognition of bioengineering as a versatile, multifunctional approach to slope stabilization. Unlike traditional, oftentimes environmentally impactful engineering solutions, these methods offer the added benefits of carbon sequestration, habitat creation, and improved water quality. Moreover, they often require less heavy machinery for implementation and less maintenance, making them suitable for sensitive or difficult-to-access environments. As climate change increases the frequency and intensity of extreme weather events, these adaptive, nature-based solutions are likely to play an increasingly crucial role in sustainable landslide risk management strategies worldwide.

III MODELLING

3.1 SLIP MODEL

SLIP (Shallow Landslides Instability Predictor) is a simplified stability model developed by Montrasio, starting from 1996, which continues to be a subject of ongoing research, to expand its capabilities and improve efficiency (Gatto et al., 2022; Gatto & Montrasio, 2023; Misiano et al., 2023; Montrasio et al., 2013, 2014, 2018, 2023; Montrasio & Valentino, 2007, 2008b, 2008a, 2016a, 2016b). This model was formulated based on observations of numerous real landslide events that occurred during the 1994 flood in Piemonte, Italy, as well as the results of laboratory flume tests. SLIP provides an analysis of the evolution of the safety factor for an infinite slope over time, correlating it with rainfall data (both actual and predicted) and the geometric, mechanical, and hydraulic characteristics of the soil (Montrasio, 2000).

This simplified, physically-based model is based on three fundamental hypotheses:

- the topsoil layer, susceptible to sliding, is typically characterized by the presence of numerous underground conduits and channels, often resulting from the activity of various living organisms, which render the soil highly heterogeneous and more permeable than the underlying layer. This behaviour is corroborated by many agronomic studies (Bouma, 1981, 1991; Bouma & Dekker, 1978). Consequently, it becomes inappropriate to consider the upper layer of soil as a continuum, which is a common assumption in traditional soil mechanics.
- the topsoil layer exists in a state of partial saturation, with water content increasing as a function of depth considered.
- the sliding surface does not coincide with the interface between soil and bedrock but is instead located within the shallow portion of the soil layers.

These hypotheses collectively form the theoretical foundation of the SLIP model, which, combined with some field studies on rainfall infiltration in unsaturated soils (C. W. W. Ng & Zhan, 2007; Zhan et al., 2007), have led to the following postulations regarding the triggering mechanisms of shallow landslides:

- shallow landslides typically involve the upper layer/s of soil (topsoil) with a maximum thickness of about 2 m. The topsoil exhibits characteristics distinctly different from those generally considered in geotechnical engineering, particularly in terms of hydraulic properties. In fact, this upper layer (typically removed when

constructing civil structures or infrastructure) contains numerous pores, small channels, and fissures. This structure provides two preferential pathways for rainfall infiltration: the first through macro-porosity, and the second through the micro-porosity of the soil matrix. SLIP model considers the first infiltration pathway as predominant, while the second is neglected.

- slopes are initially considered stable due to one of the factors contributing to shear strength, which is provided by the partial saturation of the soil. This contribution is normally referred as apparent cohesion, and it will be later discussed.
- rainfall infiltrates more rapidly through macropores than through micropores, reaching the deeper parts of the channels and, only afterwards, flowing in various directions through the micropores of the soil matrix.
- starting from the areas surrounding the macropores, infiltration through micropores causes localized saturation of those areas, creating discontinuous saturated soil zones, referred to as "saturation bubbles," whose volume increases with the amount of infiltrated rainfall. Thus, if rainfall persists, the saturation process advances, and increasingly larger portions of soil become saturated. This phenomenon renders the soil medium far from a continuum, interpretable with traditional geotechnics.
- until complete soil saturation is achieved, stability is maintained because the saturated soil portions (which would have already reached failure conditions) are not continuous within the partially saturated mass. However, if precipitation further persists, the saturated soil portions expand until they become continuous, resulting in the loss of partial saturation in most of the soil and triggering the sliding process. Therefore, the evolution can be catastrophic, depending on the thickness of the saturated layer. A greater thickness translates to a larger quantity of transported material and, more importantly, a larger quantity of water in the solid matter, which reduces friction along the path and potentially liquefies the flow.
- the geometric characteristics of hundreds of unstable slopes observed in the past years indicate that it is appropriate and opportune to employ an infinite slope scheme for stability analysis.

Thus, the above-mentioned considerations can be conceptualized into a three-step process: (i) to start with, infiltration occurs in the areas surrounding the macropores; (ii) following this, progressively larger portions of soil become saturated; (iii) finally, these saturated portions expand and become continuous, resulting in a loss of partial saturation throughout most of the soil and leading to incipient collapse. In summary, the SLIP model is predicated on the application of the limit equilibrium method, coupled with simplified models to consider the shear strength in partially saturated soils. It also incorporates a homogenization process, regarding slope imbibition and drainage processes.

The outcome of SLIP, based on which the stability of each slope is assessed, is the factor of safety (Fs), which is a function of several parameters, such as geometric factors (slope inclination, β; depth of the sliding surface, where instability occurs, H); soil state parameters (specific gravity, G_S; porosity, n; degree of saturation, S_r); mechanical soil parameters (effective angle of internal friction, φ'; effective cohesion, c'); modelling parameters related to the partial saturation and the simplification (A; λ; α); other hydraulic parameters (global drainage coefficient of slope, k_t; unit weight of water, γ_w; rainfall height occurred at each timestep, $h(i)$; infiltration coefficient, β^*). The formulation is the following:

$$Fs = \frac{cot\beta \cdot tan\varphi' \cdot [T + m \cdot (n_w - 1)] + C' \cdot \Omega}{T + m \cdot n_w} \tag{11}$$

where factors T, n_w, Ω, C', and m represent respectively

$$T = G_S \cdot (1 - n) + n \cdot S_r \tag{12}$$

$$n_w = n \cdot (1 - S_r) \tag{13}$$

$$\Omega = \frac{2}{sen(2\beta) \cdot H \cdot \gamma_w} \tag{14}$$

$$C' = c' + A \cdot S_r \cdot (1 - S_r)^{\lambda} \cdot (1 - m)^{\alpha} \tag{15}$$

$$m = \frac{\beta^*}{n \cdot H \cdot (1 - S_r)} \cdot \sum_{i=t_1}^{t_n} h(i) \cdot e^{-[k_t \cdot (t_n - i)]} \tag{16}$$

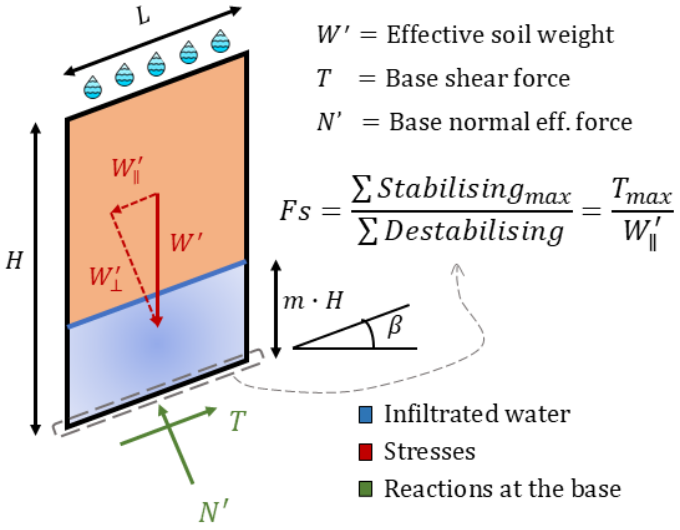

Figure III-1: A representation of the infinite slope scheme, used to evaluate the equilibrium with SLIP. The rainfall that infiltrates from the top and saturates local portions of soil is deposited and uniformed ($m \cdot H$) at the bottom of the soil volume unit. The Factor of safety (Fs) is then assessed at the sliding surface (depth H), through the ratio between the maximum total of stabilising contributions (numerator) and the total of currently acting destabilising forces (denominator). If the ratio is greater than unity, the slope can be considered as stable.

As can be observed from Equation 16, m is a function of time t, which must be discretized, typically in hours. Therefore, to assess the Fs at the timestep t_n it is necessary to know the history of the rainfall height up to the timestep t_0, which is prior and represents the starting point. In other words, SLIP requires rainfall data history to be run, which therefore constitutes a sort of memory for the model, allowing it to account for past rainfall events, as shown in Figure III-2.

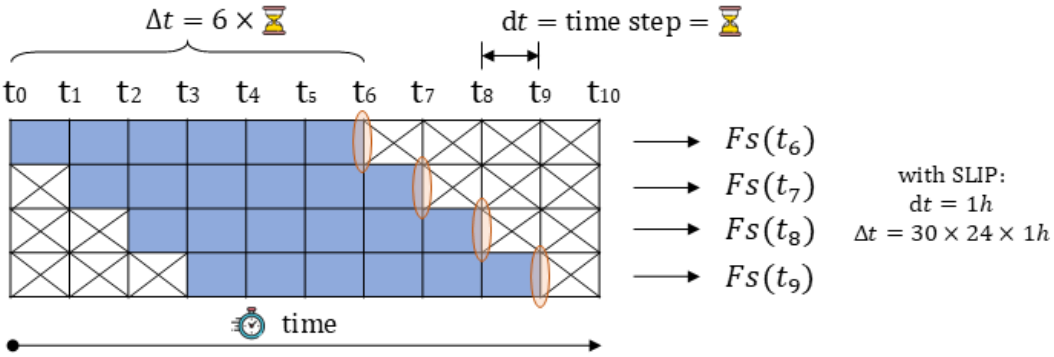

Figure III-2: Example of different Factors of Safety, evaluated at different times. The time window needed to perform each analysis maintains the same duration Δt, but the starting and ending points are shifted in time.

Normally, t_0 is set to 30 days before the timestep t_n, at which the analysis is conducted. Consequently, for multiple analyses at different timesteps, $t_n - t_0$ constitutes a dynamic time window, which must be updated in each analysis (if different t_n are considered).

The SLIP model's relative simplicity, despite the multitude of variables it considers, renders it particularly suitable for large-scale applications. This characteristic is crucial in the field of landslide risk assessment and management, where the ability to efficiently analyse vast areas is often necessary. Moreover, the model's capacity to evolve the factor of safety over time in response to rainfall input allows for dynamic risk assessment, a critical feature in regions prone to rapid-onset shallow landslides. This temporal dimension enables the model to capture the often sudden nature of shallow landslide initiation, which can be triggered by specific rainfall events rather than long-term precipitation trends.

While the simplifications inherent in the model may limit its applicability in highly complex geological settings, its efficiency and broad applicability make it a valuable tool for initial risk assessment and to target more detailed investigations where necessary, as documented in different applications experimented over the past years (Gatto et al., 2023a; Montrasio et al., 2009, 2010, 2012, 2015, 2018; Schilirò et al., 2016).

To conclude, the balance of SLIP between complexity and usability exemplifies the ongoing efforts in geotechnical engineering to develop practical tools for real-world applications, while maintaining a sound theoretical basis.

3.1.1 Mathematical Modelling And Assumptions Of SLIP

The SLIP's formulation is the result of a process of mathematical and physical simplification, which takes into consideration only those factors deemed primary and determinant in defining the processes and triggering mechanisms of landslides, at the expense of aspects considered secondary and thus deemed to have little influence on the result. The foundational hypotheses of the model are as follows:

- the problem is approached using an infinite slope assumption.
- from a hydraulic perspective, it is presumed that the permeability of the substrate is significantly lower than that of the upper soil layer.
- stability is ensured by apparent cohesion, caused by the partial saturation of the soil.
- the percentage of precipitation which infiltrate the soil is considered though the infiltration coefficient β^*, but evapotranspiration is neglected (representing a worst-case scenario, conservative from a safety perspective).
- it is presumed that the moment of collapse is characterized by the formation of a uniform saturated layer of finite thickness at the contact with the subsoil (this would be the lower part of the soil in Figure III-1, denoted as $m \cdot H$). This hypothesis simplifies the mechanism whereby saturated portions of soil progressively expand until reaching the condition of instability. The thickness ($m \cdot H$) of this saturated layer is directly linked to the rainfall height ($h(i)$).
- all mechanisms that induce water to drain away from the topsoil layer are summarized by a simplistic hypothesis, according to which $m \cdot H$ would decrease with a negative exponential time function, governed by a factor k_t, representing the global drainage capacity of the slope.

These simplifications allow the SLIP model to maintain computational efficiency while capturing the essential physics of shallow landslide triggering. By focusing on the most critical factors, the model achieves a balance between accuracy and practicality, making it suitable for large-scale applications and rapid assessments. To begin with, the infinite slope assumption (i) is appropriate for shallow landslides, where the slide plane is typically parallel to the ground surface and the length of the slide is much greater than its depth. This simplification allows for a two-dimensional analysis that is both computationally efficient and sufficiently accurate for most scenarios. In addition, the hydraulic assumption (ii) reflects the common geological setting where a more permeable soil layer overlies a less permeable substrate. This contrast in permeability is often a key factor in the development of shallow landslides, as it can lead to the formation of a perched water table during intense rainfall events. Moreover, the role of apparent cohesion (iii) in partially saturated soils is crucial in explaining why many slopes remain stable under normal conditions but fail during or after intense rainfall. As the soil becomes saturated, this apparent cohesion is reduced, leading to

a decrease in slope stability. Additionally, the conservative approach of assuming complete infiltration (iv) ensures that the model errs on the side of caution, which is appropriate for risk assessment and management purposes. Furthermore, the simplification of the saturation process (v) allows for a more tractable mathematical formulation while still capturing the essential physics of the problem. While it does not represent the complex, heterogeneous nature of actual soil saturation processes, it provides a reasonable approximation for the purposes of large-scale landslide prediction. Finally, the simplification of drainage processes (vi) allows the model to account for the dissipation of pore water pressures over time without requiring detailed hydrological modelling. The use of a single parameter (k_t) to represent the overall drainage capacity of the slope is a pragmatic approach that balances the need for physical realism with computational efficiency.

These simplifications and assumptions, while introducing some limitations, enable the derivation of a closed-form solution which allow the SLIP model to be easily implementable on vast land areas and provide valuable insights into shallow landslide susceptibility. The model's ability to incorporate key physical processes while remaining computationally efficient makes it a useful tool for both research and practical applications in landslide risk assessment and management.

3.1.1.1 Soil Suction and Apparent Cohesion

Soil suction (ψ) is a fundamental concept in unsaturated soil mechanics, crucial for understanding the behavior of partially saturated soils. It is typically expressed as the sum of matric suction ($s = u_a - u_w$) and osmotic suction (π):

$$\psi = s + \pi = (u_a - u_w) + \pi \tag{17}$$

where u_a is the pore air pressure and u_w is the pore water pressure.

Matric suction is often the more significant component in geotechnical applications, and it results from capillary and adsorptive forces between soil particles and water molecules. As the degree of saturation decreases, water in soil pores forms menisci between particles, creating negative pore water pressure. This negative pressure increases the normal effective stress between soil particles, leading to increased soil strength (Fredlund et al., 1978, 1996; Fredlund & Rahardjo, 1993). This increase is expressed via apparent cohesion, describing the additional shear strength component in unsaturated soils, which is added to the Mohr-Coulomb failure criterion for saturated soils. Therefore, the shear strength (τ) of an unsaturated soil can be expressed using the extended Mohr-Coulomb failure criterion:

$$\tau = c' + (\sigma_n - u_a) \cdot tan\,\varphi' + (u_a - u_w) \cdot tan\,\varphi^b \tag{18}$$

where c' is the effective cohesion, σ_n is the total normal stress, φ' is the effective angle of internal friction, and φ^b is the angle indicating the rate of increase in shear strength

relative to matric suction. Thus, the term $(u_a - u_w) \cdot \tan \varphi^b$ represents the contribution of matric suction to shear strength, often referred to as apparent cohesion. It is important to note that $(\sigma_n - u_a)$ is equal to σ_n', i.e., the effective (net) normal stress.

Equation 18 can be also formulated as a function of the degree of saturation S_r, though the soil-water characteristic curve (SWCC, i.e., water retention curve) (Vanapalli et al., 1996):

$$\tau = c' + (\sigma_n - u_a) \cdot tan\, \varphi' + (u_a - u_w) \cdot \frac{S_r - S_{re}}{S_{sat} - S_{re}} \cdot tan\, \varphi' \quad (19)$$

where S_{re} residual degree of saturation, and S_{sat} is the degree of saturation corresponding to a saturated soil, which is equal to 100.

Consequently, the apparent cohesion (c_ψ) can be expressed as:

$$c_\psi = (u_a - u_w) \cdot tan\, \varphi^b = (u_a - u_w) \cdot \frac{S_r - S_{re}}{S_{sat} - S_{re}} \cdot tan\, \varphi' \quad (20)$$

In SLIP, a simplification of Equation 20 is proposed, based on the interpolation of several experimental triaxial tests under controlled suction, conducted on various types of soils commonly found in Italy (Montrasio & Valentino, 2007):

$$c_\psi = A \cdot S_r \cdot (1 - S_r)^\lambda \cdot (1 - m)^\alpha \quad (21)$$

where:

- A is a constant value, related to soil type and the peak shear stress at failure
- λ is a parameter used to translate the c_ψ peak along the horizontal axis, which is however commonly located at a degree of saturation (S_r) equal to around 0.7
- α is an empirical value to consider the percentage of partial saturated soil $(1 - m)$

As it can be seen from Figure III-3, different soil types have different curves, but generally, if the starting degree of saturation S_r is equal to around 0.7 (common amount for Italian soils), then a rainfall event would led to a decrease in apparent cohesion values.

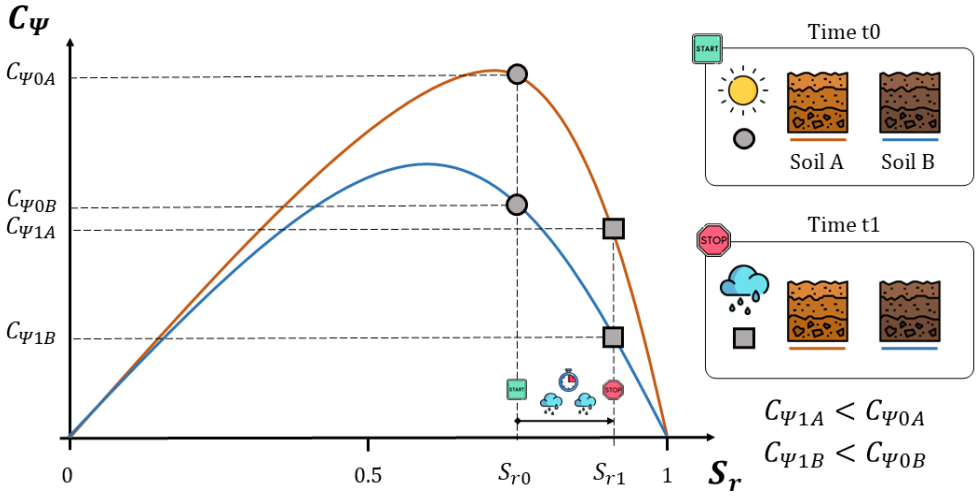

Figure III-3: Example of two different soil types, A and B. Circle markers represent the situation of both soils before water infiltration, square markers represent the situation after it. The initial condition is represented by the degree of saturation S_{r0} at the time instant t_0. After rainfall, at the time instant t_1, the degree of saturation raised to S_{r1} and the apparent cohesion of both soil types decreased.

Furthermore, the assumption according to which the maximum apparent cohesion (c_ψ) would occur with a degree of saturation (S_r) of around 0.7 is justified by the values of λ and A, reported in Table III-1.

Soil	λ	A
Soft clay (OCR=1)	0.4	100
Medium clay (OCR>1)	0.4	100
Stiff clay (OCR>>1)	0.4	100
Clayey mud	0.4	80
Mud	0.4	80
Sandy mud	0.4	80
Loose sand	0.4	40
Medium sand	0.4	40
Dense sand	0.4	40

Table III-1: List of SLIP's modelling parameters λ and A for common soil types in Italy

To conclude, the relationship between suction and apparent cohesion is particularly relevant in the context of shallow landslides. It explains why many slopes remain stable under 'dry' conditions (not fully dry, because in practice, a slight degree of suction remains, and the degree of saturation cannot be entirely nullified) but fail during or after intense rainfall events. As water infiltrates the soil, it reduces matric suction, leading to a decrease in apparent cohesion and, consequently, a reduction in slope stability. The SLIP model incorporates this mechanism in predicting shallow landslide initiation, accounting for the dynamic nature of soil strength in response to changing moisture conditions.

3.1.1.2 Water Drainage and Infiltration

SLIP considers the "double porosity effect" (Lewandowska et al., 2008; X. Li & Zhang, 2009), which describes the progressive saturation of soil volumes that are chaotically distributed due to water infiltration through soil macropores first and micropores later. During this process, the saturated zones are characterized by a null apparent cohesion, while the remaining soil maintains a certain value of apparent cohesion (c_ψ), which depends on the initial degree of saturation (S_{r0}). Therefore, when this physical phenomenon is theorized under the infinite slope hypothesis, the chaotically distributed saturated zones can be simplified into a single saturated layer whose thickness ($m \cdot H$) is dependent on the amount of rainfall. In fact, the parameter m represents the dimensionless percentage of the saturated portion of the soil layer and is therefore a fractional parameter ranging from 0 to 1. It can be constant or time-variable and is correlated to the volume of rainfall (ΔV_w) required to saturate a portion of soil that was initially characterized by a degree of saturation S_{r0} (thus, it was partially saturated). In Figure III-4, an illustrating scheme of such a process is shown.

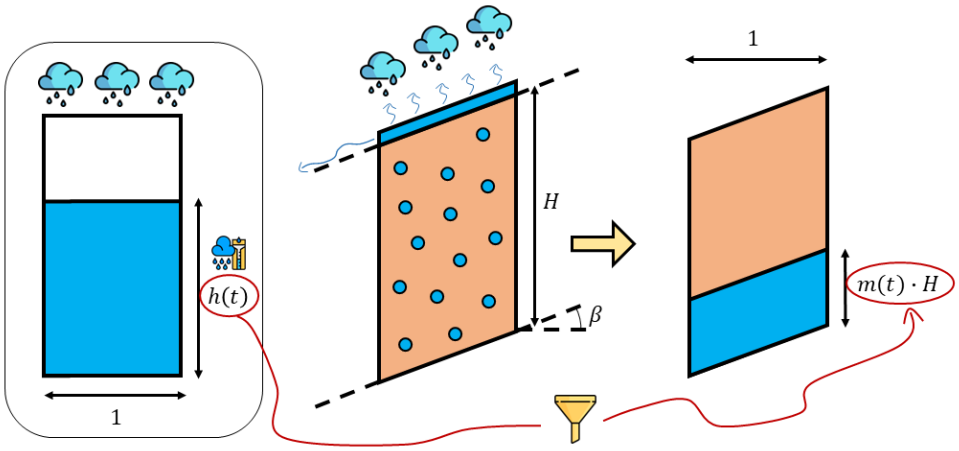

Figure III-4: Scheme of the rainfall infiltration process in SLIP: on the left, the representation of the rainfall height, recorded by a gauge station; on the middle, the actual representation of the infiltration process, where a part of rainfall does not infiltrate the soil (due to runoff and evapotranspiration) and the remaining part permeates it, creating localized areas of saturated soil; on the right, the result of SLIP's process of homogenization and uniformization is shown, with the various saturated regions converging into one single layer.

Considering the rainfall height $h(t)$, which is a time dependent variable, the runout coefficient β^*, the initial degree of saturation S_{r0}, the uniformed saturated thickness $m \cdot H$, a unit length and width, it is possible to derive a relationship between the parameter m, the infiltrated rainfall volume ΔV_w and the volume of the residual voids in soil V_{rv}. This relationship is formulated as follows:

$$m = \frac{\Delta V_w}{V_{rv}} = \frac{\beta^* \cdot h(t)}{H \cdot n \cdot (1 - S_{r0})} \tag{22}$$

Equation 22 represents the portion of saturated height caused by the rainfall at time t. This means that if the soil was initially in a configuration of partial saturation (S_{r0}), m represents the rate of soil height that become fully saturated after one or several rainfall events. Such a fraction of height must be assessed over the remaining voids in the soil, which are represented by $(1 - S_{r0})$.

Despite this, the formula would only work if rainfall infiltration were instantaneous and there was no drainage, but the latter must be considered, along with the history of past rainfall. Therefore, an exponential model for water drainage is introduced, and past rainfall is aggregated with the new, while accounting for the effect of time, which will gradually diminish the influence and amount of the earlier rainfall, as shown in Figure III-5.

The mathematical formulation of the above discussed process is described in Equation 16, by means of the term $\sum_{i=t_1}^{t_n} h(i) \cdot e^{-[k_t \cdot (t_n - i)]}$.

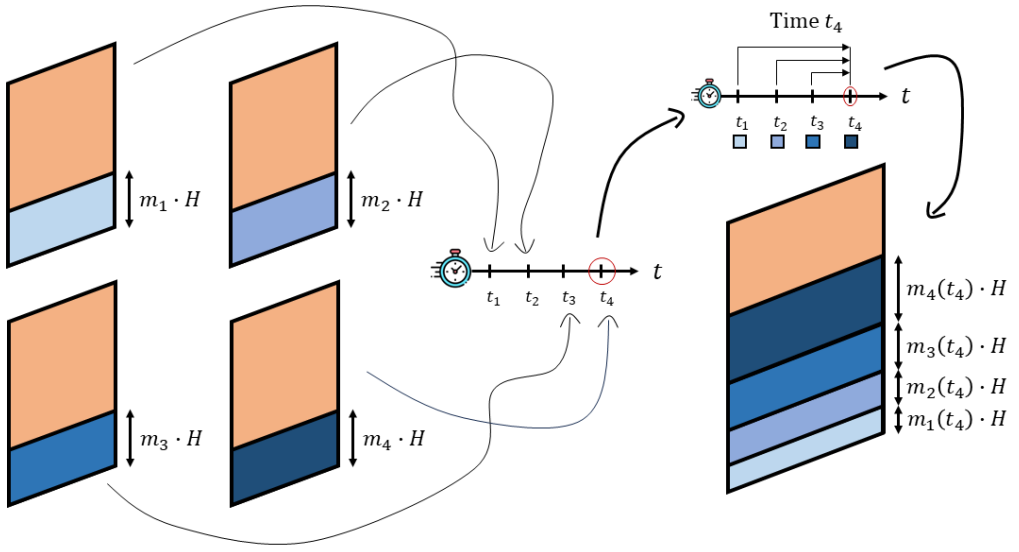

Figure III-5: Infiltration due to distributed rainfall over time. Even if the amounts of rainfall are the same in the four different time instants, the effects of the former rainfall are damped, when shifted to the final time instant. In fact, more recent rainfall (time instant t4) has greater impact, with a higher homogenized rainfall height.

To summarize, this conceptualization allows for a more accurate representation of the infiltration process and its effects on slope stability. The model's approach to homogenizing the saturated and unsaturated layers provides a practical means of accounting for the deterioration of soil shear strength characteristics due to partial saturation.

3.1.1.3 The Equilibrium of Forces

In the SLIP model, slope stability is evaluated using the factor of safety Fs. In order to understand Equation 11, it must be noted that the factor of safety is defined as the ratio

between the maximum shear stabilizing forces (T_{sMax}) and the actual destabilizing forces (T_d), calculated using the limit equilibrium method:

$$Fs = \frac{T_{sMax}}{T_d} \tag{23}$$

The model considers an infinite slope with inclination β, composed of a soil layer of thickness H. Thus, the forces acting on this slope were already illustrated in Figure III-1 and, considering the equilibrium along the slope plane of inclination β, the factor of safety Fs over a portion of slope that has a length L and a unit width, can be expressed as:

$$Fs = \frac{(\sigma'_n \cdot tan\,\varphi' + c'_{tot}) \cdot A_n}{W \cdot sin\,\beta} \tag{24}$$

$$A_n = L \cdot 1 \tag{25}$$

where:

- σ'_n is the effective normal stress of the soil, perpendicular to the sliding surface
- c'_{tot} is the sum of effective and apparent cohesion, i.e., $c'_{tot} = c' + c_\psi$
- W is the total soil weight of the reference volume
- A_n is the area at the base (sliding surface), inclined at an angle β, whose value is therefore equal to $L \cdot 1$

The stabilizing maximum forces of Equation 24 (T_{sMax}) are evaluated based on the Mohr-Coulomb failure criterion, including the contribution to soil shear strength due to partial saturation, by means of the apparent cohesion. More in detail, the effective normal stress σ'_n and total cohesion c'_{tot} can be described incorporating factors such as water unit weight (γ_w), soil porosity (n), degree of saturation (S_r), and the fraction of saturated soil thickness (m). In specific terms, it would result that:

$$\sigma'_n = \frac{W' \cdot cos\,\beta}{A_n} \tag{26}$$

$$W' = W - u_w \cdot A_n \cdot cos\,\beta = W_{sk} + W_{ss} + W_{ps} - u_w \cdot A_n \cdot cos\,\beta \tag{27}$$

$$W' = \gamma_w \cdot A_n \cdot cos\,\beta \cdot H \cdot [G_S \cdot (1-n) + n \cdot m + S_r \cdot n \cdot (1-m) - m] \tag{28}$$

$$c'_{tot} = c' + A \cdot S_r \cdot (1-S_r)^\lambda \cdot (1-m)^\alpha \tag{29}$$

where:

- W', W_{sk}, W_{ss}, and W_{ps} are vertical forces and respectively represent the effective soil weight (total soil weight reduced by the effect of water pressure at the sliding surface), the weight of the soil solid skeleton, the weight of the homogenized fully saturated soil, and the weight of the remaining partial saturated soil, as illustrated in Figure III-6

- the term $u_w \cdot A_n \cdot \cos\beta$ represents the vertical component of the soil water pressure, which must be subtracted to the total weight to obtain the effective ($\sigma' = \sigma - u_w$)

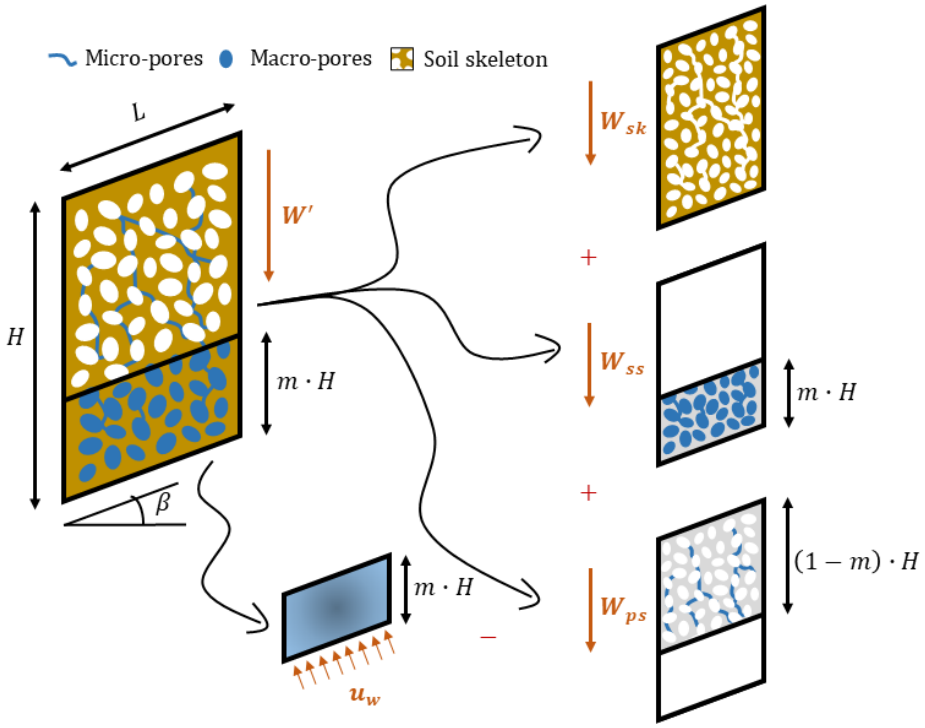

Figure III-6: Scheme of the separation of the total weight of soil volume in 3 components (on the right) and water pressure at the base, which is the sliding surface.

In contrast, the expression for the actual destabilizing forces of Equation 24 (T_d) is obtained just from the component of the total weight parallel to the slope, as follow:

$$T_d = W \cdot sin\,\beta \tag{30}$$

From which, with few steps, it can be obtained that:

$$Fs = cot\,\beta \cdot tan\,\varphi' \cdot \left(1 - \frac{m}{G_S \cdot (1-n) + n \cdot m + S_r \cdot n \cdot (1-m)}\right) + \frac{c' + A \cdot S_r \cdot (1-S_r)^{\lambda} \cdot (1-m)^{\alpha}}{\gamma_w \cdot cos\,\beta \cdot H \cdot [G_S \cdot (1-n) + n \cdot m + S_r \cdot n \cdot (1-m)] \cdot sin\,\beta} \tag{31}$$

However, if expressed in this form, the equation would become too intricate and less feasible for practical application. This led to the formulation presented at the beginning of Section 3.1 (Equation 11), through further steps and the introduction of terms such as T, n_w, Ω, C', and m.

To conclude, regardless the form of the equation applied (Equation 11 or 31), the condition of instability corresponds to $Fs \leq 1$, which means that there are no available resistance reserves, and the destabilizing forces are exceeding the maximum limits.

3.1.2 The Vegetation Update: G-SLIP

The recent update of SLIP, named as G-SLIP (Montrasio et al., 2023), introduces the effects of vegetation in slope stability. As discussed in the previous Sections, especially in Chapter II, these effects can be categorized into hydrological and mechanical. In G-SLIP, both these effects are factored in modelling.

Regarding the hydrological effects, it is assumed that the most relevant contribution is related to the runoff and the evapotranspiration, i.e., the infiltration coefficient (β^*) in Equation 16. In fact, depending on the type of vegetation that is present in a certain slope, coupled with the effects of inclination (that would modify the runoff), this coefficient β^* may range from zero to the unit. However, the resulting percentage of rainfall height that infiltrates into the soil through its pores, that is β^*, is always smaller with vegetation, compared to the case without it. This assumption stems from the fact that, with bare soil, the infiltration coefficient depends solely on slope morphology (e.g., via the cosine of the inclination β); whereas the presence of vegetation introduces beneficial effects as discussed in Chapter II. All of this results in a soil that is initially less saturated. Furthermore, given the same rainfall conditions and same starting S_r, soils with vegetation would exhibit less variation in the degree of saturation, along the experimental wetting-drying curve, as shown in Figure III-7.

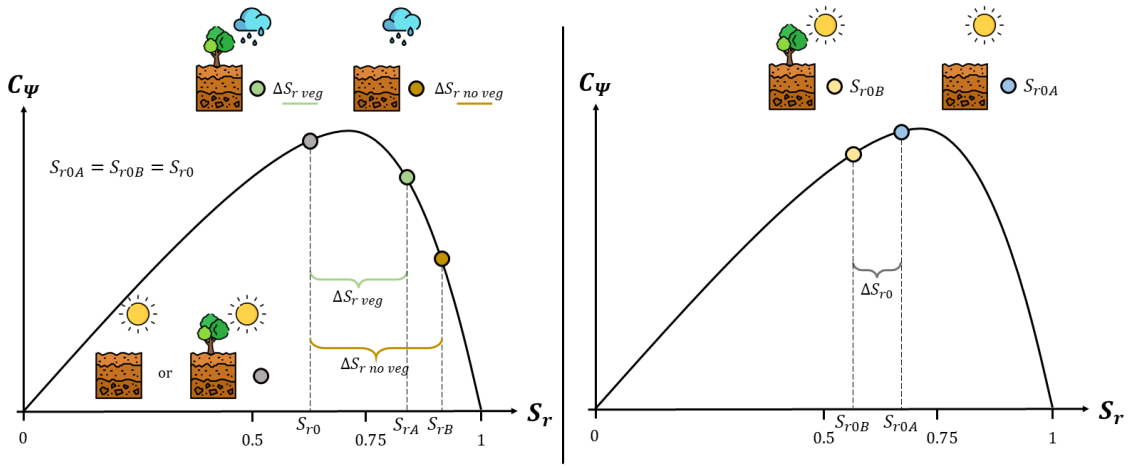

Figure III-7: Scheme of the increase in the degree of saturation starting from the same initial condition S_{r0} and same soil, except for the presence, or not, of vegetation (left); reduction of the initial degree of saturation in case of same soil but with or without vegetation (right).

Regarding the mechanical effects, it is assumed a hypothesis of root's homogenization, which means that, depending on the depth at which the analysis is conducted, the increase of the mechanical strength is uniform over the sliding surface (Figure III-8). This increase refers to the value of the root cohesion (c_r), i.e., the maximum shear strength of SLIP is increased with the root cohesion, as shown in Figure III-9. Expressed in mathematical terms, if Equation 15 and 29 are considered, they would be adjusted as follows:

$$C' = c'_{tot} = c' + A \cdot (1 - S_r)^{\lambda} \cdot (1 - m)^{\alpha} + c_r \quad (32)$$

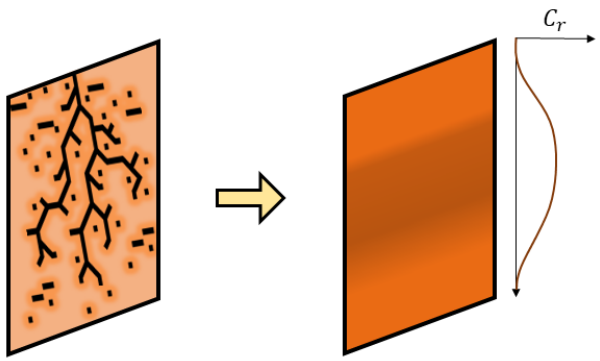

Figure III-8: Scheme of the root homogenization process adopted in SLIP: root cohesion is a function of the Ratio Area Root (RAR), which in turn can be expressed as a function of the soil depth for most vegetation species. Consequently, root cohesion becomes a function of the depth.

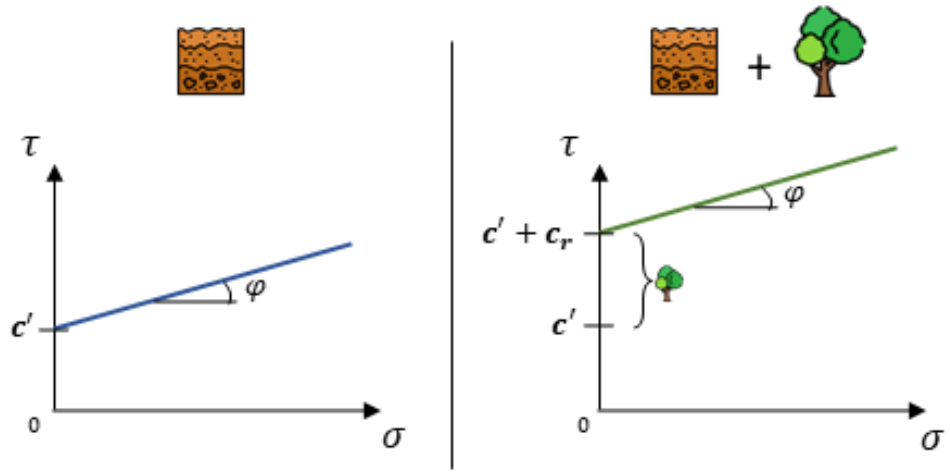

Figure III-9: Scheme of the increase of shear strength through the introduction of root cohesion in the Mohr-Coulomb failure criterion. On the left, the common Mohr-Coulomb criterion (without vegetation), on the right, the modified one (with vegetation). Root cohesion role is to shift the failure envelope along the y-axis.

To assess root reinforcement, the approach adopted in SLIP is an updated version of the Wu/Waldron model, seen in Chapter II (Section 2.2). Specifically, this approach, which is well documented in the literature (Bischetti et al., 2005, 2009; Collison, 2001; Esmaiili et al., 2021; Fan & Chen, 2010; S. Li et al., 2023; Operstein & Frydman, 2000; Schmid & Kazda, 2001), consists of considering multiple roots and their evolution with the depth, i.e., considering the differences in quantity and diameters of roots with the depth. This is factored in via the mean Root Area Ratio (RAR), also seen as a_r in Equation 1, 2, and 4. The difference relies on the fact that RAR is a function of the depth of the analysis H (and not fixed as a_r), which assumes different mathematical forms according to the type of vegetation. Generally, key values of RAR lies within the depth range of 1 to 1.5 meters, since most SLIP analyses concentrate in this interval.

3.2 LEP-AI MODEL

LEP-AI (Landslide Event Predictor - Artificial Intelligence) is one of the models developed in this work, based on AI. Particularly, this model is an Artificial Neural Network (ANN) (see Appendices Chapter) designed to be highly computationally efficient and to serve as a "filter", i.e., acting as an assistant and guide for redirecting towards more detailed and in-depth analyses of slope stability, but just for those areas that could be unstable. Its functioning principle is based on the prediction of Landslide Events, which are essentially Rainfall Events during which one or more landslides could potentially affect a specific geographical macro-area, typically defined by municipal boundaries. For a detailed description of both Landslide and Rainfall Events, or municipal Area Units used, please refer to the following Section 3.2.1 and 3.2.2.

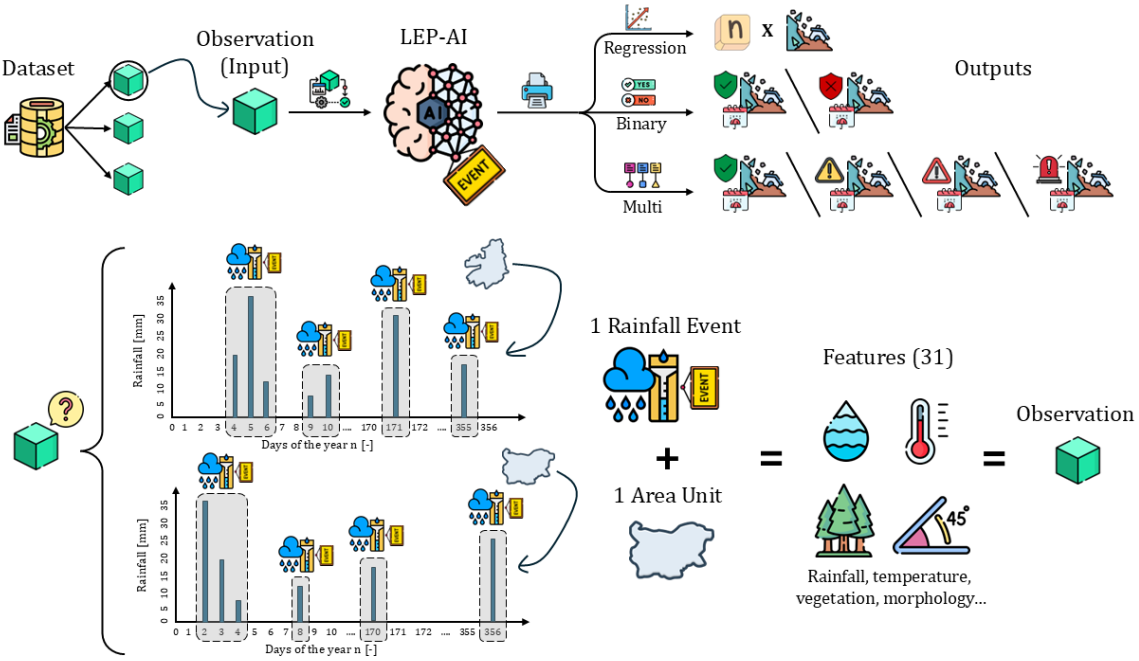

Figure III-10: Conceptual and illustrating scheme of the LEP-AI model functioning. Starting from the top, the model processing is shown. From a dataset, which is made of observations, a single observation is extracted and passed through the LEP-AI model, which in turn it will give an output that can be of three types (according to the training mode), i.e., regression, binary, or multi. The output of 'regression' mode is the number of potential landslides. The outputs of 'binary' mode are two classes, that is no landslides or at least one. The outputs of 'multi' mode are four classes, i.e., no landslide risk or low, medium, and high landslide risk. On the bottom of the figure, it is shown what is an observation for the LEP-AI model. If a Rainfall Event is associated with a certain Area Unit, then some features can be extracted. The set of all these features, for a certain Rainfall Event and Area Unit, represents an observation.

The main advantage of such a type of model is the fact that it could be used in real-time, covering very large areas as entire countries, like Italy, which is heavily affected by landslide issues throughout its geographical development. Furthermore, data to use as input of LEP-AI model is easily accessible both in regional and national (or European) web portals (Section 3.2.1), making it easy to apply on a large scale.

To conclude, LEP-AI represents one of the most efficient and practical models to be used standalone, for civil protection and prevention purposes (as it would provide information on municipalities at risk during a Rainfall Event), or as a preliminary filtering tool, to prioritize areas that, during such events, would require more detailed and focused analyses, which are often challenging and impractical to conduct over vast areas (due to computing limitations or unavailability of data).

3.2.1 Data Sources

The primary source to create datasets, needed to train and update the LEP-AI model, are landslide inventories. Commonly, in Italy these databases can be obtained from regional geoportals, such as landslide census data from the General Directorate for Territorial and Environmental Care of Emilia-Romagna region (*Geologia, Suoli e Sismica - Regione Emilia-Romagna - Ambiente*, n.d.; *Geoportale Regione Emilia-Romagna*, n.d.; *OpenDataER*, n.d.) and others (*Geoportale Della Lombardia*, n.d.; *Geoportale Regione Liguria*, n.d.; *Geoscopio*, n.d.), or alternatively from national portals (*Geoportale Nazionale*, n.d.; *ISPRA*, n.d.), or even from other open-source data, provided by other scientific studies (Ferrario & Livio, 2024; Peruccacci et al., 2023a) and open challenges (*Kaggle*, n.d.; *Nasa*, n.d.; *USGS*, n.d.; *World Bank Group*, n.d.; *Zenodo*, n.d.). However, databases must contain some essential parameters, that is occurrence dates, coordinates of triggering (or at least the municipality of occurrences), and possible triggering factors (to separate properly landslides according to their nature).

Typically, information contained in these inventories is incomplete, spatially (some landslide coordinates are missing, for a certain Rainfall Event), temporally (no landslides for a Rainfall Event where actually they occurred), or both. The reasons behind this issue could be different, such as areas that are inaccessible and cannot be seen, even with satellite; the inaccuracy on the part of the entity responsible for compiling the reports; the lack of adequate instrumentation, etc. Thus, the issue of the incompleteness of landslide inventories remains a challenging matter to this day. This is one of the reasons why, with the LEP-AI model, it was decided to treat the data at the level of areas corresponding to Italian municipalities, which typically have an extension of 40 square kilometres, on average. From this point forward, the latter areas will be referred to as Area Unit (AU) and they will represent the fundamental spatial reference units, which are in other words the objects of the predictions.

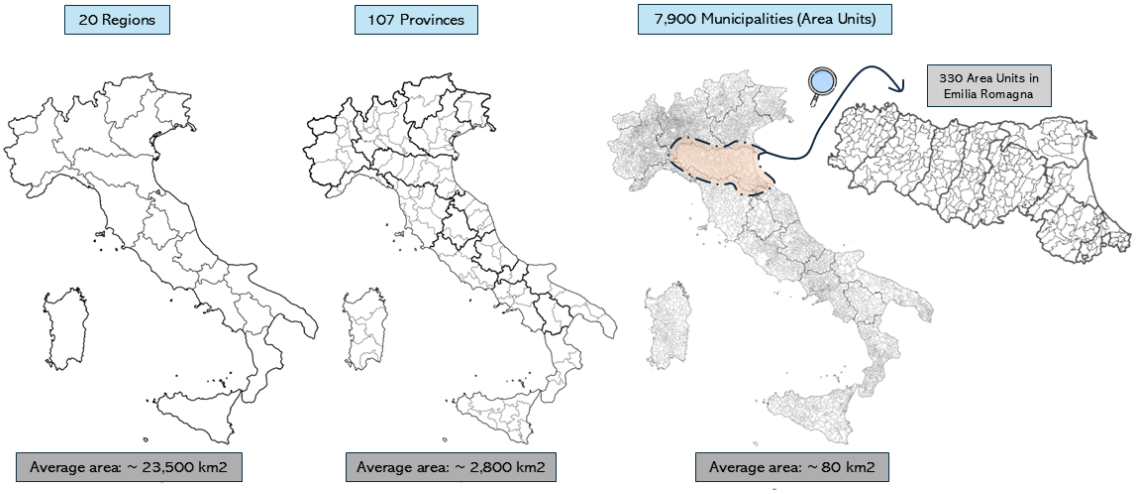

Figure III-11: Scheme of administrative units in Italy. The smallest unit is municipality, which is used as an Area Unit in LEP-AI model. Results, i.e., predictions of landslide risk, are referred to these Area Units. Just the Emilia-Romagna region has 330 municipalities.

Regarding the other data required to train or run the LEP-AI model, before delving into possible sources, an important distinction must be pointed out: data can be static, if they are time-invariant, or dynamic, if they vary over time.

Static data can be represented by static properties, that in this case are the average elevation, slope, and curvature of the AU. These average values serve the function to distinguish AUs and thus recognize similar ones. For instance, it can be expected that flat AUs, i.e., areas characterized by a low average slope, which is typical of highly urbanized areas, would be less prone to landslide activity. Therefore, it can be said that static data act as a form of long-term memory, capable of differentiating AUs based on their intrinsic characteristics, which remain constant over time.

In contrast, dynamic data can be represented by dynamic properties, that in this case are the average Normalized Difference Vegetation Index (NDVI) of the AU, or different processing of rainfall and temperature data (Section 3.2.2) over the AU. Therefore, it can be said that dynamic data act as a form of triggering factor, which, considering the associated static data and the predisposing factors (the history of the same dynamic data, but prior to the landslide trigger), can dynamically identify AUs at potential landslide risk.

The above-mentioned static properties can be derived starting from a single source, that is the Digital Elevation Model (DEM). DEM can be retrieved from the same national or regional geoportals seen for the landslide inventories, or alternatively, from other European or international portals, such as EcoDataCube, OpenLandMap, and others (*Copernicus*, n.d.; *EarthExplorer*, n.d.; *EcoDataCube*, n.d.; *OpenLandMap*, n.d.; *SoilGrids*, n.d.). Additionally, just for Italy, it can be used an open source DEM derived from the National Institute of Geophysics and Volcanology (INGV), called TINYITALY (Tarquini et al., 2023). Concerning dynamic data, the easiest and preferred way to retrieve NDVI is from the same European sources seen for

DEM, or also through regional geoportals seen for landslide inventories. Lastly, rainfall and temperature dynamic data can be obtained from regional platforms for obtaining data on hydro-climatic gauges networks, such as Dext3r for Emilia-Romagna region (*Dext3r*, n.d.), which is a webapp developed by the Regional Agency for the Prevention, Environment, and Energy of Emilia-Romagna (Arpae). Dext3r can be used to retrieve rain and temperature recordings from gauges, with a temporal discretization that can go down to 15 minutes. Other sources that could be used for rainfall and temperature are international portals with satellite data, such as GloH20 or GPM by Nasa (*GloH2O*, n.d.; *GPM*, n.d.), which contain high-resolution, globally interpolated data from satellite. A final remark regarding dynamic data pertains to the availability of historical data, since nearly all the cited portals offer data from the early 2000s onwards.

Typically, geo-data can be found under three different types: vectorial, raster, or scatter data. For instance, DEM and NDVI are generally distributed as geo-referenced raster files, i.e., regular grids containing a value per cell, where each cell represents a specific point on the Earth's surface. Consequently, the higher the resolution, the more accurate will be results. Nevertheless, in case of LEP-AI model, coarse resolutions are preferrable, since results must be averaged throughout the entire AU, and therefore, having fine resolutions would solely increase the computational load. Instead, rainfall and temperature are distributed as scatter data, in case of rain-gauges networks, or also as geo-referenced raster files, in case of satellite. Despite this, as opposed to what was previously observed with DEM and NDVI, fine grid resolutions or a dense network of rain-gauges is preferable, because data is not averaged, as it will be illustrated in Section 3.2.2. Lastly, landslide inventories could be provided as scatter data, which commonly contains coordinates of the upper scar or centroid of landslide body. Alternatively, when geometry of the entire landslide body is available, landslide inventories could be provided as vectorial data, containing coordinates of the border.

The integration of these diverse data sources enables a comprehensive analysis, maintaining consistency with the adopted municipal-scale analysis framework (AU based) and providing at the same time a sufficient temporal and spatial resolution for meaningful landslide susceptibility assessment.

3.2.2 Rainfall And Landslide Events

If we assume to discretize time into days, a Rainfall Event (RE) would be defined as a temporal sequence of precipitation days with specific characteristics, as illustrated in the conceptual Figure III-13. Specifically, with LEP-AI model, a RE consists of days recording at least 5 mm of rainfall, which may include a maximum of a single intervening dry day between wet days. The rainfall amount recorded in an entire day over a specific AU, also called Rainfall Timestamp (RT), is obtained considering the rain gauges or satellite data. In the first case, it is read only the rain gauge that contains the maximum amount of all and thus, the same AU could contain

RTs from different rain gauges over the days, even within the same RE, as shown in Figure III-12.

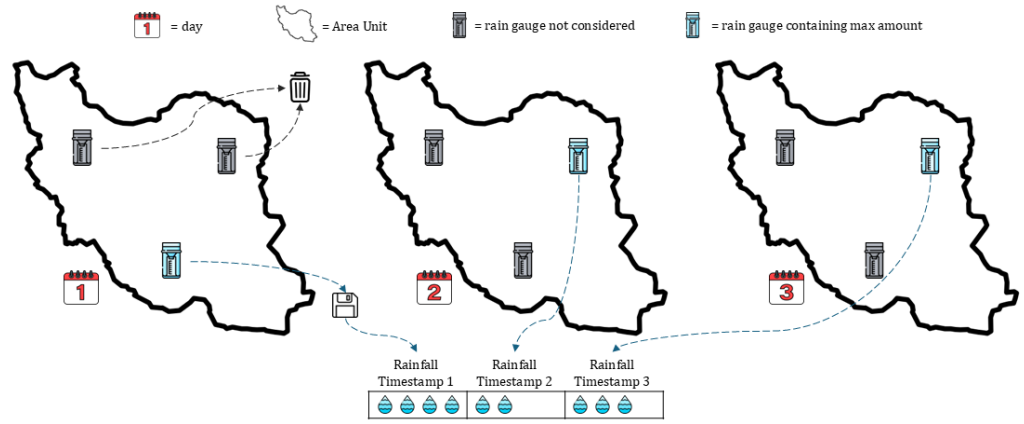

Figure III-12: Illustration of the process to create Rainfall Timestamps for a conceptual Area Unit. Despite the consecutive days, the unique rain gauge considered is the one with the maximum rainfall amount, day by day. In this case, 1st day contains the amount from a rain gauge different than the 2nd and 3rd days.

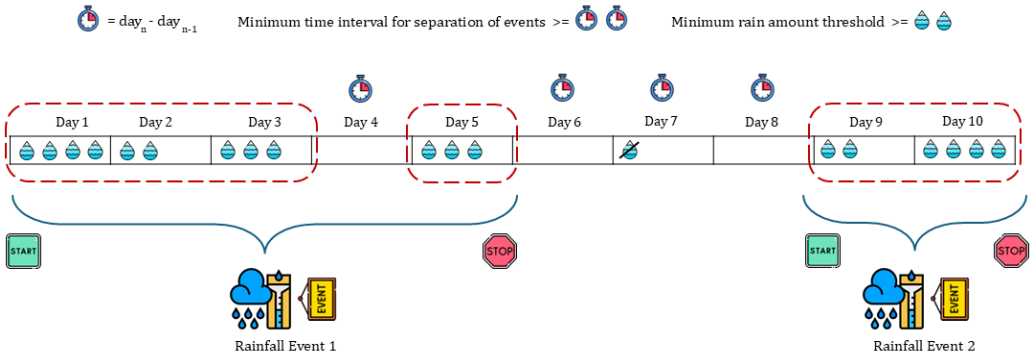

Figure III-13: Conceptual scheme of the Rainfall Event definition. Since the time is discretized in days, if more than 2 days contain less rain amount than the threshold (2 rain drops in this example), then these days cannot be included in a Rainfall Event. In fact, Rainfall Event 1 is separated from Rainfall Event 2, and Rainfall Event 1 contains just one day with less rainfall than threshold.

This definition allows for a comprehensive approach to analysing precipitation patterns related to landslide occurrence. The total rainfall amount during a RE corresponds to the cumulative precipitation throughout the event's duration, which is also called the triggering amount. In fact, in the context of the landslide trigger-cause concept (Bogaard & Greco, 2018), two distinct precipitation measurements are relevant: the triggering and cause amounts. Specifically, whenever a landslide occurs, the triggering amount is defined as the total rainfall accumulated during the RE associated with the occurrence. Instead, the cause amount, which is the accumulated rainfall during a certain period prior to the occurrence, can be quantified through two alternative approaches. The first consists of accumulating rainfall over a predetermined number of days, preceding the start of the triggering RE (purple line in Figure

III-14). The second one consists of summing the rainfall amounts of all the REs within a defined temporal window (orange line in Figure III-14).

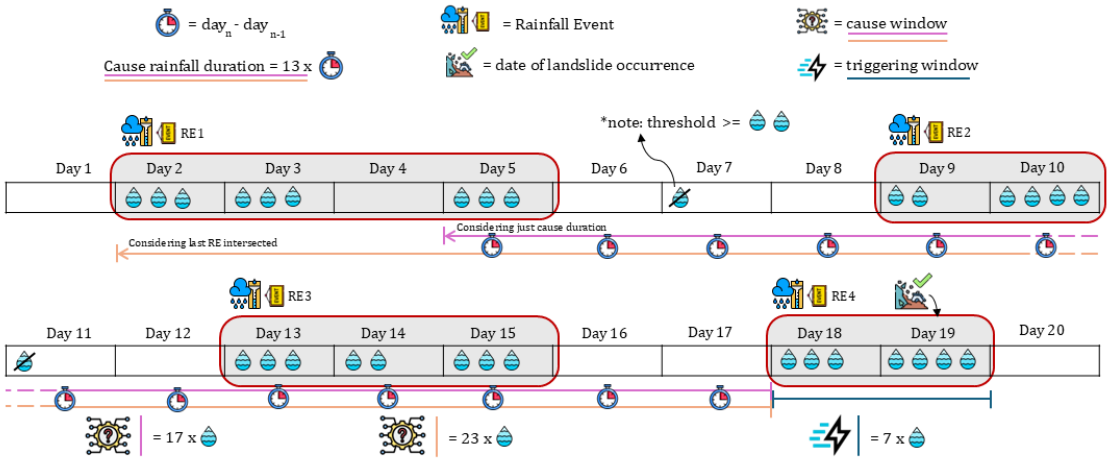

Figure III-14: Conceptual scheme of the cause and trigger time windows. If a rainfall-triggered landslide occurs, this landslide must be associated with a Rainfall Event (RE4 in this case). Therefore, such a Rainfall Event becomes the triggering event, which last for a certain number of days, i.e., the triggering window, in blue. Before the start of the triggering window, a cause window can be identified, deciding how many days may be the cause of landslide trigger (cause rainfall duration). Finally, with the cause rainfall duration, 2 different approaches can be used. The first consists in cumulating rainfall of the cause rainfall duration, the second one consists in cumulating rainfall of all the Rainfall Events intersected, which means that the earliest Rainfall Event must be considered in full, with the possibility of cumulating rainfall of more days compared to the cause rainfall duration.

According to what was shown for REs, a Landslide Event (LE) is defined as a RE during which at least one landslide occurs. Moreover, to account for potential inaccuracies in landslide inventory reporting, the temporal association between landslides and REs includes a three-day buffer period following the RE's end. This approach acknowledges the inherent uncertainties in landslide occurrence documentation while maintaining a systematic framework for analysis.

While multiple landslides may occur during a single RE, the classification of these events may present specific challenges and considerations. In fact, considering the number of landslides occurred in each LE, it is possible with LEP-AI to perform a regression or a classification, with two primary approaches in case of the last, that is binary or multi classification. Unless the available landslide inventory is large and accurate, regression is not recommended, because of the typical challenges associated with regression tasks, which requires larger datasets and a precise landslide count determination within specific AUs. Instead, classification is suggested to avoid potential issues. Specifically, the binary classification is a straightforward separation between REs with and without landslide occurrences, while the multiclassification is a more nuanced approach based on landslide intensity, since defining some minimum and maximum thresholds per class, it is possible to distinguish LEs based on their severity from a hydrogeological perspective, as shown in Figure III-15. Generally, the binary classification is the most used approach in LEP-AI.

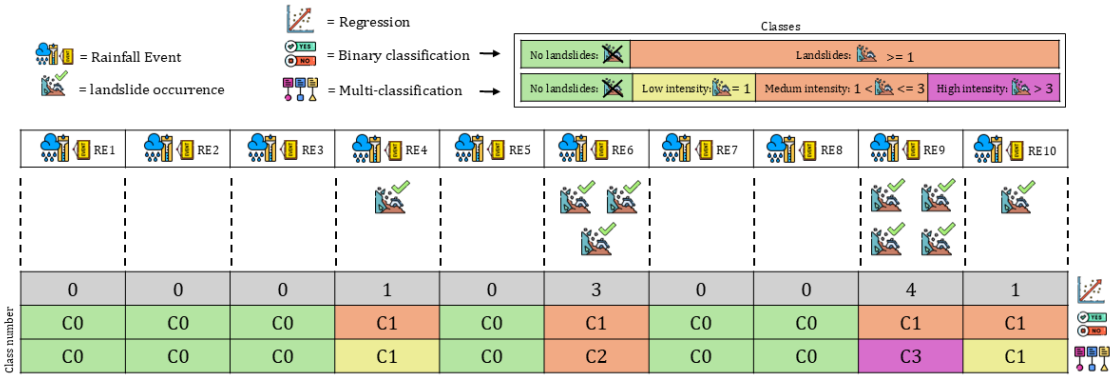

Figure III-15: Illustration of the three possible approaches for determining the Landslide Event's associated output: regression, or binary and multiclassification. For multiclassification, the associated output classes are distinguished based on the intensity, i.e., the number of landslides occurred during a certain Rainfall/Landslide Event.

As an intrinsic consequence of the LE definition, a significant challenge emerges in this analytical framework, that is the substantial output class imbalance. In fact, the resulting dataset would be characterized by a disproportionate number of REs without landslides, rather than LEs. To address this imbalance, three distinct methodological rebalancing approaches are implemented in LEP-AI: under-sampling, over-sampling, and Synthetic Minority Over-sampling Technique (SMOTE). Under-sampling involves reducing the predominant class (REs without landslides) to achieve class balance with LEs classes (Figure III-16 a). In contrast, over-sampling consists in replicating the observations of the less populated classes, i.e., the ones of LEs (Figure III-16 b). Finally, the purpose of SMOTE is the generation of synthetic observations through the interpolation of existing minority class data, to match the number of the most populated (Figure III-16 c). These rebalancing techniques ensure a more robust training of LEP-AI and help prevent bias toward the majority class in predictive applications.

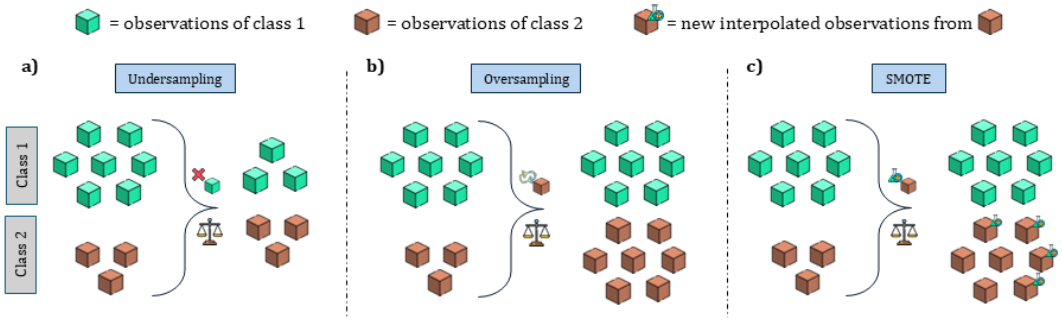

Figure III-16: Example of rebalancing techniques between two classes of data that were originally imbalanced. Class 1 has more observations than Class 2, therefore the solutions adopted in LEP-AI model are: a) under-sampling, eliminating randomly some observations from Class 1; b)over-sampling, repeating some random observations of Class 2; c) SMOTE, introducing some new observations in Class 2, obtained by interpolating data of the already existing observations of Class 2.

3.2.3 MODELLING

The LEP-AI model is the result of a process aimed at training several different configurations and structures of ANNs. During this procedure, the best configuration is sought, which will subsequently be employed for future predictions on the same AUs used for training, a subset of them, or potentially new AUs, which have characteristics similar to AUs seen during training. Specifically, the ANN architecture adopted is the Multi-Layer Perceptron (MLP) (see Appendices Chapter) and in order to obtain the best and most optimized MLP to use with LEP-AI model, a comprehensive framework is adopted, by means of the definition of some hyperparameters, input/output data, and some metrics which allow to assess the performance (also called quality) of each MLP.

The main hyperparameters, as will be discussed in Section 3.2.3.1, consist of structural parameters, activation functions, type of regularization, and other parameters to control the training process. The number of input nodes of all the MLPs is 31, while the number of outputs varies according to the selected output type, which is 2 nodes in case of binary classification, 4 nodes in case of multiclassification, and just a single node in case of regression, as will be examined in Section 3.2.3.2. Moreover, inputs can be static, when related to morphology, or dynamic, when related to rainfall, temperature or NDVI. Finally, as will be addressed in Section 3.2.3.3, the metrics adopted for the assessment of model performance are the Area Under the Receiver Operating Characteristic curve (AUROC), the Area Under the Precision Recall Curve (AUPRC), the Area Under the Precision Recall Gain Curve (AUPRGC), the Cross-Entropy Loss (CEL), and the Random Feature Importance (RFI).

3.2.3.1 Hyperparameters

Different MLP architectures are systematically and automatically evaluated through various configurations. Regarding the MLP structure, the modifiable parameters include: number of hidden layers, ranging from 1 to 5; number of neurons per hidden-layer, tested at 1, 40, 80, and 120 nodes; number of neurons in the output layer, which in case of a binary classification is configured with two neurons, corresponding to the two possible classification categories (LE and not LE, i.e., just a RE without the occurrence of landslides). The latter approach, without considering additional hyperparameters but just with a sole focus on structural parameters, would alone result in the creation of 1,364 possible distinct model configurations to evaluate, as shown in Figure III-17.

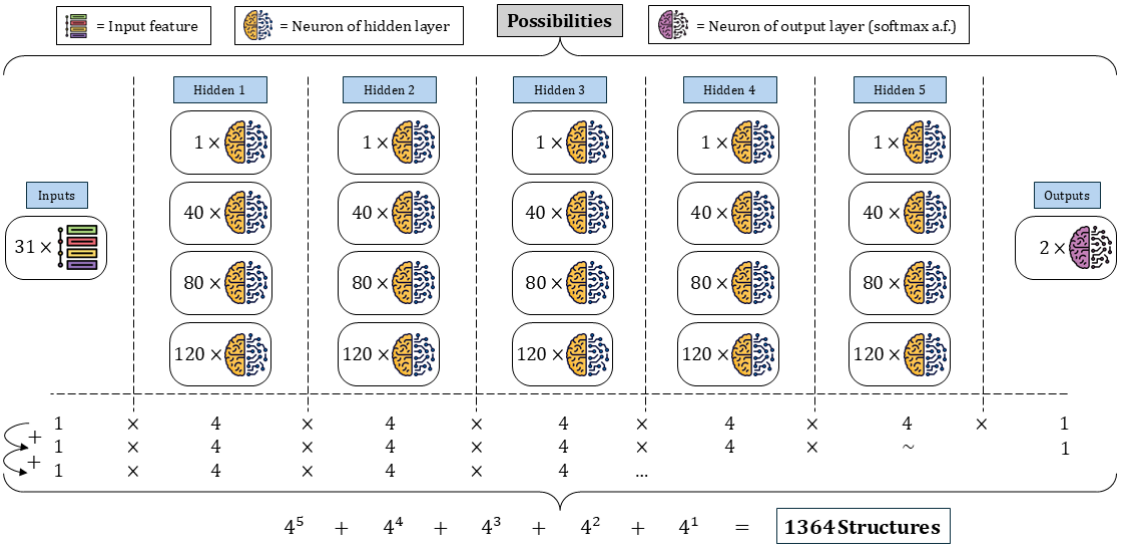

Figure III-17: Scheme of all the possible ANNs' structures to test in LEP-AI model, without considering other possible hyperparameters. If the maximum number of hidden layers is set to 5, and the possible configurations of neurons per layer are set to 1, 40, 80, or 120, the result of all the possible combinations is a total of 1364 structures to test.

Concerning the activation functions, i.e., the functions to apply after the internal neuron function (see Appendices Chapter), these can be various and even different per each hidden layer of the MLP. Some typical activation functions are ReLU, ELU, Tanh, and Sigmoid (respectively, Equation 33, 34, 35, and 36). In case of the output layer, if the MLP is set to regression mode, there is typically no activation function for the last single neuron. In contrast, if the MLP is set to classification mode, the Softmax activation function (Equation 37) is typically apply for the last neurons, thus, these last neurons will return complementary numbers in the range [0, 1], interpreted as probabilities associated to each output class.

$$Out(ReLU) = max(0, Inp) \tag{33}$$

$$Out(ELU) = \begin{cases} \alpha \cdot (e^{Inp} - 1), & Inp < 0 \\ Inp, & Inp \geq 0 \end{cases} \tag{34}$$

$$Out(Tanh) = \frac{e^{2 \cdot Inp} - 1}{e^{2 \cdot Inp} + 1} \tag{35}$$

$$Out(Sigmoid) = \frac{1}{1 + e^{-Inp}} \tag{36}$$

$$Out_i(Softmax) = \frac{e^{Out_i^*}}{\sum_j e^{Out_j^*}} \tag{37}$$

where:

- Inp is the value obtained from the neuron internal function

- Out is the value output value, to be passed to the neurons of the next layer, or, in case of the Softmax, the Out^* on the right-hand side of the equation is the output of the internal function of the final neurons
- α is a parametric value for the ELU function, which is typically set to 1, but it can be a generic finite real scalar (if not 1, commonly in the range [0, 1]).

A well-known issue of MLPs is the overfitting, that is the tendency of a model to memorize precise patterns in giving final outputs, and therefore not to learn a generalized solution for a given dataset. The more the model is complex (which means more computational power, that is, to simplify, more neurons per layer) the more this behaviour is emphasized. Typically, a direct consequence of overfitting is the fact that, when both a training and a test dataset are available, the loss history of both begins to diverge from a certain iteration onwards, as shown in Figure III-18.

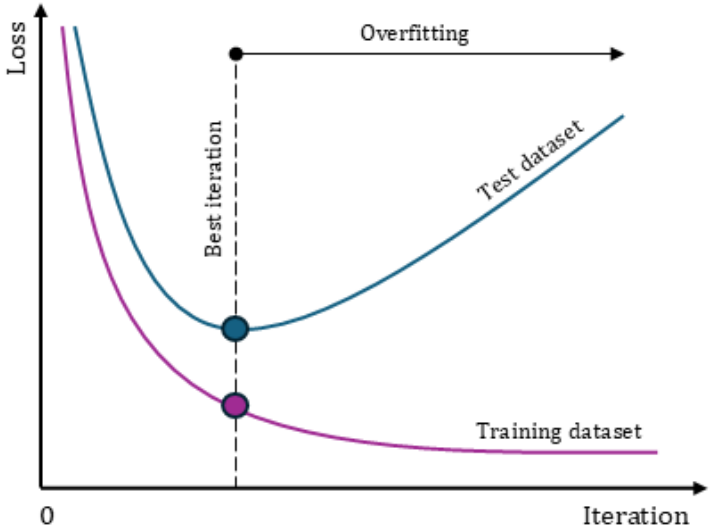

Figure III-18: Scheme of the overfitting issue for a conceptual model. The blue curve represents the history of the loss values, evaluated over the test dataset. The purple curve represents also the loss value history but evaluated over the training dataset. The best iteration is obtained when the test loss reaches the minimum. After that, the overfitting starts. The more iterations of the backpropagation are performed, the more the test loss increases.

During the past years, to overcome this issue, different solutions have been proposed. To start with, a possible cause of the overfitting is the difference in the numeric distribution of the inputs, because inputs with large values and a broad numeric range could increase the network's sensitivity to them. Therefore, since input data of different nature may have different ranges of values, the standardization, also called batch normalization (Equation 38) can be adopted. The function of the standardization is to reduce the problem of the internal covariate shift and train faster the model (Ioffe & Szegedy, 2015), because it standardizes each input around the zero mean.

$$y_i = \frac{x_i - \mu}{\sigma + \epsilon} \tag{38}$$

where:

- x_i is the initial value to standardize
- μ is the average of all the values of a batch
- σ is the standard deviation of the batch
- ϵ is the smoothing term, i.e., a number that prevent dividing by 0.

Following this, some techniques can be adopted during the training of the model. These techniques act on the error made by the model, which is the difference between actual and predicted outputs, also known as loss. Specifically, the most adopted type of error with ANNs is the cross-entropy loss (Equation 39) and one of the techniques that acts on it is the early stopping, which consists of maintaining a part of the training dataset, called the validation dataset, unseen by the model. This means that such a part of the dataset does not affect backpropagation, but is only used to evaluate the loss, with the aim to stop the training when a certain validation criterion is met. Particularly, this criterion can be related to the validation frequency and the validation patience, which they mean respectively how often the validation loss must be evaluated and how many times such a validation loss is allowed to increase consecutively. Therefore, when the validation patience is met, the training is stopped, i.e., the training of the model is stopped when the validation loss (which is evaluated according to the validation frequency) has increased continuously for a count matching the validation patience. This early stopping prevents the overfitting of the model, which often leads to a significant divergence between the loss values for the seen and unseen part of data during backpropagation. Another technique that acts on the loss is the regularization, which can be of two types: Lasso, also called L1 regularization (Equation 40), or Ridge, also called L2 regularization (Equation 41). Both the techniques consist in introducing an additional error during the backpropagation, moving slightly away from the perfect but overfitted solution, which would be reached with the minimum loss. The only difference between the two methods lies in the fact that L1 can exclude some features and tends to introduce more noise in results, while L2 is gentler and can just reduce (but not remove) the weights of the less important features. In fact, it is more appropriate to use L2 when the user assumes that all the features included in the model are relevant.

$$CEL = \frac{-\sum_{j=1}^{N}\left[R_j \cdot log\, P_j + \left(1 - R_j\right) \cdot log\left(1 - P_j\right)\right]}{N} \tag{39}$$

$$CEL_{rL1} = CEL + \lambda \cdot \sum_{j=1}^{C} \left|w_j\right| \tag{40}$$

$$CEL_{rL2} = CEL + \lambda \cdot \sum_{j=1}^{C} {w_j}^2 \quad (41)$$

where:

- R_j is the actual/real output of the dataset for a certain observation (for instance, with a binary classification, 0 if not LE and 1 otherwise)
- P_j is the probability predicted by the model, associated with a certain observation (where observations are the REs that need to be classified)
- N is the total number of observations (REs) contained in the dataset to predict
- λ is the regularization strength (0 means no regularization)
- C is the total number of connections weights of the net, considering all the layers
- w_j is the j_{th} connection weight of the net, i.e., the connection of a certain neuron of the net with a neuron of the next layer.

Finally, another common technique to avoid overfitting is the dropout technique. The dropout involves randomly removing certain neurons from the network during training. In other words, throughout the network training and during the various iterations of backpropagation, certain neurons, which are chosen randomly and with a specific percentage (set by the user and possibly different for each layer), will output a null value. This means that the selected neurons will not influence the final prediction value because they do not contribute numerically. This technique helps mitigate over-reliance on only certain neurons that might be tuned to respond well only to certain specific patterns. This approach could slightly increase errors made by the net on the training dataset, but it may simultaneously also enhance the generalization ability of the model.

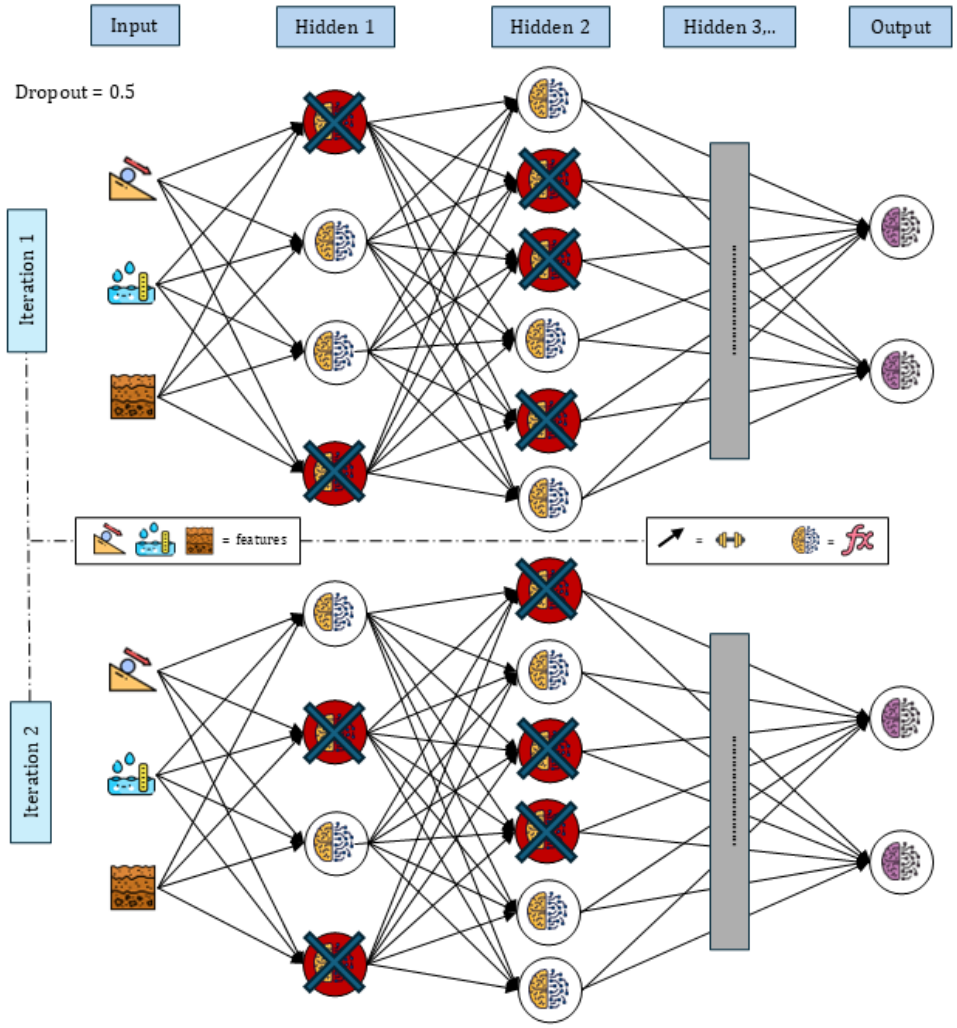

Figure III-19: Scheme of the dropout functioning for a conceptual artificial neural network, during two iterations of the backpropagation. In this example, the dropout probability is set to 0.5 for all the layers of the net. Consequently, in each layer, the number of neurons that must be drop out at a certain iteration is half of the total neurons of the layer. In the two iterations, the neurons removed are different and randomly selected.

3.2.3.2 Input And Output Data

The inputs of LEP-AI model are 31 selected features of the considered AUs, taken during a specific RE. In other words, if a single AU is considered, then the result would be that all the features (both static and dynamic) of this AU, during a specific RE, represent a single observation of the dataset, i.e., a row of a table. Moreover, since static features do not change over time, these properties remain unchanged during the various REs and therefore they can be excluded if the model is trained with just a single AU. In fact, the task of the static features is to distinguish the various AU, which can be more or less susceptible to landslides, according to their intrinsic properties. Instead, the task of the dynamic features is to define some

sophisticated and dynamic thresholds which can be used to define when a given AU is at risk, during a certain RE.

However, static features of LEP-AI model are 5 and all of these can be obtained from a single source, that is the DEM of the AU considered. Specifically, the static features are respectively the average elevation (AvgElev), the average slope (AvgSlope), the average mean curvature (AvgMnCrv), the average profile curvature (AvgPrCrv), and the average planform curvature (AvgPlCrv), as shown in Figure III-20.

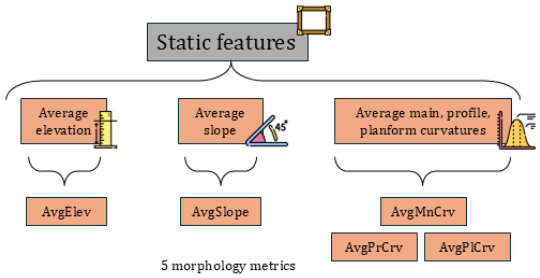

Figure III-20: Scheme of the 5 static features considered in the LEP-AI model. These features are obtained elaborating data of the Digital Elevation Model and are the result of the average over the entire Aera Unit selected.

Regarding the dynamic features used in LEP-AI model, these are 26 and can be categorized into main groups as follows and illustrated in Figure III-21:

- 1 vegetation metric – the average NDVI (AvgNDVI)
- 3 temporal metrics – the duration of the RE, in hours (DurRE); the time since the last RE, in hours (Time2LstRE); the time since the last LE, in hours (Time2LstLE)
- 6 rainfall metrics – rainfall amount of the current RE (TrigRain); maximum daily rainfall amount, recorder during the current RE (PkTrgRain); antecedent rainfall amounts, cumulated for 10, 20, 30, and 60 days before the start of the current RE, as seen in Figure III-14 (respectively CauseRain10d, CauseRain20d, CauseRain30d, and CauseRain60d)
- 15 temperature metrics – the maximum, minimum, and average temperatures recorded during the current RE (respectively MaxTrgTmp, MinTrgTmp, and AvgTrgTmp); the maximum, minimum, and average antecedent temperatures, considering a time window of 10, 20, 30, and 60 days before the start of the current RE (for the maximum, respectively MaxCsTmp10d, MaxCsTmp20d, MaxCsTmp30d, and MaxCsTmp60d; for the minimum, respectively MinCsTmp10d, MinCsTmp20d, MinCsTmp30d, and MinCsTmp60d; for the average, respectively AvgCsTmp10d, AvgCsTmp20d, AvgCsTmp30d, AvgCsTmp60d)
- 1 check metric – a random number with no physical or mathematical meaning (RandFeat), associated with each observation of the dataset and intended to verify

that the model does not extract information from it, and to act as a threshold for distinguishing key features from less relevant ones.

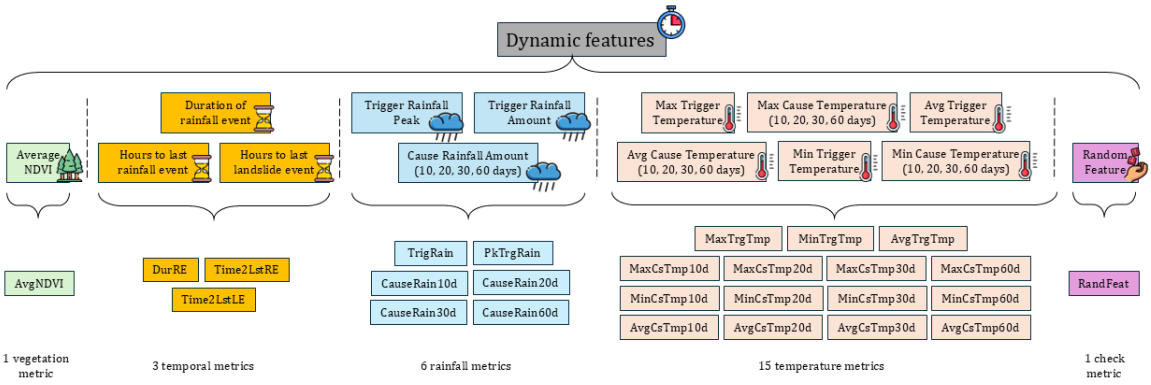

Figure III-21: Scheme of the 26 dynamic features considered in the LEP-AI model. These features are grouped based on the source used (different colours) and they must be considered as quantities of the entire Area Unit selected.

The outputs of the LEP-AI model vary from 1 to 4 and depend on the type of output desired (Figure III-15): if a regression is needed, then the output of each observation (that is a RE associated with a certain AU) is a single value, given by the unique neuron of the output layer; if a binary classification is needed, then the outputs are two, which are respectively the landslide occurrence probability and the no-landslide occurrence probability, related to the two neurons of the output layer; if a multiclassification is needed, then the outputs are four, which are respectively the probability that high, medium, and low intensity LE occurs, and the no-landslide occurrence probability. In case of the multiclassification, the high, medium, and low intensities are defined by the user, with the minimum and maximum landslide occurrences for each class.

3.2.3.3 Assessment Of Model Performance

The assessment of model performance can be achieved through various approaches. To begin, it is important to clarify that a widely adopted practice in machine learning involves dividing the total initial dataset (consisting in this case of various REs associated with different AUs) into three parts: training, validation, and test datasets. Specifically, with the LEP-AI model, a subset of 30% of the total data is allocated to testing, while the remaining 70% is further split, with 80% for training and 20% for validation. The training dataset optimizes the model parameters (through the backpropagation of errors), while the validation dataset supervises the training process, stopping backpropagation iterations when the validation criteria discussed in Section 3.2.3.1 is met. In contrast, the test dataset assesses the model's final quality with its CEL (Z. Zhang & Sabuncu, 2018), because it provides a previously unseen evaluation set. In fact, even if the validation dataset does not directly influence the parameters, it can halt the training, thus stopping the process at a favourable

point for itself, which means to affect indirectly the outcome. However, in some cases the sole reliance on test results may not fully capture model performance, prompting the use of 10-fold cross-validation (Stone, 1974; Wold, 1978) as an alternative approach. Here, the remaining 70% of data, which means the combined training and validation data, is divided into ten subsets, where each subset is used for validation in rotation and the remaining 9 subsets are merged in rotation to be used for training, allowing the metrics from each fold to be averaged for a more reliable performance estimate.

In addition to the CEL, model performance can be quantified also through other several metrics, evaluated over all the possible splits of the initial total dataset, as it happens for the CEL. Specifically, these metrics can be the AUROC (Bradley, 1997), the AUPRC, and the AUPRGC (Flach & Kull, 2015; Williams, 2021). AUROC measures the model's discrimination power, plotting the False Positive Rate (FPR) against the True Positive Rate (TPR, also called Sensitivity). In certain instances, for the AUROC, Specificity may be employed on the x-axis in place of FPR, as it is linked to FPR through the relationship $Specificity = 1 - FPR$. The results of AUROC ranges from 0 to 1 and the worst outcome of a model is when this value is equal to 0.5, considered as the reference point. Particularly, if the AUROC is 0.5, this means that the model is not able to distinguish between the various output classes, but it acts as though it is merely attempting to make random guesses. Instead, when the result of the AUROC is 1 or 0, it means respectively that the model is perfectly able to predict the correct class (AUROC=1) or to predict always the opposite of the correct one (AUROC=0). However, AUROC can be sometimes misleading in unbalanced datasets, making AUPRC or AUPRGC more suitable alternatives in such cases. AUPRC measures the model's discrimination power, as the AUROC, but prioritizing the results of the less populated classes, since it plots the Recall (which is equal to the TPR), on x-axis, against the Precision, on y-axis (for a more detailed insight into these terms, please see Appendices Section). With AUPRC the results ranges from 0 to 1, but there is no specific reference point (as 0.5 for AUROC), but the higher the result, the better the model. The unique difference between AUPRC and AUPRGC is that the latter utilizes the same metrics (Precision and Recall) but in a harmonized form, making the results more interpretable, compared to AUPRC. The harmonized metrics are referred to as Gain Recall and Gain Precision. When these are employed, the area under the curve result is more interpretable because, unlike AUPRC, the AUPRGC provides a reference point to define a good model, namely the value of 0.5. If the area exceeds this threshold, the model can be considered of good quality; otherwise, when the area falls below this value, the model struggles to accurately classify the minority class. This is not analogous to AUROC, where a value of 0 indicates a model that makes perfectly opposite predictions. In fact, in the case of AUPRGC, the result could even be negative.

Other tools to use in assessing model performance derive from the Explainable Artificial Intelligence (XAI) (Gunning et al., 2019) field, the purpose of which is to interpret machine

learning models. More in depth, XAI techniques like Permutation Feature Importance (PFI) (Altmann et al., 2010), SHapley Additive exPlanations (SHAP) (Mosca et al., 2022), Leave One Feature Out (LOFO) (Feng et al., 2013), and Partial Dependence Plots (PDP) (Greenwell, 2017) can be used to facilitate deeper understanding of the model's feature dependencies and behaviour. For instance, PFI, which ranks features by their impact on model performance, is especially useful for assessing ANN models. In fact, because of the introduction of the RandFeat, seen in Section 3.2.3.2, it is possible to recognize the meaningful features but not only: if the RandFeat ranks low, it indicates the model successfully recognized its lack of physical significance (Stoppiglia et al., 2003). Thus, low importance of this RandFeat, called RFI, suggests the model's effectiveness in feature learning and it can be considered as a performance metric (after verifying that all features left in the model are meaningful for the problem analysed).

In conclusion, given these four primary metrics, i.e., CEL, AUROC, AUPRGC, and RFI, an aggregate Quality Index (QI) can be calculated by interpreting these as vector components, with the inverse Euclidean norm, providing a single quality score as shown in Equation 42. This QI allows a comparative ranking across models. Furthermore, all these performance metrics must be compared to a simpler model, such as the Logistic Regression (LR), to ensure that it has better performance and to justify the use of more sophisticated tools as the MLPs used in the LEP-AI model.

$$QI = \frac{1}{\sqrt{(1 - AUROC)^2 + (1 - AUPRGC)^2 + CEL^2 + RFI^2}} \tag{42}$$

3.3 PIP-AI MODEL

PIP-AI (Pixel Instability Predictor - Artificial Intelligence) is another model developed in this work, based on AI, as LEP-AI. Particularly, this model can be a generic Machine Learning algorithm, such as Decision Tree Ensembles (DTE) and Support Vector Machines (SVM) (see Appendices Chapter), or something more sophisticated, such as the previously seen ANNs (specifically, MLPs) or the Kolmogorov-Arnold Networks (KANs). PIP-AI model is designed to be more precise and detailed than LEP-AI, but still computationally efficient. The best use case is after the results of LEP-AI, that is after deciding which areas should be investigated more in detail. In such a case, the PIP-AI model would act as a "magnifying glass". Nevertheless, this model could be difficult to apply over very large areas, although its speed in giving outputs. The underlying cause is the fact that input data can become very large in terms of ram space, leading to extreme computational requirements. A common personal computer can handle properly up to around 8 entire municipalities simultaneously, with a 10x10 m DEM, which is the equivalent of 3.2 billion of observations. The functioning principle of PIP-AI is based on the prediction of Landslide Pixels (see Figure III-22), which means that the model is capable to predict the possible instability of each pixel of a given DEM. In other

words, based on some input features (static and dynamic), the PIP-AI model output is the probability of instability of each pixel of a given DEM. Thus, if the initial DEM has a resolution of 10x10 m, each pixel represents an area of 100 m^2, with a related individual probability of instability.

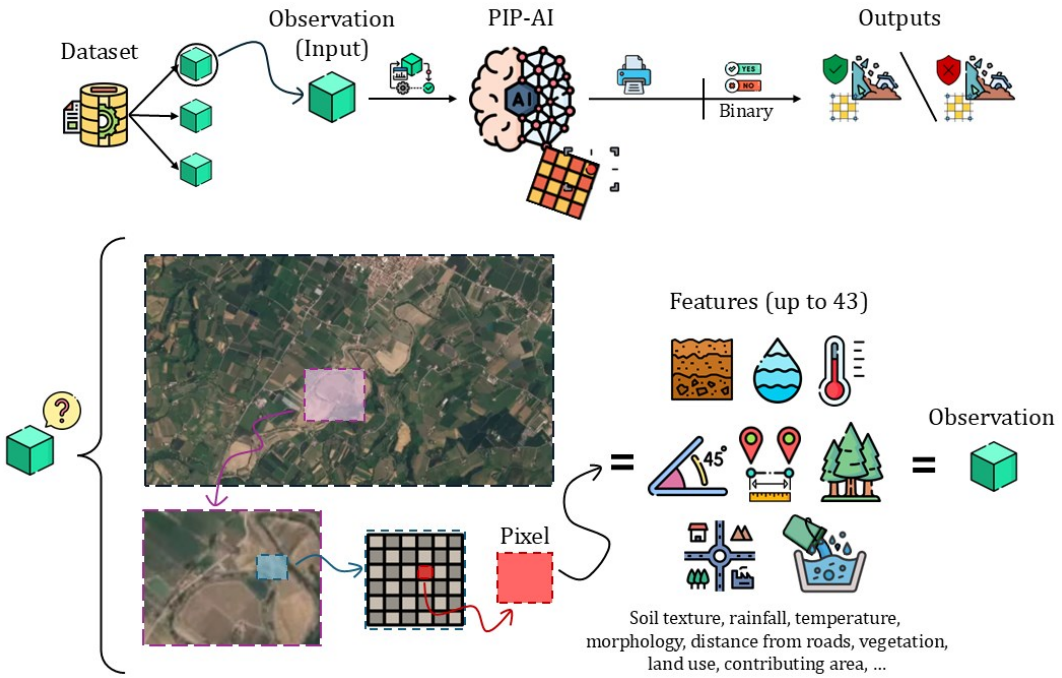

Figure III-22: Conceptual and illustrating scheme of the PIP-AI model functioning. Starting from the top, the model processing is shown. From a dataset, which is made of observations, a single observation is extracted and passed through the PIP-AI model, which in turn it will give an output, i.e., a binary classification (no instability or instability, with their relative probabilities). On the bottom of the figure, it is shown what is an observation for the PIP-AI model. If a single pixel is taken from a grid, represented by the DEM, then some features can be extracted and associated to this pixel. The set of all these features represents an observation. Since some features are dynamic, if different times are considered, then different observations are generated, referred to the same pixel.

As LEP-AI, also PIP-AI can be used in real-time, but just for the areas that could be at risk during a certain Rainfall Event. Anyway, this efficiency represents a great advantage over other types of detailed physically based models, which sometimes could require hours to run. Furthermore, data to use as input of PIP-AI model is easily accessible because it uses the same sources seen for LEP-AI model (Section 3.2.1), making it easy to apply on different areas.

To conclude, PIP-AI represents one of the most efficient and practical models to be used for civil protection and prevention purposes, as it would provide detailed information about pixels that could be unstable during a Rainfall Event. This type of output, if derived from rainfall simulations, also enables the coordination of local interventions, allowing precise identification of specific points that would benefit from targeted stabilization actions.

3.3.1 Data Sources

As seen for LEP-AI, also with PIP-AI model the primary source to create datasets are landslide inventories, which can be the same used for LEP-AI. In fact, these databases can be obtained from the same sources seen in Section 3.2.1. However, in contrast with LEP-AI, where just the municipality of the landslide is sufficient, in case of PIP-AI the inventory must contain at least the coordinates of the upper scar of the landslide body (or its centroid). Moreover, the possible triggering factors should be also included (for the same reasons of LEP-AI).

Since the information contained in these inventories is often incomplete, from a spatially or temporally (or both) point of view, the creation of special Stable and Unstable Areas is required, as will be shown in Section 3.3.5.

Regarding the other data required to train and run the PIP-AI model, both static and dynamic data type is used. Specifically, static data it is represented by different static properties, such as morphological (elevation; slope; aspect angle; curvature), distance from objects (distance from roads), soil (clay and sand content; sub/top soil and land use classes), vegetation type (vegetation classes; probabilities of vegetation species) and hydrological (contributing area; topographic wetness index) characteristics of points of the DEM. These values serve the function to distinguish the various pixels, and thus recognize similar ones, allowing the model to act through a sort of long-term memory, which is capable to recognize intrinsic characteristics. In contrast, dynamic data can be represented by the dynamic properties, that in this case are the NDVI and different processing of rainfall and temperature data (Section 3.3.3) of the DEM pixels. Therefore, dynamic data act as a predisposing and triggering factor, which combined with the static data, can dynamically identify a pixel as potentially unstable.

The above-mentioned static properties can be derived starting from the DEM, global raster maps, or local (and national) vectorial files. The sources are the same seen in Section 3.2.1, but in case of data containing classes (soil, land use classes etc), a process of class standardization is necessary (please refer to Section 3.3.4).

Generally, with PIP-AI model, the higher the resolution, the more accurate will be results. Despite this, since the model can handle different pixel resolutions, when PIP-AI is applied for new predictions, it is important to keep a pixel resolution that is near to the one used during the training. Instead, in case of scatter data, an interpolation within the area to study is performed (Section 3.3.2). The same procedure is followed in case of raster files that have a resolution different from the DEM, which therefore serves as the basis for discretization. Finally, in case of vectorial data, which in this case corresponds to polygons containing classes, a rasterization process is performed, aimed at determining which pixels belong to each possible class, as described in Section 3.3.2.

Because landslide inventories are generally provided as scatter data, with PIP-AI model there is the need to create a new polygon from scratch, which, according to the landslide type,

it will have some minimum typical dimensions of landslide body. Alternatively, when geometry of the entire landslide body is available, this polygon is directly imported and added to the other Unstable Areas (see Section 3.3.5).

The integration of these diverse data sources enables a comprehensive analysis, maintaining consistency with the grid analysis framework (DEM based) and providing at the same time a detailed spatial resolution for meaningful landslide susceptibility assessment.

3.3.2 Interpolation And Rasterization

PIP-AI model is designed to handle different type of data (scatter, vectorial, and raster), but raster-type data forms the basis of processing, demanding inherent consistency. This means that model inputs appear as points on maps containing features discretized uniformly, so that the grids across different maps consistently correspond to the same coordinates. To achieve this result, it is therefore necessary to perform data interpolation or rasterization operations.

Typically, the above-mentioned operations are needed in three main cases: (i) raster data with a resolution different from DEM; (ii) multiple scattered data points, both inside and outside the study area, all linked to the same time periods; (iii) polygons containing classes to attribute to each pixel.

In the first case (raster-raster conversion), it is sufficient to create a new raster, with the same dimensions of the DEM, which is the reference grid. For each pixel of this new raster, it is possible to attribute values from the previous raster, simply picking the nearest value (nearest neighbour interpolation). This represents one of the simplest and most direct approach, but when the previous raster has a higher resolution (i.e., it contains more pixels) than the one being created, averaging the earlier values within the new cell might be a suitable and alternative approach, as shown in Figure III-23a.

In the second case (scatter-raster conversion), i.e., when multiple scattered data points are available, the interpolation of these values can be performed over the entire study area, resulting in the association of a value for each cell of a new raster, created from scratch (Figure III-23b). In interpolating these scatter values, three different methods can be adopted: nearest (nearest neighbour interpolation, previously seen for the case of the pre-existing raster with a resolution greater than the DEM); linear (common linear interpolation between scattered points); natural (natural neighbour interpolation) (Sibson, 1981). Generally, for rainfall data, the natural method is preferable, but at least 3 scatter points must be available and must be located outside the boundary of the study area.

In the third case (polygon-raster conversion), when the information of some polygons must be converted into raster, one of the most efficient and fast algorithms is a method based on a ‘crossing-number’ test (Engwirda, 2024; Kepner et al., 2020), i.e., the count of the number of times a line, extending from a point, intersects the boundary of a polygon. If this count is odd, then the point is located inside the polygon, otherwise is outside. This is the

same principle used in the so-called ray tracing, widely employed in the gaming industry. If this procedure is repeated for each point of a new raster, created from scratch and with the same dimensions of the DEM, it is therefore possible to rasterize the polygons, based on their attributes (Figure III-23c).

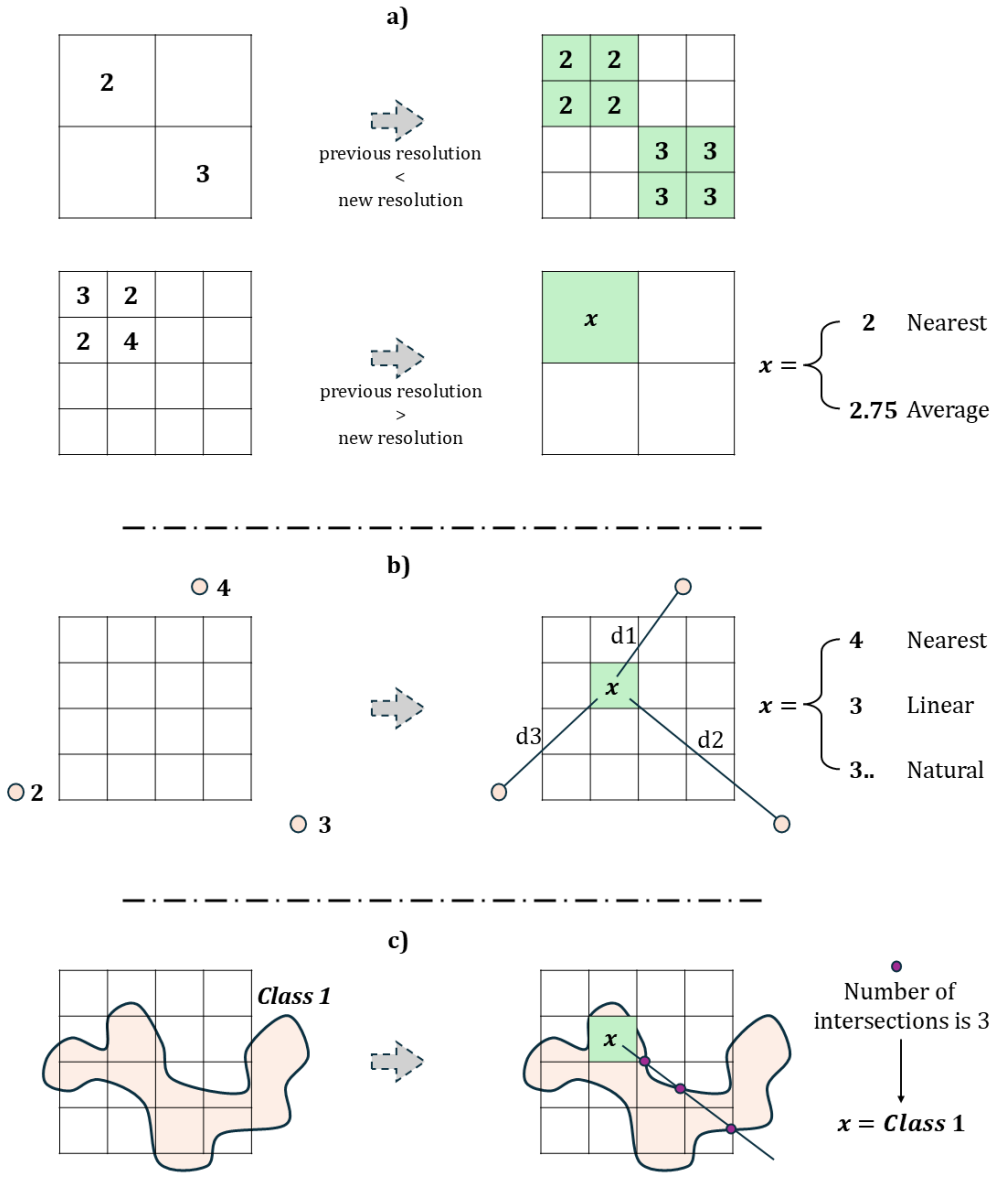

Figure III-23: Scheme of the three possible processes to perform with PIP-AI model, in order to obtain consistent raster grids. The values that are written are represented in green, on the right of the figure, and the three possible conversions are reported. a) (raster-raster) on the top, the case of a raster that must be converted into a new one with higher resolution, on the bottom, the case of a raster that must be converted into a new one with a lower resolution, where the nearest or average approaches can be adopted to define the values of the new cells; b) (scatter-raster) the case of scatter data that must be converted into a raster, therefore for each cell of the raster the interpolation is performed (with one of the three possible approaches); c) (polygon-raster) the case of a polygon that represents a class and must be converted into a raster, thus, the ray tracing procedure is performed to know if the point is inside or outside the polygon. Since the count of intersections is odd, the point is inside the polygon.

3.3.3 Rainfall, Temperature, And Landslide Processing

Rainfall and temperature represent two important dynamic properties and they are usually given under the form of scatter or raster data, respectively through rain gauges or satellite. In the former case, the conversion scatter-raster must be performed, as previously shown in Figure III-23b. In the latter case, the conversion raster-raster, previously seen in Figure III-23a, is often needed, because satellite data has coarser resolutions.

Independently from the source used, the result will be a raster, containing rainfall amounts (or temperature) in each pixel. This indicates that each cell in the raster reflects cumulative rainfall (or average temperature) values, representing the amount of rain that has fallen from a specific start time to an end time (or the temperature, averaged from a specific start time to an end time). Thus, depending on the temporal discretization chosen, different rainfall (temperature) maps will be generated. As seen for the LEP-AI, with PIP-AI model the chosen temporal discretization is set to an entire day, starting from 12.00 am.

Since each pixel of a rainfall map contains the daily cumulative rainfall, each day of the dataset can be analysed by the model, and rainfall values can be treated in three different ways (Figure III-24): (i) it is possible to generate different rainfall cumulates, such as 10, 20, 30, and 60 days, which consists basically of summing (or averaging in case of temperature) respectively 10, 20, 30, and 60 daily rainfall maps, for each day of analysis; (ii) it is possible to consider just a certain number of prior days for each day of analysis and treat rainfall of these prior days as separate inputs (features); (iii) it is possible to generate REs and LEs, dividing triggering from cause rainfall, with the same principles seen in Section 3.2.2.

These 3 different approaches can be also called Rainfall Mode 1 (RM1), 2 (RM2), and 3 (RM3) respectively and they are also valid for temperature but considering the averages. When a prediction of instability in the future is intended to be performed, rainfall (and temperature) forecast must be used. With RM1 and RM2 approaches (respectively, rainfall cumulates and rainfall of separate prior days) it is very easy and straightforward to apply PIP-AI, but the interpretation of the model could be not clear as with RM3 approach, i.e., generating REs and LEs. This is the reason why it is suggested to use RM3 for back analysis, or as a support for physical modelling, while RM1 and RM2 are suggested for real time applications or forecasting.

Regarding landslides, since with PIP-AI the time units are days, it is important to have a landslide inventory containing the day of the landslide occurrence. If both landslide days and coordinates (or polygons) are present in the available inventory, then an output raster map can be created for each day of analysis, containing the value 1 in the pixel/s where the landslide occurred (see Section 3.3.5) and if the day of occurrence is the day of the current analysis, otherwise 0 (Figure III-24). In contrast with the definition of LE of LEP-AI, with PIP-AI the landslides occurred are linked to a specific day and coordinates (cells of the raster grid). Moreover, in case the RM3 is applied, the day of the landslide occurrence is not unique,

but it is every day of the LE considered, to be consistent with RM1 and RM2, where landslides are already attributed to a specific day. For instance, if a LE lasts from October 10th to October 11th, both these days are landslide days (also if the landslide occurred in just one of these days). The reason behind this is the fact that the features of the pixels do not change during the LE, if RM3 is applied, and consequently the expected outcome must not change.

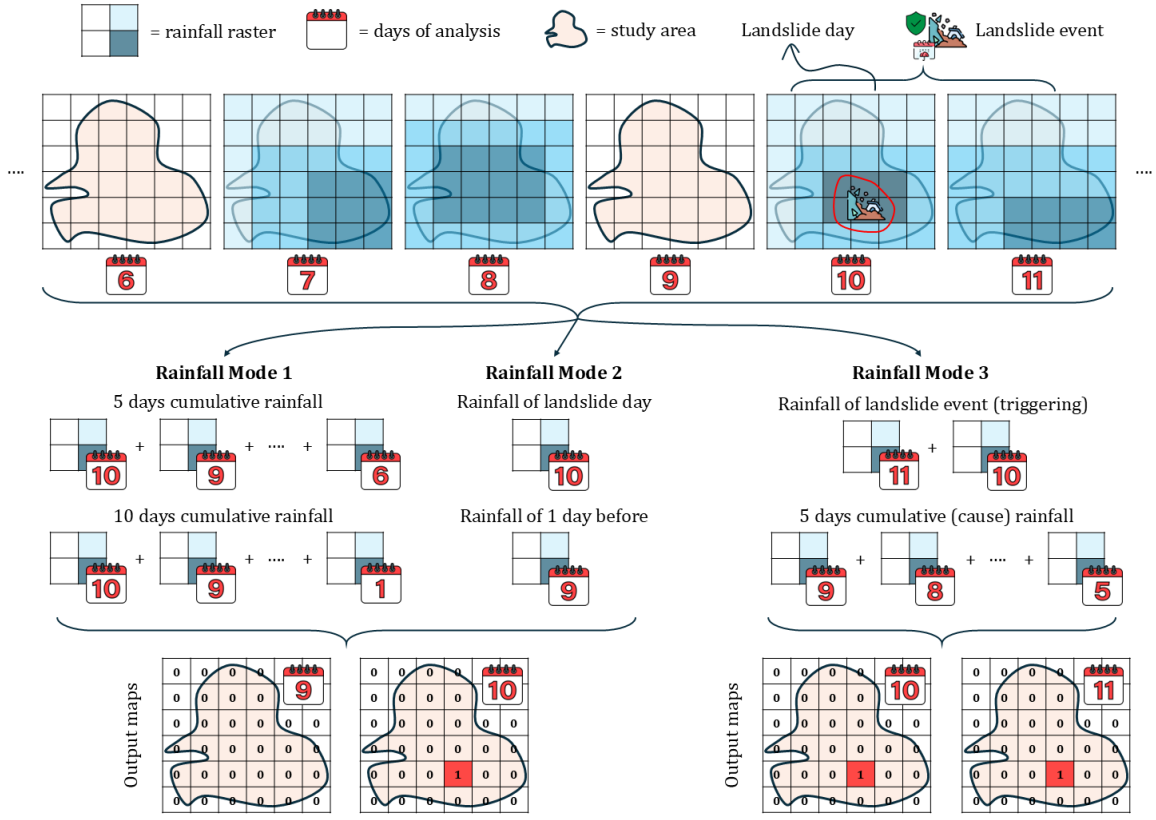

Figure III-24: Scheme of the three possible rainfall approaches with PIP-AI model. Considering multiple daily rainfall maps, which must be consistent with DEM, it is possible to define a landslide day (10th in this example). After that, rainfall to use in PIP-AI can be considered as cumulates (Rainfall Mode 1), single days (Rainfall Mode 2), or subdivided between triggering and cause cumulates (Rainfall Mode 3). Starting from Rainfall Mode 1, the cumulates considered in this example are 5 and 10 days before the landslide day (included) to backward. With Rainfall Mode 2, the single days considered in this example are two, i.e., the landslide day and the day before it. Finally, with Rainfall Mode 3, Rainfall Events are created, and the one that includes the landslide day is called Landslide Event. Therefore, rainfall is subdivided into triggering (cumulative rainfall of the Landslide Event's days, which in this example are 10th and 11th) and cause (in this example just one cause quantity, made of 5 days of cumulative rainfall, starting from the day before the begin of the Landslide Event, i.e., 9th, to backward). The expected output of the model is represented on the bottom. In case of Rainfall Mode 1 and 2, just the 10th must give a value equal to 1 (at the points were landslide occurred). In case of Rainfall Mode 3, both the 10th and 11th are landslide days, also if the actual one is the 10th.

3.3.4 Class Standardization Process

PIP-AI model can extract data from vectorial sources and convert it into raster, as explained in Section 3.3.2. Nevertheless, vectorial data often contains information that have no

standards. This means that, since polygons represent classes, these classes can be labelled differently, depending on the source used.

One of the main premises of the PIP-AI model is its applicability across various study areas, for which it may be necessary to derive data from different sources. For this reason, the need for data standardization becomes apparent. This standardization is achieved by the user, who, upon reading the polygons and their respective classes, must assign each polygon class to a new standardized class. Since the information extracted from the polygons pertains to subsoil, topsoil, vegetation, and land use, specific standardized classes have been created for each of these data categories, as shown in Table III-2, III-3, III-4, and III-5.

Title	Class	Description
Not defined	0	all the pixels that do not fall under any polygon or for polygon classes that are not well defined
Cohesive soil	1	polygons representing a soil like clay or silt
Soft non-cohesive soil	2	polygons representing a soil like soft sand
Non-cohesive soil	3	polygons representing soils that can range from dense sand to gravel
Rock	4	polygons representing impure rocks, such as rocks interlayered with marl-limestone strata
Strong rock	5	polygons representing pure and massive rock

Table III-2: Standardized classes for subsoil sources. Each raw class contained in the imported subsoil (polygonal) data must be associated to one of these new standardized classes, to be used in PIP-AI.

Title	Class	Description
Not defined	0	all the pixels that do not fall under any polygon or for polygon classes that are not well defined
Clay	1	from USDA soil texture triangle
Silty clay	2	from USDA soil texture triangle
Clay loam	3	from USDA soil texture triangle
Loam	4	from USDA soil texture triangle
Silty clay loam	5	from USDA soil texture triangle
Silt loam	6	from USDA soil texture triangle
Silt	7	from USDA soil texture triangle
Sandy clay	8	from USDA soil texture triangle
Sandy clay loam	9	from USDA soil texture triangle
Loamy sand	10	from USDA soil texture triangle
Sandy loam	11	from USDA soil texture triangle
Sand	12	from USDA soil texture triangle

Table III-3: Standardized classes for topsoil sources. Each raw class contained in the imported topsoil (polygonal) data must be associated to one of these new standardized classes, to be used in PIP-AI.

Title	Class	Description
Not defined	0	all the pixels that do not fall under any polygon or for polygon classes that are not well defined
Grass	1	polygons representing all grass types
Bush	2	polygons representing all bush types
Low tree	3	polygons representing trees with a height ranging from 3 to 10 meters
Medium tree	4	polygons representing trees with a height ranging from 10 to 20 meters
High tree	5	polygons representing trees with a height ranging from 20 to 30 meters
Very high/robust tree	6	polygons representing trees with a height greater than 30 meters

Table III-4: Standardized classes for vegetation sources. Each raw class contained in the imported vegetation (polygonal) data must be associated to one of these new standardized classes, to be used in PIP-AI.

Title	Class	Description
Not defined	0	all the pixels that do not fall under any polygon or for polygon classes that are not well defined
Sloping man-made areas	1	polygons representing sloped urbanized areas
Mountainous and rocky areas	2	polygons representing mountains
Various crops	3	polygons representing various crops
Low vegetation and meadows	4	polygons representing areas with low vegetation
Woods (Forests)	5	polygons representing forests
Flat man-made areas	6	polygons representing flat urbanized areas
Submerged areas	7	polygons representing areas underwater

Table III-5: Standardized classes for land use sources. Each raw class contained in the imported land use (polygonal) data must be associated to one of these new standardized classes, to be used in PIP-AI.

3.3.5 Stable And Unstable Areas

One of the problems of landslide inventories is the inconsistency of information. In fact, sometimes the unique information about a landslide occurred in the past are the coordinates of a single point (typically the upper scar or centroid), other times it is available also the polygon representing the boundary of the triggering landslide body. Since PIP-AI analyses landslide susceptibility at the pixel level, its outputs reflect the potential instability of these individual pixels. This necessitates defining the expected outputs for each pixel, which will be used to guide the training process, as follows.

Concerning the unstable area, i.e., the group of pixels that during a certain landslide day (or LE) must be treated as unstable, two possibilities may exist: (i) the polygon of the triggering landslide body is available, thus, if the polygon-raster conversion from Section 3.3.2 is applied, the unstable pixels can be easily defined; (ii) the unique geometrical information are the coordinates of a single point. In the latter case, starting from this point coordinates, it is possible to recreate a fictitious polygon with minimum dimensions. Accordingly, depending on the landslide class, a fictitious circular area is defined with a radius equal to the minimum. For instance, in the case of shallow landslides, this radius is assumed to be 30 meters, resulting in an area of approximately 2800 square meters, consistent with the minimum extents typical of such events.

Once the unstable area is defined, whether actual or fictious, it is necessary to define also the counterpart, namely the stable area. However, before delving into the explanation of stable areas, it is necessary to introduce the concept of the uncertainty area, also called indecision area. Specifically, by applying a certain buffer size (which depends upon the user) to the unstable area, it is possible to generate a larger buffered polygon, from which the

unstable area must be subtracted to obtain the indecision area. The indecision area is an area within which the pixels should be excluded from the model. This means that the training process of PIP-AI will not consider those pixels, due to possible uncertainties. This assumption is particularly reinforced in the case of fictitious polygons, where minimum area is used. For this reason, it is essential to include this buffer zone, beyond which pixels can then be considered as stable, if necessary.

After the definition of the indecision area, the stable area can be generated with two possible approaches: (i) if the landslide inventory is complete both in space and time, it can be assumed that the remaining area (which would be the study area, filtered from the unstable and indecision areas) is stable, and therefore all the pixels inside the remaining area would create the stable area; (ii) if the completeness of the landslide inventory is uncertain, by applying another buffer size to the unstable area (also in this case definable by the user, but larger than the indecision buffer), it is possible to create the stable area, with the same procedure seen for the indecision area. The reason behind the second approach is that when a landslide is recorded, it can be assumed that there are no other landslides in the vicinity (within a certain radius of visibility), as they would otherwise have been detected and recorded as well.

All the three types of area above discussed (unstable, indecision, and stable) are illustrated in Figure III-25. It is important to note that these areas are linked to a specific landslide day (or LE) and are generated for each landslide occurred. Furthermore, in case of two or more landslide which are near, the different generated polygons can be merged into a single one, if they overlap, creating a single landslide body.

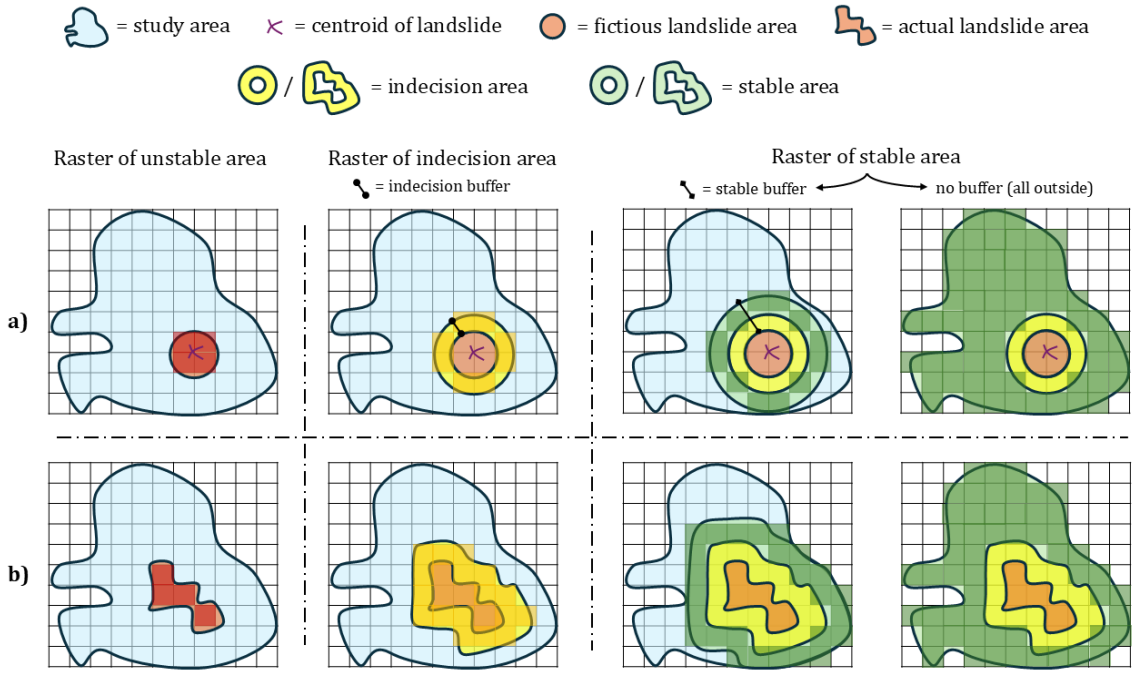

Figure III-25: Scheme of the definition of the unstable, indecision, and stable areas. Regarding the unstable area, which is the starting point, if no landslide geometry is available, a fictious unstable area is created (a). If a well-known geometry is available, that geometry is imported to define the unstable area (b). After the creation, or import, of the landslide area, the indecision area is generated, by applying a buffer to the landslide area. Finally, the stable area can be generated with two possible approaches, that is, respectively, by applying another (larger) buffer to the landslide area, or by considering all the remaining area (study area minus unstable and indecision areas).

3.3.6 MODELLING

The PIP-AI model is the result of a process aimed at training several different configurations and structures of various machine (and deep) learning algorithms, such as DTEs, SVMs, MLPs, and KANs (see Appendices Chapter). During this procedure, the best configuration is sought, which will subsequently be employed for future predictions on the same study area seen during training, a sub part of it, or potentially new study areas, which have characteristics similar to the already seen study area, used for training. Therefore, as seen for the LEP-AI, a very similar comprehensive framework is adopted with PIP-AI, by means of the definition of some hyperparameters, input/output data, and some metrics which allow to assess the performance (also called quality) of each model.

The main hyperparameters vary according to the type of model adopted, as will be discussed in Section 3.3.6.1. For instance, in case of MLPs, these hyperparameters are the same seen in Section 3.2.3.1, for LEP-AI. The number of input nodes of all the models can go up to 43, depending on the Rainfall Mode adopted (RM1, RM2, or RM3), while the number of outputs is set to 2 nodes, since each pixel follows a binary classification, with relative probabilities, as will be explained in Section 3.3.6.2. Moreover, inputs can be static, when related to morphology, soil, land use, hydrology etc.; or dynamic, when related to rainfall,

temperature, and NDVI. Finally, the metrics adopted for the assessment of each model performance are the same seen in Section 3.2.3.3, with the addition of a new metric, referred to as Time Index (*TI*), which is an index aimed at assessing the quality of the model from a timing point of view. In other words, the *TI* can quantify the precision of the model in maintaining all the pixels of a specific landslide area as stable, until the day of the landslide occurrence, where all the pixels contained in the Unstable and Stable Areas (see Section 3.3.5) should be classified respectively as unstable and stable. More info about the *TI* will be addressed in Section 3.3.6.3.

3.3.6.1 Hyperparameters

The hyperparameters adopted change according to the type of model selected. In case of MLPs, there are no differences with what was seen in Section 3.2.3.1, for LEP-AI model.

In contrast, if the chosen model type for PIP-AI is a Decision Tree Ensemble (DTE) (see Appendices Section), the hyperparameters that can be specified are different. Specifically, in this case the main hyperparameters are represent by the number of decision trees (weak learners), and the minimum leaf size, which is the minimum number of observations that a leaf node of the three must have. If the latter parameter is set to 1, it means that each final split of the three can also contains just 1 observation. Despite this, when set to 1, model can be prone to overfitting, because each tree of the ensemble could be built to classify in detail and separate every observation of the dataset, without generalizing. In addition to these two primary hyperparameters, according to the sub-type of DTE, which can be 'bagging' or 'boosting', other hyperparameters can be set. For instance, in case of 'bagging' types, particularly with Random Forest, it is possible to specify parameters like the percentage of training dataset to use for each tree (extracted randomly) and many other minor ones (MathWorks Inc., 2024a, 2024b). Instead, with 'boosting' types, a relevant hyperparameters is the learning rate, i.e., the parameter that rules the convergence speed, since 'boosting' ensemble trees are made sequentially and are based on the correction of the errors made by the previous tree. The learning rate can range from 0 to 1. The higher the learning rate, the more unstable could be the convergence of the solution, while the lower the learning rate, the slower is the training process, because it would require a greater number of weak learners to reach the same solution (more decision trees). Of course, also with 'boosting' decision trees there are several other minor hyperparameters, which will not be covered here for obvious reasons (MathWorks Inc., 2024b).

When the chosen model for PIP-AI is the SVM, the most important hyperparameter is represented by the type of kernel functions. In fact, kernel functions can be linear (if the classes can be separated by a line in a certain hyperplane), polynomial, radial basis function, or gaussian, depending on the type of data and their relationship to the expected output class. The choice of the kernel affects highly the separability of the two classes and the overall

performance of the model. Furthermore, depending on this kernel, some other minor hyperparameters can be adjusted (MathWorks Inc., 2024d).

Finally, if the chosen model is a KAN, then the hyperparameters are basically the same of the MLPs, except for the fact that the activation functions are not present. In fact, the most important difference between MLPs and KANs depends on the fact that each node of a KAN contains a special unit which can model a polynomial function from scratch. This means that the activation function of a node is not defined a priori but it is a curve shaped based on the input data and the specific problem at hand. Such flexible curves, also known as B-splines, greatly assist in interpreting model behaviours (XAI). However, they also have a downside: the nodes containing these flexible functions are generally slower and more challenging to train compared to typical neurons in an ANN, such as with MLPs.

However, all the above-mentioned hyperparameters, regardless of the type of model chosen, can be set by the user during the creation of it.

3.3.6.2 Input And Output Data

The inputs of PIP-AI model can be up to 43 selected features for each pixel, taken during (and before) a specific landslide day. In other words, if a single pixel is considered, then all the possible features (both static and dynamic) of this pixel, taken during a specific landslide day (and before it through cumulative values), represent a single observation of the dataset, i.e., a row of a table. Moreover, since static features do not change over time, these properties remain unchanged during the various days of analysis. In fact, the main task of the static features is to distinguish the various pixels, which can be more or less susceptible to landslides, according to their intrinsic properties. Instead, the task of the dynamic features is to define some sophisticated and dynamic thresholds which can be used to define when a given pixel is at risk, during a certain rainy day (or RE).

Three important aspects about the observations must be clarified: (i) the training of the model is performed only during some specific days, which are the various landslide days, 10 days before them, and 10 days after them. This approach ensures that the model can learn the timing effect for each landslide of the inventory, because the dynamic features (referred to the same pixel) change. Furthermore, 10 days before and after the landslide day there is no landslide, therefore the pixels must be stable; (ii) the pixels considered are only the ones that are inside the Unstable and Stable Areas, for each landslide occurred; (iii) all the inputs of the model are normalized (and possibly also standardized by the models). Normalization brings all values within the [0, 1] range, while also clipping values that fall outside predetermined minimum and maximum values, specific to each input type. This ensures that the models never receive input values outside the ranges encountered during training, helping to prevent artifacts in the outputs. In fact, it is worth to note that multiple types of

models might be used, as seen in Section 3.3.6.1, making this operation advisable to enhance consistency and accuracy.

However, static features of PIP-AI model are 31 and all of these can be obtained from the DEM of the study area and other sources, such as the vectorial map of roads, the vectorial maps of subsoil, topsoil, vegetation, and land use, the raster maps of clay and sand contents, or also the raster maps of the probabilities for some vegetative species. Specifically, these static features represent for each pixel some properties, as shown in Figure III-26, which can be categorized as follows:

- 6 morphological metrics – elevation (Elevation); slope (Slope); aspect angle (AspAngle); mean curvature (MnCurv); profile curvature (PrCurv); planform curvature (PlCurv)
- 2 hydrological metrics - contributing area (ContArea); Topographic Wetness Index (TWI)
- 1 distance metric - distance from roads (RoadDist)
- 4 class metrics - subsoil class (SubClass) (Table III-2); topsoil class (TopClass) (Table III-3); vegetation class (VegClass) (Table III-4); land use class (LndClass) (Table III-5);
- 2 texture metrics - clay content (ClayCont); sand content (SandCont);
- 16 vegetation species metrics - Salix Caprea probability (SalCapPrb); Quercus Robur probability (QrcRobPrb); Quercus Ilex probability (QrcIlxPrb); Quercus Cerris probability (QrcCrsPrb); Quercus Suber probability (QrcSubPrb); Prunus Avium probability (PrnAvmPrb); Pinus Sylvestris probability (PinSylPrb); Pinus Pinea probability (PinPinPrb); Pinus Nigra probability (PinNigPrb); Pinus Halepensis probability (PinHalPrb); Picea Abies probability (PicAbiPrb); Fagus Sylvatica probability (FagSylPrb); Corylus Avellana probability (CorAvePrb); Castanea Sativa probability (CstSatPrb); Abies Alba probability (AbiAlbPrb); Olea Europaea probability (OleEurPrb).

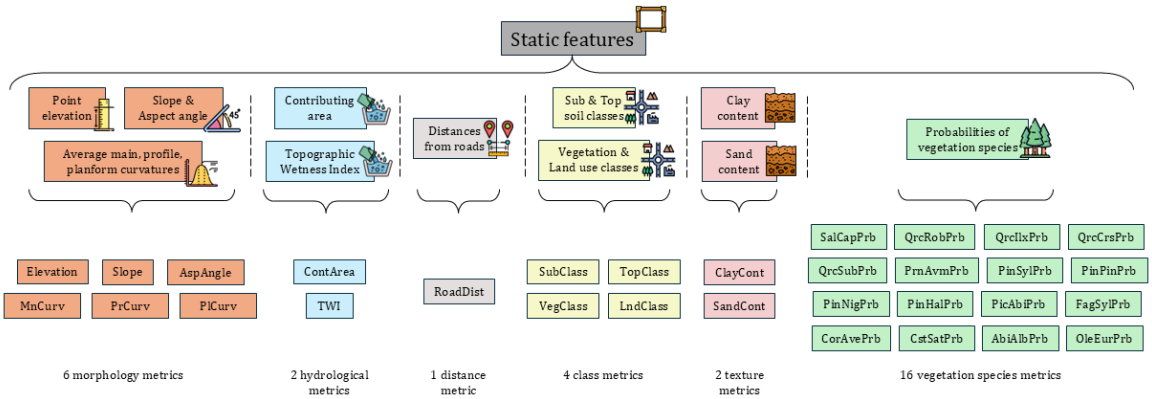

Figure III-26: Scheme of the 31 static features considered in the PIP-AI model. These features are grouped based on the category (different colours) and they must be considered as quantities referred to a single pixel.

Regarding the dynamic features used in PIP-AI model, these vary according to the Rainfall Mode used. Particularly, rainfall and temperature features change depending on Rainfall Mode, while the remaining features can be categorized as follows (Figure III-27):

- 1 vegetation metric – the Normalized Difference Vegetation Index (NDVI)
- 1 check metric – a random number with no physical or mathematical meaning (RandFeat), associated with each observation of the dataset and intended to verify that the model does not extract information from it, and plus, it can act as a threshold for distinguishing key features from less relevant ones.

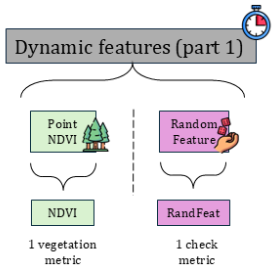

Figure III-27: Scheme of the first part of the dynamic features considered in the PIP-AI model. These features are grouped based on the category (different colours), i.e. green for vegetation and violet for random feature. They must be considered as quantities referred to a single pixel.

If the RM1 is applied, rainfall and temperature features are the following (shown in Figure III-28a):

- 4 rainfall metrics – the cumulative rainfall of 10 (CmRain10d), 20 (CmRain20d), 30 (CmRain30d), and 60 (CmRain60d) days before the landslide day, which is included
- 4 temperature metrics – the average temperature of 10 (AvTemp10d), 20 (AvTemp20d), 30 (AvTemp30d), and 60 (AvTemp60d) days before the landslide day, which is included.

If the RM2 is applied, rainfall and temperature features are the following (shown in Figure III-28b):

- 15 rainfall metrics – the 15 daily rainfalls, starting from 14 days before the landslide day to the landslide day, which is included (respectively, Rain14d2L, Rain13d2L, Rain12d2L, Rain11d2L, Rain10d2L, Rain9d2L, Rain8d2L, Rain7d2L, Rain6d2L, Rain5d2L, Rain4d2L, Rain3d2L, Rain2d2L, Rain1d2L, Rain0d2L)
- 15 temperature metrics – the 15 daily average temperatures, starting from 14 days before the landslide day to the landslide day, which is included (respectively, Temp14d2L, Temp13d2L, Temp12d2L, Temp11d2L, Temp10d2L, Temp9d2L, Temp8d2L, Temp7d2L, Temp6d2L, Temp5d2L, Temp4d2L, Temp3d2L, Temp2d2L, Temp1d2L, Temp0d2L).

If the RM3 is applied, rainfall and temperature features are the following (shown in Figure III-28c):

- 6 rainfall metrics – the triggering rainfall, that is the rainfall cumulated over the current RE (TrigRain); the peak rainfall, that is the hourly rainfall peak during the current RE (PeakRain); the cumulative rainfall of respectively 10, 20, 30, and 60 days before the day of the start of the current RE, which is not included (respectively, CauseRain10d, CauseRain20d, CauseRain30d, CauseRain60d)
- 6 temperature metrics – the triggering temperature, that is the average temperature over the current RE (TrigTemp); the peak temperature, that is the hourly temperature peak during the current RE (PeakTemp); the average temperature of respectively 10, 20, 30, and 60 days before the day of the start of the current RE, which is not included (respectively, CauseTemp10d, CauseTemp20d, CauseTemp30d, CauseTemp60d).

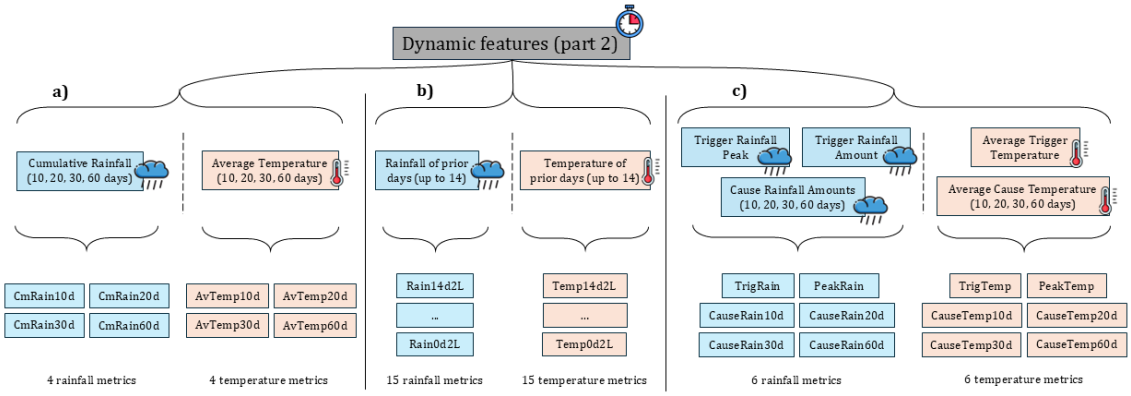

Figure III-28: Scheme of the second part of the dynamic features considered in the PIP-AI model. These features are grouped based on the category (different colours), i.e. blue for rainfall and orange for temperature. They must be considered as quantities referred to a single pixel. Based on the Rainfall Mode adopted, three different types of rainfall and temperature features can be created. The features of (a) are obtained with Rainfall Mode 1, the features of (b) with Rainfall Mode 2, and finally, the features of (c) with Rainfall Mode 3.

To conclude, the outputs of the PIP-AI are just two, because a binary classification is applied on every pixel of a certain study area. These two outputs are respectively the instability and stability probability, related to the two neurons of the output layer. Based on these two probabilities (which are complementary) the output pixel is classified as stable or unstable. If a susceptibility map is desired as output, then it is sufficient to consider the neuron that gives the instability probability. Consequently, the higher the probability, the higher the susceptibility.

3.3.6.3 Assessment Of Model Performance

The assessment of model performance can be achieved through the same metrics seen in Section 3.2.3.3. Regarding the datasets, these are also split as seen for LEP-AI, following the same rules. Therefore, some of the metrics adopted by PIP-AI model are the CEL, AUROC,

AUPRC, AUPRGC, RFI, and the overall quality index, i.e., the QI (Equation 42). In addition to these, three new metrics are introduced in PIP-AI: the Positive Polygon Rate (PPR), the Negative Polygon Rate (NPR), and the Time Index (TI).

When all the Stable Areas of a specific landslide day are defined, these areas can be merged into one. Thus, for each landslide day (included in the training, validation, and test datasets) a single, merged Stable Area can be created. Consequently, for each landslide day, the ratio between stable and unstable pixels can be assessed. Such a ratio is referred to as PPR. In other words, the PPR is a value that, for a specific landslide day, represents the proportion between stable and unstable pixels within the merged Stable Area, as described in the following Equation 43.

$$PPR = \frac{N_{SP\_SA}}{N_{SP\_SA} + N_{UP\_SA}} \tag{43}$$

where:

- N_{SP_SA} is the number of stable pixels inside the merged Stable Aera (created for a specific landslide day)
- N_{UP_SA} is the number of unstable pixels inside the merged Unstable Area (created for a specific landslide day)

If the same procedure of the PPR is repeated, but with the Unstable Area and the unstable pixels, then the NPR can be defined. In fact, the NPR can be defined as the proportion between unstable and stable pixels, within the unique, merged Unstable Area for a specific landslide day, as described in the following Equation 44.

$$NPR = \frac{N_{UP\_UA}}{N_{SP\_UA} + N_{UP\_UA}} \tag{44}$$

where:

- N_{UP_UA} is the number of unstable pixels inside the merged Unstable Area (created for a specific landslide day)
- N_{SP_UA} is the number of stable pixels inside the merged Unstable Area (created for a specific landslide day)

According to the above definitions of the PPR and NPR, both metrics should equal 1 on the landslide day, in an idealized scenario. On all other days outside of the landslide day, these metrics should be 1 and 0, respectively, as pixels within the Unstable Area should remain stable in the absence of any landslide event. Thus, it is possible to consider the time history of such metrics (PPR and NPR), for the 30 days before the landslide day (which is included). As a result, during the period between 29 and 1 days before the landslide day, the PPR should be equal, or near, to 1, while the NPR should be equal, or near, to 0. During the landslide day,

both these metrics should be equal, or near, to 1. If the importance of the landslide day is defined, against the other 29 days before it, then the TI can be defined as follows:

$$TI^* = \alpha \cdot \left(\frac{PPR(t_0) + NPR(t_0)}{2}\right) + (1-\alpha) \cdot \frac{\sum_{i=1}^{TD}\left[PPR(t_0 - i) + \left(1 - NPR(t_0 - i)\right)\right]}{2 \cdot TD} \quad (45)$$

$$TI = \frac{\sum_{j=1}^{NLD} TI_j^*}{NLD} \quad (46)$$

where:

- α is the importance of the landslide day, which ranges from 0 to 1 (by default set to 0.5, meaning that the landslide day has the half of the importance compared to the other 29 days before it)
- $PPR(\mathrm{t}_0)$, $NPR(\mathrm{t}_0)$, $PPR(\mathrm{t}_0 - \mathrm{i})$, and $NPR(\mathrm{t}_0 - \mathrm{i})$ are respectively the Positive and Negative Polygon Rates, which are assessed during the landslide day (t_0) and during i-days before it ($\mathrm{t}_0 - \mathrm{i}$)
- TD is the total number of days considered before the landslide days, which in this case is equal to 29
- TI^* is the partial Time Index, assessed for a specific landslide day
- NLD is the number of landslide days included in a dataset

Thus, the TI, which is the average of all the partial TI (i.e., all the TI^* assessed over all the possible landslide days, for a given dataset) can be summarily described as the index that quantifies the model's accuracy in providing correct predictions over time, i.e., during the landslide day and the days before it. A comprehensive scheme of what was discussed above is shown in Figure III-29.

To conclude, when the TI is near to the unit, the model maintains a good predictive quality, from a time perspective. In contrast, if the TI is null, or near to 0, it can be deduced that the model has a very bad predictive quality, from a time point of view.

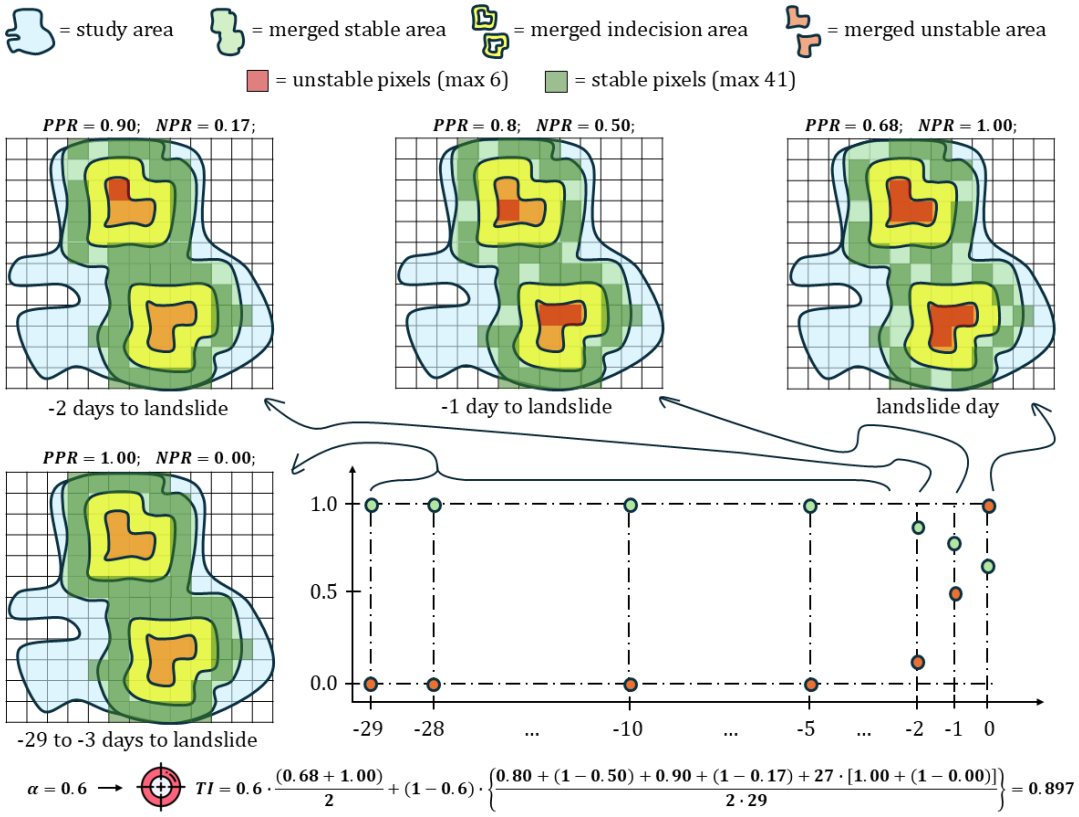

Figure III-29: Scheme of the PPR, NPR, and TI metrics. In this example, the TI is evaluated for a single landslide event. From 29 to 3 days prior to landslide day, the PPR and NPR metrics are 1 and 0, respectively. Starting from 2 days before the landslide day, PPR and NPR change. The scatter graph of PPR and NPR is reported on the bottom-right part of the figure. Finally, if the importance of the landslide day (α) is set to 0.6, then the resulting TI is 0.897.

3.4 H-SLIP Model

The Hybrid - Shallow Landslide Instability Predictor model (H-SLIP) is a natural evolution of SLIP and PIP-AI. Specifically, this model is not built from scratch, as SLIP and PIP-AI, but it consists of the combination of the two. Particularly, by means of the weighted average of the results, it is possible to generate new, combined predictions, which in most cases are better than considering just one of the two models. In fact, it was seen with different real cases applications that SLIP tends to be 'conservative', while PIP-AI tends to be 'pessimistic' with predictions. In other words, if the results of both the models are converted into susceptibility maps, then the high susceptible areas assessed with SLIP are less and smaller compared to PIP-AI, which, in contrast, it often gives large areas with high susceptibility.

Before performing the combination of the two types of models, it is necessary to convert the results of SLIP from Fs to instability probabilities, for each pixel. This conversion is possible through a simple mathematical formulation, as follows:

$$p_{SLIP} = 1 - \frac{log\ Fs - log\ Fs_{min}}{log\ Fs_{max} - log\ Fs_{min}} \tag{47}$$

where:

- Fs is the Factor of Safety of a given pixel and $\log Fs$ is the natural logarithm of it
- $Fs_{\min}$ is the maximum value allowed for the Factor of Safety (which by default can be set to 100, meaning that the stabilizing forces are 100 times greater than the destabilizing ones). Values above the maximum are cut
- $Fs_{\max}$ is the minimum value allowed for the Factor of Safety (which by default can be set to .01, meaning that the stabilizing forces are 100 times smaller than the destabilizing ones). Values below the minimum are cut
- p_{SLIP} is the converted, instability probability of the current pixel.

After this operation, it is possible to decide the importance of the two models and combine the results, with a weighted average, using the following expression:

$$p_{H-SLIP} = \alpha \cdot p_{SLIP} + (1 - \alpha) \cdot p_{PIP-AI} \tag{48}$$

where:

- α is the importance of SLIP against PIP-AI, which ranges from 0 to 1 (by default set to 0.5, meaning that the two models have the same importance)
- p_{SLIP} is the converted probability of SLIP, from Equation 47
- p_{PIP-AI} is the instability probability of the current pixel, given by the PIP-AI model.

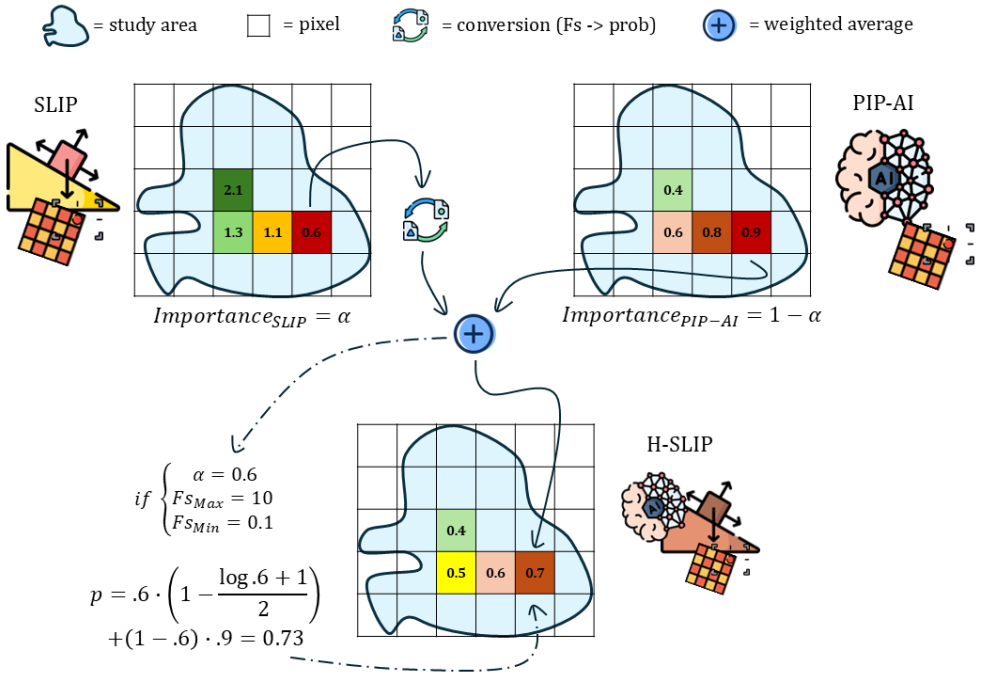

Figure III-30: Scheme of the H-SLIP functioning. For a given pixel, the Fs is converted into a probability. Then, the importance (weight) of SLIP is specified, but also the maximum and minimum Fs. After this, the weighted average is assessed, between the converted probability from SLIP and the instability probability from PIP-AI. This process is repeated for each pixel of the map.

IV PLATFORM

The X-SLIP platform is the culmination of extensive and intensive efforts aimed at transforming all the models presented in Chapter III into executable codes, within a comprehensive and integrated platform. The programming language (interpreter) chosen for X-SLIP is MATLAB, as it is more familiar to Civil and Environmental Engineers, who are thus more likely to expand or enhance its functionalities with greater ease. A graphical UI is also implemented, to facilitate the use, without necessarily run manually the source code. In order to create the above-mentioned UI, the MATLAB built-in App Designer was adopted, and the result is shown in Figure IV-1.

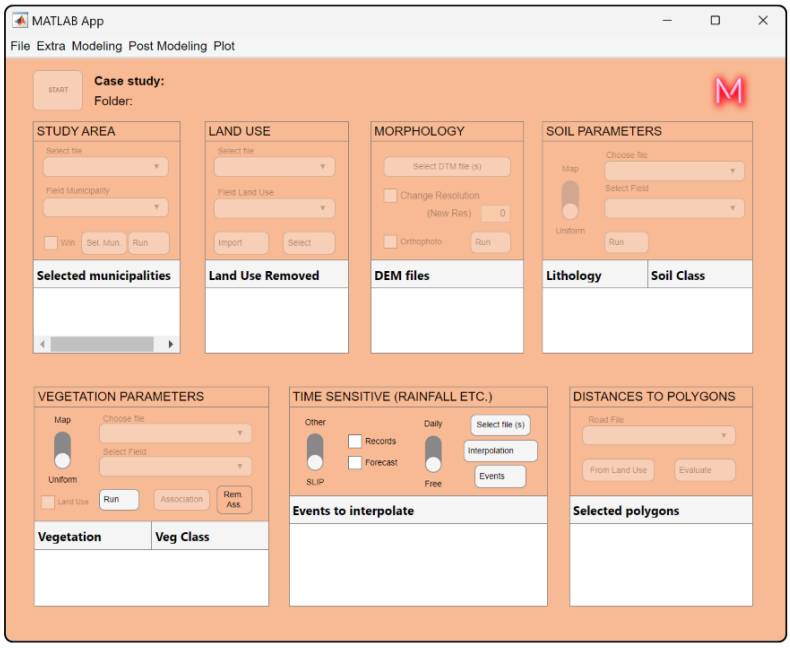

Figure IV-1: The X-SLIP main user interface.

To develop the X-SLIP platform, it was necessary to integrate various functions and routines that interact with each other and can be categorized as follows: app code, main source code (i.e., scripts also referred to hereafter as main modules), general functions, and scripts for generating pictures (also called plot modules). A more detailed representation of the code is provided in the Appendices Section.

The starting interface of X-SLIP is divided into main panels (Section 4.1), where each panel represents a type of processing, i.e., a certain data type. These panels can be grouped into study area (Section 4.1.1), land use (Section 4.1.2), morphology (4.1.3), soil (Section 4.1.4), vegetation (Section 4.1.5), time sensitive (i.e., rainfall and temperature) (Section 4.1.6), and distances (Section 4.1.7). In addition to these, a menu on the top is available, with other functionalities, as will be explained in Sections 4.2, 4.3, and 4.5.

The following sections will describe the functionalities and capabilities of X-SLIP, serving as a user guide for the platform's operation. Before delving into the user guide, in Figure IV-2 it is reported how to create new analyses, or open old ones. In fact, the <File> menu on the top of the UI contains the <New> and <Open> buttons, to create respectively a new analysis, or to open (and continue) a pre-existing one. It must be noted that the autosave feature is implemented, thus, there is no need to save the state of a work-in-progress analysis.

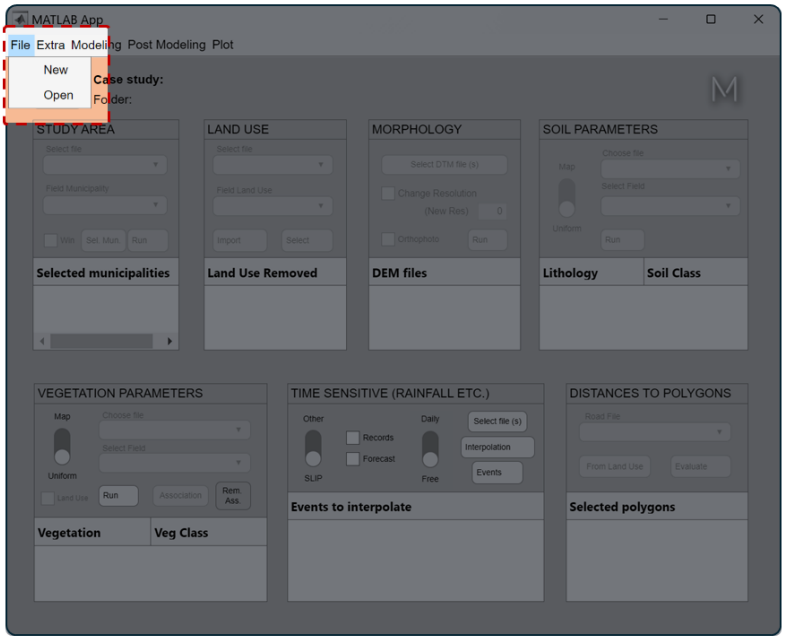

Figure IV-2: Detail of the <File> menu in X-SLIP UI. With the <New> button a new analysis can be started. With the <Open> button, a pre-existing analysis can be open, with the possibility to modify or just continue it.

Each analysis performed with X-SLIP has a main folder, which reflects the structure of the program. In fact, inside the main folder of every analysis, there is a single file, called 'os_folders.mat' and 5 subfolders, which are respectively 'Figures', 'Raw Data', 'Results', 'User Control', and 'Variables', as it can be seen in Figure IV-3a. The file 'os_folders.mat' is a MATLAB file containing variables with all the paths used for the various analyses and some basic information such as the case study name etc. The 'Figures' subfolder contains all the possible pictures of the maps, graphs, etc., plotted through the Plot Menu of Section 4.5. The 'Raw Data' subfolder contains the raw source data to be used for the analysis, such as shapefiles, raster maps, etc., which in turn is organized in other subfolders, as shown in Figure IV-3b. The

'Results' subfolder contains the outcomes of the Modelling Menu of Section 4.3, stored as '.mat' files in their relative, further subdivided, subfolders, according to the type of model used, as shown in Figure IV-3c. The 'User Control' subfolder contains some files, which typically are spreadsheets, to control the behaviour of some aspects, such as the soil and vegetation attribution of parameters' classes (for SLIP analyses), the class standardization process (for PIP-AI analyses) seen in Chapter III (Section 3.3.4), etc. Finally, the 'Variables' subfolder contains several internal '.mat' files, where all the variables and objects used by the platform are stored and read when needed.

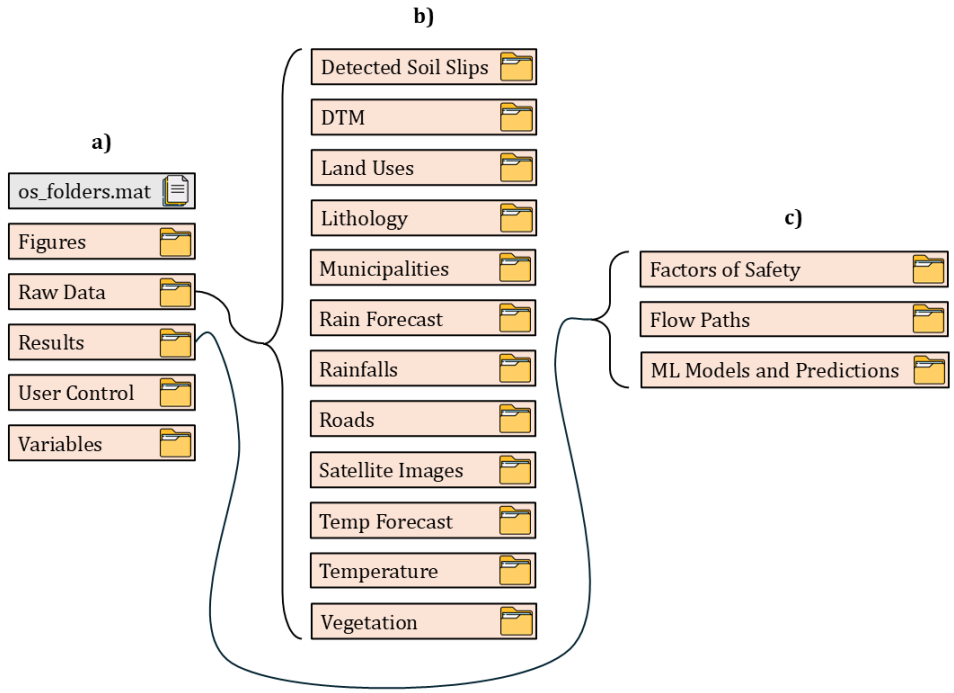

Figure IV-3: Scheme of the folders' structure of a typical X-SLIP analysis. The main folder of the analysis contains the subfolders and files on the left (a). The 'Raw Data' subfolder contains in turn all the subfolders on the middle (b). Every subfolder contained in 'Raw Data', contains in turn raw files, such as the DEM raster files (for instance, '.tif' files) in the 'DTM' subfolder. Instead, the 'Results' subfolder contains in turn all the subfolders on the right (c). Thus, depending on the type of modelling, 'Factor of Safety', 'Flow Paths', or 'ML Models and Predictions' folders can be used. Each of these subfolders, contains in turn other subfolders, named by the user, based on the analysis performed. Inside this final subfolder, the '.mat' files, containing the results, are present.

4.1 MAIN PANELS OF X-SLIP

In order to explain the functionalities of the main panels of X-SLIP, an existing analysis is opened and shown in Figure IV-4. This case refers to the municipality of Enna, Sicily, where in 2014 a landslide occurred. Independently from the case and the possible results of the analysis, which are discussed in the appropriate Chapter V, it can be see how the platform is structured and how it would appear once it is completed.

The main panels are group of operations that can be performed over a certain data type, i.e., study area, land use, morphology, soil, vegetation, time sensitive (rainfall and

temperature), and distances. Additionally, the operations available within these panels are designed to be sequential, unlocking progressively. For instance, the first panel that can be used is the analysis panel (Figure IV-4a), where the button <Start> creates the main folder of the analysis and all the subfolders' structure, already seen in Figure IV-3.

Generally, the functionalities and results derived from these main panels are independent of the specific type of modelling desired (accessible through the top menu Modelling, Section 4.3). This approach was chosen to make the main interface a versatile tool suitable for various purposes, potentially integrating with other software and analyses.

Indeed, this tool, although rudimentary, offers a valuable alternative to commercial GIS software. All variables are accessible and modifiable via MATLAB, providing a significant advantage in terms of both efficiency and simplicity, particularly for engineers.

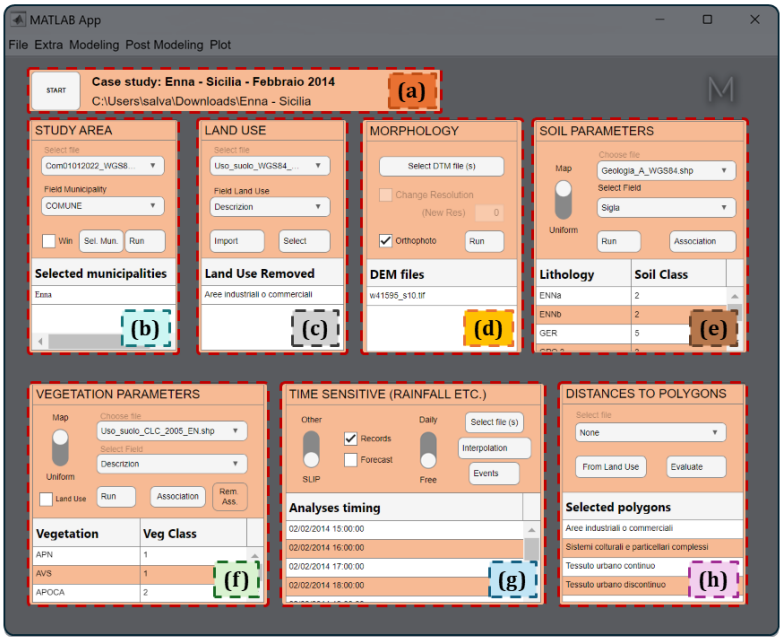

Figure IV-4: Main panels of X-SLIP UI. The analysis panel (a) contains the <Start> button (to start a new analysis), the Case Study name, and the folder where the analysis is stored. The study area panel (b) contains the buttons to select a shapefile and extract from it the boundary of the study area, while on the bottom there is a summary of the areas selected. The land use panel (c) contains the buttons to select the shapefile of the land use, and from it, some classes of polygons can be excluded from the analysis (i.e. subtracted from the study area), while on the bottom there is a summary of the land uses removed. The morphology panel (d) contains the buttons to select the DEM files, the orthophoto, and change the resolution of the analysis (which by default is the same of the source DEM file), while on the bottom there is a summary of the DEM files selected. The soil panel (e) contains a switch to attribute uniform soil parameters over the entire area or to use a map, thus with the buttons to select the sub/topsoil shapefile and associate a new class of parameters to each former class polygon, while on the bottom there is a small summary table of the latter association. The vegetation panel (f) is similar to the soil panel, but for vegetation and with the possibility to use the land use shapefile also for vegetation. The time sensitive panel (g) processes data like rainfall and temperature, containing switches/buttons to select files, type of approaches, and timing, while on the bottom there is a summary of the timestamps selected for the modelling. The distances panel (h) has buttons to select the shapefile containing infrastructures, like roads, buildings, etc, and assessing the distances between each pixel and the nearest object, while on the bottom there is a summary of the object classes selected.

4.1.1 Study Aera Panel

The study area panel, in Figure IV-4b, must be used from the top. In fact, starting from the top, there is a button to select the shapefile containing the boundary of the study area directly, or multiple polygons, among which is included the study area. The possible shapefiles should be manually placed in the 'Municipalities' folder, which in turn is inside 'Raw Data'. If the 'Municipalities' folder is empty, a prompt will appear (Figure IV-5) to ask the user the location of the desired file/s (click <Search file> button), which once selected, are automatically copied inside 'Municipalities' folder. Alternatively, if the user has no shapefile available at all, the prompt allows to click the <Manual coords> button. If the latter button is clicked, the <Win> checkbox (explained below) is automatically flagged and the <Run> button is enabled.

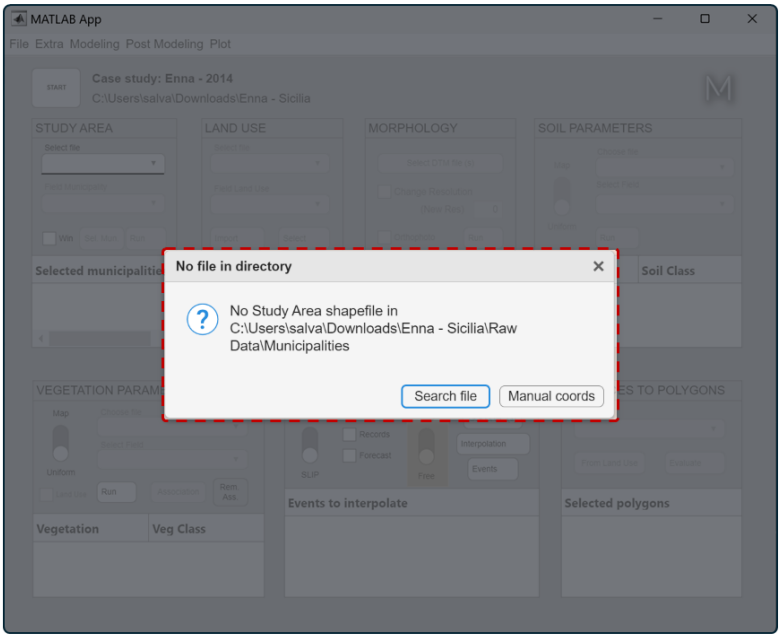

Figure IV-5: Prompt of X-SLIP in case of no files inside the Municipalities sub-folder (inside Raw Data). If the <Search file> button is pressed, then the UI will ask you to search for the file to use. Alternatively, if the <Manual coords> button is clicked, then the <Win> toggle of the study area panel will be flagged, and a manual coordinates window will be asked to fill by the user, which is therefore the "manual" study area.

After this, the second button from the top is the field selector, i.e., the button that asks for the field of the shapefile which contains names of municipalities, based on which the study area can be created. Once the field is chosen, it is possible to select the desired municipalities through the <Sel. Mun.> button, which asks for the municipalities to use and merges them, to create the study area (see Figure IV-6). When the <Sel. Mun.> button completes the process, a list of the selected municipalities appears at the bottom of the panel, as in Figure IV-4b. Alternatively, if the selected shapefile contains just the study area and nothing else (single polygon inside the shapefile), the field 'None' must be selected, and there is no need to use the <Sel. Mun.> button.

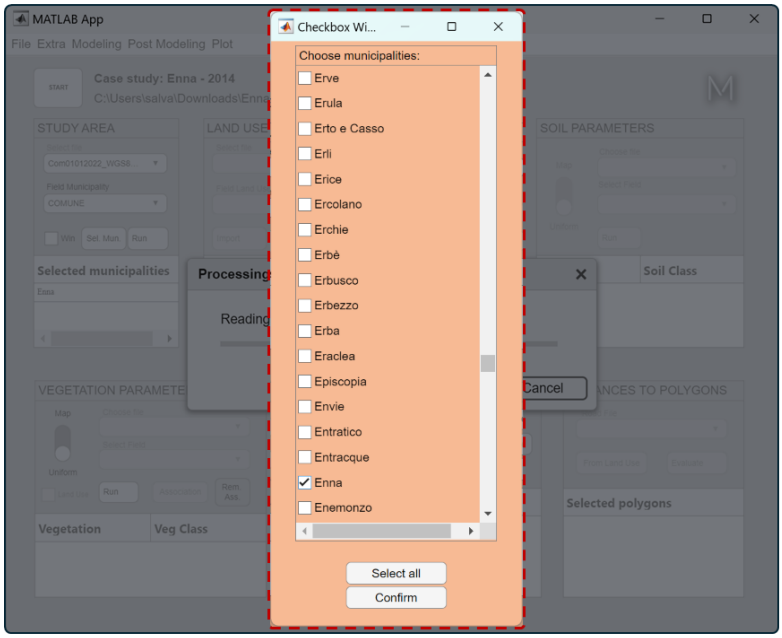

Figure IV-6: The prompt of X-SLIP to select the municipalities that (once merged) will create the study area of the analysis. This prompt is triggered by the <Sel. Mun.> button of the study area panel.

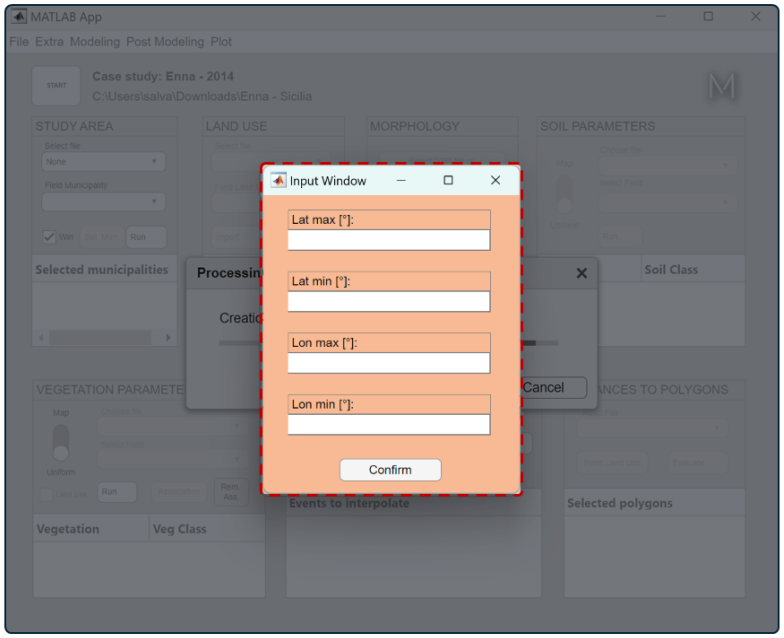

Figure IV-7: The manual definition of the study area in X-SLIP, triggered if the <Win> checkbox is flagged before clicking the <Run> button. This rectangular window will become the study area.

The remaining two actions to explore are the <Win> checkbox and the <Run> button. The first (<Win>) is to create a study area from scratch (based on some coordinates, as shown in Figure IV-7. In case the shapefile with municipalities is simultaneously selected, the resulting study area is the intersection between the "manual" window and the boundaries of

the selected municipalities. The second (<Run>) is the final command of the study area panel, which, once clicked, triggers the 'A_StudyArea_Step1.m' main module of X-SLIP. If the process had no issues, the land use panel and the morphology panels are activated, and the analysis can continue.

4.1.2 Land Use Panel

The land use panel, in Figure IV-4c, must be used from the top. In fact, starting from the top, there is a button to select the shapefile containing the various land uses. The possible shapefiles should be manually placed in the 'Land Uses' folder, which in turn is inside 'Raw Data'. If the 'Land Uses' folder is empty, a prompt will appear (similarly to the one seen in Figure IV-5, but only with <Search file> button) to ask the user the location of the desired file/s (click <Search file> button), which once selected, are automatically copied inside 'Land Uses' folder. After this, the second button from the top is the field selector, i.e., the button that asks for the field of the shapefile which contains names of the classes for the land use.

Once the field is chosen, it is possible to import land uses through the <Import>. This button triggers the 'A_StudyArea_Step2.m' main module of X-SLIP. When the <Import> button completes the process, different polygons are created, depending on the number of classes contained in the selected field and on how many raw polygons intersect the study area. Alternatively, if the selected shapefile contains just one land use and nothing else (single polygon inside the shapefile), the field 'None' must be selected, and a single polygon (i.e., a single land use class) is generated. However, the output polygon/s of land use/s is the result of the intersection with the study area polygon. The name of the classes created can be seen in the file called 'LandUsesAssociation.xlsx' (inside the 'User Control' folder), which is generated if the <Import> button worked with no issues. This file is a spreadsheet structured as shown in Figure IV-8 and can be used to change the class labels of the future land use plots.

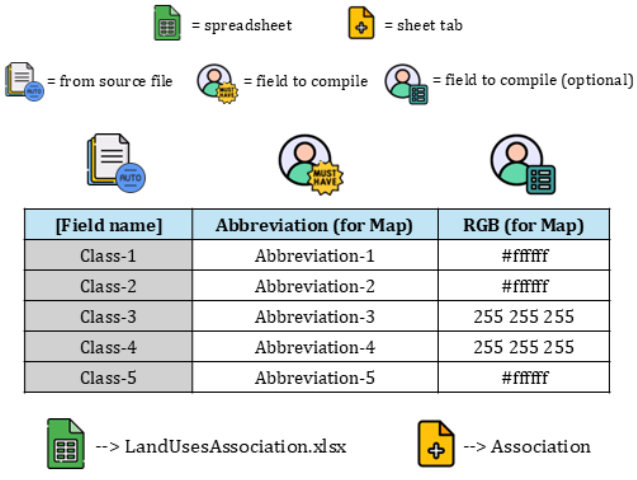

[Field name]	Abbreviation (for Map)	RGB (for Map)
Class-1	Abbreviation-1	#ffffff
Class-2	Abbreviation-2	#ffffff
Class-3	Abbreviation-3	255 255 255
Class-4	Abbreviation-4	255 255 255
Class-5	Abbreviation-5	#ffffff

Figure IV-8: Scheme of the 'LandUsesAssociation.xlsx' spreadsheet, in the 'User Control' folder. The first column is automatically compiled and contains the chosen field as title and the name of classes below. The second column

contains the abbreviations for all the possible classes and must be compiled by the user. The third column is optional and contains the colours to use while plotting. This column should be compiled by the user, either as hex code or as RGB set of values. If colours are not specified, random colours are generated by X-SLIP.

The last optional step consists of eventually removing some classes from the study area, by clicking on the <Select> button. If the latter button is clicked, the main module 'A_StudyArea_Step3.m' is triggered and a prompt will appear, asking for the classes to remove from the study area (which must be flagged), as shown in Figure IV-9. Once done, if the process run with no issues, the list of the removed classes appears at the bottom of the land use panel, as shown in Figure IV-4c.

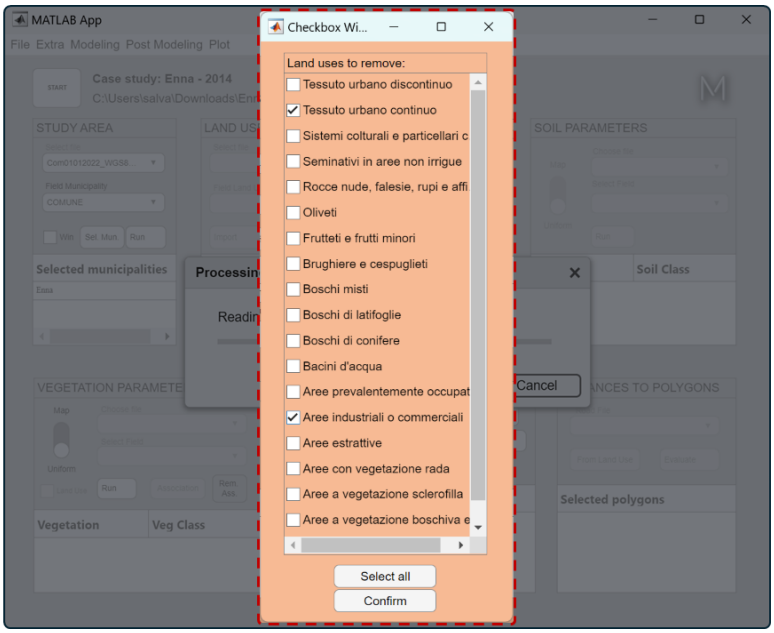

Figure IV-9: The prompt for the selection of the land uses to remove from the study area. This prompt is triggered by the <Select> button of the land use panel.

4.1.3 Morphology Panel

The morphology panel, in Figure IV-4d, must be used from the top. In fact, starting from the top, there is the <Select DTM file (s)> button to select the raster files containing the Digital Elevation (or Terrain) Model. Therefore, a prompt will appear asking for these files (placed in the 'DTM' folder), as shown in Figure IV-10.

The possible raster files should be manually placed in the 'DTM' folder, which in turn is inside 'Raw Data'. Nevertheless, if the 'DTM' folder is empty, a prompt will appear (similar to the one of Figure IV-5, but just with the <Search file> button) to ask the user the location of the desired files (click <Search file> button), which once selected, are automatically copied inside 'DTM' folder. Once files are selected, the list of the selection performed by the user appears at the bottom of the morphology panel, as shown in Figure IV-4d. After this, there is the possibility to change the resolution of the selected files, by flagging the <Change

Resolution> checkbox. It this checkbox is flagged, the <New Res> input box is unlocked and the new resolution, which must be expressed always in meters, can be write.

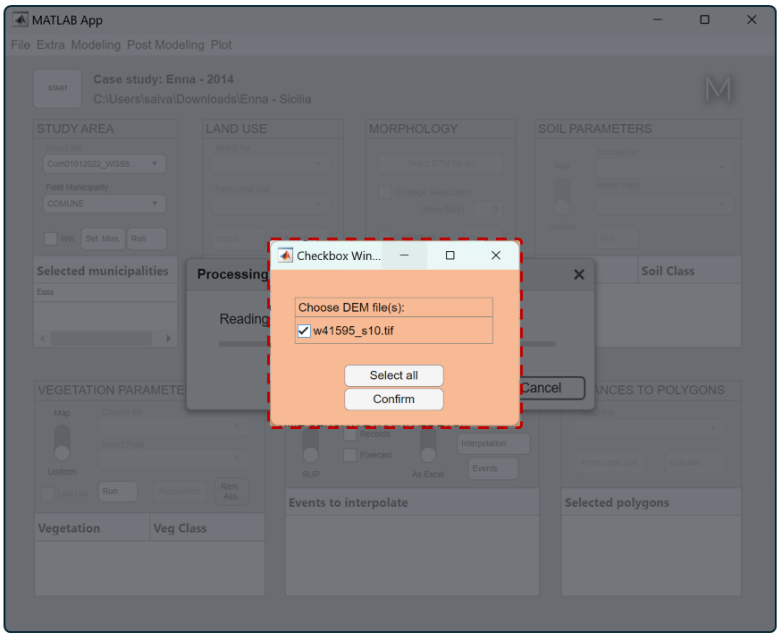

Figure IV-10: The prompt for the selection of the DTM (DEM) files, inside 'DTM' subfolder (which in turn is inside 'Raw Data'). After this selection, the summary appears at the bottom of the morphology panel. This prompt is triggered by the <Select DTM file (s)> button.

One of the last options that can be selected before the <Run> button is the <Orthophoto> checkbox. If this option is flagged, then during the reading of DTM (DEM) files it is read also the orthophoto of the study area. The orthophoto can be read if there are raster files in the 'Satellite Images' sub-folder (inside 'Raw Data') or if there is a txt containing the links of the WMS service. The latter txt file must be named as 'UrlMap.txt', otherwise it will not be recognized. If the <Orthophoto> checkbox is flagged but there are no raster files or txt, during the processing of the <Run> button a prompt will ask the user to give a URL of the WMS service, from which the satellite images can be extracted.

Finally, the last button of the morphology panel is the <Run> button, which, once clicked, triggers the main module 'B_Morphology.m' of X-SLIP. If the process run with no issues, a green lamp will appear beside the <Run> button and all the other main panels (soil, vegetation, time sensitive, and distances panels) are activated. Moreover, a fast "check" plot appears, returning a colored figure with a gradient scale ranging from blue (indicating areas of lower elevation) to yellow (indicating areas of higher elevation). Instead, the excluded areas, due to the removal of specific land-use classes (as explained in Section 4.1.2), are displayed in red, as shown in Figure IV-11. If this plot looks like expected by the user, the first three main panels successfully processed data. In contrast, if some areas inside the boundary of the study area are blank, or if the red areas are not the desired ones, it is necessary to

perform again the operations of study area and land use panels respectively. After this, it is possible to click again directly the <Run> button of the morphology panel, to update the internal variables and see the new check plot.

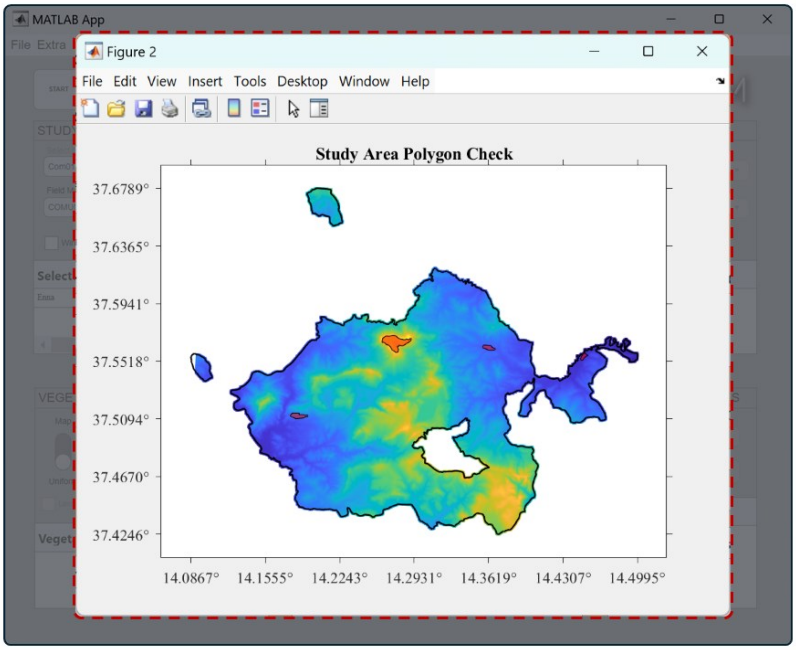

Figure IV-11: The 'check' figures plotted after running the final step of the morphology main panel. This plot appears when the <Run> button of the morphology panel is clicked and there were no issues during the process. In this case, the municipality of Enna is shown, with a gradient scale that ranges from blue (for lower elevation) to yellow (for higher elevation). Since some land uses were removed from the study area, these are merged, coloured in red, and excluded from the current analysis.

4.1.4 SOIL PANEL

The soil panel, in Figure IV-4e, must be used also from the top, but the first option to set is the switch on the top-left of the panel. This switch can be set to <Uniform> or <Map>, depending on what data is available.

If the switch is set to <Uniform>, it means that no map is used to attribute soil properties, thus the entire area will have the same uniform values. If this option is selected, it is possible use directly the <Run> button, which triggers the 'C_Soil_ParametersAttribution_Step0.m' main module. Consequently, a prompt will appear, asking for some mechanical and hydraulic properties of soil (also the A and k_t modelling parameters of SLIP), as reported in Figure IV-12. After the definition of these values, the soil panel is completed and there is no need to perform other operations.

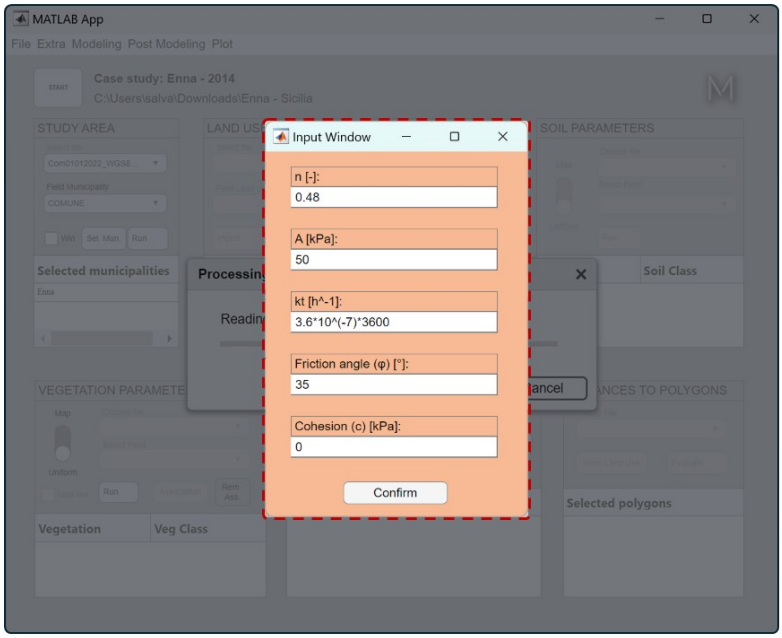

Figure IV-12: The prompt for the attribution of the uniform soil properties over the entire study area, which appears when the switch of the soil main panel is set to <Uniform> and the <Run> button is clicked. It is possible to specify the soil cohesion and friction, the k_t and A modelling parameters of SLIP, and the soil porosity.

Alternatively, if the switch is set to <Map> there are different actions to perform. Starting from the top-right, there is a button to select the shapefile containing the various top/sub soil polygons. The possible shapefiles should be manually placed in the 'Lithology' folder, which in turn is inside 'Raw Data'. If the 'Lithology' folder is empty, a prompt will appear (similar to the one of Figure IV-5, but just with <Search file> button) to ask the user the location of the desired file/s (click <Search file> button), which once selected, are automatically copied inside 'Lithology' folder. After this, the second button from the top is the field selector, i.e., the button that asks for the field of the shapefile which contains names of the classes for the top or sub soil. Once this field is chosen, it is possible to import soil polygons through the <Run> button. This button triggers the 'C_Soil_ParametersAttribution_Step1.m' main module of X-SLIP. There is the possibility to choose if the file is related to top or sub soil, by clicking one of the two options that are immediately prompted after the <Run> button is pressed, as shown in Figure IV-13. When the <Run> button completes the process, different soil polygons are created, depending on the number of classes contained in the selected field and on how many raw polygons intersect the study area. Moreover, a fast "check" plot containing all the soil classes appears at the end of this process. The output polygon/s of soil is the result of the intersection with the study area polygon. Despite this, in contrast with the switch set to <Uniform>, the operations to perform are not finished. In fact, a file called 'LuDSCAssociation.xlsx' is generated inside the 'User Control' folder and must be completed. This file is a spreadsheet with two structured sheets. The 'Association' sheet contains the

rules for the associations between the just read raw soil classes and some uniform soil classes, defined by the user, as shown in Figure IV-14a. Both the mechanical and hydraulic properties of these uniform soil classes (also called DSC) are described in the 'DSCParameters' sheet, as shown in Figure IV-14b Once this spreadsheet is compiled, it is possible to run the last step of the soil main panel, i.e., the <Association> button, which triggers the 'C_Soil_ParametersAttribution_Step2.m' main module of X-SLIP. A prompt will be also shown, asking for a check of the associations between raw classes (also called Lithology Units, LU) and DSC, but also asking if the user wants to attribute manual colours to each LU or DSC, as shown in Figure IV-15. If the last two options regarding the colours are not flagged, then the colours are read from the 'LuDSCAssociation.xlsx' file, where the last columns of the two possible tabs ('Association' and 'DSCParameters') should be filled, with the desired colours. If these columns are also not flled by the user, then X-SLIP will generate random colours for each possible polygon class. However, with this "association" process, each point is assigned mechanical and hydraulic properties according to the DSC to which it belongs. In other words, the properties of Figure IV-12 are attributed based on DSC polygons, and they are not uniform. If this final step run with no issues, the list of all the LUs and their associated DSCs appears at the bottom of the soil panel, as shown in Figure IV-4e.

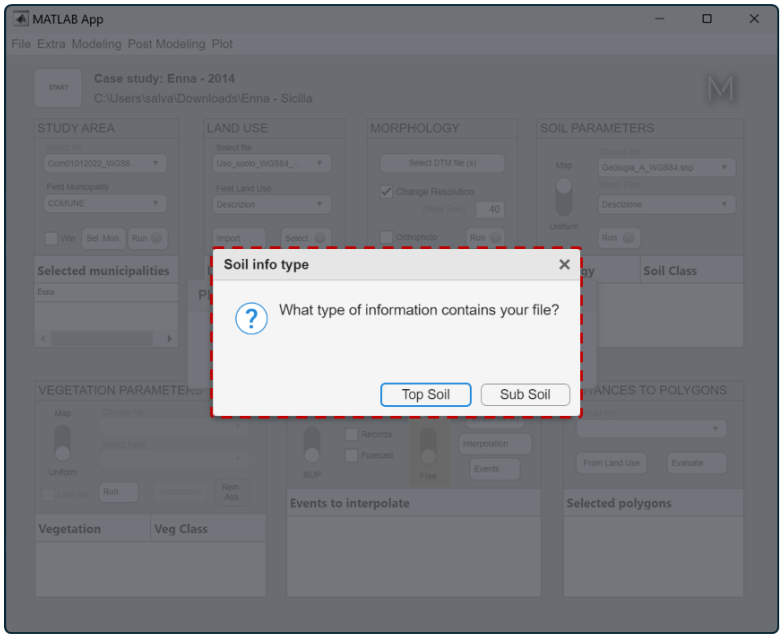

Figure IV-13: The prompt to decide if the file that will be imported by X-SLIP is referred to the top or sub soil, which appears if the switch of the soil main panel is set to <Map> and the <Run> button is pressed. This choice has no impact if the model the user wants to use SLIP. The difference is present when the model that will be used is PIP-AI, because the possible input classes are different. In this case, if it is required that the training PIP-AI contains both, it is necessary to perform twice the soil main panel, once with the top and once with the sub soil.

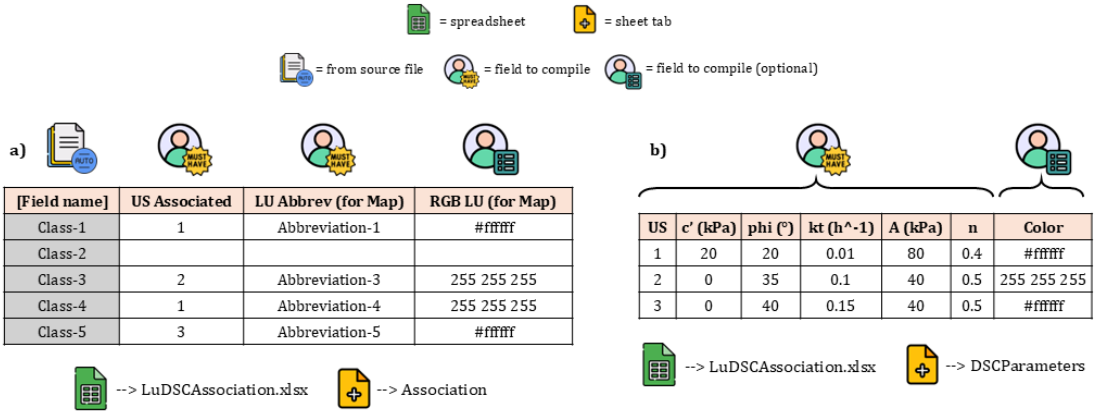

[Field name]	US Associated	LU Abbrev (for Map)	RGB LU (for Map)
Class-1	1	Abbreviation-1	#ffffff
Class-2			
Class-3	2	Abbreviation-3	255 255 255
Class-4	1	Abbreviation-4	255 255 255
Class-5	3	Abbreviation-5	#ffffff

US	c' (kPa)	phi (°)	kt (h^-1)	A (kPa)	n	Color
1	20	20	0.01	80	0.4	#ffffff
2	0	35	0.1	40	0.5	255 255 255
3	0	40	0.15	40	0.5	#ffffff

Figure IV-14: Scheme of the 'LuDSCAssociation.xlsx' spreadsheet, in the 'User Control' folder. The spreadsheet has two sheet tabs, i.e., the 'Association' (a) and 'DSCParameters' (b) tabs. Starting with the 'Association' tab (on the left), the first column is automatically compiled and contains the chosen field (from the soil shapefile) as title and the name of classes below. The second column contains the associations with the uniform soil units (DSC) for all the possible raw classes and must be compiled by the user. If the user wants to exclude a certain class, it is sufficient to leave blank the row. The third column contains the abbreviations of each class, which will be used in the various plots, and must be compiled by the user. The fourth column is optional and contains the colours to use while plotting. This column should be compiled by the user, either as hex code or as RGB set of values. If colours are not specified, random colours are generated by X-SLIP. Finally, the 'DSCParameters' tab contains the mechanical and hydraulic parameters for each uniform soil unit (cohesion c', friction φ', porosity n, and also some modelling parameters of SLIP, which are k_t and A). It is important that all the classes associated in the 'Association' tab are also present in the 'DSCParameters' tab. All the columns of 'DSCParameters' must be compiled by the user, except for the last one (Colour), which is optional.

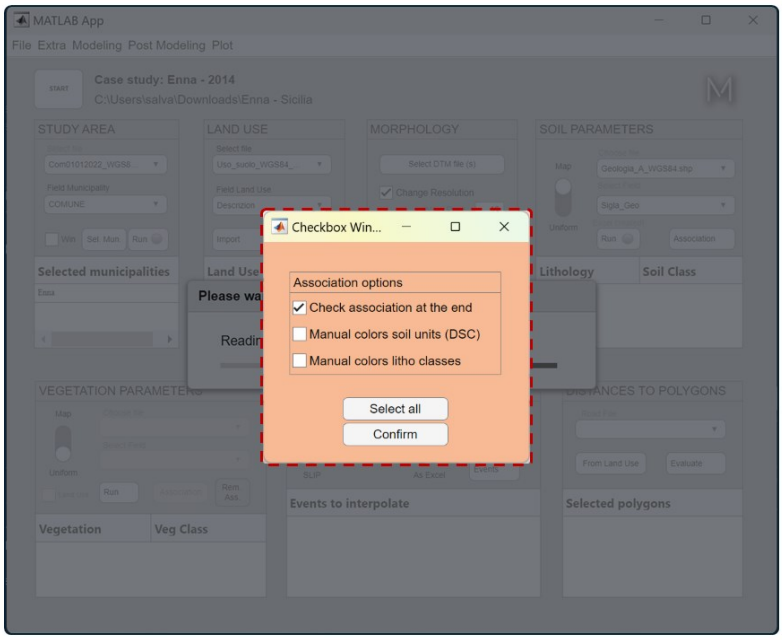

Figure IV-15: The prompt of the options for the association between lithology units (LU) and the uniform soil classes (DSC). If the <Check association at the end> is flagged, then the maps of the soil values will be check at the end, to ensure that there is correspondence between excel and the various soil grids. This process could be slow, depending on the resolution and extension of the Digital Elevation Models used. Concerning the <Manual colours soil units (DSC)> and <Manual colours litho classes> checkboxes, if these are flagged, X-SLIP will prompt a colour palette for

each polygon class and asks the user to pick a colour for each one. If these are not flagged, colours are read from the spreadsheet 'LuDSCAssociation.xlsx' or attributed randomly (if columns of colours are empty).

4.1.5 VEGETATION PANEL

The vegetation panel, in Figure IV-4f, is basically the same as the soil panel described in Section 4.1.4, with just a few minor differences (e.g., shapefiles should be put in 'Vegetation').

As seen for the soil, also in this case there is the possibility to set the switch to <Uniform> or <Map> mode. With the first option (<Uniform>), the mechanical and hydraulic parameters related to the vegetation can be specified manually (as shown in Figure IV-16) and they will be uniform over the entire study area, with the same procedure seen in Section 4.1.4.

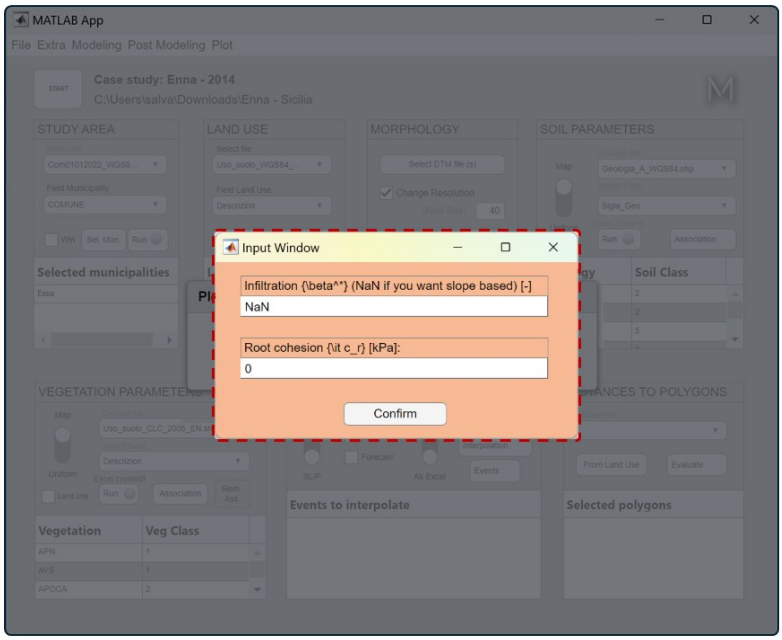

Figure IV-16: The prompt for the attribution of the uniform vegetation properties over the entire study area, which appears when the switch of the vegetation main panel is set to <Uniform> and the <Run> button is clicked. It is possible to specify the root cohesion (c_r) and infiltration coefficient (β^*).

With the second option (<Map>), the procedure to follow is the same of Section 4.1.4. The difference is that now, instead of LUs, some Vegetation Units (VU) are read from the source shapefile (these are essentially the raw polygon classes contained in the shapefile, as seen for the LUs) and they are associated with some uniform vegetation classes (also called DVC, which are the equivalent of DSC but for vegetation). As seen in Section 4.1.4, also in this case the user controls the association, by means of the spreadsheet 'VuDVCAssociation.xlsx' (see Figure IV-17), which is equivalent of the 'LuDSCAssociation.xlsx' and it is also located in the 'User Control' subfolder. This file must be compiled before running the <Association> button. Then, when the <Association> button is clicked, a prompt appears for the last options to choose, as shown in Figure IV-18. As can be observed, this prompt has the same functions of the prompt seen in Figure IV-15 for the soil panel.

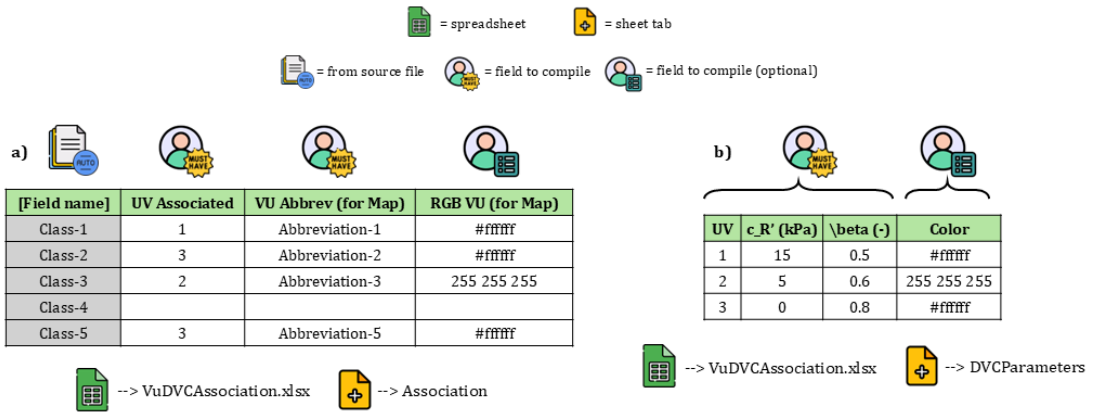

[Field name]	UV Associated	VU Abbrev (for Map)	RGB VU (for Map)
Class-1	1	Abbreviation-1	#ffffff
Class-2	3	Abbreviation-2	#ffffff
Class-3	2	Abbreviation-3	255 255 255
Class-4			
Class-5	3	Abbreviation-5	#ffffff

UV	c_R' (kPa)	\beta (-)	Color
1	15	0.5	#ffffff
2	5	0.6	255 255 255
3	0	0.8	#ffffff

Figure IV-17: Scheme of the 'VuDVCAssociation.xlsx' spreadsheet, in the 'User Control' folder. The spreadsheet has two sheet tabs, i.e., the 'Association' (a) and 'DVCParameters' (b) tabs. Starting with the 'Association' tab (on the left), the first column is automatically compiled and contains the chosen field (from the soil shapefile) as title and the name of classes below. The second column contains the associations with the uniform vegetation units (DVC) for all the possible raw classes and must be compiled by the user. If the user wants to exclude a certain class, it is sufficient to leave blank the row. The third column contains the abbreviations of each class, which will be used in the various plots, and must be compiled by the user. The fourth column is optional and contains the colours to use while plotting. This column should be compiled by the user, either as hex code or as RGB set of values. If colours are not specified, random colours are generated by X-SLIP. Finally, the 'DVCParameters' tab contains the mechanical and hydraulic parameters (root cohesion c_r and infiltration coefficient β^*) for each uniform vegetation unit. It is important that all the classes associated in the 'Association' tab are also present in the 'DVCParameters' tab. All the columns of 'DVCParameters' must be compiled by the user, except for the last one (Colour), which is optional.

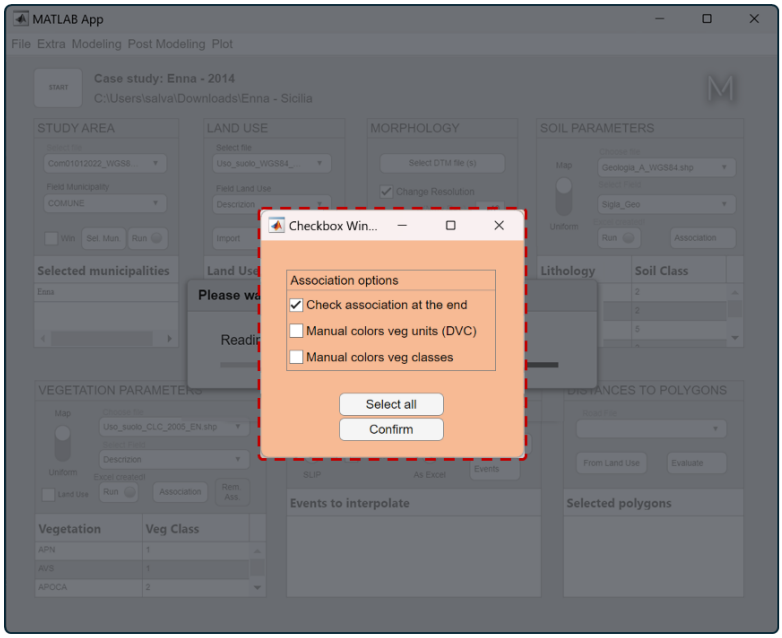

Figure IV-18: The prompt of the options for the association between vegetation units (VU) and the uniform soil classes (DVC). If the <Check association at the end> is flagged, then the maps of the vegetation values will be check at the end, to ensure that there is correspondence between excel and the various vegetation grids. This process could be slow, depending on the resolution and extension of the Digital Elevation Models used. Concerning the <Manual colours veg units (DVC)> and <Manual colours veg classes> checkboxes, if these are flagged, X-SLIP will prompt a colour palette for each polygon class and asks the user to pick a colour for each one. If these are not

flagged, colours are read from the spreadsheet 'VuDVCAssociation.xlsx' or attributed randomly (if columns of colours are empty).

Concerning the other differences between the vegetation panel and the soil panel of Section 4.1.4, two additional options are present in the vegetation panel: the <Land Use> checkbox and the <Rem. Ass.> button.

The <Land Use> can be used when the switch is set to <Map>. It means that instead of specifying a new shapefile which contains vegetation data, the user wants to use the same shapefile used for the land use, because sometimes info about vegetation is also included in the land use map. Thus, in case no vegetation shapefile is available, but land use shapefile contains also vegetation, it is suggested to flag the <Land Use> checkbox.

The <Rem. Ass.> button can be used to completely remove the vegetation contribution from the analysis (in case it was previously associated, either with <Uniform> or <Map> mode). Basically, with this button it is possible to remove the β^* and c_r parameters from the analysis, because β^* will depend again on only slope and c_r will be reset (null value), restoring the situation to its state prior to the use of the vegetation panel.

To conclude, it is important to note that with the <Run> button, the main modules of X-SLIP which can be triggered are:

- 'C_Vegetation_ParameterAttribution_Step0.m'
- 'C_Vegetation_ParameterAttribution_Step1.m'
- 'C_Vegetation_ParameterAttribution_Step1_LU.m'

respectively if the switch is set to <Uniform>, <Map> with <Land use> checkbox not flagged, or <Map> with <Land Use> checkbox flagged. Instead, the <Association> button triggers the 'C_Vegetation_ParameterAttribution_Step2.m' main module of X-SLIP.

4.1.6 Time Sensitive (Rainfall/Temperature) Panel

The time sensitive panel of Figure IV-4g can read, import, and interpolate over the study area both rainfall and temperature data, or any other data that it is time sensitive. This panel can be run completely more than one time, if there is multiple data to read, such as rainfall and temperature simultaneously. Data can be read as scattered, i.e., from gauges, or from satellite, namely raster files. However, independently from the read data, rainfall is required to be the first one. Consequently, the start and end datetimes that rule the analysis are dictated by rainfall, which means that for instance, temperatures will have the same time intervals and datetimes of rainfall data.

The use of the time sensitive panel starts with the first switch on the top-left, which can be set to <Other> or <SLIP>. In case the switch is set on <Other>, the data records that will be used are just the selected ones (with the <Select file (s)> button, explained below) and the imported (and interpolated) data can be applied for different types of models (as LEP-AI and

PIP-AI). If the switch is set on <SLIP>, the data records that will be used are more than the one selected. In fact, with SLIP model it is necessary to use also the 30 days before the beginning of the possible landslide day (that is the analysis day). Thus, in case of multiple datetimes selected for the analysis, with the <SLIP> mode the records that will be used starts from 30 days before the first datetime selected and ends with the last datetime selected. If some datetimes between the start and the end are not selected, with <SLIP> mode these unselected datetimes will be anyway included (due to the SLIP functioning).

The options that should be used after the first switch are the <Records> and <Forecast> checkboxes. Both these options can be flagged simultaneously. If the <Records> checkbox is flagged, then X-SLIP will read past actual data inside 'Rainfalls' or 'Temperature' subfolders (which in turn are inside 'Raw Data'). If the <Forecast> checkbox is flagged, then X-SLIP will read forecast data inside 'Rain Forecast' or 'Temp Forecast' subfolders (which in turn are inside 'Raw Data'). At least one of these two options must be selected. If both are flagged, then the analysis can be performed with a mix between actual (past) and forecast data.

After this, another option that can be used is the second switch on the right, which can be set to <Daily> or <Free>. If the switch is set to <Daily>, the source data will be read and condensed into days, which means that if the raw interval is less than a day (for instance hours), this data will be grouped to obtain a new time interval of 1 day. If the switch is set to <Free>, the source data is read with its raw time discretization and datetimes, but it can also be modified based on the user preferences (right after the <Select file(s)> button is clicked, as will be shown below).

The next step consists of running the three remaining buttons: <Select file (s)>, which is necessary; <Interpolation>, which is necessary and must be run after <Select file (s)>; <Events>, which is optional and can be run after <Select file (s)>. In the following lines, it is illustrated an example obtained with the first switch set to <SLIP>, the <Records> checkbox flagged, and the second switch set to <Free>. Irrespective of this, all the other possible combinations of switchers and checkboxes would prompt the same options.

The <Select file (s)> button triggers the 'D_TimeSensitive_Step1_DataReading.m' main module of X-SLIP. During this process, the source files contained in 'Rainfalls', 'Rain Forecast', 'Temperature', or 'Temp Forecast' (which in turn are inside 'Raw Data') are read, and different options can be specified. If no file is detected inside the required folder, a prompt like the one of Figure IV-5 appears (but just with the <Search> button), asking for the location of the spreadsheets or raster files to use, which are then automatically copied. In case of scattered data from gauges, it is necessary to use spreadsheets files that are structured with the scheme of Figure IV-19. Briefly, these spreadsheets must contain two tabs, i.e., 'Data table' and 'Stations table', containing respectively the raw data recorder from gauges (with the start and end datetimes of the record), and the location of these gauges (geographic coordinates, which is latitude and longitude of each gauge used in the 'Data table').

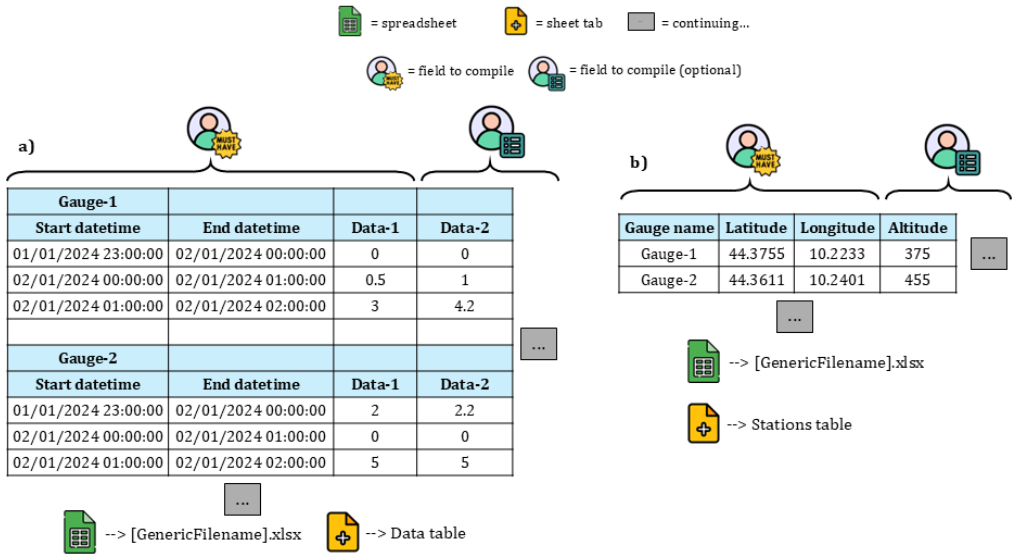

Gauge-1			
Start datetime	End datetime	Data-1	Data-2
01/01/2024 23:00:00	02/01/2024 00:00:00	0	0
02/01/2024 00:00:00	02/01/2024 01:00:00	0.5	1
02/01/2024 01:00:00	02/01/2024 02:00:00	3	4.2
Gauge-2			
Start datetime	End datetime	Data-1	Data-2
01/01/2024 23:00:00	02/01/2024 00:00:00	2	2.2
02/01/2024 00:00:00	02/01/2024 01:00:00	0	0
02/01/2024 01:00:00	02/01/2024 02:00:00	5	5

Gauge name	Latitude	Longitude	Altitude
Gauge-1	44.3755	10.2233	375
Gauge-2	44.3611	10.2401	455

Figure IV-19: Scheme of the structure for the time sensitive spreadsheets, i.e., for rainfall or temperatures scattered data recorder by gauges. The spreadsheet can be name with a generic name but must contains two sheet tabs. The first one is the 'Data table' (a), which have the raw data of the gauges in the various columns. It is necessary to have the first two columns with the start and end datetimes respectively, and at least one numerical column containing recorded data. Other numerical columns can be added, and they will be read by X-SLIP. The second tab is the 'Stations table' (b), which contains some necessary info about the gauges of the 'Data table', namely the same gauge names used in the 'Data table' and their coordinates (latitude and longitude). Other columns can be also added but they will not be read by X-SLIP (just additional info for the user).

Multiple files (both spreadsheet and raster) can be placed inside the above-mentioned folders, with generic names upon the user choice. Regardless, the first option to select is the type of data, that currently can be set only on rainfall or temperature, as shown in Figure IV-20. Subsequently, various "matching" options, related to the source file to use, can be prompted (especially if the source file is a spreadsheet), as shown in Figure IV-21. Specifically, the first prompt asks for the source filename (Figure IV-21a). In case the file is a spreadsheet, also other two prompts will appear: the first will ask to specify which is the tab containing data and the one containing the gauge stations info (Figure IV-21b); the second will ask to match the fundamental columns of the "Stations table" tab with their info (name of the gauge, latitude, longitude) (Figure IV-21c). Since in this instance the data is scattered, it is possible also to use additional functions ("adjusting" prompts of Figure IV-22a): a filter on the gauges of the spreadsheet, which allows to select stations to maintain (in a further prompt shown in Figure IV-22c), and also the auto-fill feature, which fills the missing data during the timeseries (sometimes gauges can have problems, or just updates, due to which they do not record data). Particularly, the auto-fill feature can work with 5 different modes (Figure IV-22b), which are respectively (i) <OtherSta>, if there are multiple gauges and the user wants to replace missing values of a gauge with the average values of the gauges that instead are filled with data; (ii) <Zeros>, if the user wants to replace missing values with null values; (iii) <AverageYr>, if the user wants to replace the missing values with the average values of that

same gauge but recorded in other years (particularly useful with temperature); (iv) <AverageLNE>, if the user wants to fill each gap with the value obtained from the average between the last not missing value and the next one (again, particularly useful with temperature); (v) <NaN>, if the user wants to replace missing values with Not a Number values. After selecting these options, since in this example the second switch was set to <Free>, other three "aggregating" prompts will appear. With the first "aggregating" prompt (Figure IV-23a) it is possible to adjust the delta time between the records, writing the number of hours desired (the default number is the delta time read from the spreadsheet). The second "aggregating" prompt appears if the delta time selected by the user is greater than the default one, asking for each column containing numerical values, what is the aggregation mode desired (Figure IV-23b). In fact, the new delta time will create less timestamps (records) and for each one of these it is necessary to decide what to do with the multiple values contained. It is possible to select for each numerical column of the 'Data table' an option among <sum>, <avg>, <min>, or <max>, to respectively sum, take the average, take the minimum, or take the maximum of these values (Figure IV-23c). With the third "aggregating" prompt it is possible to specify a name for each numerical column of the 'Data table' tab (Figure IV-23d) (e.g., cumulative rainfall etc.). Finally, the last prompt that appears during the processing of the <Select file (s)> button is a list of the possible events (timestamps) to analyse with the various models, as shown in Figure IV-24. If the process run with no issues, the list of the selected datetimes will appear at the bottom of the time sensitive panel, as shown in Figure IV-4g.

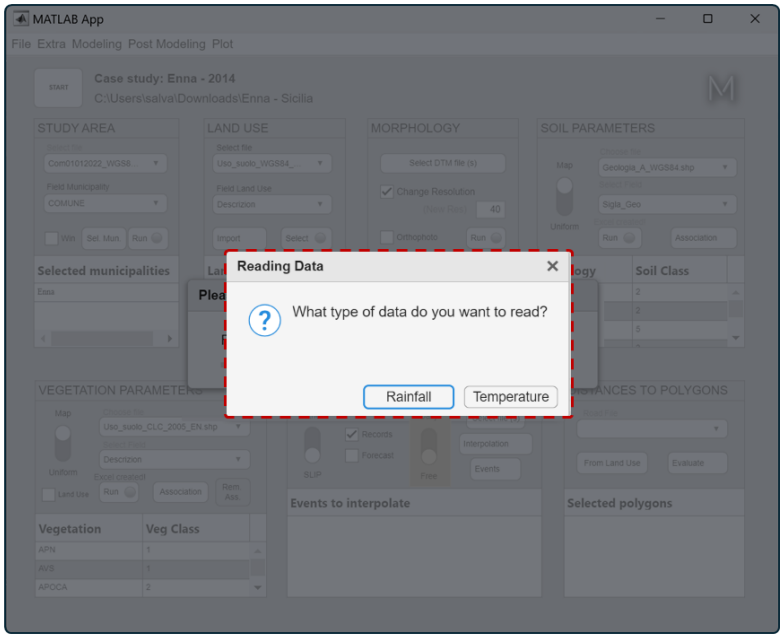

Figure IV-20: The prompt to decide if the file that will be imported by X-SLIP is referred to the rainfall or temperature. In case the <Select file (s)> button is clicked for the first time, it is necessary to import first rainfall, because rainfall rules all the possible time sensitive features (e.g., rainfall recording datetimes dictates also the time discretization of temperature).

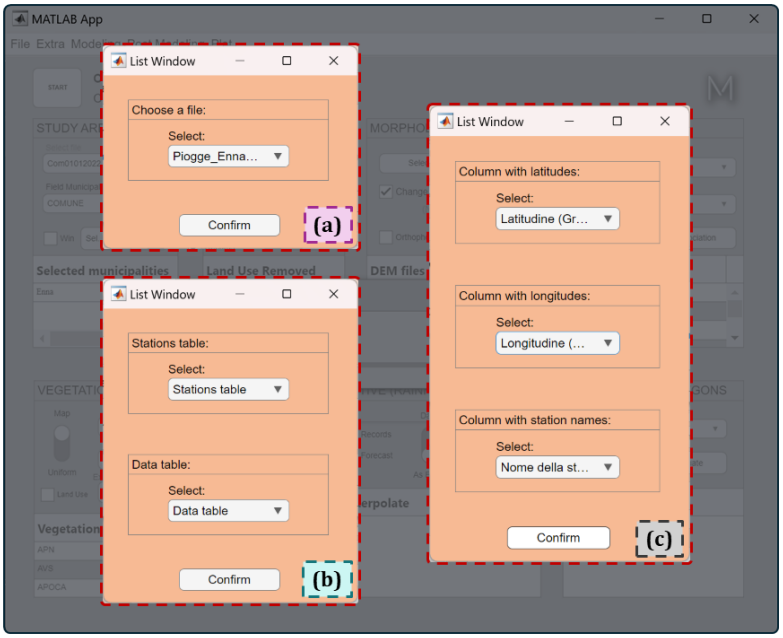

Figure IV-21: The "matching" prompts for the time sensitive panel, which appear after pressing the <Select file (s)> button. It is possible to select the file to use (a). If the file is a spreadsheet, it is necessary to specify the match between the various tabs of the file and the 'Data table' and 'Station table' ones (b). Similarly, if the file is a spreadsheet, it is also necessary to match the three main columns of the 'Station table', containing the names of the gauges and their geographic coordinates (c).

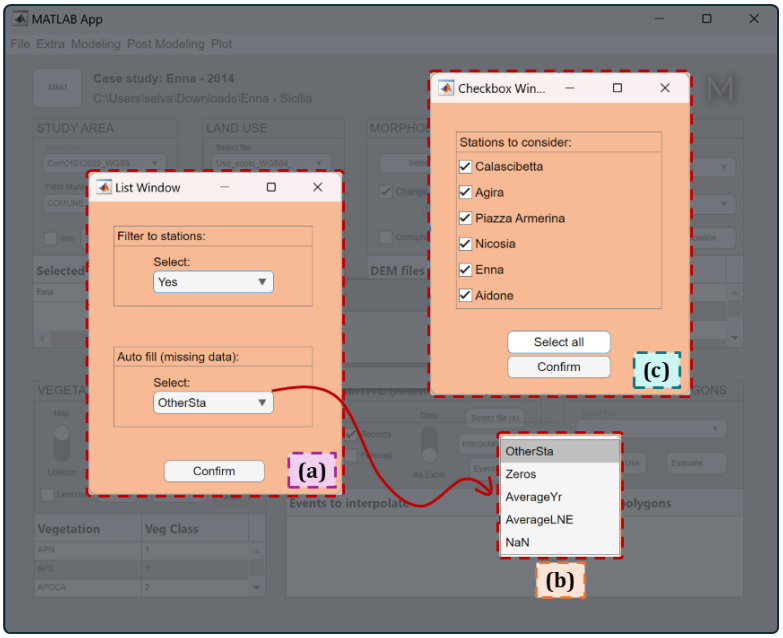

Figure IV-22: The "adjusting" prompts for the time sensitive panel, which appear after pressing the <Select file (s)> button. If the selected file is a spreadsheet, it is possible to filter the gauges to use for the interpolation of data (a) and it is also possible to fill the possible gaps (missing values) between records, through different techniques (b). If the filter is set on <Yes>, then a further prompt will asks for the stations to maintain (c).

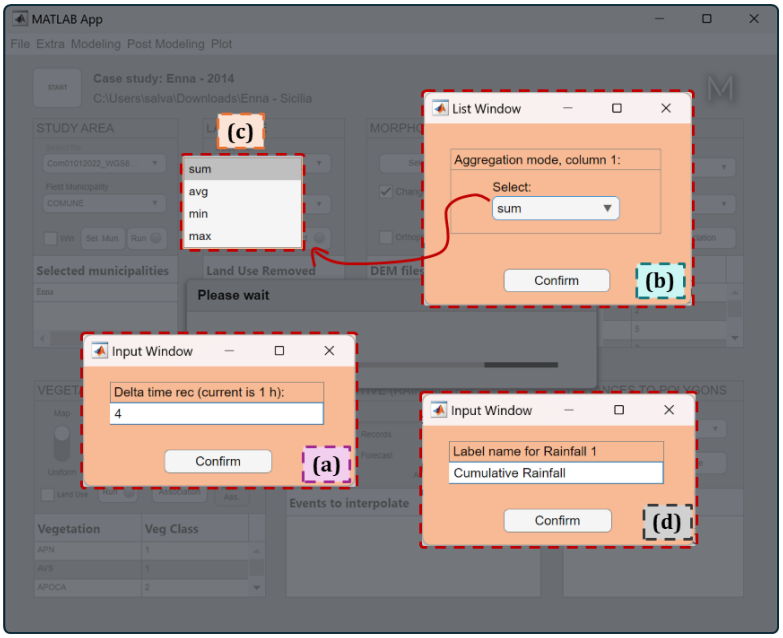

Figure IV-23: The "aggregating" prompts for the time sensitive panel, which appear after pressing the <Select file (s)> button. It is possible to specify a different delta time between records (a). This field is automatically filled with the time delta read from the source file. If the time delta specified is greater than the default one, it is necessary to specify how to aggregate the existing values (c). Finally, for each numerical column contained in the 'Data table' it is possible to specify a specific name, different from the suggested one (d).

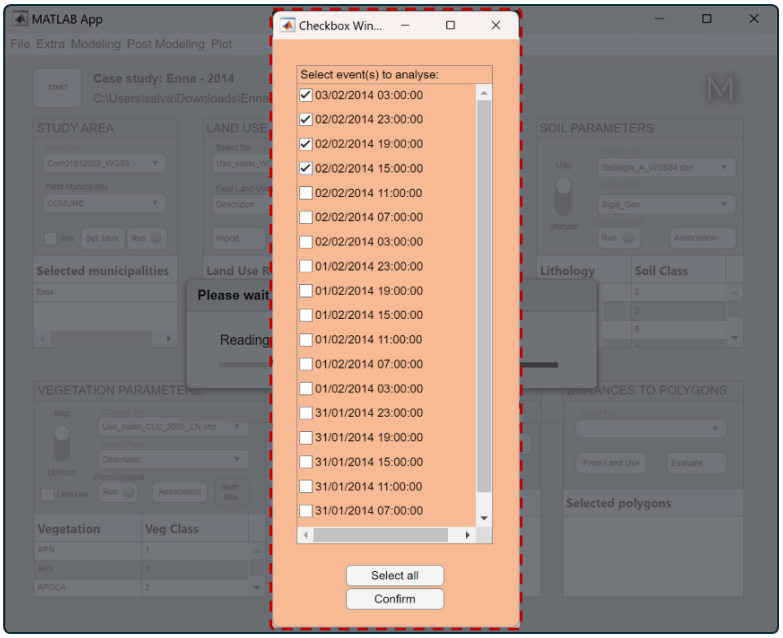

Figure IV-24: The prompt to decide the datetimes of the analyses, at the end of the process of the <Select file (s)> button. Multiple, nonadjacent datetimes can be selected. After this selection, the list of the selected datetimes is reported at the bottom of the time sensitive panel.

The <Interpolation> button triggers the 'D_TimeSensitive_Step2_InterpolationDaily.m' main module of X-SLIP if the second switch is set on <Daily>, otherwise it triggers the main module 'D_TimeSensitive_Step2_Interpolation.m'. Independently from the module triggered, there is no action to perform by the user, which will see a progress bar indicating the progress of the interpolation. If the imported DEM files from the morphology panel were in high-resolution and the study area was large, this process could require several minutes, and the resulting file, to store in the 'Variables' subfolder, may be very large in terms of disk space, especially when the delta time of the time sensitive sources is in hours or even minutes. This is because each timestamp needed for the analyses is stored in a separate raster map. Moreover, if the source file was already a raster, the interpolation will pick the nearest value for each pixel of the new output maps, dictated by the morphology panel.

The <Events> button triggers the 'D_TimeSensitive_Step2_Events.m' main module of X-SLIP. During this process, the rainfall patterns, imported with the <Select file (s)> button are analysed and the REs seen in Chapter III (Section 3.2.2) are generated. Basically, this process stores the indices of the datetimes (thus, the indices of the rainfall maps) to pick and use (after aggregating data) for the generation of the various triggering and cause time windows of each RE occurred. This button can be used also if the selection of the datetimes (at the end of the <Select file (s)> process) is not continuous, because that selection impact just the interpolation datetimes. Despite this, if the user wants to use the PIP-AI model, it is also necessary to select continuous datetimes, otherwise the aggregation of data in the various pixels would fail.

4.1.7 Distances Panel

The distances panel, in Figure IV-4h, can be used multiple times to create various maps containing for each pixel the minimum distance from the nearest infrastructure. The resolution, in analogy to rainfall and temperature maps, has the same resolution of the morphology maps, processed with the morphology panel.

It is possible to use a specific shapefile, containing some infrastructure polygons, or some of the classes imported in the land use panel. In the first case, it is necessary to select from the <Select file> dropdown button on the top the desired shapefile. The possible shapefiles should be placed inside the 'Roads' subfolder (which in turn is inside 'Raw Data'). If no file is inside that subfolder, a prompt like the one shown in Figure IV-5 appears (but with just the <Search> button), asking for the location of this file, which is then automatically copied inside the 'Roads' subfolder. Instead, if the user wants to use some classes of the land use map, it is necessary to the <From Land Use> button, which will prompt a multiple checkbox list, similar to the one of Figure IV-9, asking for the land use to maintain as infrastructures from which the distances must be assessed. After the selection of the land uses, a list of the selected ones appears at the bottom of the distances panel, and the <Select

file> dropdown will be set to 'None', which means that no shapefile is used, but instead the land use in its place.

After the decision about infrastructures shapefile or land uses, it is possible to continue with the <Evaluate> button. When this button is clicked, the 'C_Distances.m' main module of X-SLIP is triggered. During this process, some options can be selected. For instance, if an infrastructures shapefile is selected, a prompt will ask for the field containing the names of the polygon classes, as shown in Figure IV-25.

Subsequently, another prompt will ask for the polygon classes mode and the type of interpolation to use, as reported in Figure IV-26. This prompt appears independently from the type of source used in the distances panel (both in case of land use or infrastructures shapefile). The polygon classes mode can be <Separated> or <Merged>. With the <Separated> mode, each polygon classes will generate a respective distances map. In other words, if three classes of polygons are present, then three distances maps are generated, with each pixel containing the minimum distance from the respective class of polygons (classes can be conceptualized as different types of infrastructures). With the <Merged> mode, the various polygon classes are merged into a unique one (therefore the various polygons are merged) and the resulting distances map is just one. Concerning the type of interpolation, it should be noted that the 'C_Distances.m' module creates a new single grid (sometimes with a coarser resolution to reduce processing time) as reference to assess distances. Then, once distances are processed, it performs an interpolation with the output maps, which have resolution and coordinates based on the morphology panel. The possible options to perform this interpolation are <nearest>, <linear>, and <natural>, which were already discussed in Section 3.3.2 of Chapter III. Anyway, <nearest> is the fastest and it is suggested if the resolutions are detailed down to 10x10 meters per pixel.

Finally, one last prompt (which again appears both in case of land uses or infrastructures shapefile) will ask for the names of the infrastructures used, as shown in Figure IV-27. This feature could be useful in case the classes were merged, because it would be necessary to define a new name for the merged polygons. In case the classes were maintained as separated, then the default names are the classes read from the infrastructure's shapefile, or the land use selected, but they can be also changed.

As previously stated, the distances panel can be run multiple times. After the first time, there is the possibility to add maps to the existing ones or to replace them (with the prompt in Figure IV-28). This feature could be particularly useful in case there are multiple shapefiles to use, containing different infrastructures from which distances should be assessed.

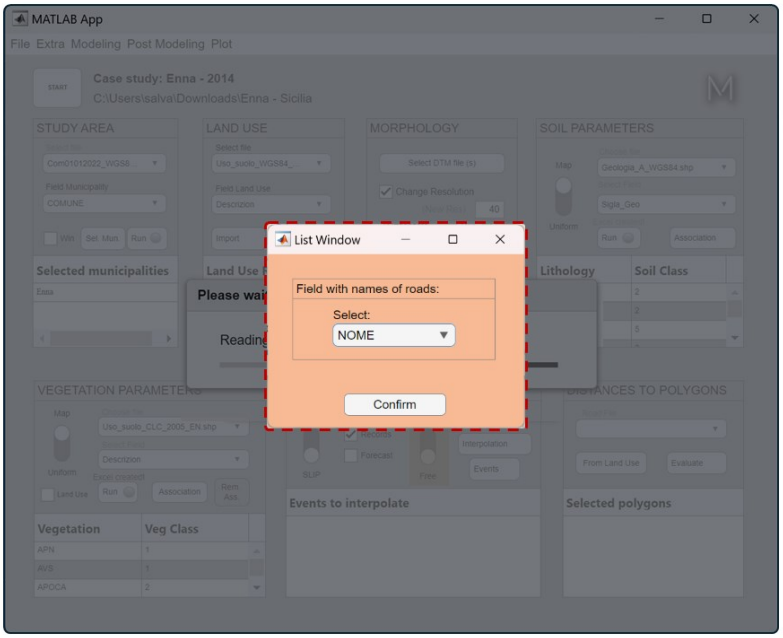

Figure IV-25: The prompt to select the field of the shapefile containing the names of polygon classes. This prompt appears after the <Evaluate> button of the distances panel is clicked, but just in case the source file selected is an infrastructure shapefile and not land uses.

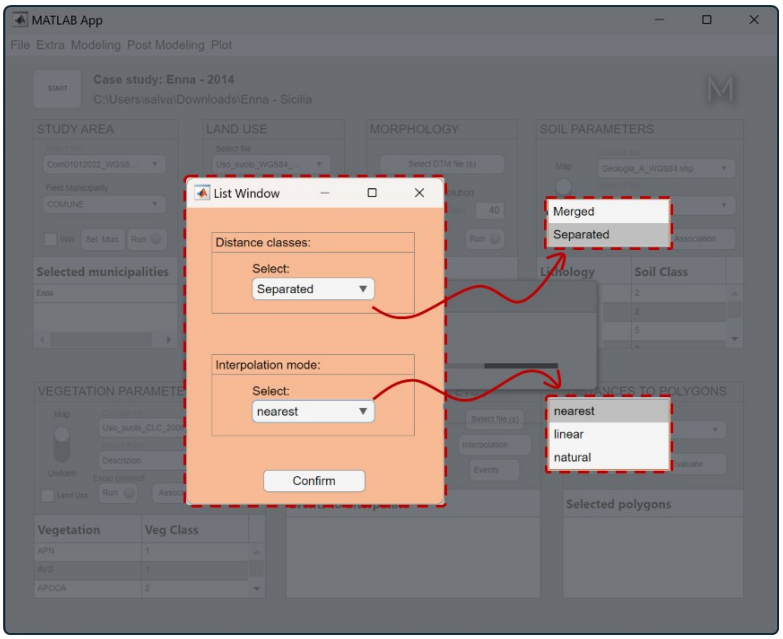

Figure IV-26: The prompt to select how to manage the various polygon classes, which can be merged or maintained separated, and the interpolation mode to use during the creation of the final output maps. This prompt is shown during the processing of the <Evaluate> button of the distances panel.

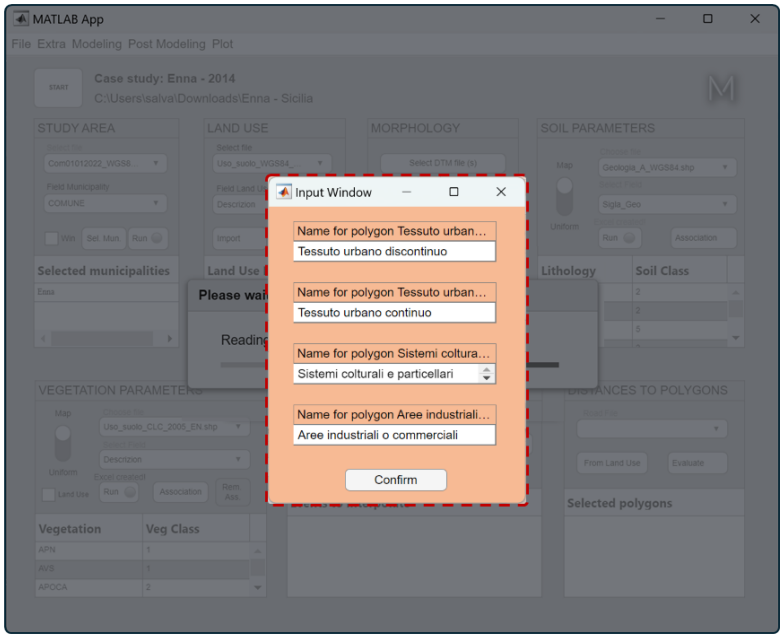

Figure IV-27: The prompt to change the names of the infrastructure polygons, read during the creation of the distance maps. Each class name of the polygons used can be changed and stored as title of the map created. In this example, four different maps were generated, and the default names are the same read from the land use.

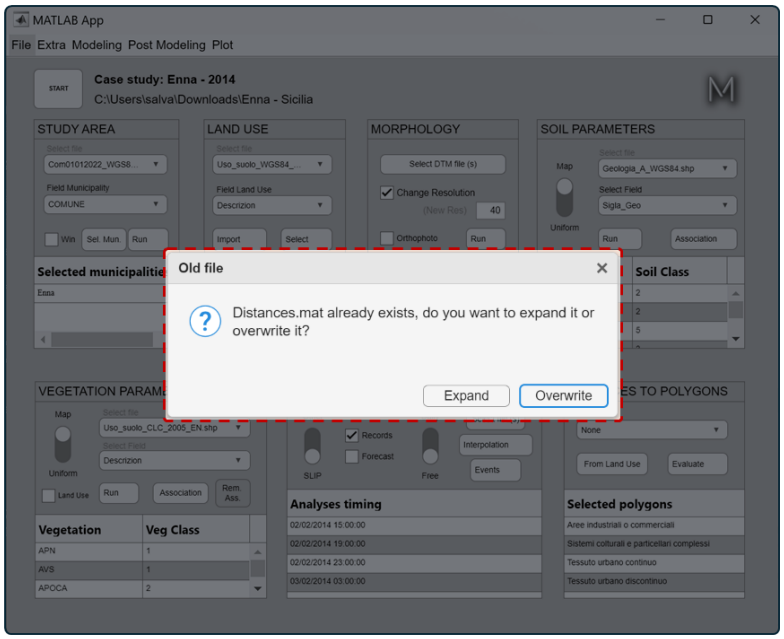

Figure IV-28: The prompt that allows to expand or overwrite the already existing distances maps. This prompt appears in case the <Evaluate> button of the distances panel is clicked after some distances maps were already generated in a previous session.

4.2 EXTRA FUNCTIONALITIES MENU OF X-SLIP

The top menu "Extra" of X-SLIP contains different sections, integrating several functionalities that may be necessary or not, depending on the type of analysis that the user intends to perform. A general overview of these functionalities is shown in Figure IV-29.

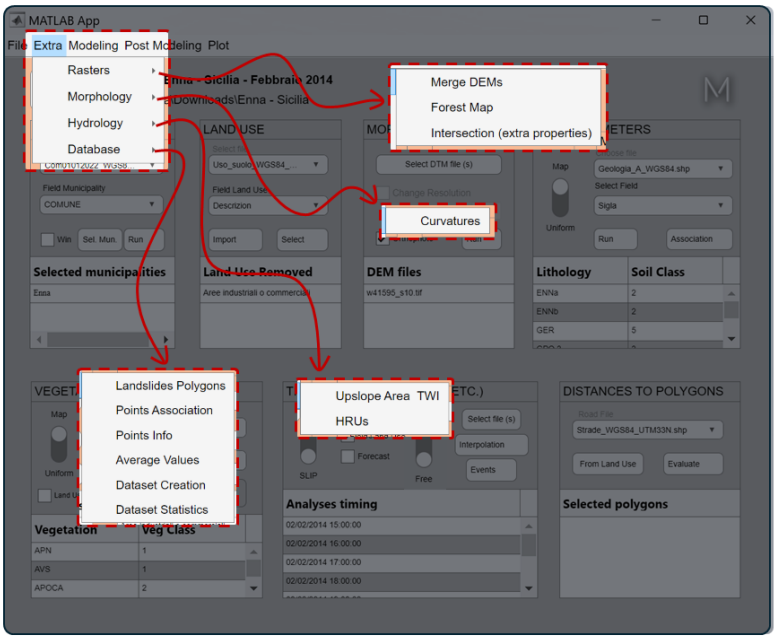

Figure IV-29: Scheme of the possible functionalities of the "Extra" top-menu in X-SLIP. The functionalities are grouped into four macro-categories, each one with its buttons. Each button triggers a main module (or function) of the X-SLIP platform.

As it can be seen, the "Extra" top menu is organized into four macro-groups. The "Rasters" macro-group contains functionalities related to the raster files, such as the merge of the imported DEMs, the creation of a forest raster map, etc. The "Morphology" macro-group contains functionalities related to some extra properties of the morphology, such as the curvatures. The "Hydrology" macro-group contains functionalities related to some extra hydraulic properties, such as the assessment of the TWI and HRU for each pixel of the study area (see Appendices section for more info). Finally, the "Database" macro-group contains some important functionalities related to the inventoried landslides and the creation of datasets that can be used with ML models, such as LEP-AI and PIP-AI.

In the following sections, only some of the main features will be explained in detail.

4.2.1 RASTERS FUNCTIONALITIES (MENU EXTRA)

The "Rasters" macro-group is dedicated to operations that can be performed on raster sources, containing three possible buttons to use.

The <Merge DEMs> button serves to merge the eventually multiple raster source files (imported through the morphology panel, as described in Section 4.1.3). Specifically, the

separate raster files containing the elevation of each pixel may undergo resolution changes when imported, but anyway they will remain as separate grids and be treated as such throughout the analysis. If, for any reason, it is necessary to work with a single, unified grid, the <Merge DEMs> button can be used, but only after importing the separated files via the morphology panel. In fact, the <Merge DEMs> button triggers the 'merge_dems.m' function of X-SLIP, which combines all existing grids into one and saves the resulting merged grid in a new file. Specifically, the newly created merged DEM will be saved in geographic coordinates under the name 'Merged-DTM-[GridSize]-Geographic.tif' within the 'DTM' subfolder, which in turn is inside 'Raw Data'. Once this file is generated, the morphology panel can be re-run in its entirety (as described in Section 4.1.3), allowing the user to select the newly created file as the base grid for subsequent analyses.

The <Forest Map> button, whose functionality will not be discussed in detail due to space constraints (the reader is referred to the source code in the Appendices section), serves to create a forest raster file, containing two values: 0 or 1. If one pixel of the output map has a 0 value, then there is no forest inside that pixel, otherwise the pixel is inside a forest area. During this process, a prompt will ask for the files containing vegetation information, thus the output file is stored inside the same folder of the source files used. The <Forest Map> button triggers the <forested_areas.m> function of X-SLIP.

The <Intersection (extra properties)> button, whose functionality will not be discussed in detail due to space constraints (the reader is referred to the source code in the Appendices section), serves to create new raster maps containing some extra properties of the pixels, such as the clay and sand content, or the NDVI, and others. These maps are structured as the morphology ones (generated with the morphology panel in Section 4.1.3), thus they have same coordinates and pixel resolution. In case the model to use is PIP-AI, this functionality may be necessary, when the user wants to include NDVI but also clay and sand contents as features of the pixels. The <Intersection (extra properties)> button triggers the main module of X-SLIP called <C_SoilGridsProperties.m>.

4.2.2 Morphology Functionalities (Menu Extra)

The "Morphology" macro-group is dedicated to operations that are related to information regarding the morphology of the study area, containing just one possible button at the moment, i.e., the <Curvatures> button.

With this button, the main module of X-SLIP called 'C_Curvatures.m' is triggered, adding some grids to the ones already generated with the morphology panel of Section 4.1.3. In fact, it is possible to add three new grids containing respectively for each pixel the following information: main, profile, and planform curvatures. These grids are appended to the file containing the pre-existing morphology variables, that is 'MorphologyParameters.mat',

inside the 'Variables' subfolder. In case the model to use is LEP-AI or PIP-AI, this functionality may be necessary, when the user wants to include curvatures as features of the AUs or pixels.

4.2.3 Hydrology Functionalities (Menu Extra)

The "Hydrology" macro-group is dedicated to operations that are related to information regarding the hydrology of the study area, containing two possible buttons.

The <Upslope Area TWI> button, whose functionality will not be discussed in detail due to space constraints (the reader is referred to the source code in the Appendices section), serves to create two new raster maps, triggering the main module of X-SLIP called 'C_FlowRouting.m'. The first generated map contains for each pixel a value representing the "contributing area" (see Appendices section), which basically means that each pixel has an area above it that would channel water, directing it toward the pixel in question. This process depends on slopes and considerations regarding ridges and valleys. Pixels corresponding to watercourses undoubtedly have high contributing area values, because these points collect water from higher elevations, resulting in a large area "contributing" to the pixel. The second generated map contains for each pixel the Topographic Wetness Index (TWI, see Appendices section), which basically represents how much a pixel could be "wet".

Instead, the <HRUs> button, whose functionality will not be discussed in detail due to space constraints (the reader is referred to the source code in the Appendices section), serves to create the Hydrologic Response Units (HRU, see Appendices section), triggering the main module of X-SLIP called 'D_HRUs.m'. In other words, this process will generate a new map containing for each pixel a unit that should represent common physical characteristics, where it is expected to respond to precipitation and weather events in a similar way.

In both cases, with the two buttons, the generated maps are stored in two different files inside the 'Variables' subfolder and, as happens for all the maps, they are ruled by the morphology grids, namely they have same coordinates and resolutions.

4.2.4 Database Functionalities (Menu Extra)

The "Database" macro-group is dedicated to operations aimed at creating a dataset usable with LEP-AI and PIP-AI, or alternatively just to obtain information about the factors that may have triggered landslides. This macro-group contains six possible buttons, with some of them that must be run sequentially to work.

4.2.4.1 Landslides Polygons button

The first button is <Landslides Polygons>, which triggers the main module of X-SLIP called 'B_DetectedSoilSlipsPolygons.m'. The functionality will not be discussed in detail due to space constraints (the reader is referred to the source code in the Appendices section). However, this button serves to import the geometry of the landslides that occurred in the

past, from shapefiles that must be placed into the 'Detected Soil Slips' subfolder (which in turn is inside 'Raw Data'). Some prompts will ask for the files to import and the fields containing the ID of these landslides, which may be used subsequently. The resulting polygons are then stored in a specific file inside 'Variables'. Anyway, this button is optional, since oftentimes there is no available shapefile with landslides polygons.

4.2.4.2 Points Association button

The <Points Association> button, which triggers the 'C_InfoDetectedSoilSlips.m' main module of X-SLIP, is the first crucial step to create datasets. Its functioning is to import the landslide inventories, which must be stored as spreadsheet files in the 'Detected Soil Slips' subfolder. The structure of these spreadsheets can be of two types: (i) if some landslide polygons were imported with the <Landslide Polygons> button, then each row of the spreadsheet must contain at least the municipality of the occurrence (first column) and one of the IDs imported from the landslide shapefiles (second column), with the same structure shown in Figure IV-30a; if landslide polygons were not imported, then each row of the spreadsheet must contain at least 4 columns, i.e., the name of the municipality, the name of the specific location (e.g., Highway A1), and the latitude and longitude of the triggering point (upper scar or centroid), with the same structure reported in Figure IV-30b. In both cases, it is possible to add other optional columns, such as the datetime of the landslide occurrences or the area of the landslide body.

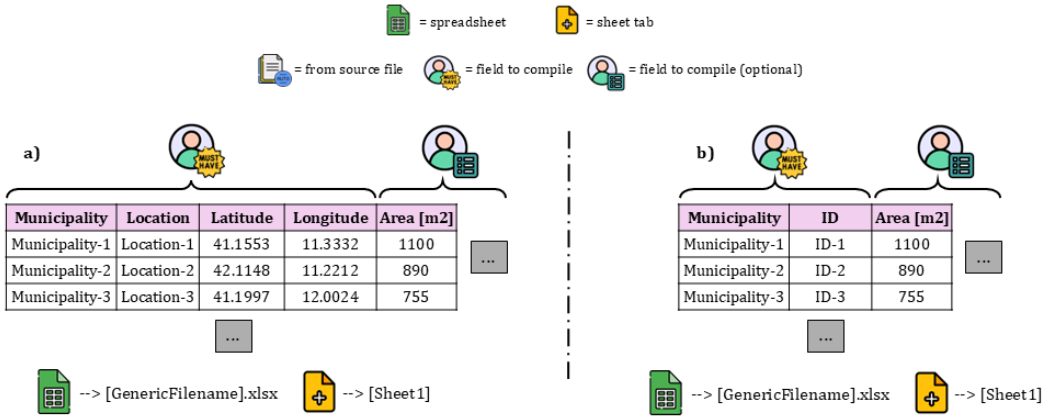

Figure IV-30: Scheme of the possible spreadsheet structures for the detected landslides info, to put inside the 'Detected Soil Slips' subfolder (in turn inside 'Raw Data'). Multiple files, referred to different landslides events, can be put inside this folder, with generic names. These files must contain a single sheet tab, which can have one of the two possible structures, depending on the type of landslide data available. If the landslide polygons are available and were imported through the <Landslides Polygons> button, then the structure to use is the one on the right (b), containing the ID of the imported polygons as second column. If no landslides were imported, then the structure to use is the one on the left (a), containing the coordinates of the landslide body centroid (or upper scar). In both cases, extra info can be added, as triggering areas, datetime of the occurrences, etc. This info will not be imported but it can be useful to better identify the various landslides.

In the following example it is reported the procedure to follow when the landslide inventory is not obtained from a shapefile (for which the IDs are necessary), but just with coordinates contained in the spreadsheet to import (as seen in Figure IV-30a).

The first option after triggering the <Points Association> button is related to the files to import for the landslides' info, as shown in Figure IV-31a. Even a selection of multiple files is supported. This option can be useful because the spreadsheets of Figure IV-30 are intended to be related to a single landslide event (a day when a single or multiple landslides occurred), thus, in case of multiple landslide events, it is suggested to create a different spreadsheet for each event.

After this, a second prompt (Figure IV-31b) asks for some extra options, that is the <Datetimes>, <Allow overlap of DTMs>, and <Sub area for each point> checkboxes. If the <Datetimes> checkbox is flagged, it means that the user has created spreadsheets containing also the datetime of the landslide events, as extra and optional column. Thus, it will be asked to select the column containing the datetime (if the name of the column is different from 'Datetime'). If an error occurred while the program read that column, then another prompt will ask to assign a datetime manually. If the <Datetimes> checkbox is not flagged, then a Not a Time value is assigned to each detected point inside the current spreadsheet. Regarding the <Allow overlap of DTMs> checkbox, if it is flagged, the program is allowed to assign a detected point to more DEMs simultaneously (if there is an overlap of DEMs at the border and the detected point is located there), otherwise the program will choose just one of the possible DEMs (normally following the import order used in the morphology panel). The <Sub area for each point> checkbox allows to create areas around each detected point, when flagged.

The third prompt that appears (Figure IV-31c) asks for the type of spreadsheet to import. If the dropdown list is set on <Circle> the imported spreadsheet type is the one containing coordinates (see Figure IV-30a), otherwise, when set on <ImportPolygons> the spreadsheet contains the ID of each polygon to import (see Figure IV-30b).

Finally, the last prompt that could appear asks for the diameter to use around each detected point (Figure IV-31d), in order to create fictitious landslide polygons, which can be consulted to understand what are the properties of the points near the coordinates of the detected landslides. This visibility of the last prompt depends on the <Sub area for each point> checkbox, because the prompt appears only if it was previously flagged.

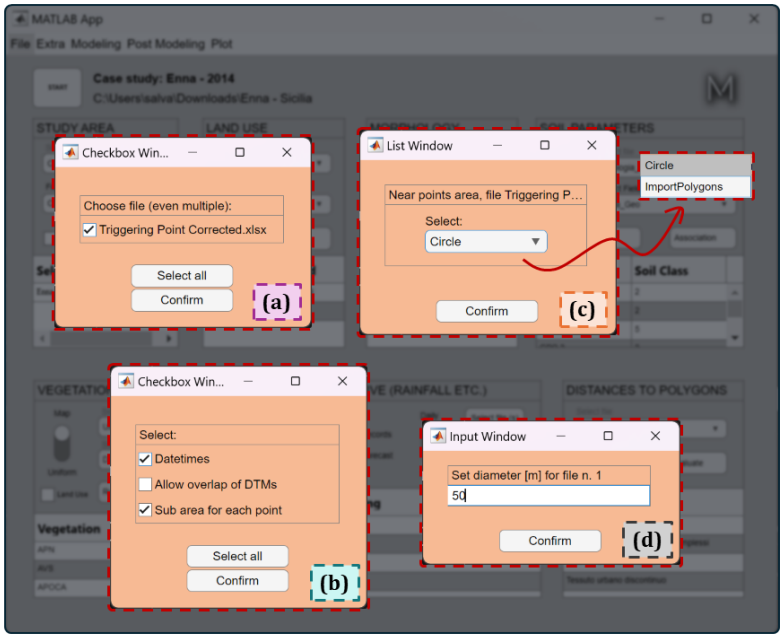

Figure IV-31: The options that can be used after running the <Points Association> button of the menu Extra-Database. The first prompt (a) asks for the spreadsheets to import, with the possibility to select multiple files (related to different landslide events). The second prompt (b) asks for some extra properties during the reading of the files, such as the import of the column containing the datetimes, the possibility to overlap DTMs, which means that if there is a point included in two or multiple DEMs this point will be considered multiple times in each DEM, and also the creation of some circular areas around each detected point, containing information of points near every detected landslide. The third prompt (c) asks for the type of spreadsheet to import. If <Circle> is selected, then the spreadsheet to import must contains coordinates, otherwise, if <ImportPolygons> is selected, the spreadsheet must contain the IDs of the landslide polygons. The fourth prompt (d) asks for the diameter to use around the detected point, only when the <Circle> option from the previous prompt is selected.

4.2.4.3 Points Info button

The <Points Info> button, which triggers the 'D_InfoDetectedSoilSlips_Parameters.m' main module of X-SLIP, is an optional step. This process does not require any input by the user and can be run only after the end of the <Points Association> process. Its functioning is to read the coordinates of landslides, imported though the previous <Points Association> button, and to add some relevant properties to each detected point. Specifically, these properties are related to the morphology, sub/top soil, vegetation, and land use. Thus, for each detected landslide point (imported from the spreadsheets of the previous Section 4.2.4.2) a series of parameters, such as the elevation, slope, soil cohesion, etc., is shown in a table that will appear at the end of the processing. Moreover, if the <Sub area for each point> checkbox was flagged during the <Points Association> process, an additional table containing the averaged values over these sub areas will appear.

4.2.4.4 Average Values button

The <Average Values> button, which can trigger both the main modules of X-SLIP called 'B_AvgValues_Static.m' and 'B_AvgValues_TimeSentitive.m', is a required step if the user wants to use the LEP-AI model. This process require different inputs by the user and can be run only after the morphology main panel and the <Curvatures> button, of Sections 4.1.3 and 4.2.2 respectively. Its functioning is to create averaged and representative values for the study area and each municipality of it.

The first options that can be select are the <Time Sensitive> and <Static> checkboxes of Figure IV-32. With the <Static> checkbox is possible to run the 'B_AvgValues_Static.m' main module of X-SLIP, which will assess the average elevation, slope, aspect angle, and main, profile, and planform curvatures, over the entire study area and also each of its municipalities. No input is needed by the user, because this properties are read automatically from the grids generated trough the morphology panel (Section 4.1.3) and the <Curvatures> button (Section 4.2.2). In contrast, with the <Time Sensitive> checkbox is possible to run the 'B_AvgValues_TimeSentitive.m' main module of X-SLIP, which will assess the average time sensitive properties (such as rainfall, temperature, NDVI, etc.), varying with the time intervals dictated by the source files. In other words, for each property that is intended to use, it is possible to run this module multiple times, because it will simply add the new read properties to the existing one. Despite this, it is important that each time that this module is run, the selected folder and the selected files are related to just one property (over the history). In fact, the first prompt that will appear with the 'B_AvgValues_TimeSentitive.m' module, triggered by the <Time Sensitive> checkbox is a window that asks for the folder where the time sensitive source data is stored. After this, a new prompt will ask for the files to read, as shown in Figure IV-33a, which can have a '.tif' or '.nc' file extension. As stated in the title of this prompt, it is important to select only the files that represent the time history related to a single property. If the user wants to add another property, it is possible to run again the <Average Values> button, flagging only the <Time Sensitive> checkbox and selecting different files (and eventually a different folder at the beginning). Once the files are selected, the user must specify the name of the property that is going to be read, as shown in Figure IV-33b. Finally, in the case of files with the extension '.nc', it is necessary to specify the fields containing the data, the longitude, and the latitude of the points forming the source raster. Instead, in case of '.tif' files, the grid is read automatically.

Once the time sensitive grid is read, an intersection between the various polygons (study area and municipalities) and the source grids is performed, with the same technique described in Section 3.3.2 of Chapter III. The values within the polygon are then averaged and stored inside a table, in the 'Variables' subfolder.

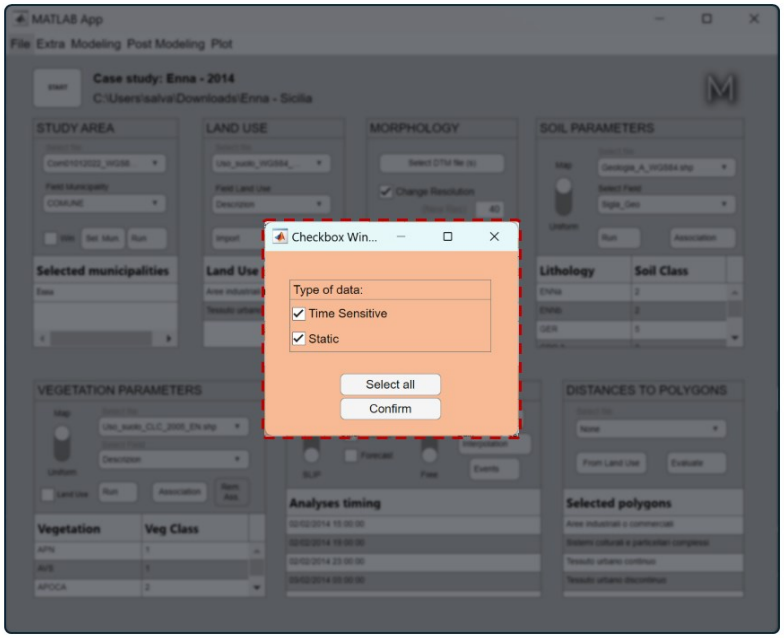

Figure IV-32: The types of average values to assess, after running the <Average Values> button of the menu Extra-Database. If <Time Sensitive> is flagged, then the average values for the time sensitive parameters (such as rainfall, temperature, NDVI, etc) are assessed, for the study area and each of its municipalities. If <Static> is flagged, then the average values for the static properties (such as elevation, slope, aspect angle, etc) are assessed, for the study area and each of its municipalities.

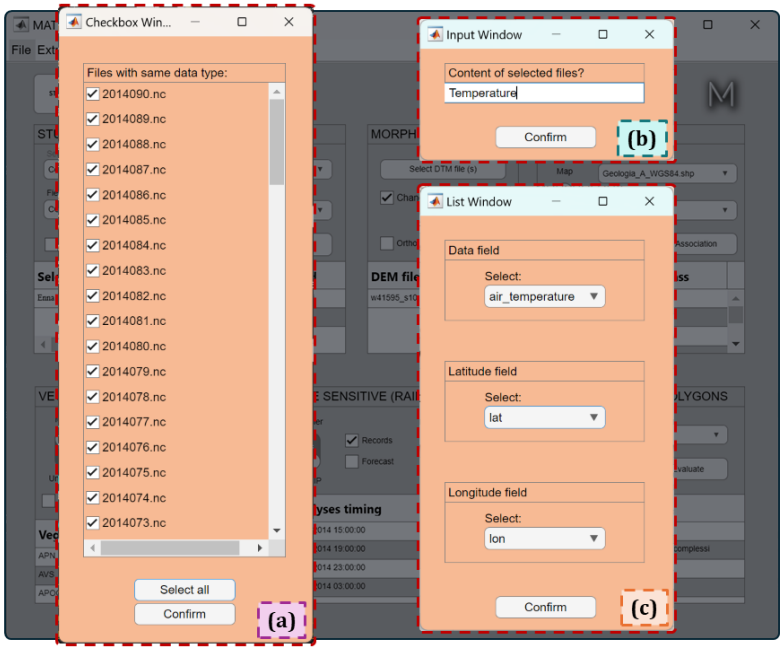

Figure IV-33: The prompts of the <Time Sensitive> checkbox, during the process of the <Average Values> button, inside the menu Extra-Database. First, the files to use must be selected (a). These files must contain a single property, such as the temperature. Secondly, the name of the property just read from the source files must be specified manually (b). Finally, in case of files with the '.nc' extension, it is necessary to select the fields containing respectively the data, the latitudes of the grid, and the longitudes of the grid (c).

4.2.4.5 Dataset Creation button

The <Dataset Creation> button, which can trigger both the main modules of X-SLIP called 'E_MLA_Step1_DatasetCreation.m' and 'E_MLB_Step1_DatasetCreation.m', is a required and crucial step if the user wants to use either LEP-AI or PIP-AI models ('MLA' is for LEP-AI and 'MLB' is for PIP-AI). This process requires different inputs by the user and can be run only after processing all or just some of the functionalities seen in the previous sections, depending on the features to include. Its functioning is to create the final datasets to pass to LEP-AI or PIP-AI models. This button can be run multiple times because it can create and store different sub-datasets for each AU (with LEP-AI) or for each spreadsheet contained in the 'Detected Soil Slips' subfolder (with PIP-AI). Thus, during the training of the models, it is possible to decide which parts of the dataset to use.

However, the first options that can be select after pressing the <Dataset Creation> button are the <Dataset for LEP-AI> and <Dataset for PIP-AI> checkboxes of Figure IV-34, with which it is possible to create datasets for LEP-AI or PIP-AI model respectively.

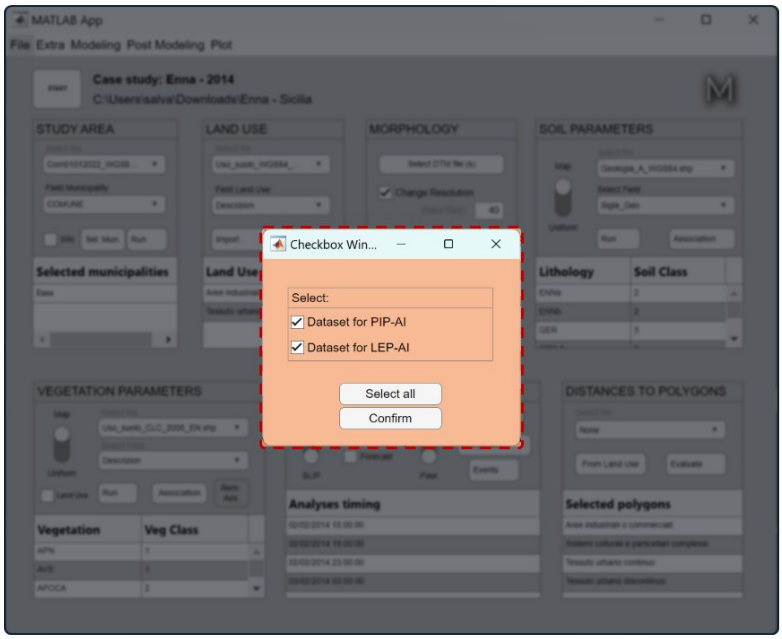

Figure IV-34: The types of datasets that can be built, after running the <Dataset Creation> button of the menu Extra-Database. If <Dataset for LEP-AI> is flagged, then the dataset for LEP-AI model is built, containing as observations the various REs and LEs. If < Dataset for PIP-AI > is flagged, then the dataset for PIP-AI model is built, containing as observations the pixels that forms the base grid (and their properties).

If the <Dataset for LEP-AI> is flagged, then the 'E_MLA_Step1_DatasetCreation.m' main module is triggered, and several options are available. To start with, it is necessary to specify which source to use for rainfall and temperature data, as shown in Figure IV-35. Both the types of data have the possibility to use data from gauges or satellite (data from satellite must be imported with the <Average Values> button and the checkbox <Time Sensitive> flagged).

In case of rainfall, there is also the possibility to synthetize data, to create synthetic datasets which can be used as benchmarks.

Subsequently, some options related to REs and LEs can be specified, as shown in Figure IV-36. Specifically, these options are related to the thresholds to define REs, the number of days to use for the cause windows (see Section 3.2.3.2), the start and end datetimes to filter the REs that will be generated, and the buffer to use for the match between REs and LEs (<Extra days for RE-LE match?> of Figure IV-36a). The buffer means some extra days that can be used after the end (or also before the start) of each RE to allow the match with a certain landslide occurrence (if the match is encountered, the RE is also a LE). In fact, sometimes landslides occurrences are reported with inaccurate datetimes (but close to the actual ones). Regarding this buffer, it is possible to specify where to place it (Figure IV-36b), i.e., only after the end of each RE (<Forward>) or both after the end and before the start of each RE (<Forward&Backwards>). The last option to select is the type of match (Figure IV-36b), which can be <MaxAmount>, <LastEvent>, <Nearest>, or <AllowMultipleMatches>. This rule is needed because it may happen that a certain landslide occurrence can be assigned to multiple RE. In these cases, if <MaxAmount> is selected, the unique RE that becomes a LE is the one containing the maximum amount of rainfall. If <LastEvent> is selected, then the unique RE that becomes a LE is the last one, from a time perspective. If <Nearest> is selected, then the unique RE that becomes a LE is the one that has the smaller difference (in hours) between the start or end datetimes of the possible REs. If <AllowMultipleMatches> is selected, then all the REs that have a match become LEs.

To continue, some options related to the static features must be selected, as illustrated in Figure IV-37. First, it is required to specify which are the columns of the static table (created with the <Average Values> button and the checkbox <Static> flagged) containing the 5 static features of LEP-AI (Figure IV-37a). After this, the user can decide to select, or not, the municipalities to use (Figure IV-37b1). This possibility is implemented because, as mentioned above, the <Dataset Creation> button can be run multiple times, with the possibility to create different separated sub-datasets for each municipality (i.e., each AU). If the user does not want to select the area for the static features, then the extracted values are related to the entire study area (averaged), otherwise, it is possible to select the municipality (or municipalities) to use (Figure IV-37b2). When more than one municipality is selected, the values to use are the averages of the averages (because the static properties were already averaged over their respective municipalities).

Following this, in case of source data for rainfall or temperature retrieved from gauges, the same process seen for the <Select file (s)> of the time sensitive panel (Section 4.1.6) is followed, two times in case of both data from gauges. Data is not directly read from the outputs of the time sensitive panel because those outputs have usually less datetimes and are interpolated (for a long-time window the result would be several rainfall maps, that would

require several gigabytes of storage with no reason). In fact, those outputs are used for PIP-AI and SLIP, rather than LEP-AI. Anyway, for the NDVI or rainfall and temperature from satellite, it is needed to specify which are the columns of the required features (Figure IV-38a), that are read from the time sensitive table (after <Average Values> with <Time Sensitive> flagged), and it is also possible to specify which municipalities to use (Figure IV-38b1, IV-38b2, IV-38c), for the same reason explained above for static data.

After this, the landslide inventories are imported and it is possible to specify, also in this case, which are the municipalities to maintain (Figure IV-39).

At this point, it is necessary to clarify the reason why there is this need to specify 5 times the areas to use (for static data, rainfall, temperature, NDVI, and landslide inventories). The reason behind this repetition is quite simple: sometimes, a certain type of data is not available for a specific municipality, therefore, it is possible to use data from municipalities that are near to the one that the user wants to analyse. For instance, in case of gauges, some of them can be used for multiple municipalities because there could be just few for a wide area.

Continuing, some options related to the LEs can be selected, as reported in Figure IV-40. Particularly, it is possible to specify the type of output, which can be <L-NL classes> for a binary classification, <4 risk classes> for a multiclassification, and <Regression> for a regression analysis (Figure IV-40a). Moreover, it is possible to specify how to create the test split of the dataset, which can be <RandomSplit> if the user wants to take a random part of the dataset for test purposes, or it can be <AfterYear> if the use wants to maintain the REs and LEs after a specific year for test purposes (Figure IV-40a). Another multiple checkbox prompt will be also displayed after that (Figure IV-40b), where the user can decide to resample the dataset (rebalancing techniques, oftentimes needed with Machine Learning), introduce noise in the dataset (<Random outputs>), select the features to maintain, create a part of the dataset for the validation (<Normal validation (NV)>), or create a cross-validation dataset (<Cross validation (CV)>).

Depending on the options selected from the previous prompts, further prompts will appear, as shown in Figure IV-41. For instance, if <L-NL classes>, <RandomSplit>, <Resampling (except regression)>, <Normal validation (NV)>, and <Cross validation (CV)> are selected, it is possible also to specify the percentage of the dataset to maintain for test (Figure IV-41a1), the percentage for the normal validation (Figure IV-41a2), and the number of folds for the cross validation (Figure IV-41a3). Additionally, it is possible to specify the minimum number of landslides occurrences required in a certain RE to define it as LE (Figure IV-41b), the type of resampling (Figure IV-41c), which can be <Undersampling>, <Oversampling>, or <SMOTE> (see Section 3.2.2, Figure III-16), and the ratio between LEs (part of unstable) and REs (part of stable). Finally, since the <Selection of features> was flagged, it is possible to select the features to maintain (Figure IV-42).

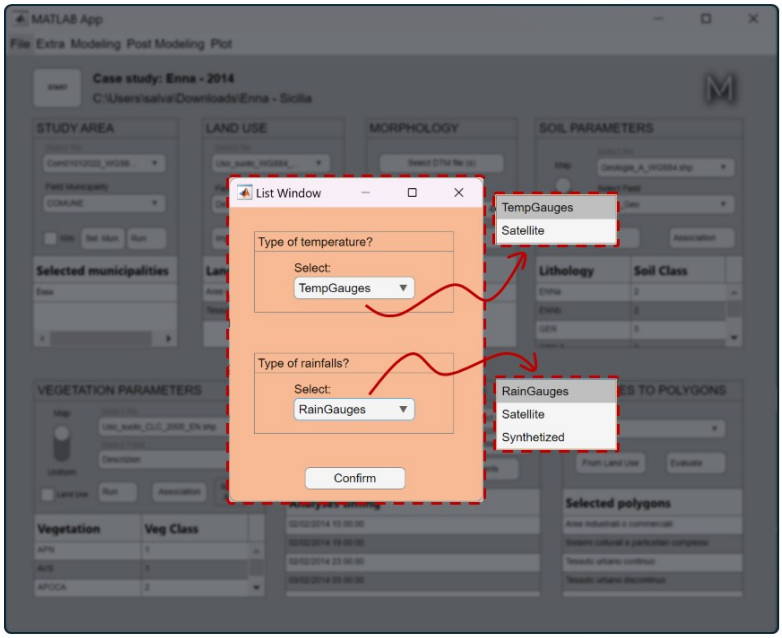

Figure IV-35: The selection of the time sensitive sources for the LEP-AI dataset, during the processing of the <Dataset Creation> button (with <Dataset for LEP-AI> flagged). Sources for rainfall and temperature can be gauges or satellite. Moreover, with rainfall it is possible to synthetize data, to create synthetic datasets.

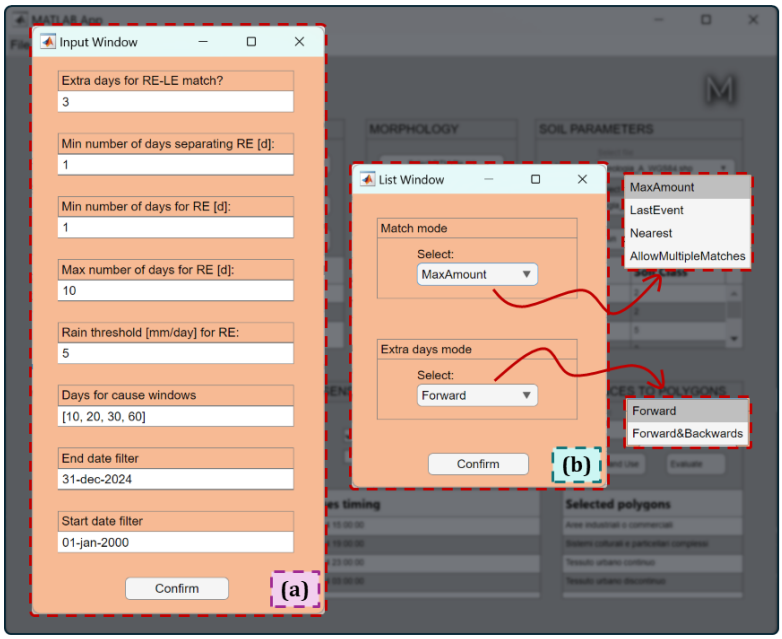

Figure IV-36: The Rainfall Events (REs) options for the construction of LEP-AI dataset, during the processing of the <Dataset Creation> button (with <Dataset for LEP-AI> flagged). It is possible to input different values (a), such as the start and end datetimes to filter REs, the days for the cause windows, the thresholds to define a RE and the buffer that is allowed for the match between REs and Landslide Events (LEs). Regarding this match, it is possible to specify some extra options in another dropdown panel (b), where the rule to select a unique match can be selected (<MaxAmount>, <LastEvent>, <Nearest>, or <AllowMultipleMatches>), and the direction of the buffer can be also selected between <Forward> or <Forward&Backwards>.

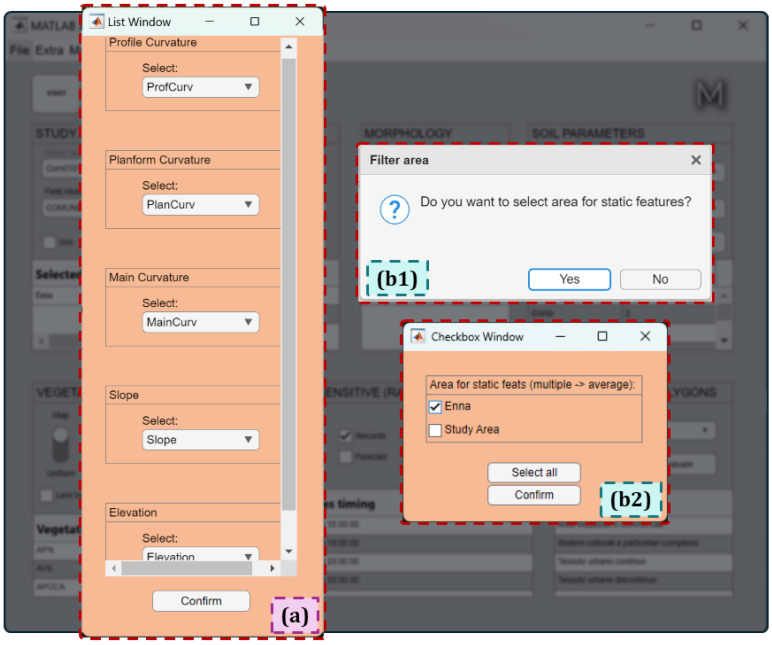

Figure IV-37: The static features options for the construction of LEP-AI dataset, during the processing of the <Dataset Creation> button (with <Dataset for LEP-AI> flagged). It is possible to associate each field of the table containing the static averaged values to its property (a). Moreover, it is possible to decide which area to use for the static features (b1). If the user does not want to select the area, the average values of the entire study area will be used, otherwise, it is possible to select the municipality (or municipalities) to use (b2). In case of a multiple selection of municipalities, the extracted values will be merged.

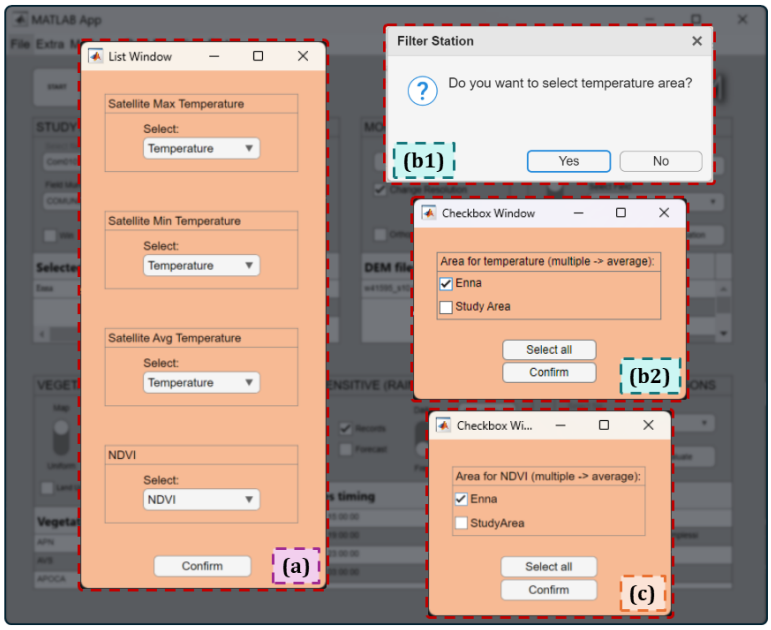

Figure IV-38: The satellite features options for the construction of LEP-AI dataset, during the processing of the <Dataset Creation> button (with <Dataset for LEP-AI> flagged). It is possible to associate each field of the table containing the time sensitive averaged values to its property (a). Moreover, it is possible to decide which area to use for these features (b1). If the user does not want to select the area, the average values of the entire study area will be used, otherwise, it is possible to select the municipality (or municipalities) to use (b2 and c). In case of a multiple selection of municipalities, the extracted values will be merged.

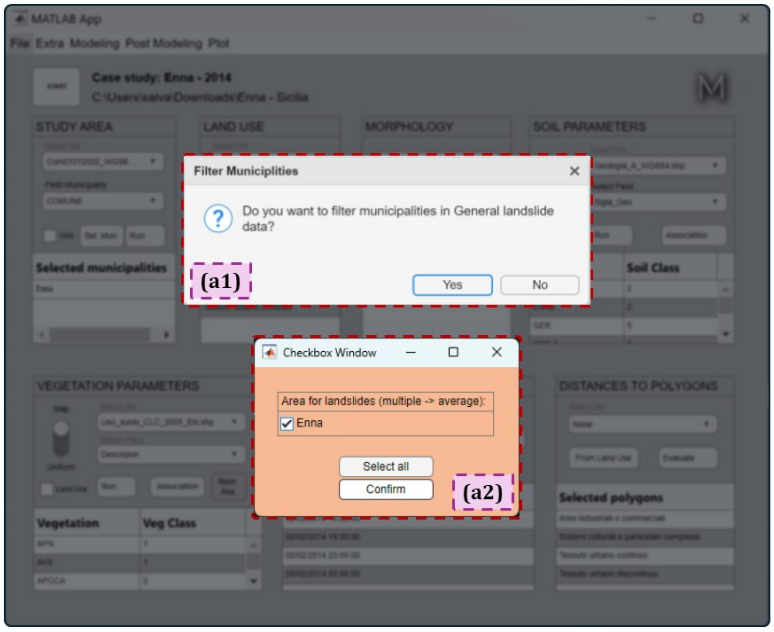

Figure IV-39: The landslide area options for the construction of LEP-AI dataset, during the processing of the <Dataset Creation> button (with <Dataset for LEP-AI> flagged). It is possible to decide which area to use for the occurred landslides (a1). If the user does not want to select the area, the occurred landslides will be considered regardless the municipality of the occurrence, otherwise, it is possible to select the municipalities to use (a2).

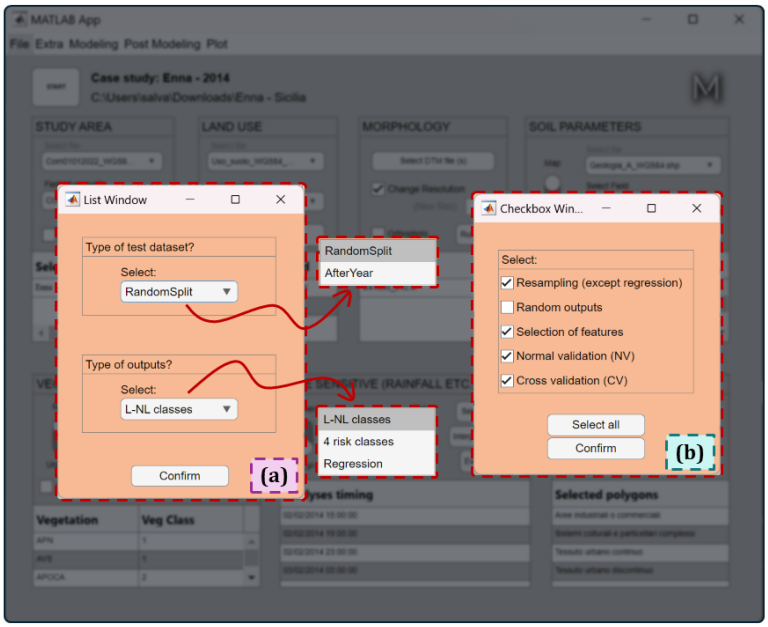

Figure IV-40: The Landslide Events options for the construction of LEP-AI dataset, during the processing of the <Dataset Creation> button (with <Dataset for LEP-AI> flagged). It is possible to decide what type of output to create (a), i.e., binary classification <L-NL classes>, multi-classification <4 risk classes>, or regression <Regression>, and the type of slip for the test dataset (a), i.e., a random split regardless the datetime of the occurrence <RandomSplit>, or considering just the events after a certain datetime for the test <AfterYear>. After this, it is possible to decide some extra options with a checkbox prompt (b), such as the resampling, the noise (introduced artificially) <Random outputs>, the selection of the features to maintain in the final dataset, and the creation of datasets for the normal or cross validation.

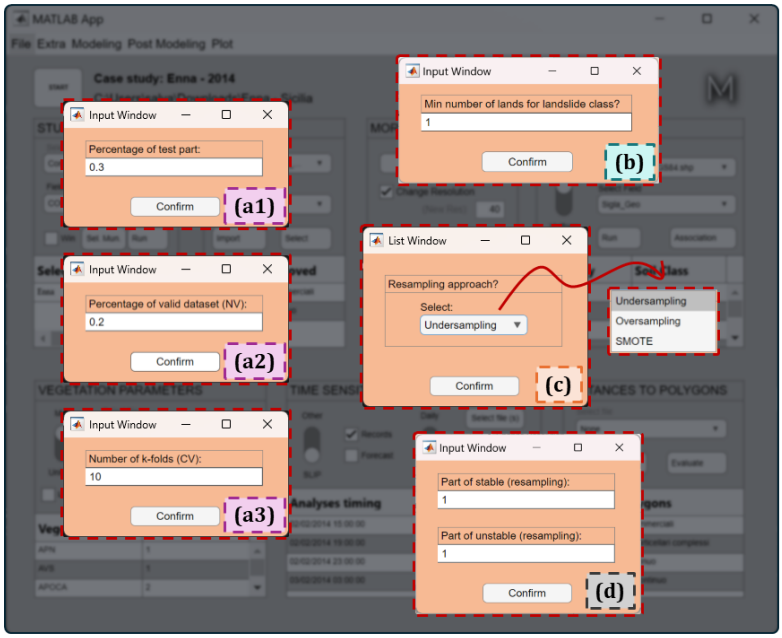

Figure IV-41: The split and rebalancing options for the construction of LEP-AI dataset, during the processing of the <Dataset Creation> button (with <Dataset for LEP-AI> flagged). It is possible to decide the percentages of data to maintain for test (a1) (in case the <RandomSplit> was previously selected), the percentage for validation (a2) (in case <Normal validation (NV)> was previously flagged), and the number of folds to build with the cross-validation (a3) (in case <Cross validation (CV)> was previously flagged). Moreover, in case of a binary classification, it is possible to specify how many landslides must occur to consider a Rainfall Event as a Landslide Event (b). Finally, it is possible to select the type of resampling approach (c) (in case <Resampling (except regression)> was previously flagged), and the ratio between the two classes of the binary classification (d).

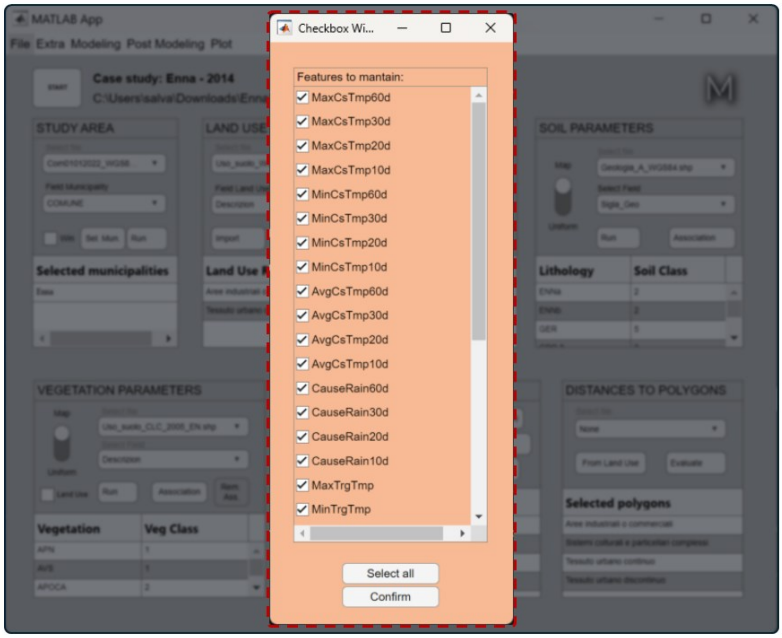

Figure IV-42: The selection of the features to maintain for the construction of LEP-AI dataset, during the processing of the <Dataset Creation> button (with <Dataset for LEP-AI> flagged). This checkbox is shown only if <Selection of features> is flagged, otherwise all the features are considered.

If the <Dataset for PIP-AI> is flagged, then the 'E_MLB_Step1_DatasetCreation.m' main module is triggered, and several options are available. To start with, it is possible to select the features to import, as shown in Figure IV-43.

Subsequently, different other options can be selected. In fact, it is possible to select the type of structure of the dataset (Figure IV-43a) (see Section 3.3.6.2), which can be <CondensedDays>, <SeparateDays>, or <TriggerCausePeak>, if the rainfall mode RM1, RM2, or RM3 is adopted respectively. Then, it is possible to include the NO landslide day (Figure IV-43b), which means that it is possible to include a prior day where no landslides occurred, to increase the time sensitivity of the model. It is also possible to select other options from a checkbox menu (Figure IV-43c), namely the creation of normal and cross validation datasets, the use of classes for some inputs (such as vegetation, soil, and land use classes) instead of class numbers, and the normalization of input data, which means that input values will vary from 0 to 1 and will be cut if outside of the ranges specified by the user. After this, it is possible to specify the split mode for the training, validation, and test datasets (Figure IV-43d), which can be <RandomSplit> or <PolySplit>. If <RandomSplit> is selected, then the percentage of test, percentage of validation and number of folds for the cross validation may be asked (Figure IV-43e1, IV-43e2, and IV-43e3), depending on the previous options. In other words, the observations (pixels) to use for these datasets are taken randomly, independently from the coordinates. Instead, if <PolySplit> is selected, it is possible to select some polygons for validation, test, and cross validation, which means that in this case the pixels to use for those datasets are within specific polygons, that will not be seen during training.

To continue, some options related to the stable and unstable area, but also the resampling approaches, can be selected (Figure IV-45). Specifically, it is possible to select what is the approach to use for the creation of the Stable Areas (Figure IV-45a) (seen in Section 3.3.5), which can be thus one of the following: <BufferedUnstablePolygons>, <SlopeOutsideUnstable>, or <AllOutsideUnstable>. If <BufferedUnstablePolygons> is selected, then some buffered polygons will be created around each unstable polygon, and it will be necessary to indicate what are the buffer sizes (Figure IV-45b). If the landslides were not associated to a polygon, it will be also required to assign the diameter of a fictious minimum landslide area (<Window side of unstable points>). If <SlopeOutsideUnstable> is selected, then the unstable area is made of the pixels that have a slope below a certain threshold, which can be specified by means of a prompt. Also in this case, if the landslides are not associated to a polygon, the unstable area is fictious and defined through the <Window side of unstable points> input. If <AllOutsideUnstable> is selected, then the stable area is made of all the pixels that are not within the unstable and indecision areas. Moreover, it is possible to perform a resampling of the dataset (Figure IV-45c). If the user decides to resample the dataset, then it is necessary to decide which is the method to use (Figure IV-45d) and what is the ratio between the stable and unstable pixels (Figure IV-45e).

Following this, it is necessary to specify the day of the event that is under analysis and if this day was a landslide day or not (Figure IV-46a). Regarding this point, it should be considered that, since the main module 'E_MLB_Step1_DatasetCreation.m' can be run several times, the user has the possibility to include also specific days where no landslide occurred but an important RE occurred, without causing damages. This can improve the quality of the model in predicting landslides. In addition, concerning the days were no landslide occurred, if with the prompt of Figure IV-44b the user decided to include the NO landslide day, then a further prompt will appear (Figure IV-46b), asking for the number of days prior to the landslide day, when inside the current unstable areas no landslide occurred. This is different from selecting a generic day with no landslides (i.e., <Is this a landslide day> set on <No>), because when a landslide day is selected and the NO landslide day is present, then this part of the dataset is a unique 'block', containing observations for both the days. Instead, if a generic day is specified with the dropdown <Event date (start of 24 h) :> and <Is this a landslide day> is set on <No>, that day will be considered alone and there is no possibility to add the NO landslide day, since the selected day is actually already a "NO landslide day".

After these options, the 'datasetstudy_creation.m' main function of X-SLIP is called. This function will not be investigated in detail due to space constraints (the reader is referred to the source code in the Appendices section). Anyway, it can be mentioned that when <Normalize data> option is flagged, a new prompt will ask for the ranges of each feature inside the just created dataset. Furthermore, if the user selected one of the features among <Vegetation>, <Land Use>, <Top Soil>, and <Sub Soil>, then the 'ClassesML.xlsx' spreadsheet (inside 'User Control' subfolder) must be compiled, as shown in Figure IV-47. This spreadsheet must be compiled associating each raw class imported from the land use, soil, and vegetation panels to the generalized classes of Table III-2, III-3, III-4, and III-5, depending on the type of data. In fact, the first tab of the spreadsheet contains the above-mentioned tables (Figure IV-47a), while the other four tabs (Figure IV-47b, IV-47c, IV-47d, IV-47e) must contain the name of the possible raw polygon classes (first column) and the generalized class associated (second column). The first column of these tabs should be filled with the same raw names of the classes contained in the other spreadsheets of the 'User Control' folder (Figures IV-8, IV-14, and IV-17). In other words, it is possible to just copy and paste, from the first column [Field name] of these spreadsheets, to the first columns of these new tabs, depending on data type (for instance, the first column of the 'Vegetation' tab of Figure IV-47d is the same [Field name] column of the 'VuDVCAssociation.xlsx' spreadsheet, from the 'Association' tab). To conclude, it must be noted that the 'Raw data name' columns of Figure IV-47b, IV-47c, IV-47d, and IV-47e, can contain also more classes than the imported ones, thus it can contain also the names of the raw classes from shapefiles that are different from the one imported. This means that the 'ClassesML.xlsx' spreadsheet can be transfer from a project to another without issues, but remembering that at least the same classes contained in the other current

spreadsheets (Figures IV-8, IV-14, and IV-17) must be also present inside the 'Sub soil', 'Top soil', 'Vegetation', and 'Land use' tabs of 'ClassesML.xlsx'.

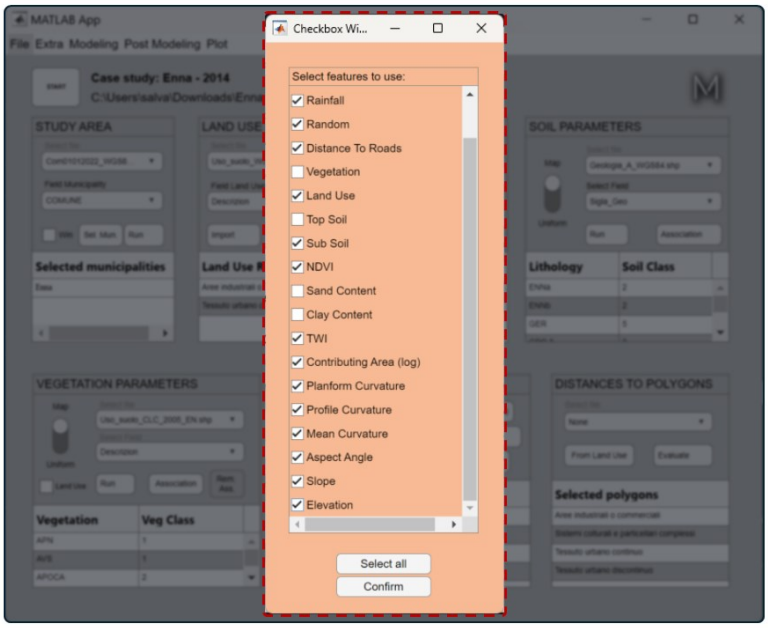

Figure IV-43: The selection of the features to import for the construction of PIP-AI dataset, during the processing of the <Dataset Creation> button (with <Dataset for PIP-AI> flagged).

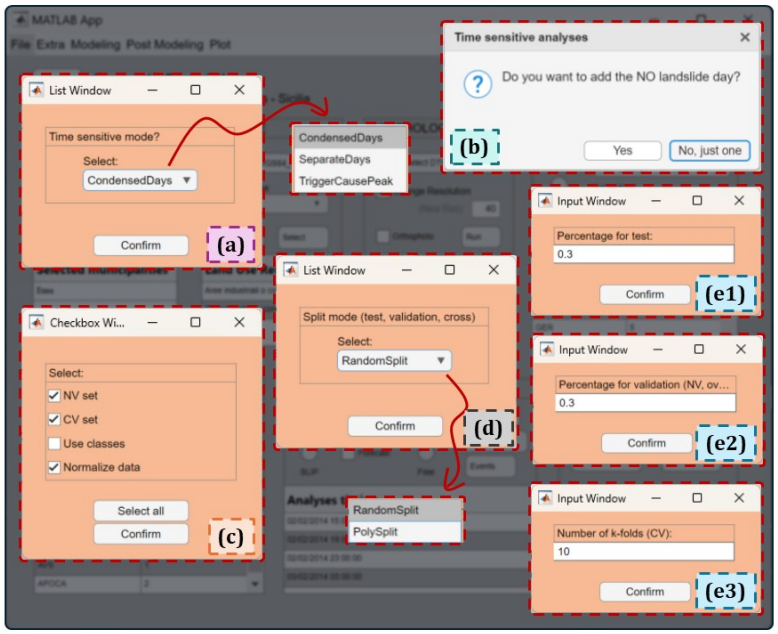

Figure IV-44: Part I of the possible options for the construction of PIP-AI dataset, during the processing of the <Dataset Creation> button (with <Dataset for PIP-AI> flagged). It is possible to select the structure of the dataset (a); include the NO landslide day (b); decide to create normal and cross validation datasets, but also normalize input data or use classes as inputs, instead of numbers (c); select the split mode for the test, validation and cross datasets (d); the percentages of test, normal validation and the number of folds for the cross validation (e1, e2, e3), if the <RandomSplit> is selected, otherwise a prompt will asks for the polygons to use for train, test, validation etc.

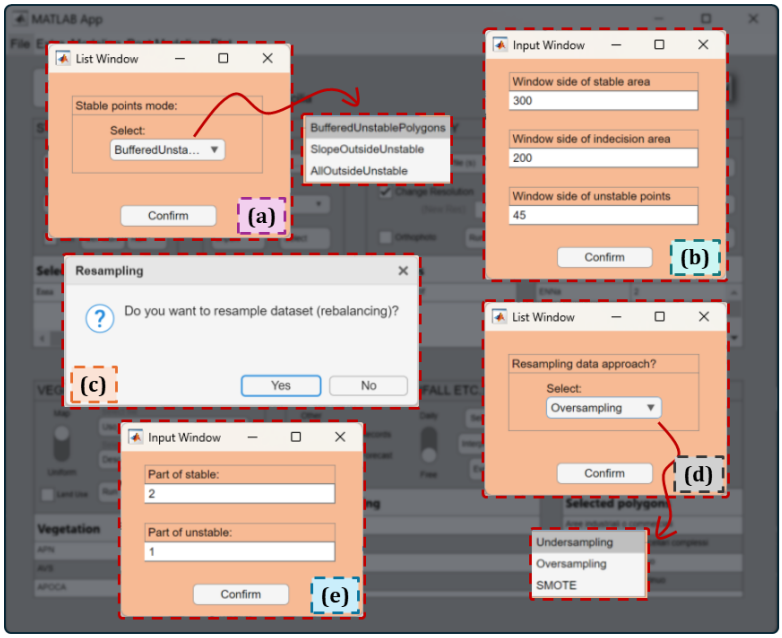

Figure IV-45: Part II of the possible options for the construction of PIP-AI dataset, during the processing of the <Dataset Creation> button (with <Dataset for PIP-AI> flagged). It is possible to select the type of stable area (a); select the buffer sizes for the stable areas (b); decide to resample the dataset (c); select the type of resampling (d) and the ratio between stable and unstable pixels (e), if the user decides to continue with the resampling.

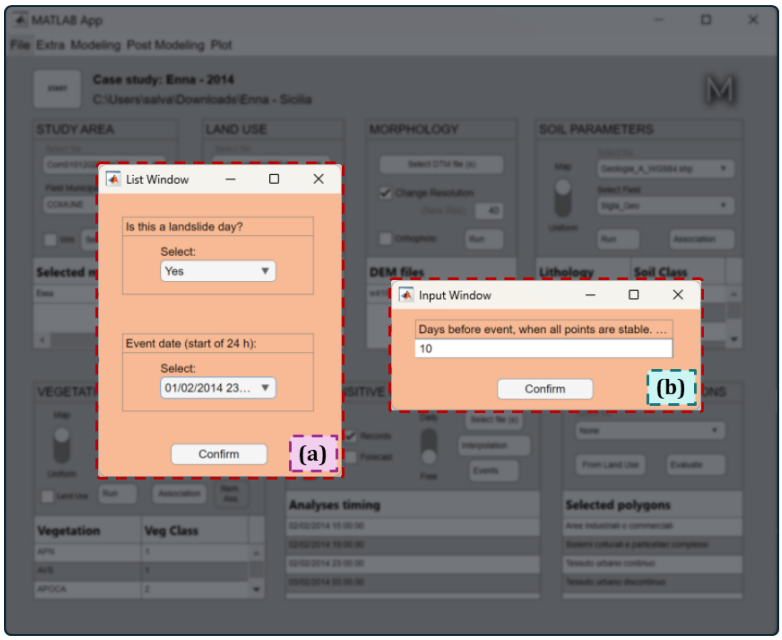

Figure IV-46: Part III of the possible options for the construction of PIP-AI dataset, during the processing of the <Dataset Creation> button (with <Dataset for PIP-AI> flagged). It is possible to select the datetime associated with the dataset that is being created and specify if this datetime is related to a landslide day (a); specify how many days before the previously selected datetime all the points are stable (b), but only in case the user decided to include the NO landslide day.

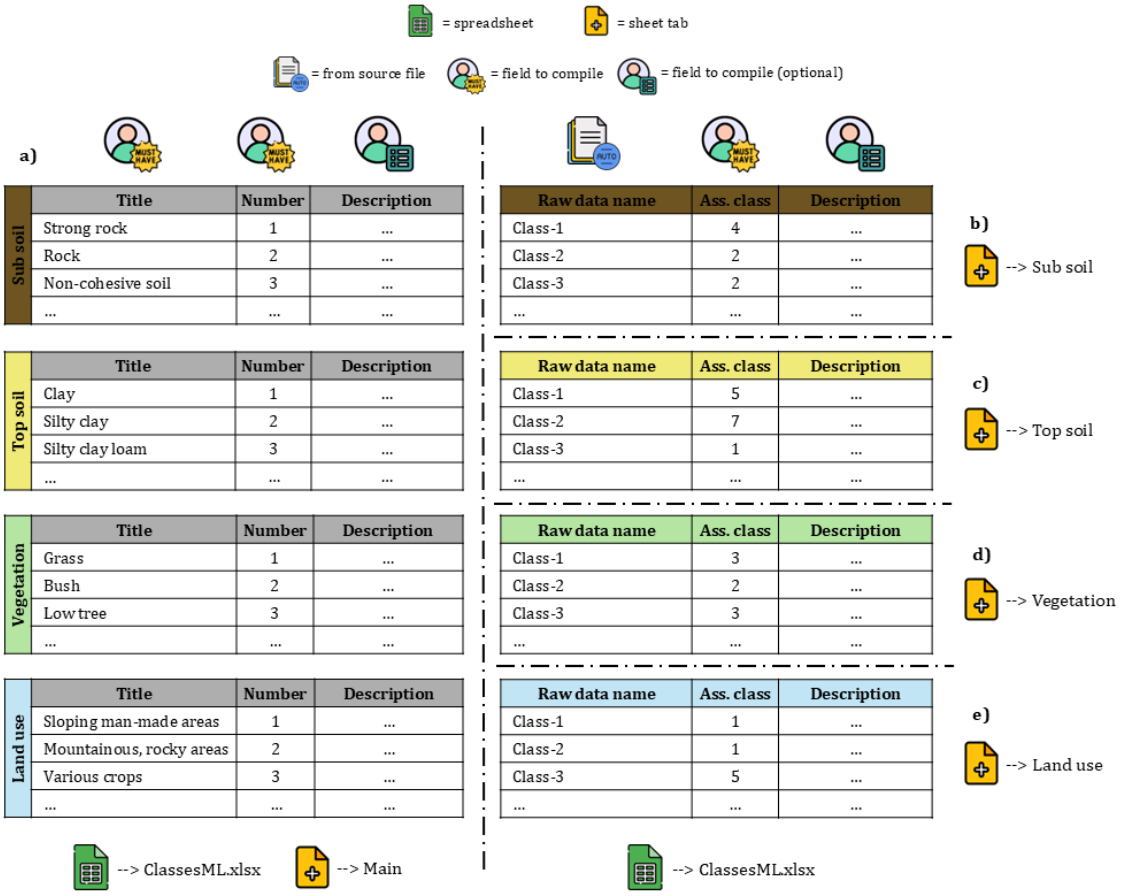

Figure IV-47: Scheme of the 'ClassesML.xlsx' spreadsheet, in the 'User Control' folder. The spreadsheet has five sheet tabs, i.e., the 'Main' (a), 'Sub soil' (b), ' Top soil' (c), 'Vegetation' (d), and 'Land use' (e). Starting with the 'Main' tab (on the left), different sub tables must be created (for each data type), with the first column containing the names of the generalized classes for each data type and the second column containing the number of the class (to use for the association between raw and generalized classes). A third optional column, containing the descriptions of the generalized classes, can be also created. Regarding the remaining tabs, these must contain at least 2 columns. The first column must contain the raw names of polygon classes, representing a semi-automatic field, because the user can just copy and paste these raw classes from other spreadsheets such as 'LuDSCAssociation.xlsx', 'VuDVCAssociation.xlsx' etc. The second column must be compiled by the user, with the number corresponding to the generalized class to associate to each raw polygon class. If the user wants to exclude a certain raw class, it is sufficient to leave blank the cell with the 'Ass. class', or to fill it with a 0. Finally, in these tabs it is possible to add a third optional column, containing a description of the raw polygon class.

4.2.4.6 Dataset Statistics button

The <Dataset Statistics> button, which triggers the 'F_DatasetStatistics.m' main module of X-SLIP, is an optional step if the user has created datasets for the LEP-AI or PIP-AI models. This process will not be investigated in detail due to space constraints (the reader is referred to the source code in the Appendices section) and can be run only after the <Dataset Creation> button, of the previous Section 4.2.4.5. Its functioning is to create statistics for all the features contained in the dataset that is passed (for LEP-AI or PIP-AI model, Section 3.2.3.2 or 3.3.6.2 respectively). The metrics assessed are the minimum, maximum, mean, median, and standard

deviation values, but also the 1st, 2nd, and 3rd quantiles. These values are computed for three types of datasets: the total dataset, the observations of the dataset related to the landslide events, and the observations of the not-landslide events. With these metrics, it could be possible to separate the characteristic values associated with landslides from the not-landslide ones.

4.3 Modelling Menu Of X-SLIP

The top menu "Modelling" of X-SLIP contains two sections, integrating the processes needed to create the various landslide susceptibility models, i.e., SLIP, LEP-AI, and PIP-AI. A general overview of this menu is shown in Figure IV-48.

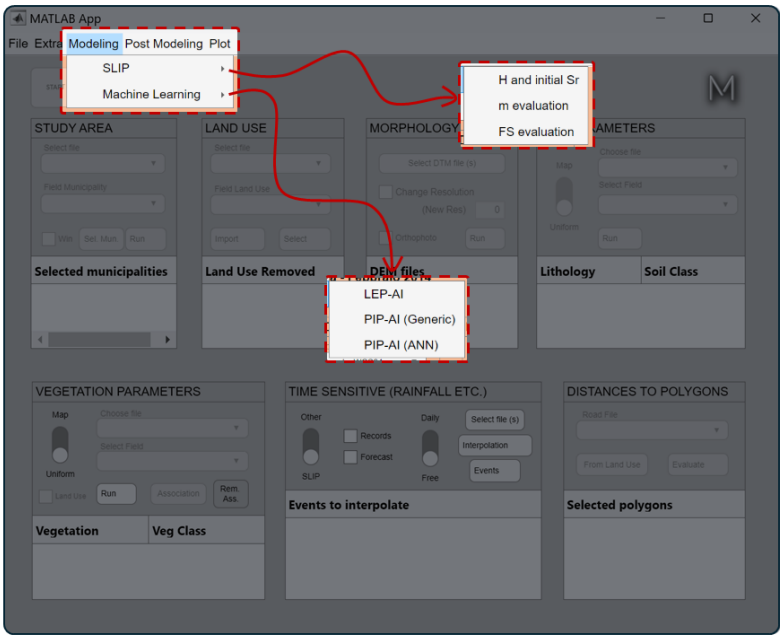

Figure IV-48: Scheme of the possible models to use with the "Modelling" top-menu in X-SLIP. The functionalities are grouped into two macro-categories, each one with its buttons. Each button triggers a main module (or function) of the X-SLIP platform.

As it can be seen, the "Modelling" top menu is organized into two macro-groups. The "SLIP" macro-group contains functionalities related to SLIP model, such as the definition of the depth of the analysis (H) and the initial degree of saturation (S_r), the evaluation of the percentage of saturated soil (m), and finally the evaluation of the factors of safety for each pixel (Fs). Instead, the "Machine Learning" macro-group contains the buttons to train the LEP-AI and PIP-AI models.

4.3.1 SLIP (Modelling Menu)

The "SLIP" group of the "Modelling" top-menu must be use from the top to the bottom. At the end of this process, some maps containing the Fs values for each pixel are stored inside a

folder with a name defined by the user, which is located inside the 'Factors of Safety' folder (which in turn is inside the 'Results' folder). Each timestamp analysed has its own maps.

However, after clicking the <H and initial Sr> button, a prompt will appear, asking for the depth at which the analysis must be performed (H) and the initial degree of saturation (S_r), as shown in Figure IV-49.

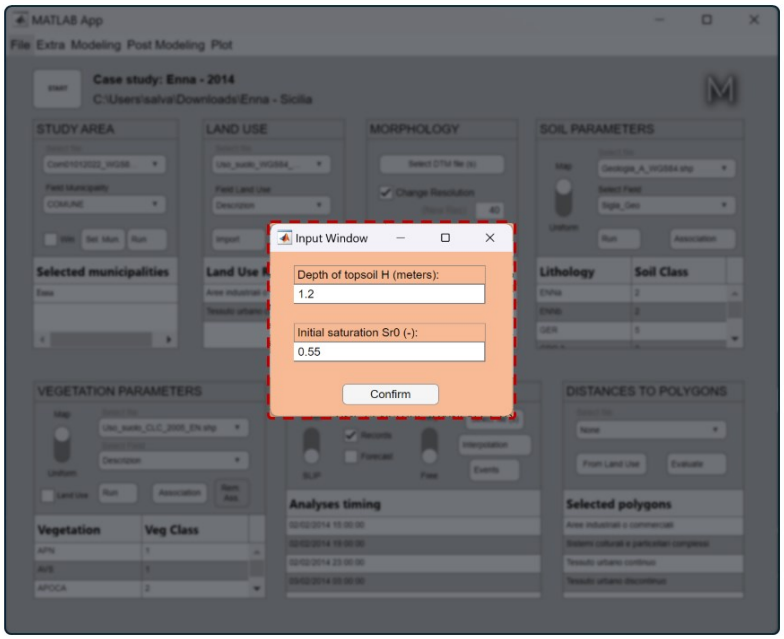

Figure IV-49: The prompt triggered with the <H and initial Sr> button, inside the "SLIP" group of the "Modelling" top-menu. It is possible to specify the depth pf the SLIP analysis (H) and the initial degree of saturation (Sr0).

After this, it is possible to run the <m evaluation> button, which triggers the main module of X-SLIP called 'E_SLIP_Step1_mEvaluation.m'. With this module, no action is required by the user and the outcome are the maps containing the values of m for each timestamp analysed.

To conclude the SLIP analysis, the <FS evaluation> button must be run. This button triggers the main module of X-SLIP called 'E_SLIP_Step2_FS.m'. In this case, just a single prompt appears at the beginning of the process, asking for the remaining values needed by SLIP to perform the analysis (Figure IV-50a), such as the internal modelling parameters λ and α, but also the specific gravity of the soil G_S (which normally is around 2.7). Some default values will be already written. At the end of this process, if there were no issues, a final prompt (Figure IV-50b) will ask for the name of the folder where the current analysis should be stored (inside Results -> Factors of Safety). A suggested name will also fill the entry. This default name follows the rule <dd-MM-yy-hh-mm-[Vegetation_Case]-[DEM_Resolution]m>, where dd-MM-yy is the datetime of when the analysis was performed, and hh-mm is the hour.

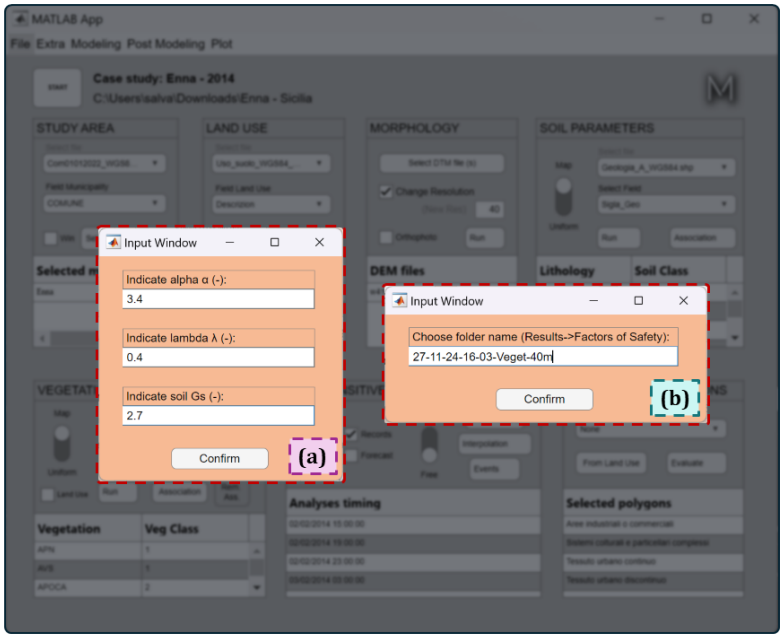

Figure IV-50: The initial prompt to specify the remaining parameters required by SLIP (a), and the prompt to specify the name of the folder to use (b), inside Results->Factors of Safety. Both these prompts are part of the process triggered with the <FS evaluation> button, inside the "SLIP" group of the "Modelling" top-menu.

4.3.2 Machine Learning (Modelling Menu)

The "Machine Learning" group of the "Modelling" top-menu has not a proper sequence to follow, but each button can be run in whatever order. However, the <LEP-AI> button is referred to the creation and training of the LEP-AI model, triggering the main module of X-SLIP called 'E_MLA_Step2_Training.m'. In contrast, <PIP-AI (ANN)> and <PIP-AI (Generic)> represent two alternatives of the PIP-AI model. The <PIP-AI (ANN)> button triggers the main module of X-SLIP called 'E_MLB_Step2_TrainingANNs.m', creating a model based on artificial neural networks. The <PIP-AI (Generic)> button triggers the main module of X-SLIP called 'E_MLB_Step2_TrainingGeneric.m', creating a model based on some generic ML techniques.

In the following sub-sections, these possibilities will be described in detail.

4.3.2.1 LEP-AI training

After clicking on <LEP-AI> button, the 'E_MLA_Step2_Training.m' main module of X-SLIP is triggered, and several options can be selected.

First, it is possible to select the type of training (Figure IV-51a), which can be <Classic (L)>, <Classic (V)>, <Cross Validation (K-Fold M)>, <Cross Validation (K-Fold V)>, <Deep (L)>, <Deep (V)>, <Auto>, <Logistic Regression>, or <Sensitivity Analysis>. If <Classic (L)> is selected, then it is possible to train a classic ANN (i.e., using three possible activation functions, namely ReLU, Tanh, and Sigmoid) using just the training dataset. If <Classic (V)> is selected, then it is possible to train a classic ANN with the early stopping, which means that

validation dataset is used, in addition to training dataset. If <Cross Validation (K-Fold M)> is selected, then it is possible to create a cross validation of ANNs, therefore a few ANNs equal to the number of folds will be generated. The various splits of the training dataset are randomly generated by MATLAB, and the model that will be selected as default for future predictions is the one that had the best performance among the various folds. If <Cross Validation (K-Fold V)> is selected, then it is possible to create a cross validation of ANNs, as seen with <Cross Validation (K-Fold M)>. The difference rely on the fact that in this case the various splits of the training dataset are not random, but the same defined during the processing of <Dataset Creation> button (<Dataset for LEP-AI>) if <Cross Validation (CV)> was flagged (see Section 4.2.4.5 and Figure IV-40b). If <Deep (L)> is selected, then it is possible to train an advanced ANN (i.e., using more activation functions and techniques, such as dropout and others) using just the training dataset. If <Deep (V)> is selected, then it is possible to train an advanced ANN using the early stopping, i.e., using training and validation datasets. If <Auto> is selected, then there is no need to specify layers and activation functions because X-SLIP will start an optimization routine aimed at finding the best hyperparameters to use. Nevertheless, this routine might take too long and fail under certain scenarios. If <Logistic Regression> is selected, then it is possible to build a logistic regression model, which can be used as reference. If <Sensitivity Analysis> is selected, then it is possible to store the history of the ANNs and their metrics during the various training iterations. This method makes use of classic ANNs, just with the training dataset, but evaluating the metrics also over the validation and test parts. Thus, these datasets do not affect the training, because they are used only to evaluate metrics and not for the early stopping technique or other purposes.

Subsequently, it is possible to flag some additional options (Figure IV-51b), like the possibility to store the various model in a compact format (less storage memory) with the <Compact models> checkbox; use a filter to select and train only certain structures (above a certain number of hidden layers) with the <Structures filter> checkbox; standardize the inputs of the models, with the <Standardize inputs> checkbox; manually specify the structures to train, with the <Manual structures> checkbox; use a filter to select the models to maintain, based on performance that they achieve, with <Performance filter> checkbox.

Following this, since <Manual structures> was not flagged in this instance, the rules to create the various permutations of structures must be defined (Figure IV-51c). Specifically, for each layer of the possible ANNs, the maximum number of neurons must be specified, and the increase of neurons to use in each permutation must be also defined (see Section 3.2.3.1, Figure III-17). Moreover, because <Structures filter> was flagged, the minimum number of hidden layers that each ANN can have must be specified, excluding all the structure permutations that have less hidden layers of this number (Figure IV-51d). Additionally, for each possible layer, the type of activation function to use must be selected (possible activation functions vary depending on the type of training that is currently in use) (Figure IV-51e).

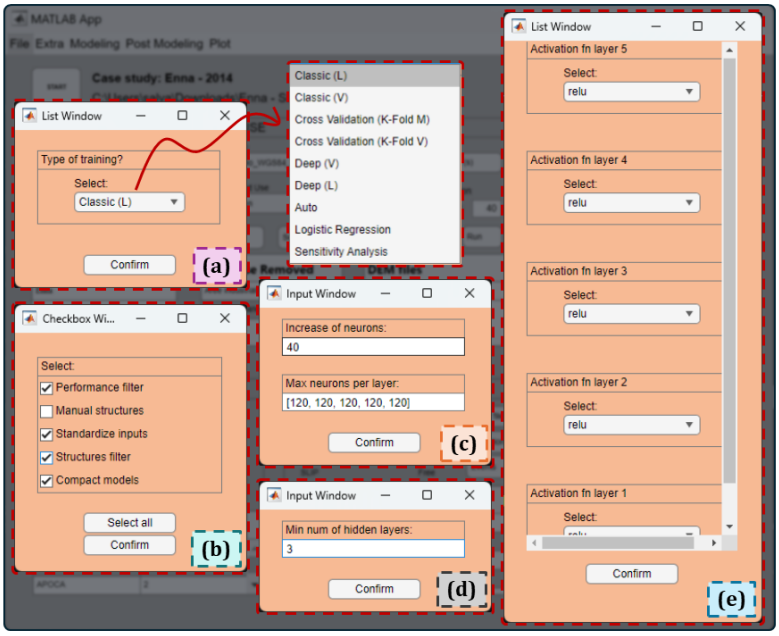

Figure IV-51: Part I of the possible options during the process triggered by the <LEP-AI> button, inside the "Machine Learning" group of the "Modelling" top-menu. It is possible to select the type of training (a); some options related to the possible structures of the various models and the type of storing (b); the increase of neurons per structure and the maximum neurons per layer (c); the minimum number of hidden layer that a structure must have (if <Structures filter> is flagged (d); the activation function to use in each layer (in this case maximum 5 layers) (e).

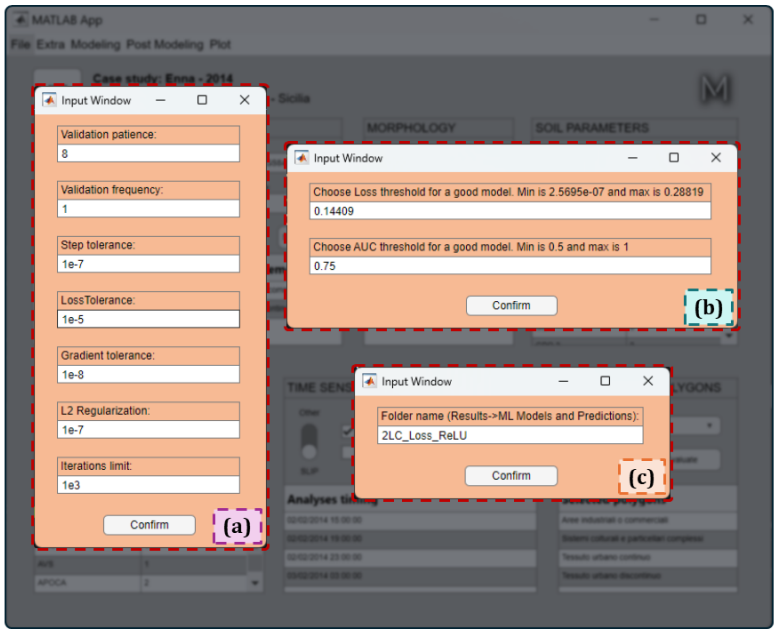

Figure IV-52: Part II of the possible options during the process triggered by the <LEP-AI> button, inside the "Machine Learning" group of the "Modelling" top-menu. It is possible to select the relevant hyperparameters of neural networks (a); specify the thresholds for the filter based on performance (if <Performance filter> was previously flagged) (b); specify the name of the folder where the models will be stored (which in turn is inside the following path: Results->ML Models and Predictions) (c).

Finally, it is possible to specify some main hyperparameters of ANNs (validation parameters effective only in case of a training with early stopping) (Figure IV-52a), the thresholds to filter the structures that had a good performance (Figure IV-52b), because <Performance filter> was flagged. To conclude, the name of the folder that will contain the analysis must be specified (Figure IV-52c). This folder is located inside 'ML Models and Predictions', which in turn is inside the 'Results' subfolder.

4.3.2.2 PIP-AI training (ANN)

After clicking on <PIP-AI (ANN)> button, the 'E_MLB_Step2_TrainingANNs.m' main module of X-SLIP is triggered, and several options can be selected.

First, it is possible to select the part of the dataset to consider (Figure IV-53a), using one of the options among <1T>, <2T>, <All>, and <Manual>. If <1T> is selected, then the part of the dataset that will be extracted is related to the days where landslides occurred. If <2T> is selected, then the part of the dataset that will be extracted is related to the days where landslide occurred and the NO landslide days seen in Section 4.2.4.5 (a NO landslide day is a day that is prior to the one of the occurrence, when for the same area no landslides occurred). If <All> is selected, then the entire dataset, which may include also days when no landslide occurred and are next to landslide days, for the same area. If <Manual> is selected, then it is possible to specify manually which are the days to extract from the total dataset.

Subsequently, it is possible to select some additional options (Figure IV-53b), some of which were already discussed in Section 4.3.2.1. Now, it is possible to select also the <Check plot> option, which if flagged, it will generate a fast check plot of the study area for a specific day, selected by the user; the <Modified cost>, which when flagged allows to select a specific cost for the unstable pixels, that can alter the training of the ANN; the <Deep plot>, which if flagged, it will generate a dynamic plot during the training, containing the history of the loss, accuracy and AUROC for each ANN to train. This last option works only if the training mode, which can be selected on the next prompt, is <Deep (L)> or <Deep (V)>.

Following this, with the next prompt (Figure IV-53c) it is possible to select the type of training. The possibilities are the same discussed in Section 4.3.2.1. Since in this instance it was flagged <Manual structures>, unlike before it is now necessary to specify each structure manually, as shown in Figure IV-53d. The user can add a variable number of structures through the <Add> button, but it is important to write the structure with the following scheme: [neurons of 1st layer, neurons of 2nd layer, neurons of 3rd layer, …]. Once the structures are defined, it is necessary to specify the activation function to use in each layer, consistently with the previous Section 4.3.2.1, as shown in Figure IV-53e.

Finally, the same main hyperparameters seen in Section 4.3.2.1 can be specified, as illustrated in Figure IV-54a and IV-54b. In this case it is also possible to specify how to assess the best probability threshold (Figure IV-54c), which separates landslide pixels from non-

landslide pixels. If <MATLAB> is selected, then X-SLIP will use the default optimal operating point, with the MATLAB internal method (MathWorks Inc., 2024c). If <MaximizeRatio-TPR-FPR> is selected, then the optimal point is the point of the AUROC curve where the ratio between TPR and FPR is maximized. If <MaximizeArea-TPR-TNR> is selected, then the optimal point is the point of the AUROC curve where the area, obtained multiplying the TPR by the True Negative Rate (TNR), is maximized. As last prompt (Figure IV-54d) it is possible to specify the name of the folder where the analysis will be stored, which is in turn inside 'ML Models and Predictions' (in turn inside 'Results').

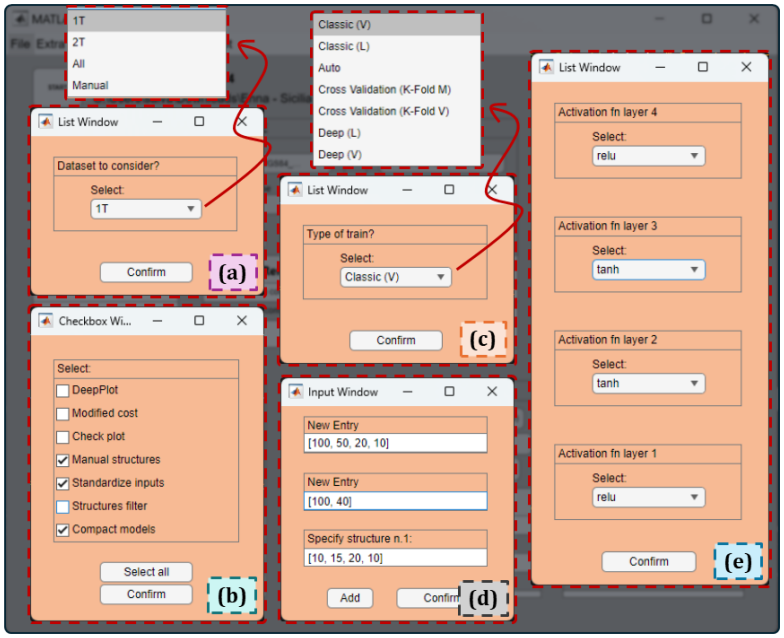

Figure IV-53: Part I of the possible options during the process triggered by the <PIP-AI (ANN)> button, inside the "Machine Learning" group of the "Modelling" top-menu. It is possible to select what are the datetimes to use from the general dataset (a); select some options related to the type of structures and the type of storing method (b); select the type of training (c); specify the structures to use, manually (if <Manual structures> is flagged) (d); select the activation function to use per each layer.

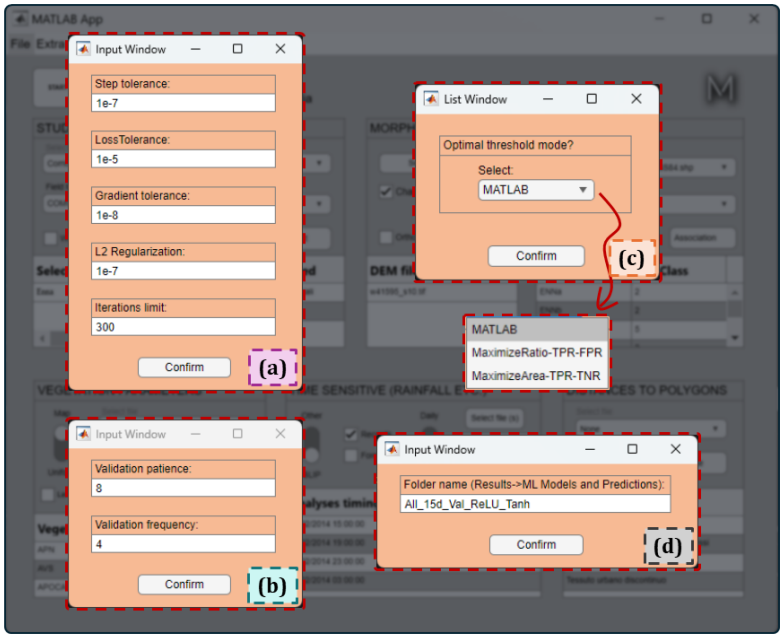

Figure IV-54: Part II of the possible options during the process triggered by the <PIP-AI (ANN)> button, inside the "Machine Learning" group of the "Modelling" top-menu. It is possible to specify some typical hyperparameters of neural networks (a); specify the validation metrics (if the type of training includes the validation dataset) (b); specify how to assess the best probability threshold, which separates landslide pixels from not landslide pixels (c); specify the name of the folder where the models will be stored (inside Results->ML Models and Predictions) (d).

4.3.2.3 PIP-AI training (Generic)

After clicking on <PIP-AI (Generic)> button, the 'E_MLB_Step2_TrainingGeneric.m' main module of X-SLIP is triggered, and several options can be selected.

First, it is possible to select the part of the dataset to consider (Figure IV-55a), with the same considerations of Section 4.3.2.2. Then, few extra options can be selected (Figure IV-55b), which were already discussed previously.

Regarding the type of training, in contrast with Section 4.3.2.2, the choice made by the user impacts not only the datasets that will be used but also the type of model (Figure IV-55c). If <KAN (L)> is selected, then it is possible to train KANs just with the training dataset. If <KAN (V)> is selected, then it is possible to train KANs with the early stopping techniques, because also the validation dataset will be used. All the remaining datasets make use of the training dataset only, and the name of the button reflects the type of model. If <Auto ML (L)> is selected, then it is possible to let X-SLIP decide which could be the best model to use, but just among the various ensemble methods. Of course, according to the type of model chosen, different prompts can appear and ask for some main hyperparameters (Figure IV-55d, IV-56a1, IV-56a2, IV-56b, IV-56c, IV-56d).

Finally, it is possible to select the method for the best threshold (Figure IV-56e) and the name of the folder where models will be store (Figure IV-56f), as seen in Section 4.3.2.2.

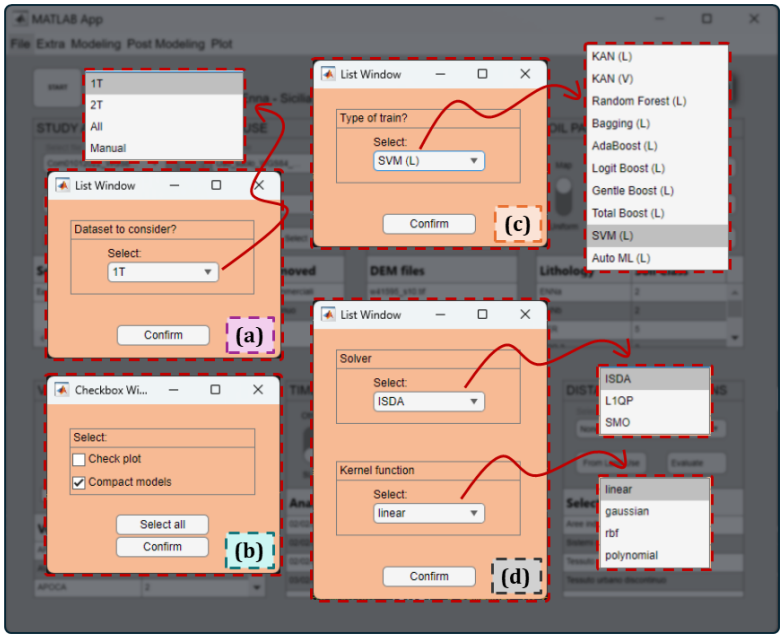

Figure IV-55: Part I of the possible options during the process triggered by the <PIP-AI (Generic)> button, inside the "Machine Learning" group of the "Modelling" top-menu. It is possible to select what are the datetimes to use from the general dataset (a); select if the models must be stored as compact and to create a fast 'check' plot (b); select the type of machine learning model and training (c); specify some of the main hyperparameters for the Support Vector Machines (if <SVM (L)> was selected) (d).

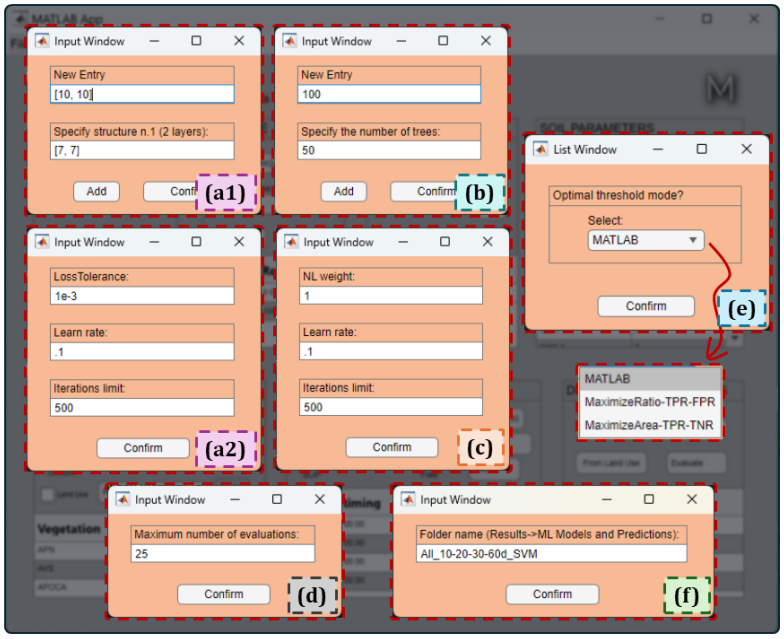

Figure IV-56: Part II of the possible options during the process triggered by the <PIP-AI (Generic)> button, inside the "Machine Learning" group of the "Modelling" top-menu. According to the type of machine learning model selected, it is possible to specify different options. In case of <KAN (L)> and <KAN (V)> models, it is possible to specify the various structures to train, i.e., the number of nodes for the bottom and top layer (2 numbers for each structure, not more, not less) (a1). Additionally, it is possible to specify the main hyperparameters of KAN networks (a2). In case of <Random Forest (L)> and <Bagging (L)> models, it is possible to specify the number of decision trees (b). In case

of all the remaining cases, except for <Auto ML (L)>, it is possible to specify the weights of the not landslides pixels over the landslide ones, the learning rate, and the limit of iterations (c). Finally, it is possible to decide how to assess the optimal probability threshold, which separates not landslide pixels from landslide ones (e), and the name of the folder where the models will be stored (inside Results->ML Models and Predictions) (f).

4.4 POST-MODELLING MENU OF X-SLIP

The top menu "Post Modelling" of X-SLIP contains six sections, integrating the possible processes that can be performed after the creation of the various models, namely SLIP, LEP-AI, or PIP-AI. A general overview of this menu is shown in Figure IV-57.

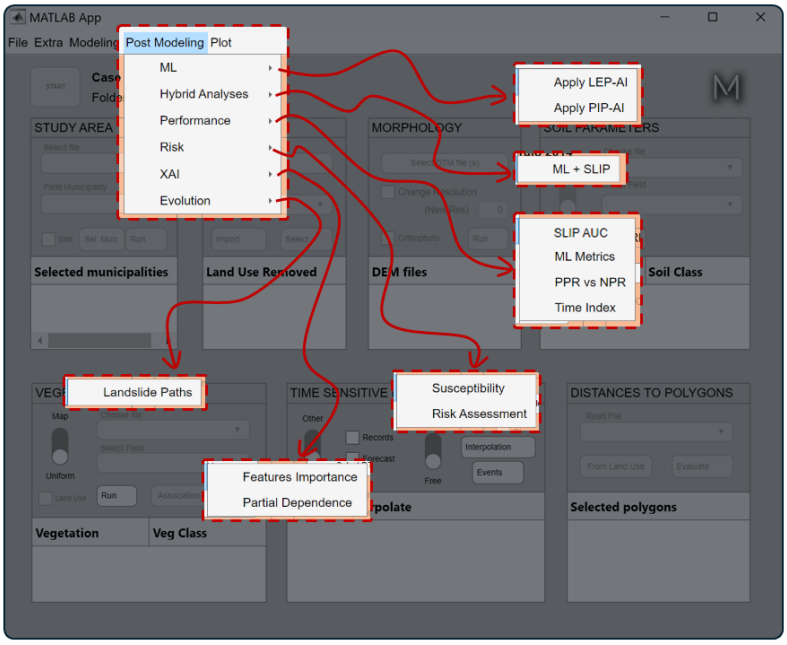

Figure IV-57: Scheme of the possible processes to perform with the "Post Modelling" top-menu in X-SLIP. The functionalities are grouped into six macro-categories, each one with its buttons. Each button triggers a main module (or function) of the X-SLIP platform.

The functionalities of this menu will be briefly treated. For a more detailed insight into the various modules, the reader is referred to the source code in the Appendices section.

To start with, the "ML" group contains the button <Apply LEP-AI>, which triggers the main module of X-SLIP called 'F_MLA_ApplyANN.m', serves to apply the LEP-AI model in contexts that are different from the one of the training, therefore also for future predictions. Instead, the button <Apply PIP-AI> serves for the same reasons but triggering the main module of X-SLIP called 'F_MLB_ApplyANN.m', which makes use of the PIP-AI model.

The "Hybrid Analyses" contains just a single button. The <ML + SLIP> button serves to create the H-SLIPmodel, triggering the 'F_HybridAnalysis.m' main module of X-SLIP.

To continue, the "Performance" group contains different buttons related to the assessment of model performance. The <SLIP AUC> button triggers the main module called 'F_PerfSLIP.m' and serves to create a special AUROC, where the true positives are evaluated

differently. In fact, if a certain percentage of pixels inside a specific unstable area is true, then all the pixels of that area are assumed as true positives. With this button, it is required to perform a SLIP analysis before. Moving forward, the <ML Metrics> button triggers the 'F_PerfSLIP.m' main module and serves to assess different quality metrics both for LEP-AI and PIP-AI models. Specifically, these metrics are the same seen in Section 3.2.3.3 and 3.3.6.3. Instead, <PPR vs NPR> and <Time Index> buttons, which trigger 'F_MLB_PPRvsNPR.m' and 'G_MLB_TimeIndex.m' main modules of X-SLIP, serve to create the PPR and NPR (with the first button), and also the TI (with the second button, for more info please see Section 3.3.6.3).

The "Risk" group contains the <Susceptibility> button, which triggers the main module 'F_Susceptibility.m', and the <Risk Assessment> button, which triggers the main module 'F_WeightedRiskAnalysis.m'. Both these buttons are related to risk analyses, i.e., analyses that consider different factors, such as mechanical susceptibility but also the presence of people and buildings. In other words, a risk analysis involves the interaction between different factors to assess a final level of risk for each pixel of the map (Corominas et al., 2014; Dai et al., 2002; Fell et al., 2020; Moraci et al., 2017).

The "XAI" group contains the functionalities related to the eXplainable Artificial Intelligence, that currently is given by the ranking of the feature importance, through the <Features Importance> button, and the PDP, by means of the <Partial Dependence> button.

To conclude, the "Evolution" group contains functionalities related to the assessment of cinematic aspects of landslides, thus everything that happens after the triggering of a landslide. Currently, just a single button is present, i.e., <Landslide Paths>, which triggers the main module of X-SLIP called 'G_LandslidePathEvolution.m'. With this module, the preferential paths that the possible landslide may follow are assessed, but also the cinematic and dynamic aspects, such as the speed, acceleration, dynamic friction, and eroded depth of the moving landslide body in each point of its path. For this purpose, a simplified and efficient model was created and implemented in X-SLIP (see the following Section 6.1 of Chapter VI).

4.5 Plot Menu Of X-SLIP

The top menu "Plot" of X-SLIP contains different sections, integrating the several plots that can be generated, according to what the user wants to show. Once generated, these plots are stored inside the 'Figures' subfolder.

Despite the numerous possibilities in creating these figures, the various functionalities will not be elaborated upon in this text, due to reasonable space constraints. The reader is therefore invited to consult the code in the Appendices section. However, a general overview of this menu is shown in Figure IV-58.

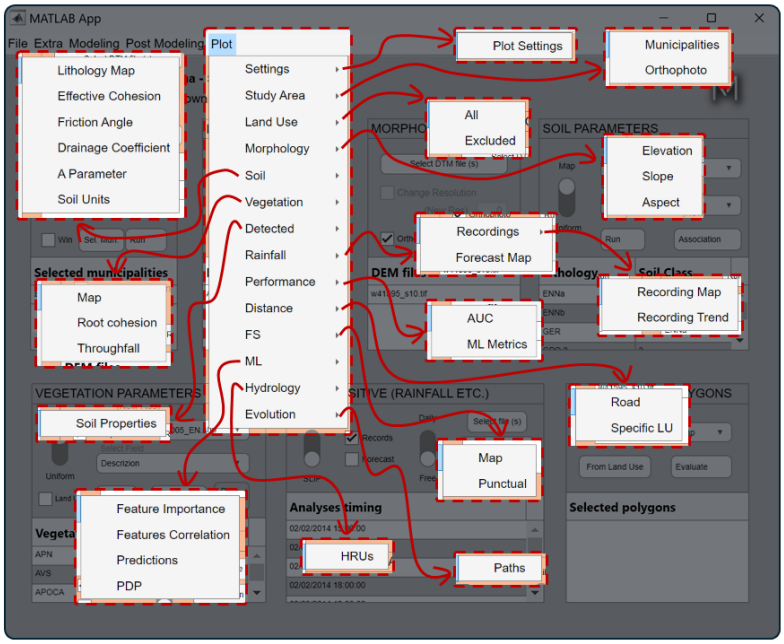

Figure IV-58: Scheme of the possible figures to plot with the "Plot" top-menu in X-SLIP. The functionalities are grouped into several macro-categories, depending on the type of result to show, and each macro-group has its buttons. Each button triggers a main module (or function) of the X-SLIP platform.

V RESULTS

This chapter will present the latest recent results obtained from analyses of a vast mountainous and hilly area in the provinces of Reggio Emilia and Parma, which have historically been affected by several rainfall-induced shallow landslide events.

Specifically, REs and LEs that occurred during the last century, starting from the early 2000s, have been analysed. Several preliminary analyses were conducted to identify areas on which to focus the studies, which will be explored in greater detail in the following sections. Furthermore, it was necessary to conduct extensive data research across various portals to consolidate everything into a single and general database, designed for easy access and consultation.

Therefore, in the upcoming sections, we will first provide a brief overview of the study area (for all models used, since different selections of municipalities and LEs were analysed depending on the model used) (Section 5.1), and present the results obtained respectively with LEP-AI (Section 5.2), PIP-AI (Section 5.3), SLIP (Section 5.4), and H-SLIP (Section 5.5).

5.1 THE CASE STUDY

5.1.1 STUDY AREA AND DATASET OF LEP-AI MODEL

The study area selected for the LEP-AI model is located in the hilly and mountainous zones of the Parma and Reggio Emilia provinces (Figure V-1). Specifically, 40 municipalities (AUs) were selected, each containing at least 4 rainfall-induced shallow landslides, which occurred during a defined reference period, that is from January 1, 2000, to December 31, 2023 (see Table V-1 and V-2 for a more in detail view).

Regarding the landslide inventory used, a single generalized database was created from various sources. In fact, a total of five sources were used to create the final inventory: (i) a dataset obtained from the Emilia Romagna geoportal (*Geoportale Regione Emilia-Romagna*, n.d.), containing approximatively 3,500 historical rainfall-induced landslides in the provinces of Parma and Reggio Emilia, from the 17th century until January 1, 2020, which is the date of the last recorded event; (ii) the ITALICA dataset (Peruccacci et al., 2023b), containing approximately 6,300 rainfall-induced shallow landslides throughout Italy, starting from January 12, 1996, the date of the first event, until December 31, 2020, which is the date of the last recorded landslide; (iii) the dataset of landslide events that occurred in Emilia Romagna

during the intense rainfall event of May 17, 2023, which was obtained from the OpenDataER (*OpenDataER*, n.d.) platform and contains around 82,000 landslides; (iv) the dataset of some shallow landslides (97) that occurred in the Parma Apennines during the rainfall event of April 5, 2013, obtained from internal studies conducted at the Department of Civil and Environmental Engineering (DIA) of the University of Parma; (v) another dataset containing landslides (32) that occurred in the Reggio Emilia Apennines during the rainfall event of April 11, 2005, also obtained from internal studies conducted by the DIA of the University of Parma.

Unfortunately, there is a lack of data for the years 2021 and 2022, which were excluded. Furthermore, for the creation of various REs to be included in the LEP-AI training dataset, it was decided to exclude, depending on the AU, the years in which no landslide events were recorded. This was done with the intent to minimize potential dataset deficiencies in reporting landslide events. In other words, for each AU, only the REs and LEs from years in which at least one landslide event was recorded are included in the final dataset. A general summary of the events is provided in Figure V-4, V-5, and Table V-1, V-2.

Regarding rainfall and temperature data, it was decided to use raster maps containing such data across the globe for each day of the year (*GloH2O*, n.d.), to ensure data continuity. Indeed, although rain gauge station data are more precise, these often-present temporal gaps where no recordings are available, thus complicating the generation of REs, which must be guaranteed with continuity from 2000 to 2023. Concerning NDVI, this was obtained through raster maps from EcoDataCube (*EcoDataCube*, n.d.), with temporal discretization equal to 4 months. Finally, regarding static data, such as elevation and slope (Figure V-2 and V-3 respectively), which in the case of LEP-AI can be derived from a single source (DEM) the Emilia-Romagna Geoportal (same source of dataset i) was use, which contains the DEM of the entire region with 5x5 m resolution, dated 2014. To conclude, using these sources, the total number of REs and LEs from 2000 to 2023 is equal to 10,501 and 391, respectively.

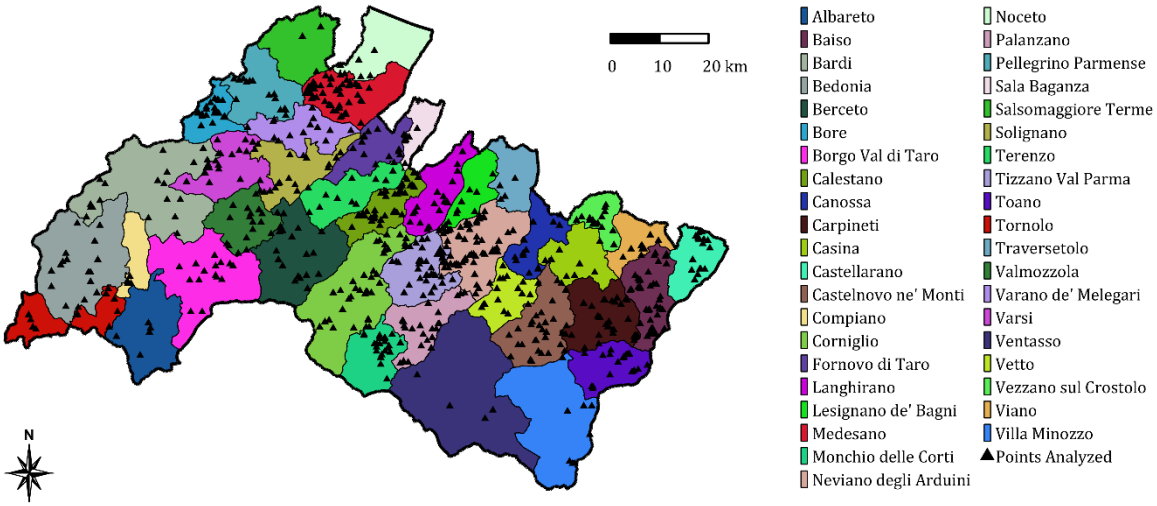

Figure V-1: Map of the 40 municipalities (Area Units) used for the LEP-AI model.

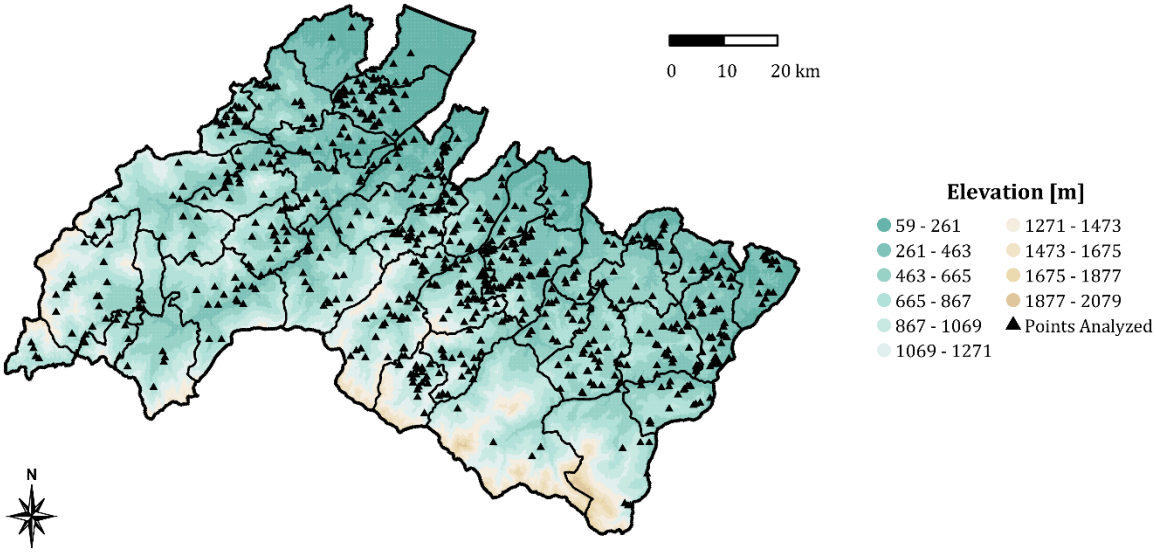

Figure V-2: Representative elevation map (with ranges), for the 40 area units used with the LEP-AI model.

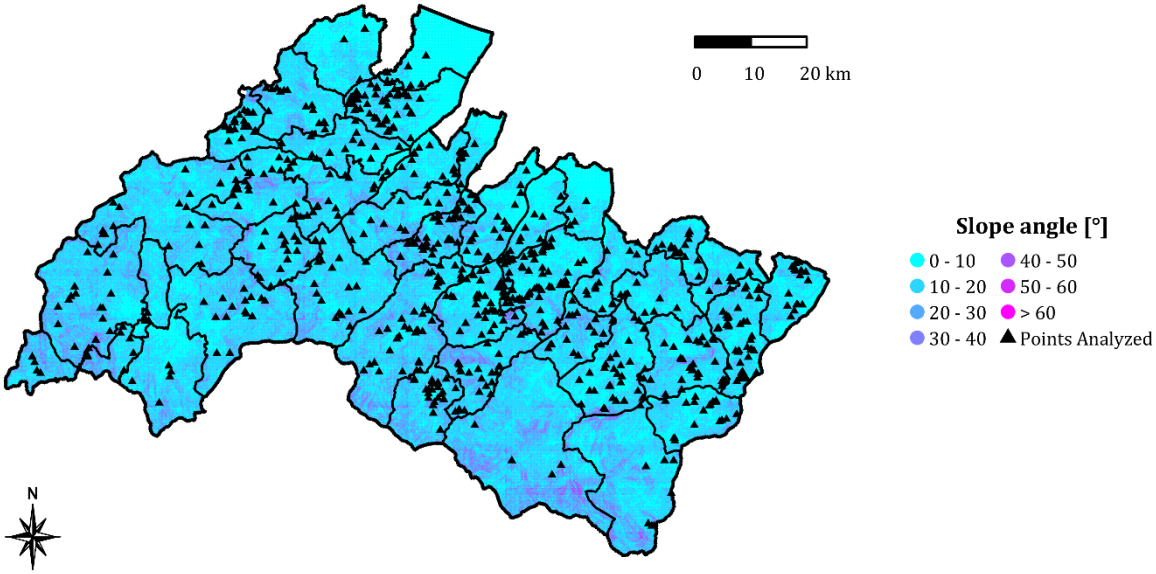

Figure V-3: Representative slope map (with ranges), for the 40 area units used with LEP-AI model.

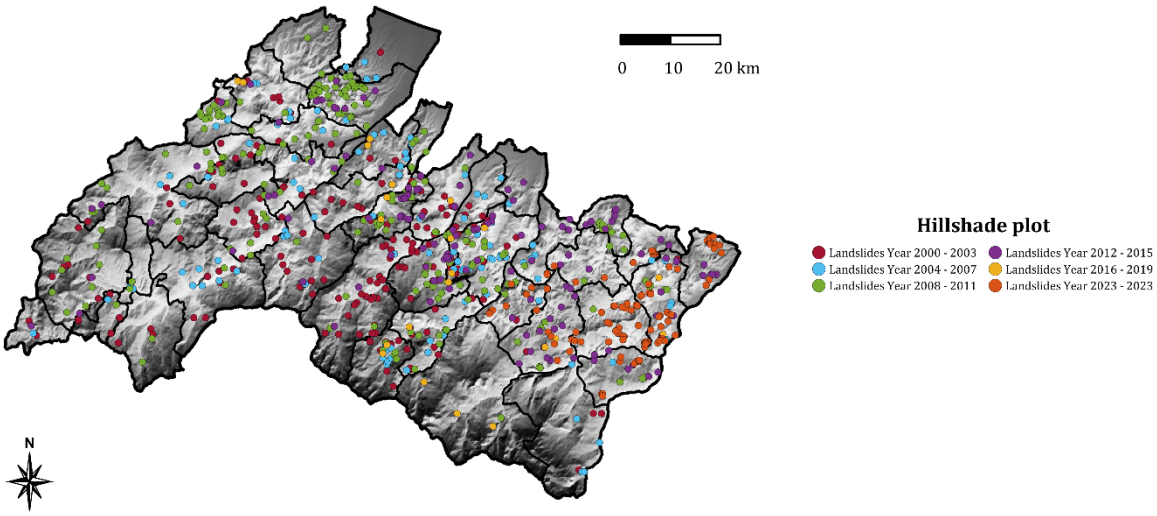

Figure V-4: Map of the Landslide Events used for the training of the LEP-AI model, grouped per range of years.

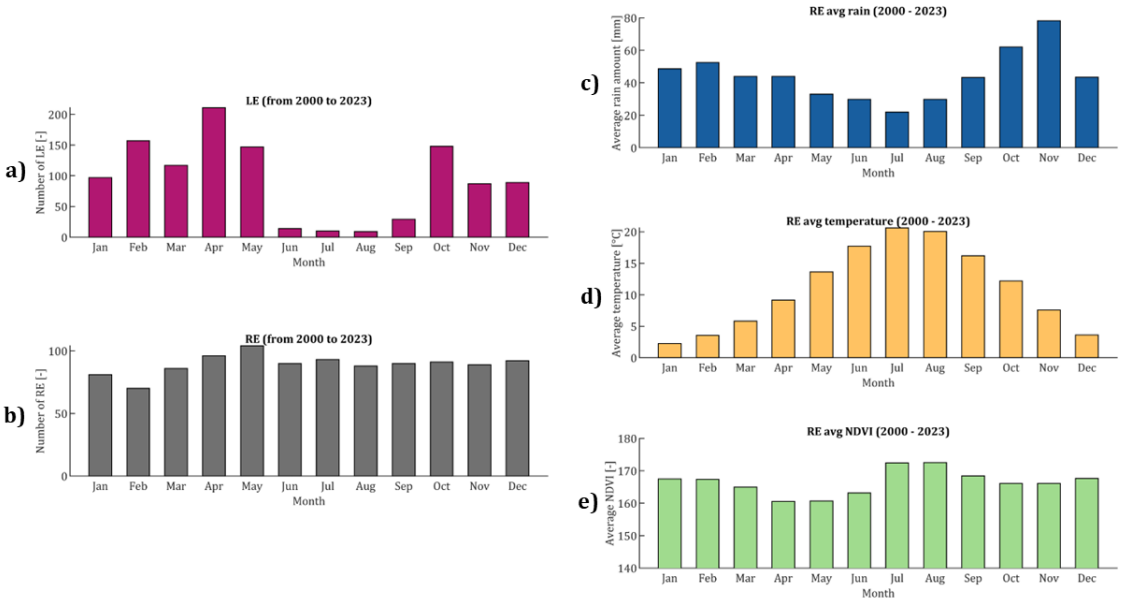

Figure V-5: Monthly statistics and metrics (from 2000 to 2023) of the data contained in the general dataset used for LEP-AI training. Particularly, the various bar plots contain the number of Landslide Events per month (a); the number of Rainfall Events per month (b); the monthly average rain (c); the monthly average temperature (d); the monthly average NDVI (e).

Area Unit	'00	'01	'02	'03	'04	'05	'06	'07	'08	'09	'10
Albareto	0	0	2	0	0	0	0	0	1	0	1
Baiso	2	1	2	0	2	13	0	0	2	1	6
Bardi	2	0	4	0	2	3	0	0	0	9	2
Bedonia	5	0	2	0	0	0	0	1	0	4	4
Berceto	12	2	0	0	4	0	0	0	0	1	3
Bore	1	0	1	0	1	0	0	4	2	9	3
Borgo Val di Taro	5	1	0	3	4	0	0	2	0	0	0
Calestano	4	3	0	0	0	1	0	2	0	20	2
Canossa	0	0	0	0	3	1	0	0	0	0	0
Carpineti	0	0	0	0	1	3	0	0	0	1	0
Casina	0	0	0	0	0	5	0	0	0	0	1
Castellarano	0	0	0	0	0	2	0	0	0	0	1
Castelnovo ne' Monti	0	1	0	0	0	1	0	0	2	0	2
Compiano	0	0	0	0	0	0	0	0	0	0	0
Corniglio	30	1	2	3	2	1	0	1	1	1	3
Fornovo di Taro	0	2	0	2	1	0	0	0	0	0	0
Langhirano	5	2	3	0	2	1	4	0	0	0	1
Lesignano de' Bagni	0	0	1	0	2	0	0	0	2	1	2
Medesano	2	2	0	1	6	1	3	0	0	44	0
Monchio delle Corti	6	6	4	2	5	0	0	0	0	8	1
Neviano degli Arduini	7	10	3	2	18	3	2	5	7	5	15
Noceto	0	0	0	0	0	0	0	0	0	0	0
Palanzano	9	4	5	0	9	2	2	0	0	0	0
Pellegrino Parmense	0	0	0	0	0	0	1	0	3	4	2
Sala Baganza	1	0	0	0	0	0	0	0	0	0	0
Salsomaggiore Terme	3	1	1	0	0	0	0	0	0	0	0
Solignano	1	0	2	0	3	1	2	0	0	6	1
Terenzo	2	2	0	0	0	3	0	0	1	5	0
Tizzano Val Parma	17	5	1	1	3	0	2	0	3	7	6
Toano	0	0	0	0	0	0	0	0	0	0	0
Tornolo	0	0	0	0	0	0	0	0	0	0	0
Traversetolo	0	0	0	0	0	1	0	0	0	0	0
Valmozzola	5	0	2	0	1	2	0	0	0	1	3
Varano de' Melegari	8	0	0	0	1	0	0	0	0	0	2
Varsi	8	1	0	0	3	0	0	1	0	7	0
Ventasso	0	0	0	0	1	0	1	0	0	2	0
Vetto	7	0	0	0	0	0	0	0	0	6	1
Vezzano sul Crostolo	3	1	0	0	2	0	0	0	0	8	1
Viano	0	0	0	1	0	1	0	0	0	11	2
Villa Minozzo	0	0	0	0	0	12	0	0	0	0	1

Table V-1: General statistics of landslides occurred during the period 2000-2010 for each Area Unit included in the dataset used for the LEP-AI model, part I.

Area Unit	‘11	‘12	‘13	‘14	‘15	‘16	‘17	‘18	‘19	‘20	‘23
Albareto	0	0	0	0	0	0	0	0	0	0	1
Baiso	1	0	4	3	3	0	2	1	1	0	36
Bardi	0	0	2	2	0	0	0	0	0	0	0
Bedonia	0	0	0	2	1	0	0	0	0	0	0
Berceto	0	0	1	2	0	0	0	0	0	0	0
Bore	3	0	1	2	1	0	0	0	0	0	0
Borgo Val di Taro	4	0	1	0	0	0	0	0	0	0	0
Calestano	1	0	6	8	0	0	0	0	1	0	0
Canossa	0	0	0	1	4	2	0	0	0	0	2
Carpineti	0	0	7	3	0	0	0	0	0	0	39
Casina	0	0	0	2	1	0	0	0	0	0	1
Castellarano	0	0	4	0	0	0	0	0	0	0	16
Castelnovo ne' Monti	1	1	14	2	1	0	0	0	0	0	9
Compiano	0	0	4	0	0	0	0	0	0	0	0
Corniglio	1	0	16	2	4	1	0	1	1	0	0
Fornovo di Taro	0	0	14	0	0	0	0	0	0	0	0
Langhirano	0	0	3	1	1	1	0	0	1	0	0
Lesignano de' Bagni	1	0	4	0	0	0	0	0	0	0	0
Medesano	0	0	5	1	0	1	0	0	0	0	0
Monchio delle Corti	0	0	9	0	0	0	0	0	0	0	0
Neviano degli Arduini	1	0	20	12	1	4	1	0	2	0	0
Noceto	0	0	7	0	0	0	0	0	0	0	0
Palanzano	0	0	14	0	0	0	0	0	0	0	0
Pellegrino Parmense	0	0	6	0	0	1	0	0	0	0	0
Sala Baganza	0	0	6	0	0	0	0	0	0	0	0
Salsomaggiore Terme	0	0	0	0	0	0	0	0	0	0	0
Solignano	1	0	1	2	0	2	0	0	0	0	0
Terenzo	0	0	1	0	0	0	0	0	0	0	0
Tizzano Val Parma	10	0	36	1	0	0	0	1	0	0	0
Toano	1	0	10	13	0	2	0	0	0	0	0
Tornolo	0	0	0	0	0	1	1	0	1	0	9
Traversetolo	0	0	0	0	0	0	0	0	0	0	4
Valmozzola	0	0	5	1	4	0	0	0	0	0	0
Varano de' Melegari	0	0	3	2	0	0	0	0	0	0	0
Varsi	0	0	2	0	0	0	0	0	0	0	0
Ventasso	0	0	0	0	0	0	0	0	0	0	0
Vetto	0	0	1	1	0	0	0	0	0	0	0
Vezzano sul Crostolo	1	0	1	0	0	0	3	0	0	0	8
Viano	1	0	1	1	1	0	0	0	0	0	1
Villa Minozzo	0	0	4	2	5	0	0	0	0	0	9

Table V-2: General statistics of landslides occurred during the period 2011-2023 (2021 and 2022 excluded) for each Area Unit included in the dataset used for the LEP-AI model, part II.

5.1.2 Study Area And Dataset of PIP-AI, SLIP, And H-SLIP Models

The study area used with the PIP-AI, SLIP, and H-SLIP models is a subset of some municipalities seen for the LEP-AI model. Specifically, the municipalities most susceptible to landslides were chosen, i.e., those where the recorded landslides, obtained from the LEP-AI general database, exceeded a threshold of 70 during the reference period (from 2000 to 2023). As a result, four municipalities were selected (Figure V-6): Baiso (80 landslides), Corniglio (71 landslides), Neviano Degli Arduini (118 landslides), and Tizzano Val Parma (93 landslides). A summary of the landslides is presented in Figure V-7.

Regarding the LEs considered, these are seven, corresponding to the seven main events that occurred in these areas since 2000. Specifically, the events analysed are:

- November 1, 2000 (LE1) - approximately 190 mm of rainfall from October 30 to November 10, 2000.
- March 1, 2004 (LE2) - approximately 293 mm of rainfall from February 18 to March 1, 2004.
- April 11, 2005 (LE3) - approximately 137 mm of rainfall from April 9 to April 12, 2005.
- November 1, 2010 (LE4) - approximately 246 mm of rainfall from October 30 to November 3, 2010.
- April 5, 2013 (LE5) - approximately 376 mm of rainfall from March 28 to April 9, 2013.
- March 5, 2014 (LE6) - approximately 96 mm of rainfall from March 1 to March 5, 2014.
- May 17, 2023 (LE7) - approximately 203 mm of rainfall from May 10 to May 20, 2023.

These events represent excellent case studies due to their diverse characteristics, including varying temporal windows and different rainfall patterns preceding the events.

The resources used to obtain the input data necessary for training, calibrating, and testing the models are varied. For rainfall and temperature data, unlike the LEP-AI model, this study utilized data from rain gauge stations retrieved from Dext3r (*Dext3r*, n.d.), as they are generally more precise. Unfortunately, for event LE1, the only available data came from a single station, resulting in uniform data across the area.

For NDVI, vegetation species probability maps, clay content, and sand content, the data were obtained from EcoDataCube (*EcoDataCube*, n.d.). Morphological data (derived from DEM processing), as well as maps of sub/top-soil classes, vegetation, land use, and road networks, were retrieved from the Geoportal of Emilia-Romagna (*Geoportale Regione Emilia-Romagna*, n.d.) and ISPRA (*ISPRA*, n.d.). A summary of the main aspects is provided in Figures V-8, V-9, V-10, V-11, V-12, V-13, and V-14.

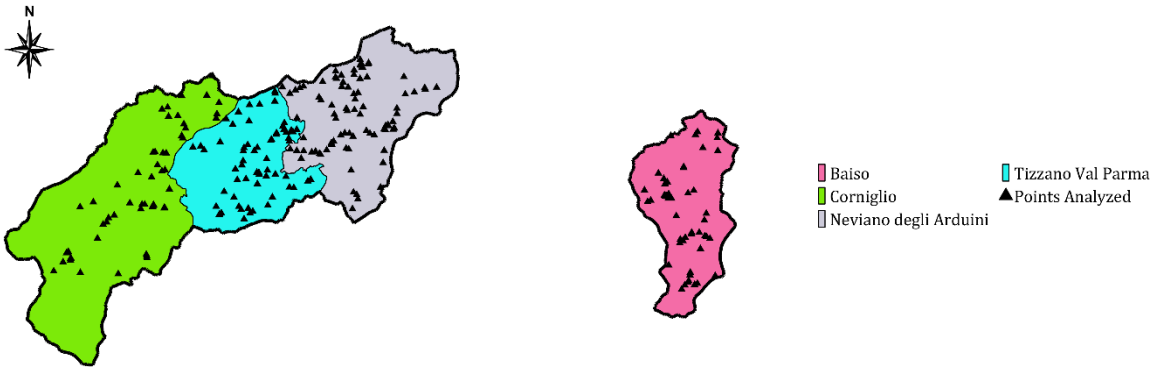

Figure V-6: Map of the four municipalities used as study are for PIP-AI, SLIP, and H-SLIP models.

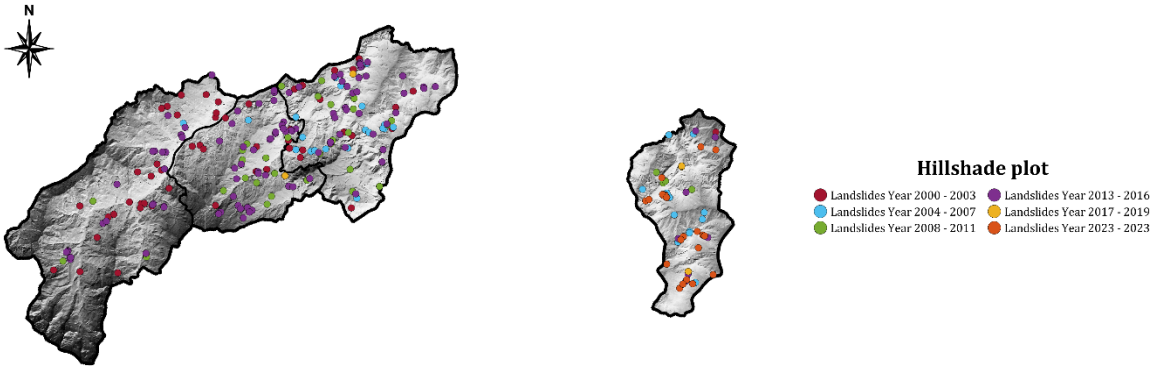

Figure V-7: Map of the Landslide Events used for the training of PIP-AI model and the calibration of SLIP, grouped per range of years.

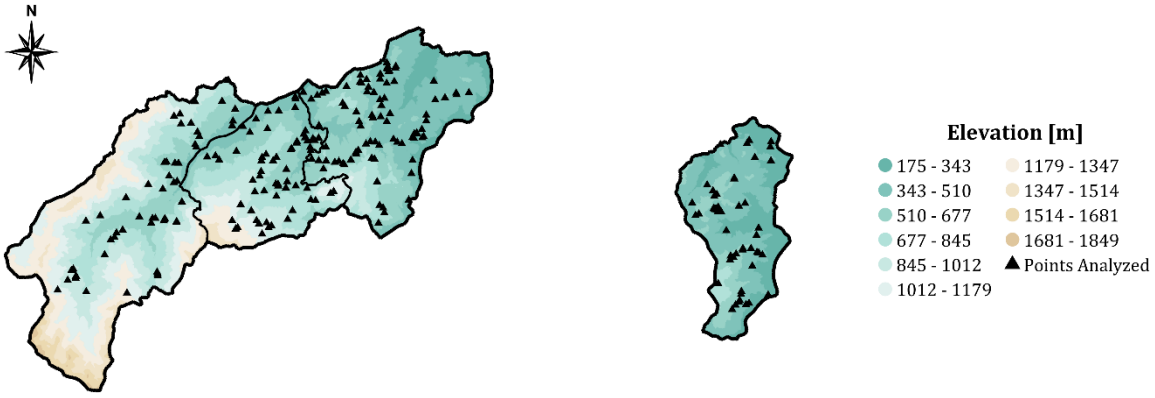

Figure V-8: Representative elevation map (with ranges), for the study area used with the PIP-AI, SLIP, and H-SLIP models, which is made of four municipalities.

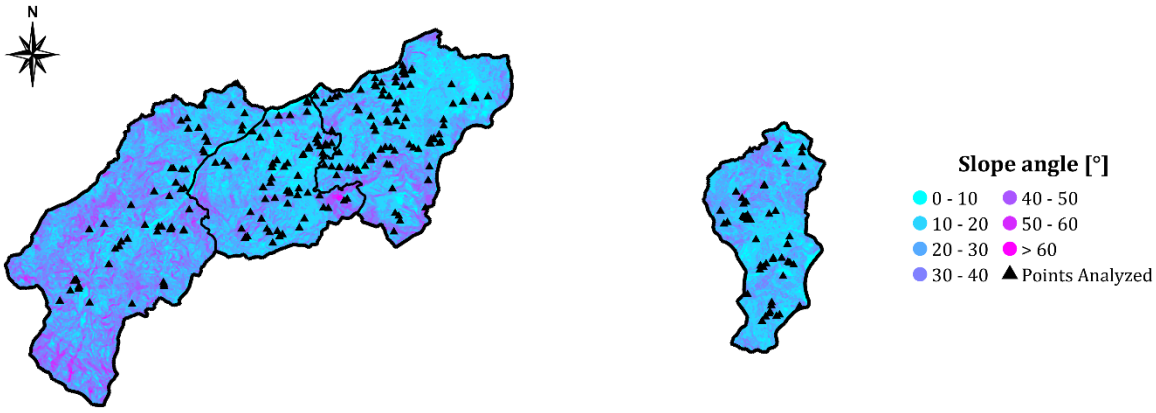

Figure V-9: Representative slope map (with ranges), for the study area used with the PIP-AI, SLIP, and H-SLIP models, which is made of four municipalities.

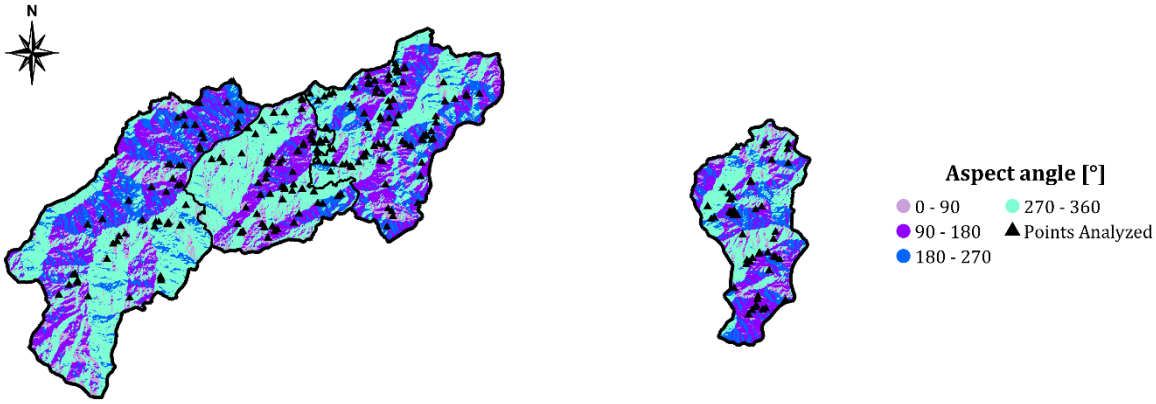

Figure V-10: Representative aspect angle map (with ranges), for the study area used with the PIP-AI, SLIP, and H-SLIP models, which is made of four municipalities.

Figure V-11: Representative map of the distances from road network (with scalebar), for the study area used with the PIP-AI, SLIP, and H-SLIP models, which is made of four municipalities.

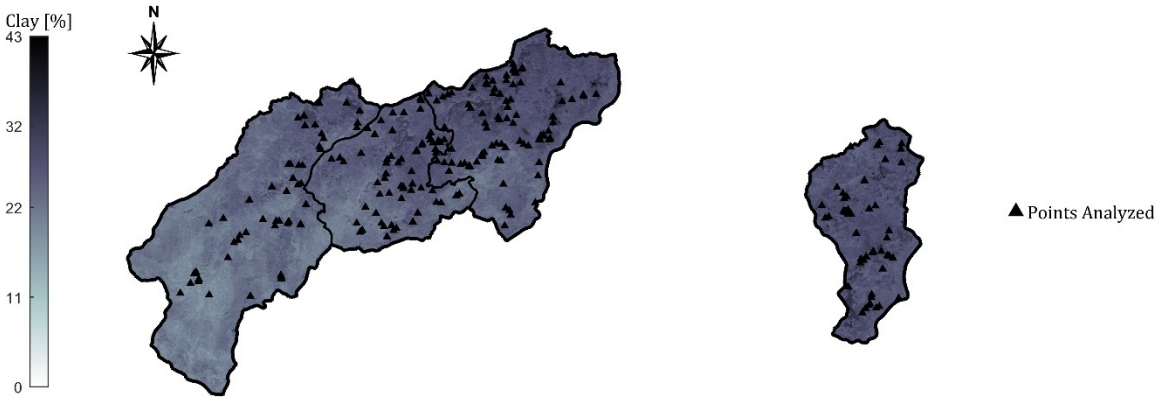

Figure V-12: Representative map of the clay content (with scalebar), for the study area used with the PIP-AI, SLIP, and H-SLIP models, which is made of four municipalities.

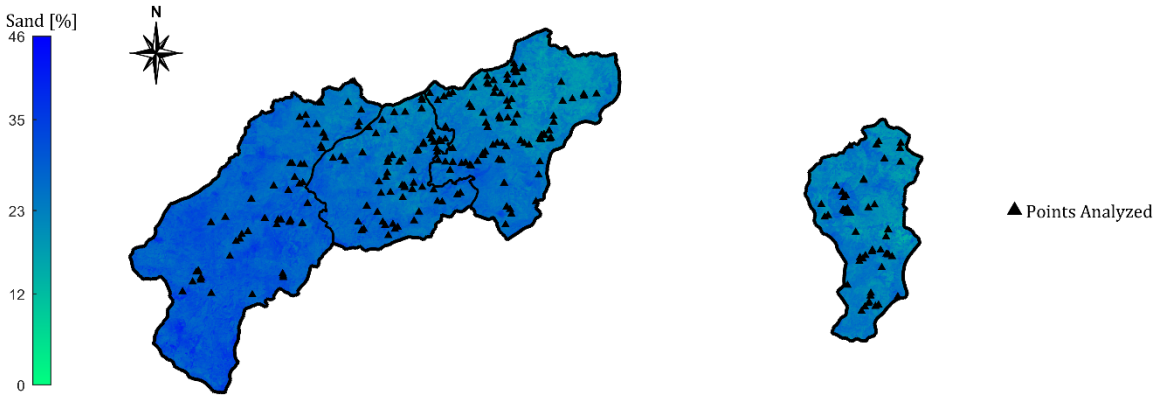

Figure V-13: Representative map of the sand content (with scalebar), for the study area used with the PIP-AI, SLIP, and H-SLIP models, which is made of four municipalities.

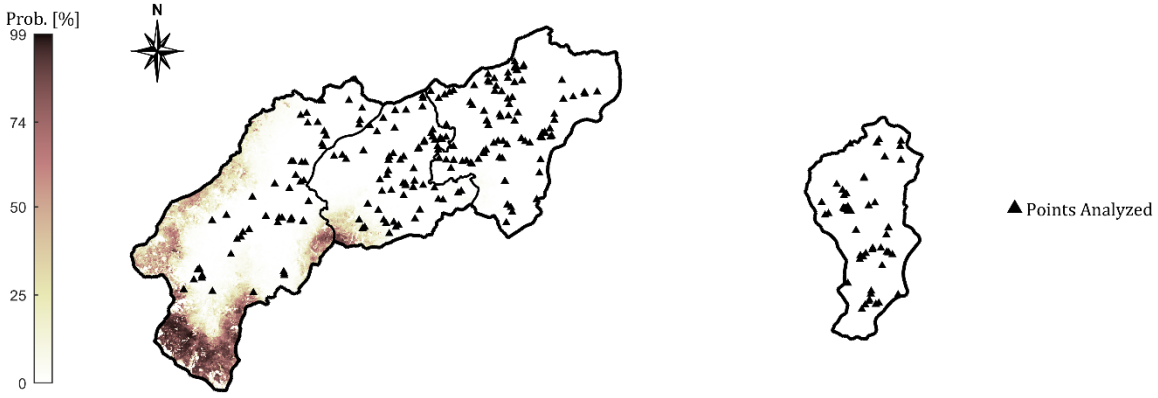

Figure V-14: Representative map of the probability of Abies Alba vegetation species (with scalebar), for the study area used with the PIP-AI, SLIP, and H-SLIP models, which is made of four municipalities.

5.2 The Application Of The LEP-AI Model

The LEP-AI model was developed following a training process involving several ANNs, which differed in their adopted architectures (structures). Consequently, the best-performing ANN was selected based on its Quality Index (QI). Specifically, ANN's architectures were generated considering three factors: the maximum number of layers, set to 5; the maximum number of neurons per layer, set to 120; and the increment in neurons per layer, set to 40. This process led to the generation of 1,024 structures to train (the permutation of the numbers 1, 40, 80, and 120 across a depth of 5).

For activation functions, ReLU was used in all layers except the third, where Tanh was applied. As a result, for networks with three or more layers, the third layer always included neurons with Tanh activation. This decision can be motivated by the fact that deep networks without output limits (as is the case with ReLU, which has no upper bound) tend to "explode." This could lead to excessively large values at the network's end, which can slow down or even prevent training, as small changes at the end of the network may cause significant changes at the beginning, hindering convergence. Thus, incorporating Tanh in the middle of the network offers two main advantages: recentring the values to oscillate symmetrically around 0 ([-1, 0], [0, 1]) and rescaling them to lie within a bounded range of -1 to 1.

Three datasets were utilized, and they are identical across all the tested ANN's structures: a training dataset, a validation dataset, and a test dataset. Therefore, for each analysed structure, reference metrics (see Section 3.2.3.3 and 3.3.6.3) were obtained for all three datasets, with the focus placed on the test dataset, which the trained network had never encountered. These datasets were created with a random split, following these proportions relative to the original dataset: 56% for training, 14% for validation (20% of the 70% initially allocated to training), and 30% for testing. The Pearson Correlation Matrix, shown in Figure V-15, depicts the relationships between the adopted features (see Section 3.2.3.2), calculated over the full dataset. The statistics of the five most important features are shown in Table V-3.

Finally, the QI evaluation was performed on the test portion of the dataset, leading to the identification of the best structure: ANN281. This architecture consisted of four layers with respectively 1 (ReLU), 40 (ReLU), 1 (Tanh), and 120 (ReLU) neurons, to which the final two neurons of the output layer, employing a Softmax activation function, were added.

The results of ANN281 are presented in the following Figures V-16, V-17, V-18, V-19, and V-20. Additionally, a 10-fold cross-validation was performed with this architecture of ANN and the results are shown in Table V-4. Overall, the model demonstrates only marginal performance, with the AUPRGC slightly surpassing the acceptable threshold of 0.5. Furthermore, cross-validation highlights general instability in the results, with acceptable thresholds not consistently achieved. This may be due to limitations in the temporal completeness of the dataset. As evident in Figures V-17, V-18, V-19, and V-20, showing the

results of the predictions for some significant REs over the main four AUs, certain events with high triggering rainfall did not result in LEs.

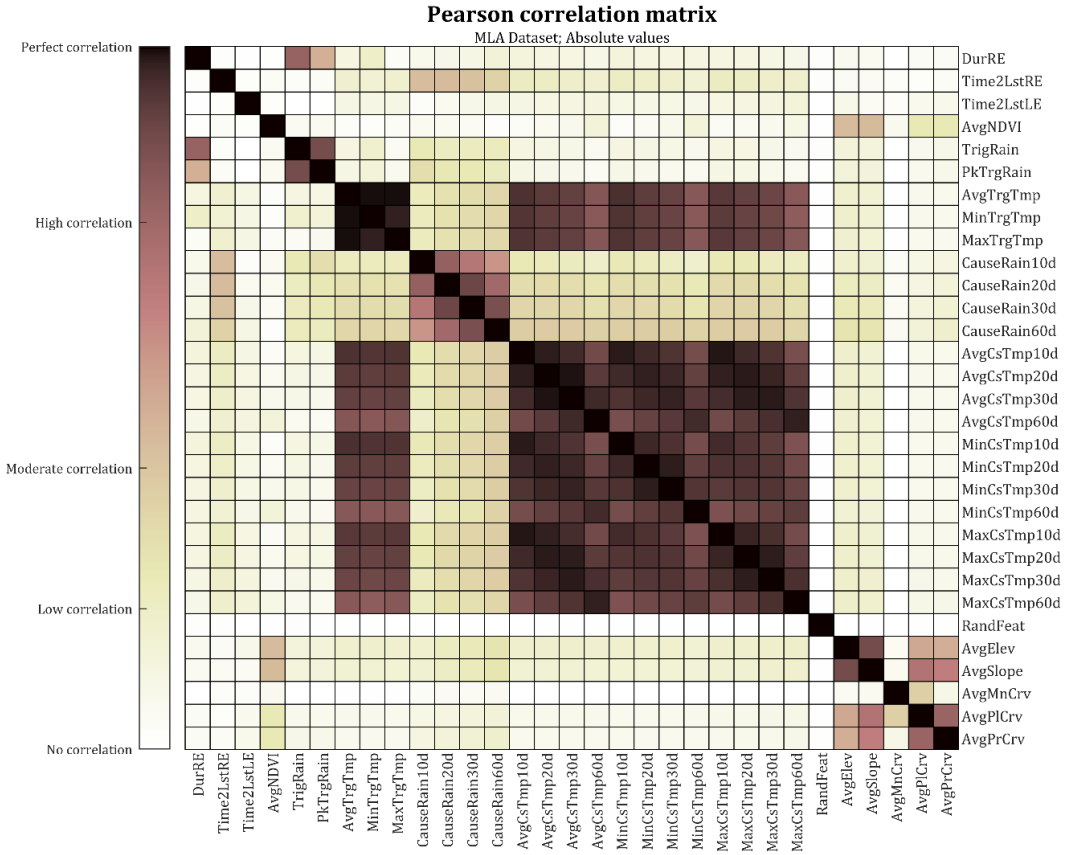

Figure V-15: The correlation between the features adopted for the LEP-AI model. Brown means perfect correlation (both direct and inverse), white means no correlation at all.

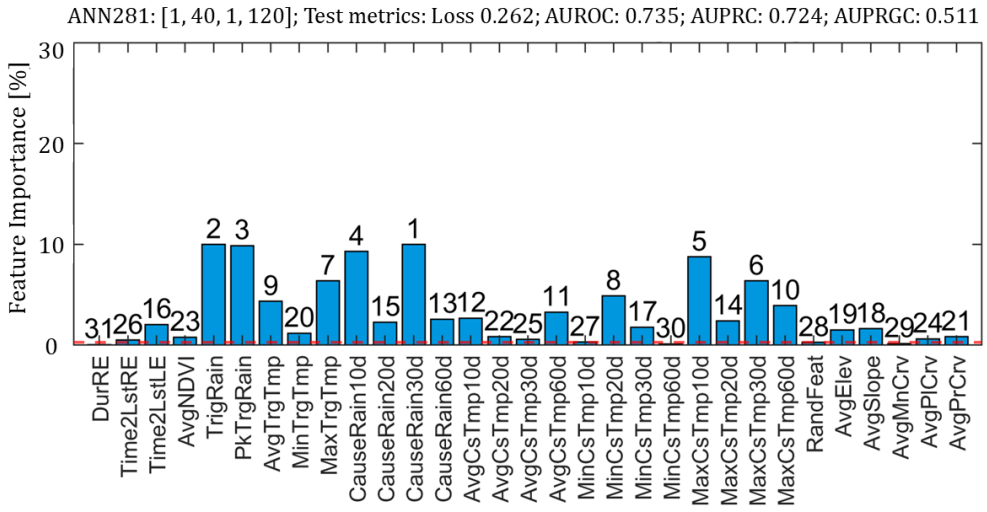

Figure V-16: The ranking of the features used with the LEP-AI model, based on their importance. The method applied to assess the importance is the feature permutation. The most important feature (1st) is the CauseRain30d, the least one (31st) is the DurRE, instead the RandFeat importance, which can be used as a threshold, is the 28th.

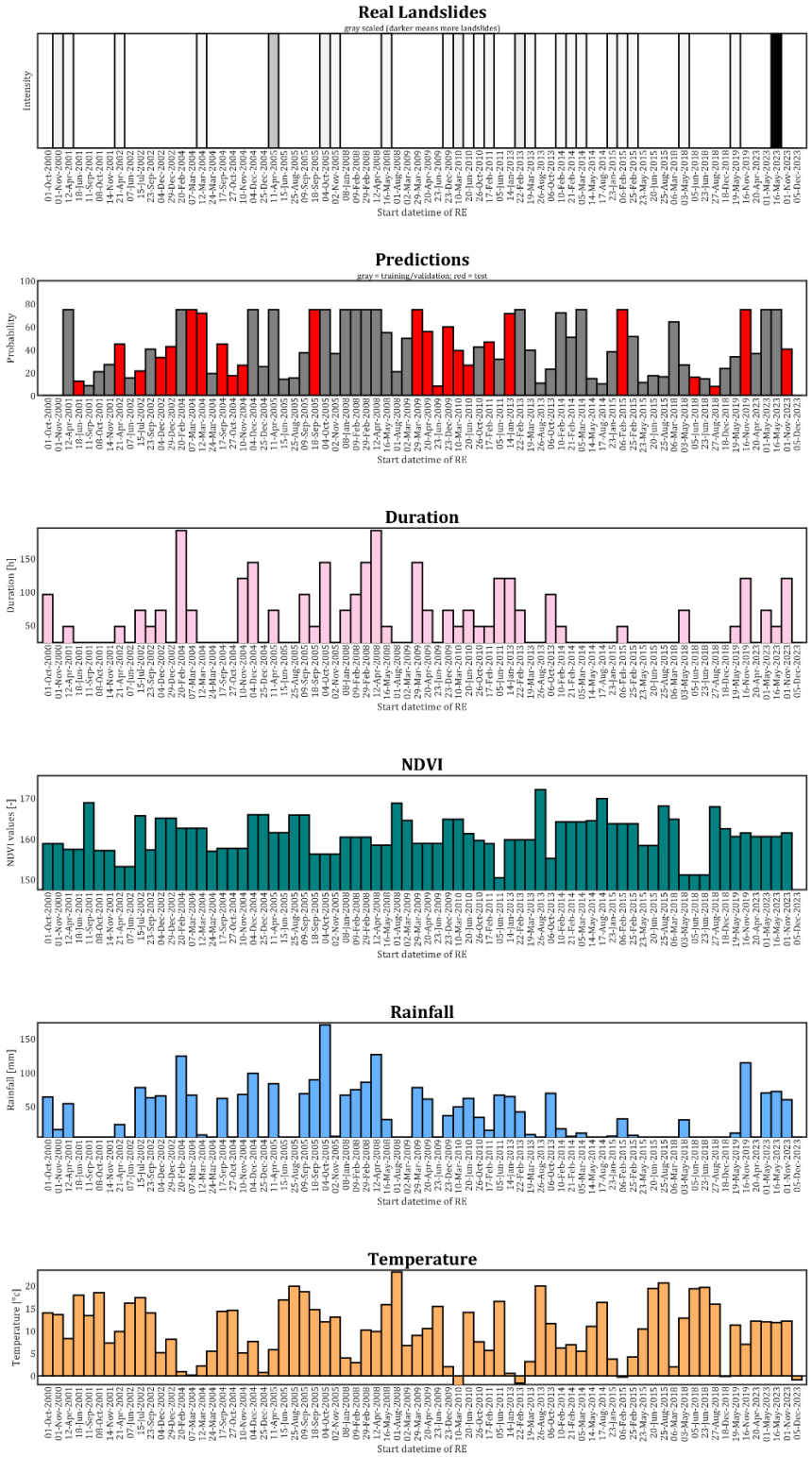

Figure V-17: The results of the predictions for a selection of significant Rainfall Events (REs), over the Baiso Area Unit, where more than 70 landslides occurred during the reference period (2000-2023). The start of the RE is the x-axis and the six plots show: landslide event magnitude; predicted probabilities from ANN281 (red bars are part of test dataset); duration of RE; average NDVI during RE; triggering rainfall of RE; average temperature during RE.

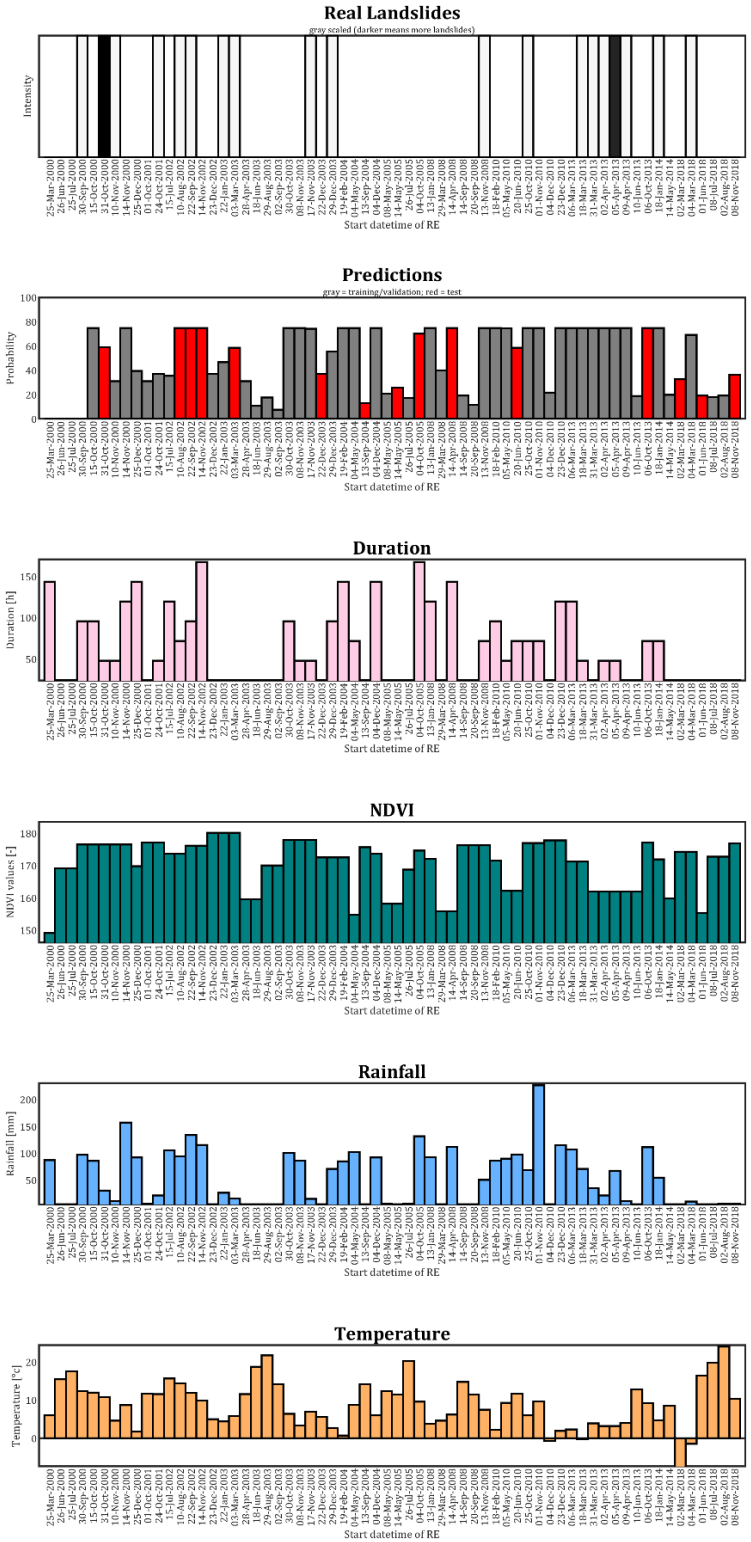

Figure V-18: The results of the predictions for a selection of significant Rainfall Events (REs), over the Corniglio Area Unit, where more than 70 landslides occurred during the reference period (2000-2023). The start of the RE is the x-axis and the six plots show: landslide event magnitude; predicted probabilities from ANN281 (red bars are part of test dataset); duration of RE; average NDVI during RE; triggering rainfall of RE; average temperature of RE.

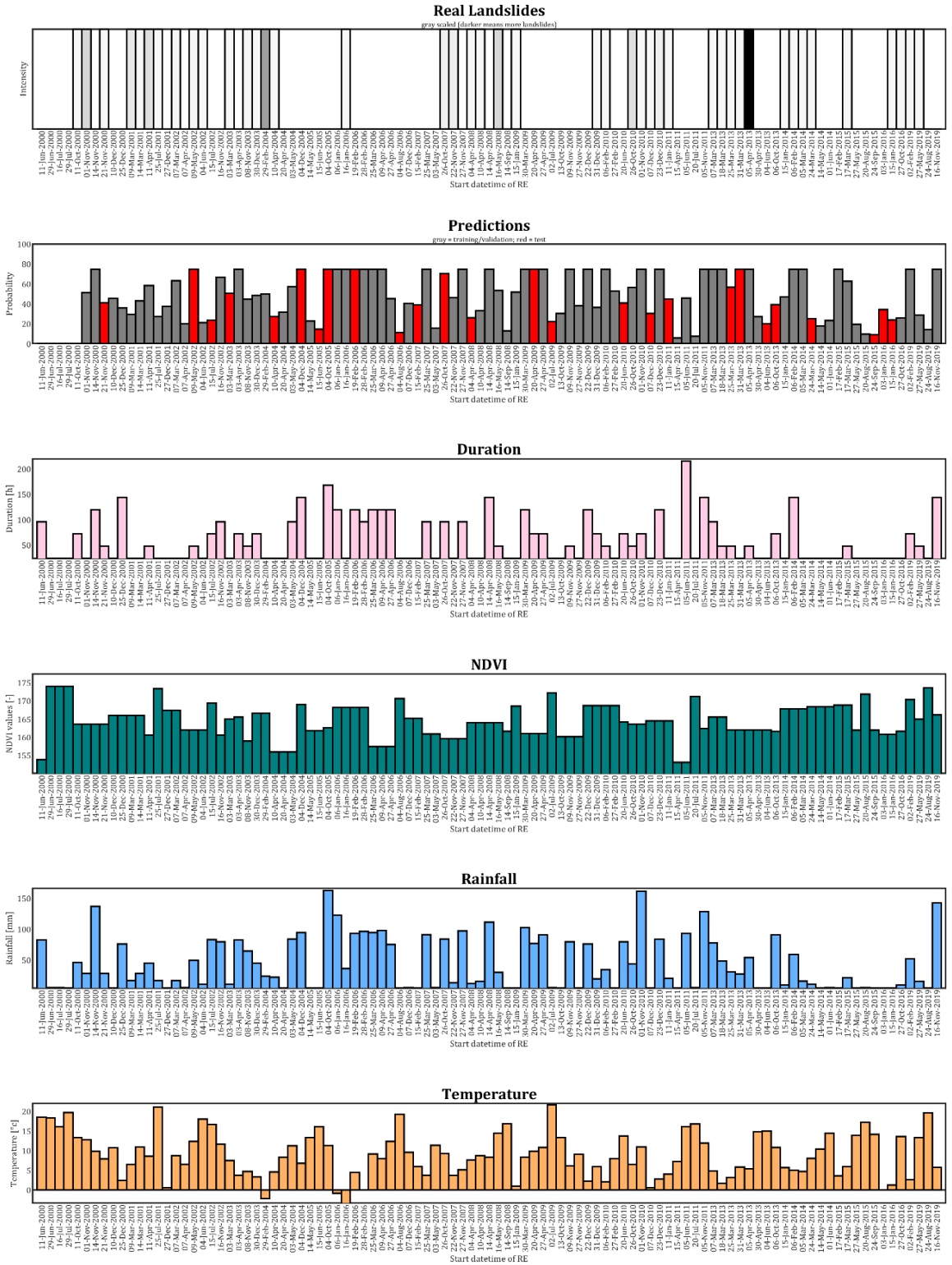

Figure V-19: The results of the predictions for a selection of significant Rainfall Events (REs), over the Neviano Degli Arduini Area Unit (> 70 landslides during the reference period, 2000-2023). The start of the RE is the x-axis and the six plots show: landslide event magnitude; predicted probabilities from ANN281 (red bars are part of test dataset); duration of RE; average NDVI during RE; triggering rainfall of RE; average temperature of RE.

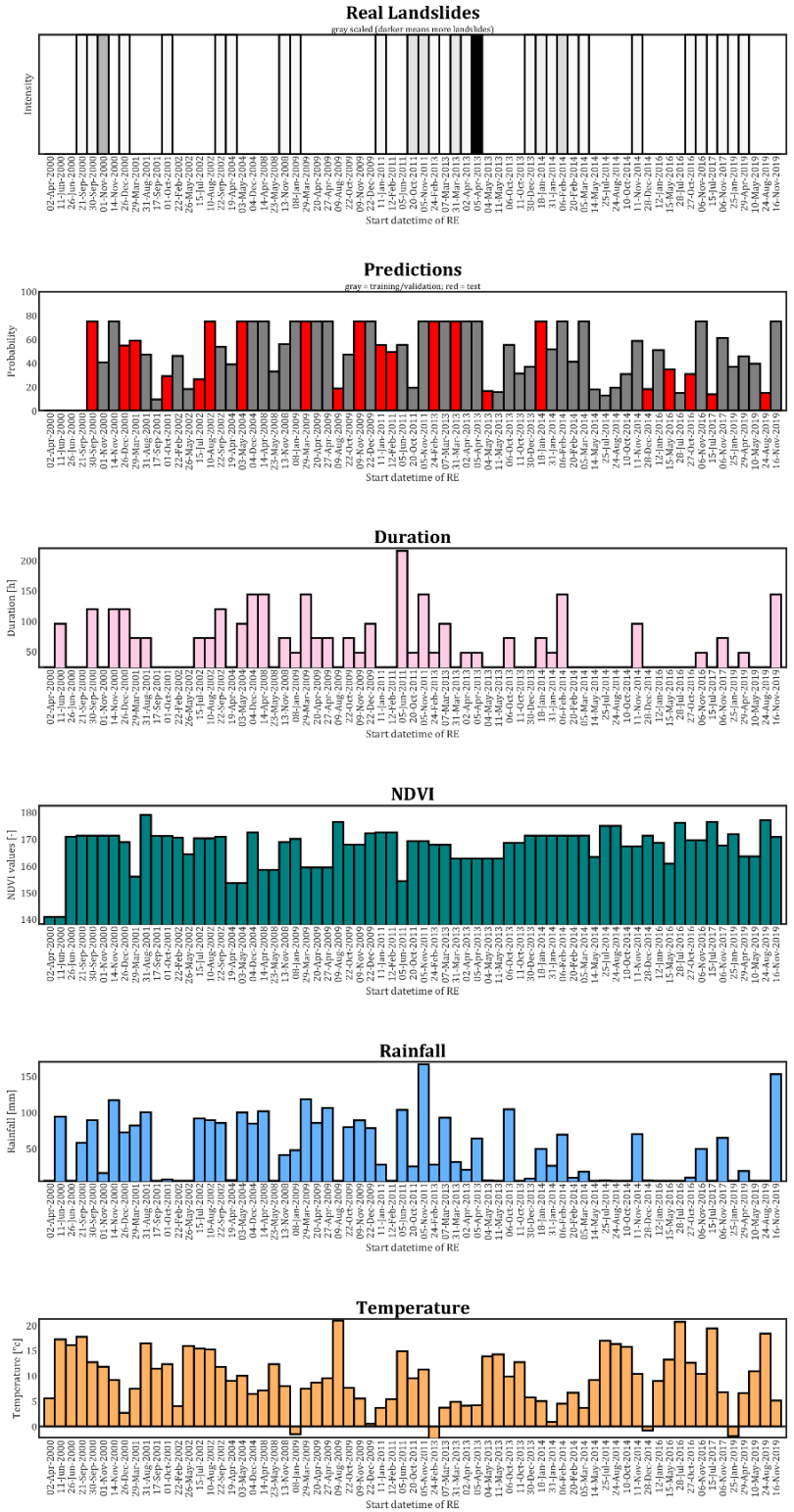

Figure V-20: The results of the predictions for a selection of significant Rainfall Events (REs), over the Tizzano Val Parma Area Unit (> 70 landslides during the reference period, 2000-2023). The start of the RE is the x-axis and the six plots show: landslide event magnitude; predicted probabilities from ANN281 (red bars are part of test dataset); duration of RE; average NDVI during RE; triggering rainfall of RE; average temperature of RE.

Metric	CauseRain30d	TrigRain	PkTrgRain	CauseRain10d	MaxCsTmp10d
MinTLE	9.0	5.0	5.0	5.2	-1.4
MinNLE	5.7	5.0	5.0	5.1	-1.9
MaxTLE	542.5	309.4	115.6	346.8	26.5
MaxNLE	686.0	337.0	158.9	438.4	30.3
AvgTLE	151.3	45.1	25.2	57.5	9.3
AvgNLE	123.2	27.1	18.1	46.1	13.1
MdnTLE	137.1	30.9	21.5	52.1	8.3
MdnNLE	107.0	17.4	13.6	35.8	12.5
StdTLE	88.3	43.9	17.2	42.5	5.4
StdNLE	82.3	27.8	13.6	36.5	6.7
1QrTLE	85.1	15.1	11.4	24.0	5.5
1QrNLE	64.0	8.9	8.3	19.9	7.7
3QrTLE	198.7	63.8	33.6	75.0	12.1
3QrNLE	159.1	34.9	23.6	62.3	18.6

Table V-3: Statistics of the 5 most important features for ANN281 architecture, from the total dataset of LEP-AI. The importance was assessed through the feature permutation technique and the labels of the metrics are abbreviated, with the following criteria -- Min = minimum, Max = maximum, Avg = average, Mdn = median, Std = standard deviation, 1Qr = 1st quartile, 3Qr = 3rd quartile, NLE = not Landslide Events, i.e. the part of the dataset of Rainfall Events without a landslide, TLE = true Landslide Events, that is the part of the dataset containing just Rainfall Events when at least one landslide occurred.

CV	TrROC	VlROC	TsROC	TrPRG	VlPRG	TsPRG	TrLss	VlLss	TsLss	RFI
F1	0.718	0.778	0.713	0.495	0.625	0.474	0.262	0.245	0.270	0.008
F2	0.699	0.683	0.683	0.439	0.444	0.399	0.267	0.274	0.281	0.003
F3	0.685	0.691	0.654	0.413	0.411	0.329	0.269	0.264	0.287	0.012
F4	0.726	0.653	0.681	0.524	0.338	0.395	0.259	0.284	0.288	0.008
F5	0.686	0.750	0.670	0.416	0.522	0.372	0.267	0.242	0.288	0.002
F6	0.729	0.676	0.663	0.538	0.416	0.370	0.258	0.276	0.291	0.003
F7	0.679	0.641	0.652	0.390	0.302	0.339	0.270	0.281	0.289	0.007
F8	0.682	0.771	0.670	0.405	0.554	0.373	0.267	0.239	0.286	0.007
F9	0.694	0.656	0.652	0.437	0.367	0.344	0.274	0.284	0.284	0.020
F10	0.703	0.671	0.682	0.458	0.383	0.400	0.262	0.282	0.280	0.018
Avg	**0.700**	**0.697**	**0.672**	**0.451**	**0.436**	**0.380**	**0.266**	**0.267**	**0.284**	**0.009**

Table V-4: Results of the main metrics for the 10-fold cross-validation performed on the ANN281 architecture of LEP-AI. For each fold there is a training, validation, and test dataset. CV column identifies the fold analysed. Tr = Train, Vl = Validation, Ts = Test, ROC = Area Under the Receiver Operating Characteristic curve, PRG = Area Under the Precision Recall Gain Curve, Lss =cross-entropy loss, RFI = Random Feature Importance.

5.3 The Application Of The PIP-AI Model

The PIP-AI model was developed through a training process involving several neural networks with varying structures (architectures), from which the best one was selected based on the QI. Specifically, the network structures were generated considering three factors: the maximum number of layers (set to 5), the maximum number of neurons per layer (set to 100), and the incremental step in the number of neurons per layer (set to 50). This process resulted in the creation of 243 network structures for training (the permutation of 1, 50, and 100 neurons for up to 5 layers).

The activation functions were chosen as ReLU for all layers, except for the third layer, which employed Tanh for the same reasons described in the previous Section 5.2.

The total dataset was created using unstable landslide polygons (both real and synthetic) and stable polygons generated through the buffering technique (set to 150 m for the inner boundary and 200 m for the outer boundary). These polygons were derived for each of the 7 events using the methods outlined in Section 3.3.5. The RM3 technique (refer to Section 3.3.3) was used to compute rainfall and temperature-related features. Thus, for each of the 7 events, landslide polygons (stable and unstable) were associated with specific LEs.

In addition to the LEs linked to the 7 historical events, a duplicate dataset was created for each event, considering rainfall and temperatures 20 days before the onset of the LE, while maintaining the same polygons, which were treated as stable in this case. In other words, since there are 7 LEs, there are 7 datasets to merge, along with an additional 7 datasets associated with the conditions 20 days prior to the respective LEs.

This process resulted in a total dataset of approximately 222,000 pixels, of which 1,325 were unstable, making the dataset highly imbalanced. Using the SMOTE technique, the dataset was expanded to approximately 441,000 pixels, distributed across various splits. Three sub-datasets were then created and kept consistent for training all network structures: a training set, a validation set, and a test set. For each analysed structure, metrics were computed for all three datasets, with the primary focus on the test set, which remained unseen during training. The dataset was split randomly as follows: 56% for training, 14% for validation (20% of the 70% potentially available for training), and 30% for testing. The Pearson Correlation Matrix, shown in Figure V-21, depicts the relationships between the adopted features (see Section 3.3.6.2) of the total dataset.

The QI evaluation on the test set led to the identification of the best-performing structure: ANN3. This structure featured one layer with 100 (ReLU) neurons, in addition to the final output layer with two neurons employing the Softmax function. To validate this architecture, which demonstrated generally good performance, a cross-validation was conducted. The results, shown in Table V-6, highlight the strong stability of the structure.

Additionally, for ANN3, the feature importance results are displayed in Figure V-22, while the statistics of the top five features are reported in Table V-5. It can be observed that,

unlike the LEP-AI model, which attributed little importance to the NDVI feature (representing vegetative contribution), vegetation plays a significant role in this case, not through NDVI but rather through the probabilities of specific plant species. Among these species, Abies Alba, Quercus Ilex, and Quercus Robur stand out as the most influential.

The results of the Partial Dependence Plots (PDPs) for the 10 most important features are also presented (Figure V-23). Notably, the first feature in terms of importance (TrigRain) and the second (CauseTemp20d) both show a directly proportional relationship with the probability of landslides, increasing it as their values rise. Instead, regarding the main vegetation-related features, it is evident that all three species (Abies Alba, Quercus Ilex, and Quercus Robur) increase the likelihood of landslides when present, rather than reducing it as one might expect. This unexpected behaviour could be due to the network's tendency to associate the presence of these species with potential landslides, given that the majority of landslides occur in areas where these species are prevalent. However, the landslides may have occurred in zones where the vegetation coverage of these species was not uniform. Therefore, it would be advisable to investigate this behaviour at more detailed scales, as it contrasts with findings commonly reported in the literature.

The graph displaying the values of PPR and NPR is shown in Figure V-24. This curve illustrates the trend of these values for the day of the landslide and the 20 days preceding it, for each of the 7 landslide events (indicated with dashed lines). It should be noted, however, that since the adopted rainfall mode is RM3, the maximum value of NPR is often reached a few days prior to the actual landslide day. This behaviour is entirely normal and aligns with the concept of REs and LEs.

Regarding the TI, if the thresholds on PPR and NPR are set to 60%, 70%, and 80%, and the importance of the landslide day is set to 50%, then the three resulting TIs are respectively equal to 63.32% (threshold = 60%), 69.70% (threshold = 70%), and 74.46% (threshold =80%). These results are certainly acceptable but highlight the need for further work on improving the timing of the predictions, because sometimes the NPR increases with REs that are not related to landslides (Figure V-24).

Finally, the model's predictions for the entire study area across the 7 analysed events are shown in Figures V-25, V-26, V-27, V-28, V-29, V-30, and V-31. In these figures, areas highlighted in green and red represent the regions containing the stable and unstable pixels allocated to the training, validation, and test datasets. In other words, the 222,000 pixels of the total dataset were sampled from these areas but at different time intervals.

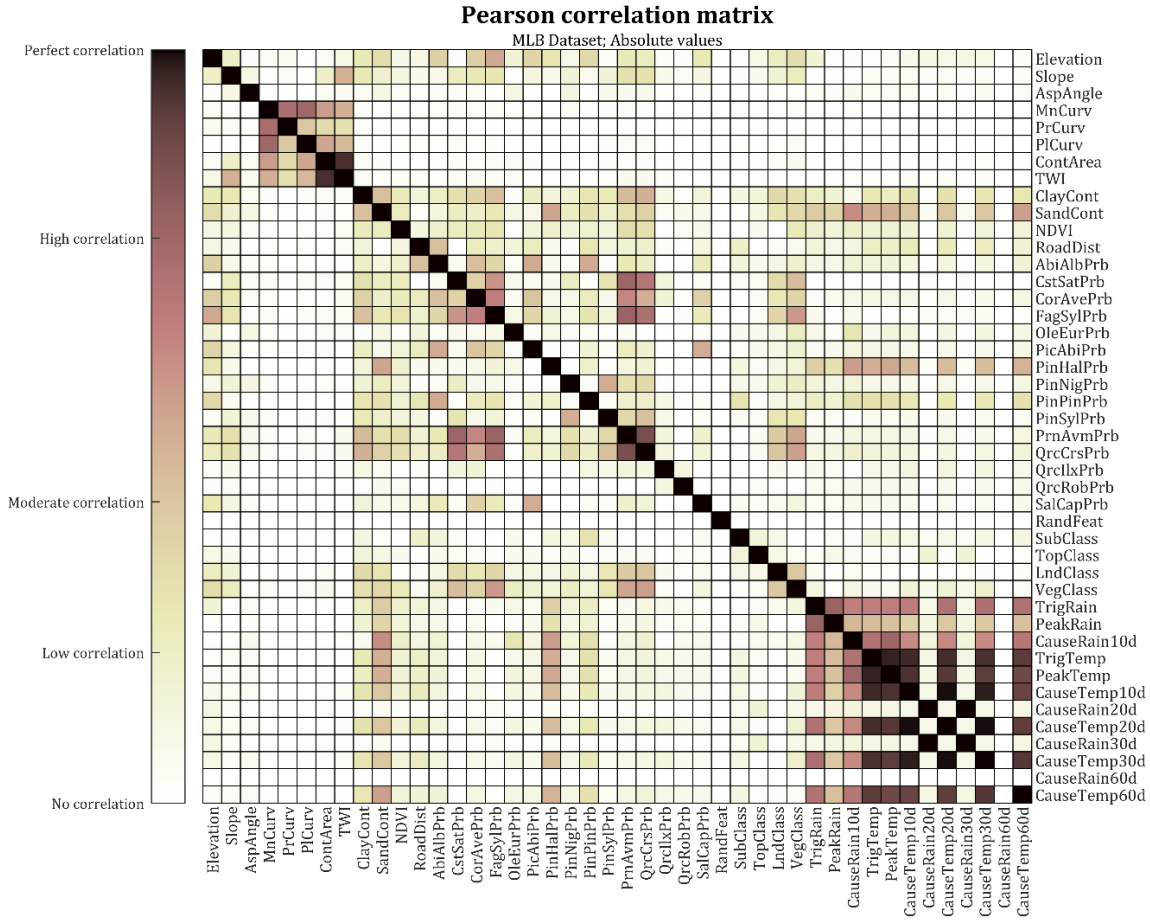

Figure V-21: The correlation between the features adopted for the PIP-AI model. Brown means perfect correlation (both direct and inverse), white means no correlation at all.

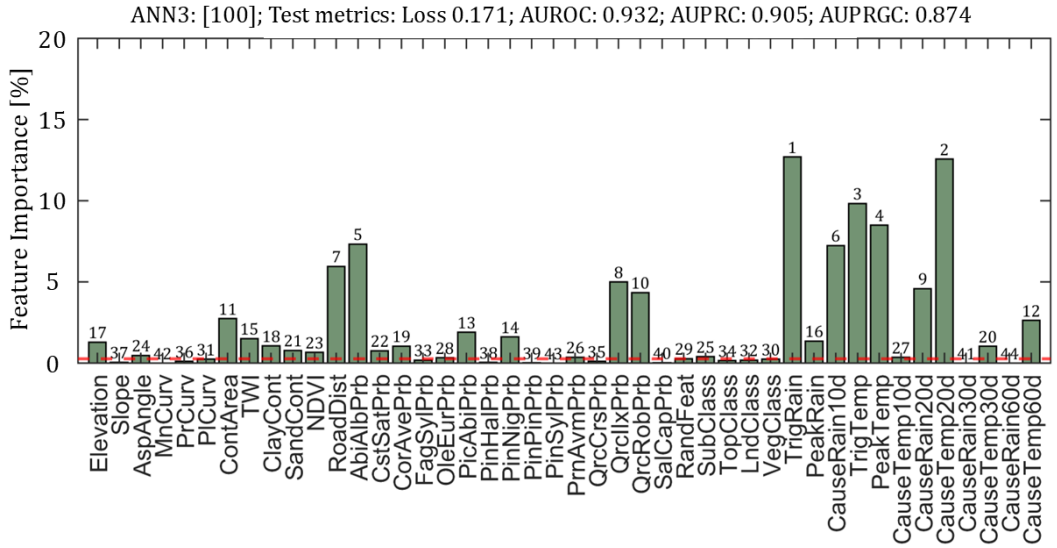

Figure V-22: The ranking of the features used with the PIP-AI model, based on their importance. The method applied to assess the importance is the feature permutation. The most important feature (1st) is the TrigRain, the least one (44th) is the CauseRain60d, instead the RandFeat importance (threshold) is the 29th.

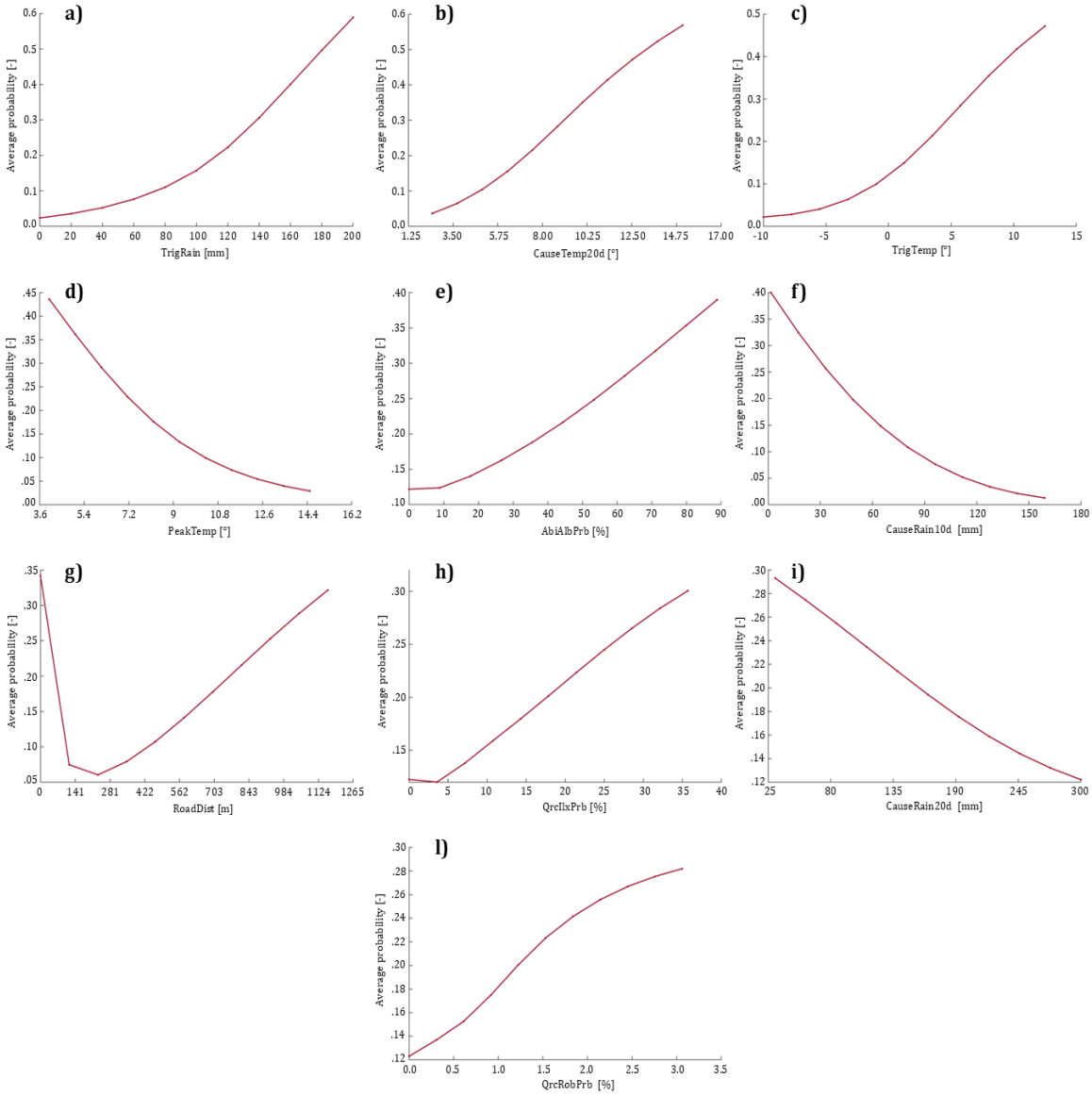

Figure V-23: Partial Dependence Plots for the first 10 important features. On the y-axis, the final averaged probability that the feature can achieve is displayed, while on the x-axis, the values of the features are reported. The graphs respectively represent the following features: TrigRain (a); CauseTemp20d (b); TrigTemp (c); PeakTemp (d); AbiAlbPrb (e); CauseRain20d (f); RoadDist (g); QrcIlxPrb (h); CauseRain20d (i); QrcRobPrb (l).

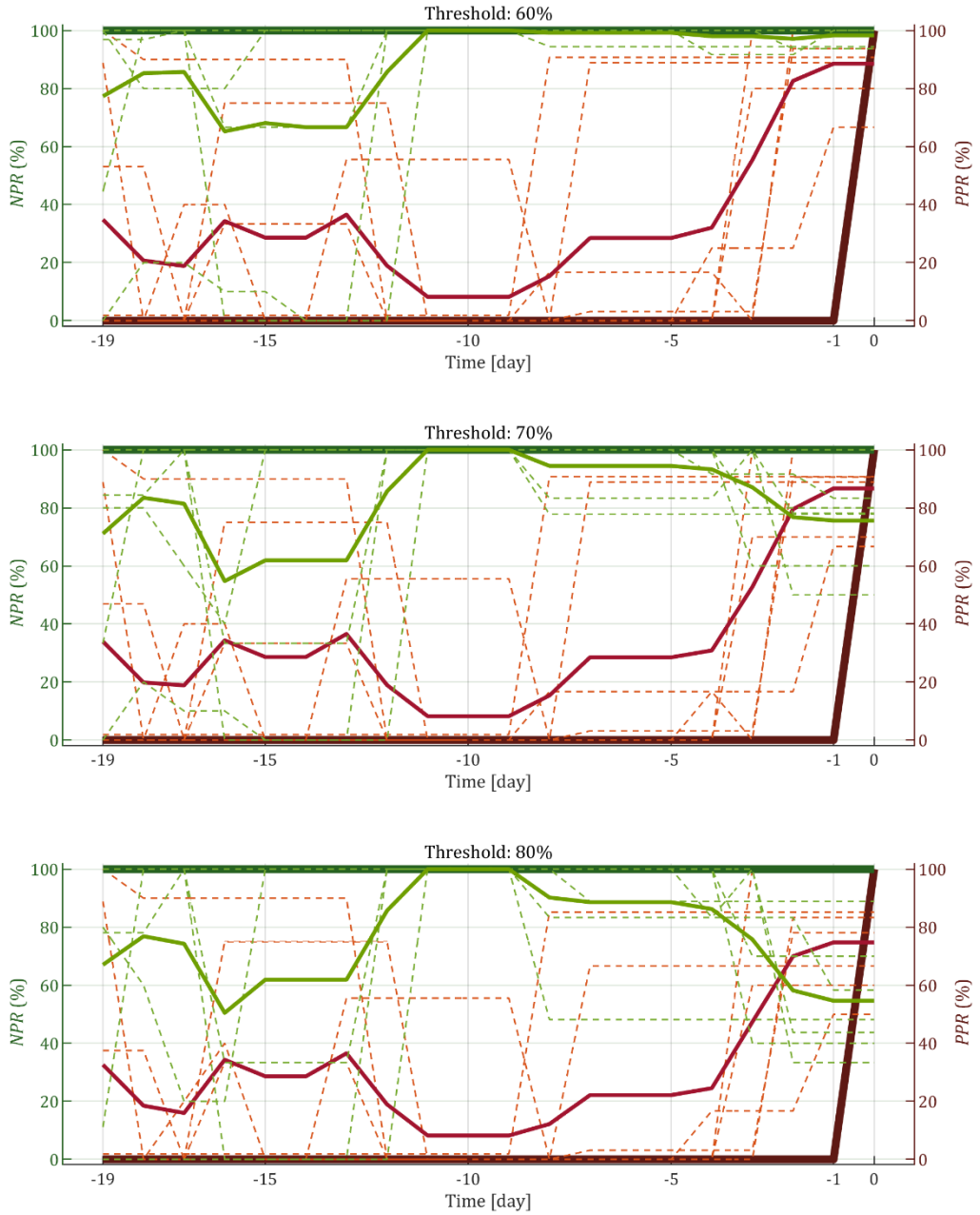

Figure V-24: The trends of the PPR and NPR curves for all seven events (dashed lines) and their averaged trend (solid line) are shown, varying with the pixel activation threshold based on the type of polygon. Specifically, if the threshold is set to 60%, then at least 60% of the pixels in unstable polygons must activate, while at least 60% of the pixels in stable polygons must remain stable.

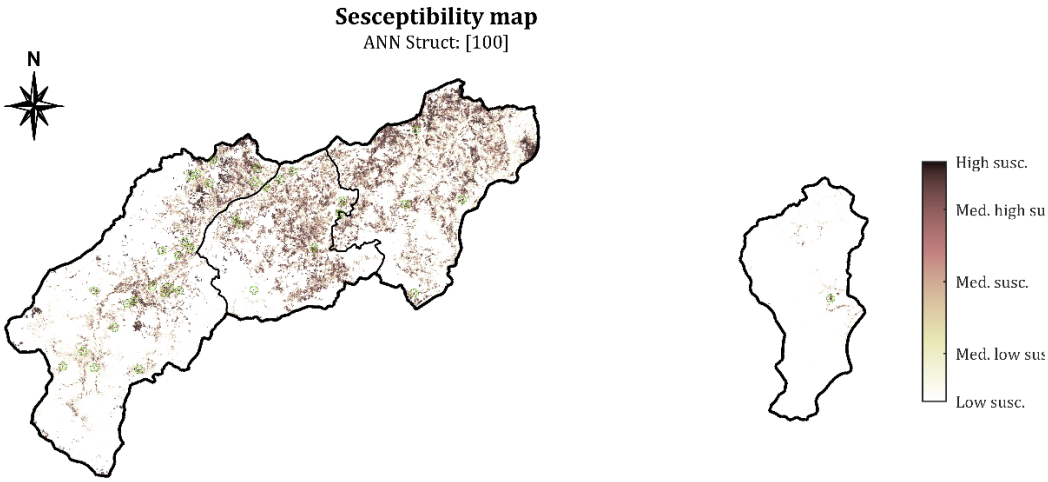

Figure V-25: Susceptibility map of the entire study area, obtained from the instability predictions of PIP-AI, during the event of November 1, 2000. Green and red polygons represent the stable and unstable polygons of the event.

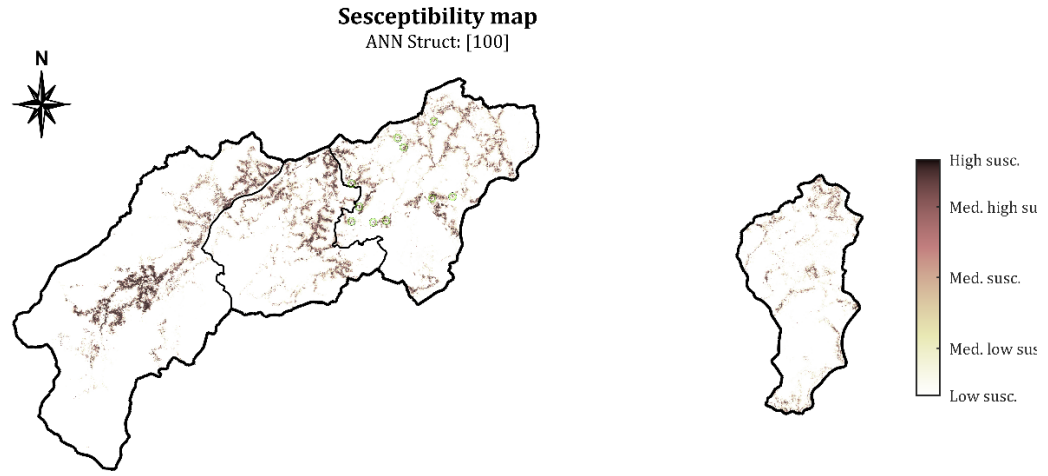

Figure V-26: Susceptibility map of the entire study area, obtained from the instability predictions of PIP-AI, during the event of March 1, 2004. Green and red polygons represent the stable and unstable polygons of the event.

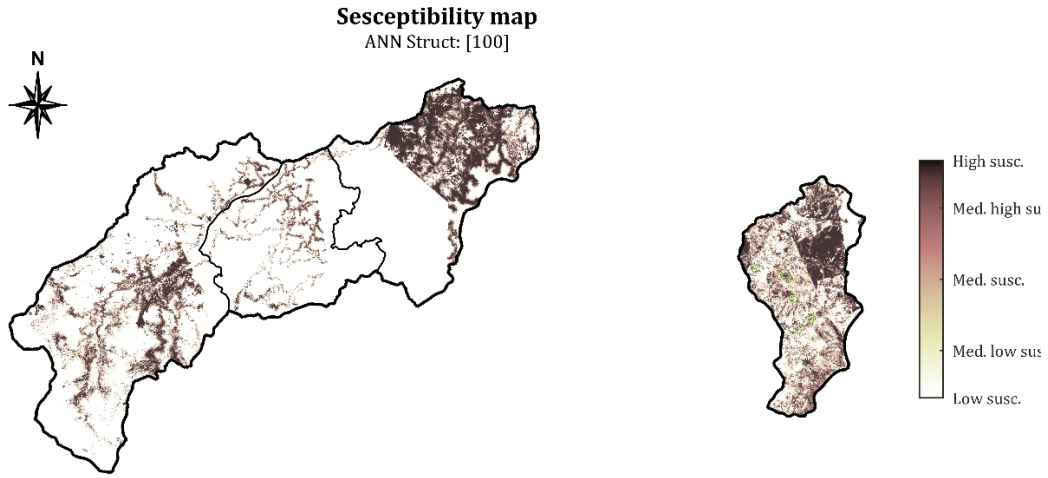

Figure V-27: Susceptibility map of the entire study area, obtained from the instability predictions of PIP-AI, during the event of April 11, 2005. Green and red polygons represent the stable and unstable polygons of the event.

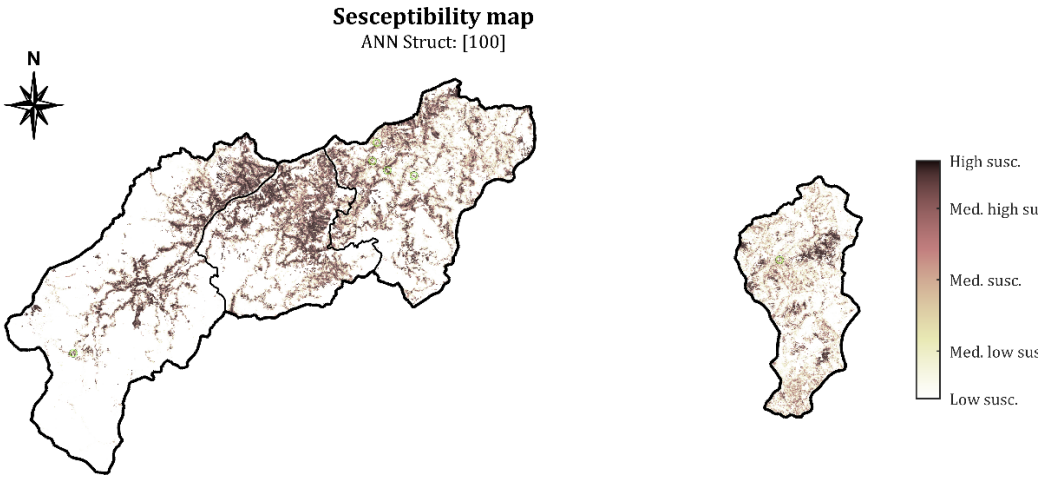

Figure V-28: Susceptibility map of the entire study area, obtained from the instability predictions of PIP-AI, during the event of November 1, 2010. Green and red polygons represent the stable and unstable polygons of the event.

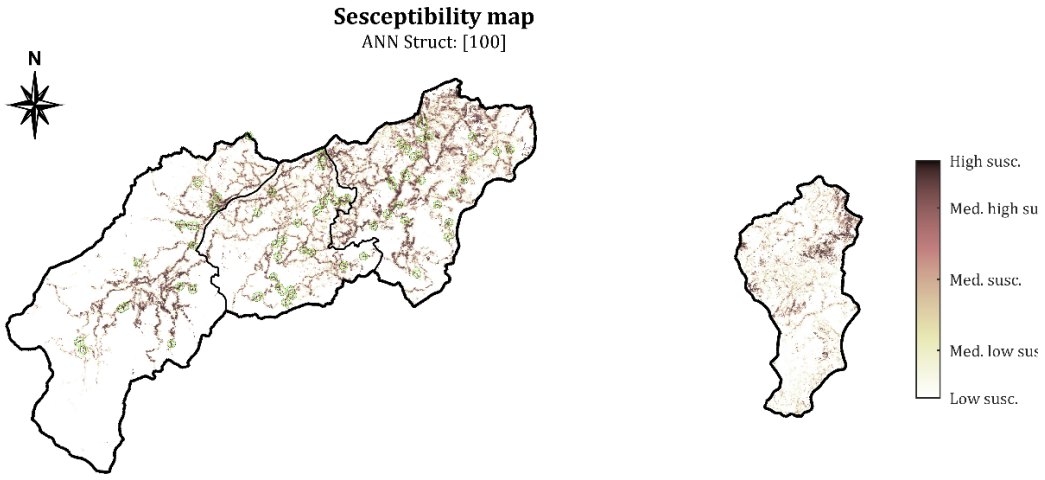

Figure V-29: Susceptibility map of the entire study area, obtained from the instability predictions of PIP-AI, during the event of April 5, 2013. Green and red polygons represent the stable and unstable polygons of the event.

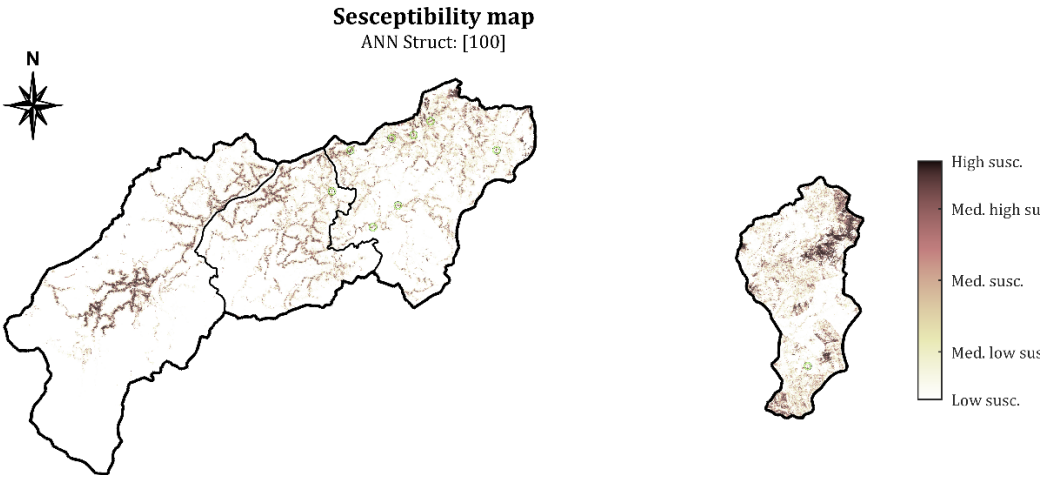

Figure V-30: Susceptibility map of the entire study area, obtained from the instability predictions of PIP-AI, during the event of March 5, 2014. Green and red polygons represent the stable and unstable polygons of the event.

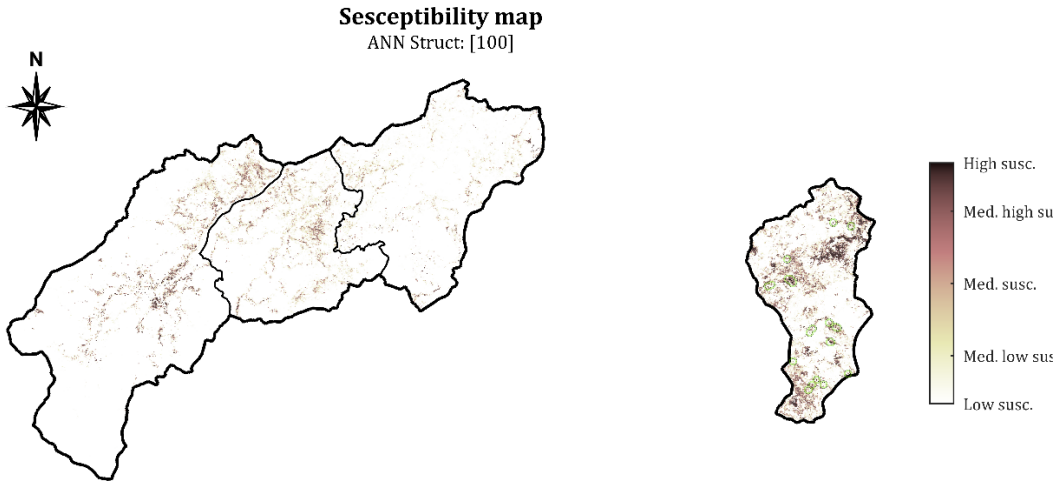

Figure V-31: Susceptibility map of the entire study area, obtained from the instability predictions of PIP-AI, during the event of May 17, 2023. Green and red polygons represent the stable and unstable polygons of the event.

Metric	TrigRain	CauseTemp20d	TrigTemp	PeakTemp	AbiAlbPrb
MinUP	6.0	2.5	0.0	4.4	1.0
MinSP	0.0	2.5	0.0	4.0	1.0
MaxUP	200.0	14.0	12.3	13.5	78.0
MaxSP	200.0	15.1	13.5	14.5	88.0
AvgUP	115.8	7.0	7.0	9.2	1.5
AvgSP	80.7	7.6	7.3	9.6	1.9
MdnUP	118.4	4.9	5.8	8.5	1.0
MdnSP	92.2	6.0	5.8	9.2	1.0
StdUP	60.8	-5.8	3.6	2.9	6.1
StdSP	64.8	-5.6	4.1	3.1	7.2
1QrUP	56.4	3.4	4.4	6.5	1.0
1QrSP	7.6	3.4	4.1	6.7	1.0
3QrUP	171.2	12.9	10.6	10.9	2.1
3QrSP	124.0	12.9	11.5	12.3	3.4

Table V-5: Statistics of the 5 most important features for ANN3 architecture, from the total dataset of PIP-AI. The importance was assessed through the feature permutation technique and the labels of the metrics are abbreviated, with the following criteria -- Min = minimum, Max = maximum, Avg = average, Mdn = median, Std = standard deviation, 1Qr = 1st quartile, 3Qr = 3rd quartile, SP = Stable Pixels, i.e. the part of the dataset containing just the pixels whose output values must be 0 (stability), UP = Unstable Pixels, that is the part of the dataset containing the pixels whose output values is 1 (instability).

CV	TrROC	VlROC	TsROC	TrPRG	VlPRG	TsPRG	TrLss	VlLss	TsLss	RFI
F1	0.953	0.927	0.920	0.912	0.869	0.853	0.111	0.154	0.161	0.004
F2	0.964	0.935	0.933	0.931	0.880	0.879	0.093	0.155	0.154	0.002
F3	0.950	0.899	0.919	0.904	0.796	0.850	0.115	0.180	0.159	0.002
F4	0.951	0.923	0.917	0.905	0.862	0.847	0.112	0.155	0.164	0.003
F5	0.930	0.890	0.908	0.867	0.788	0.825	0.138	0.198	0.163	0.004
F6	0.950	0.916	0.923	0.904	0.854	0.858	0.114	0.173	0.154	0.000
F7	0.951	0.923	0.922	0.907	0.848	0.858	0.111	0.155	0.162	0.002
F8	0.972	0.947	0.936	0.946	0.900	0.885	0.080	0.131	0.160	0.002
F9	0.962	0.911	0.923	0.929	0.836	0.859	0.097	0.190	0.167	0.003
F10	0.968	0.948	0.934	0.939	0.903	0.879	0.087	0.125	0.153	0.002
Avg	**0.955**	**0.922**	**0.924**	**0.914**	**0.854**	**0.859**	**0.106**	**0.161**	**0.160**	**0.002**

Table V-6: Results of the main metrics for the 10-fold cross-validation performed on the ANN3 architecture of PIP-AI. For each fold there is a training, validation, and test dataset. CV column identifies the fold analysed. Tr = Train, Vl = Validation, Ts = Test, ROC = Area Under the Receiver Operating Characteristic curve, PRG = Area Under the Precision Recall Gain Curve, Lss =cross-entropy loss, RFI = Random Feature Importance.

5.4 THE APPLICATION OF THE SLIP MODEL

The SLIP model was applied to the same events as the PIP-AI model, and thus the same considerations are valid.

Regarding the parameters used in the model, it is possible to have an overview of the uniform units with Figure V-32, which present the homogeneous units of soil and vegetation, and with their relative parameters, listed in Tables V-7 and V-8. The two soil units represent a typical natural sand (DSC1) and a typical over-consolidated clay (DSC2). The six vegetative units represent different types of vegetation, ranging from common grass and shrubs to trees that provide a high contribution to mechanical resistance, in increasing order. Thus, DVC1 offers the lowest contribution, while DVC6 provides the highest, both from a mechanical and hydraulic perspective, although the latter was kept constant for simplicity of processing. As can be observed, vegetation data is missing in the municipality of Baiso due to a lack of data in the available vegetation map. This could represent a critical issue in standard analyses relying solely on the SLIP model. However, in this case, for reasons discussed later, it was decided to proceed with the analyses regardless.

Regarding the analysis depth, it was set at 1.2 meters, reflecting the average depth recorded.

The initial degree of saturation (S_{r_0}) was set to 0.7 for all events.

Following the analyses, the Fs values were converted into pseudo-probabilities to facilitate a better comparison between SLIP and PIP-AI results. Unfortunately, the final results often fell short of acceptable thresholds when evaluated using the same metrics adopted for PIP-AI. However, the model seemed to perform better on days not associated with landslide events, which could be advantageous in a potential hybrid model.

The low performance of the SLIP model might be attributed to the fact that SLIP requires detailed calibration for each event to enhance its sophistication. This is often infeasible due to a lack of mechanical, hydraulic, and vegetative characterization data. Nevertheless, the focus of this application is to explore how the performance of SLIP and PIP-AI could be improved if combined. In such a case, SLIP would provide a physical reality check (related to morphology, etc.) to the PIP-AI model, which appears to concentrate primarily on rainfall patterns while ignoring physical properties (in Section 5.3, it can be seen that the slope and curvatures of pixels have low importance).

For this reason, more in-depth analyses of the various soil types (and their properties) within the study area were not conducted, and the already available data was used as it was. Therefore, the results of the susceptibility maps are shown in Figures V-33, V-34, V-35, V-36, V-37, V-38, and V-39.

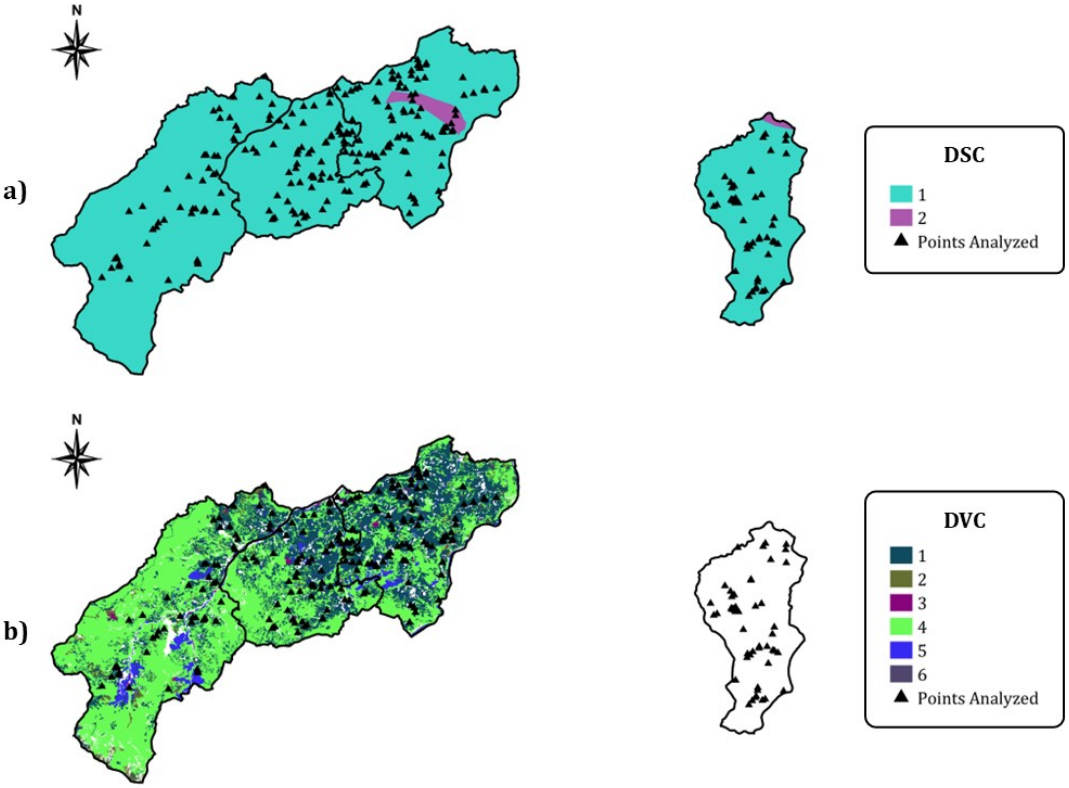

Figure V-32: Map of the uniform soil units (DSC) (a) and uniform vegetation units (DVC) (b). Each of these units is used to attribute specific mechanical and hydraulic properties to the pixels that fall within these areas.

DSC	c' [kPa]	φ [°]	k_t [h^{-1}]	A [kPa]	n
1	0	35	0.01	40	0.4
2	10	20	0.001	80	0.3

Table V-7: Mechanical and hydraulic parameters used with the SLIP model for the various uniform soil units. Each uniform soil class (DSC) has its own parameters, i.e., effective cohesion, friction angle, drainage coefficient of the slope, the internal SLIP modelling parameter A, and soil porosity n.

DVC	c'_r [kPa]	β^* [-]
1	0	0.6
2	2	0.6
3	4	0.6
4	5	0.6
5	10	0.6
6	12	0.6

Table V-8: Mechanical and hydraulic parameters used with the SLIP model for the various uniform vegetation units Each uniform vegetation class (DVC) has its own parameters, i.e., root cohesion and infiltration coefficient.

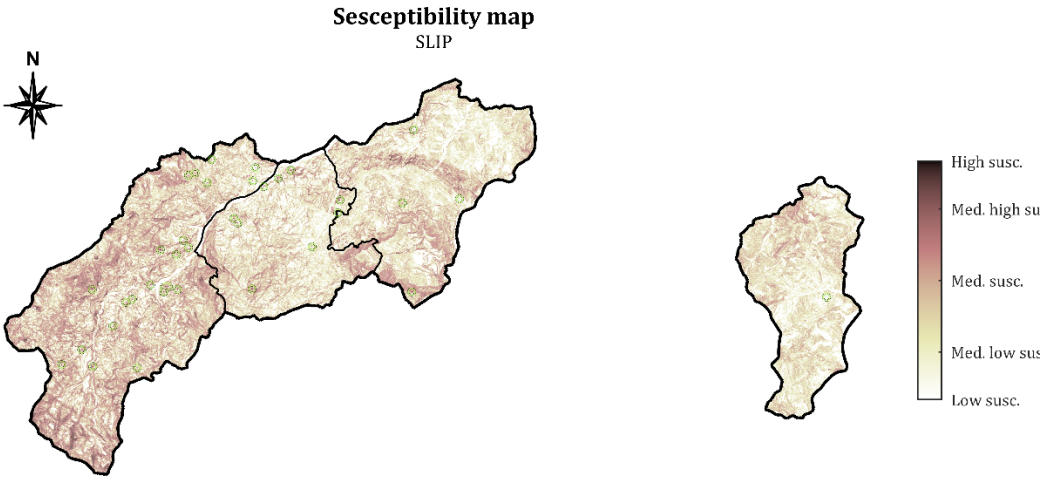

Figure V-33: Susceptibility map of the entire study area, obtained from the instability predictions of SLIP, during the event of November 1, 2000. Green and red polygons represent the stable and unstable polygons of the event.

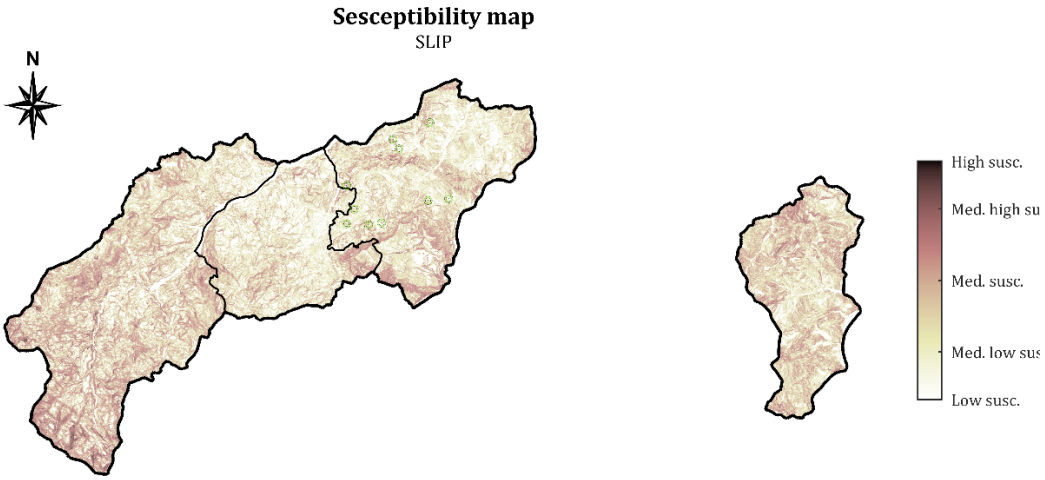

Figure V-34: Susceptibility map of the entire study area, obtained from the instability predictions of SLIP, during the event of March 1, 2004. Green and red polygons represent the stable and unstable polygons of the event.

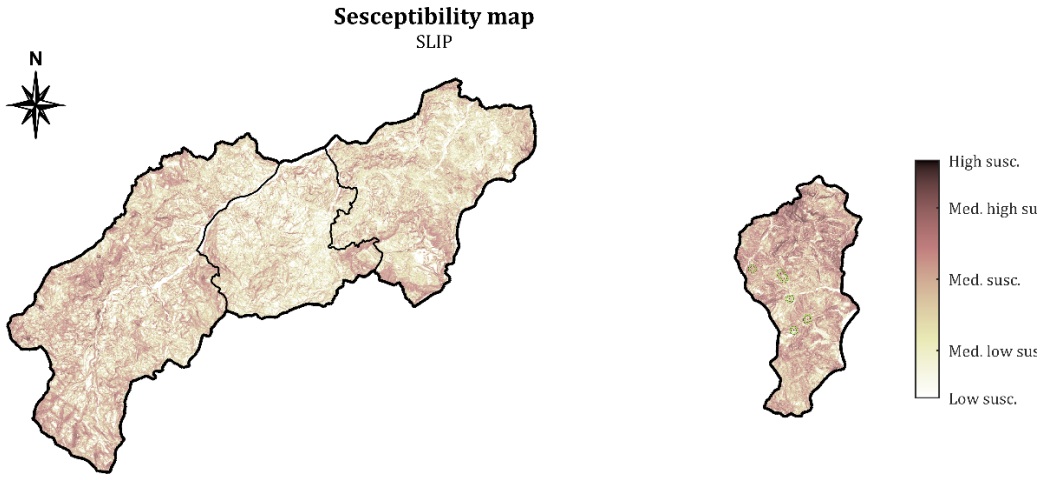

Figure V-35: Susceptibility map of the entire study area, obtained from the instability predictions of SLIP, during the event of April 11, 2005. Green and red polygons represent the stable and unstable polygons of the event.

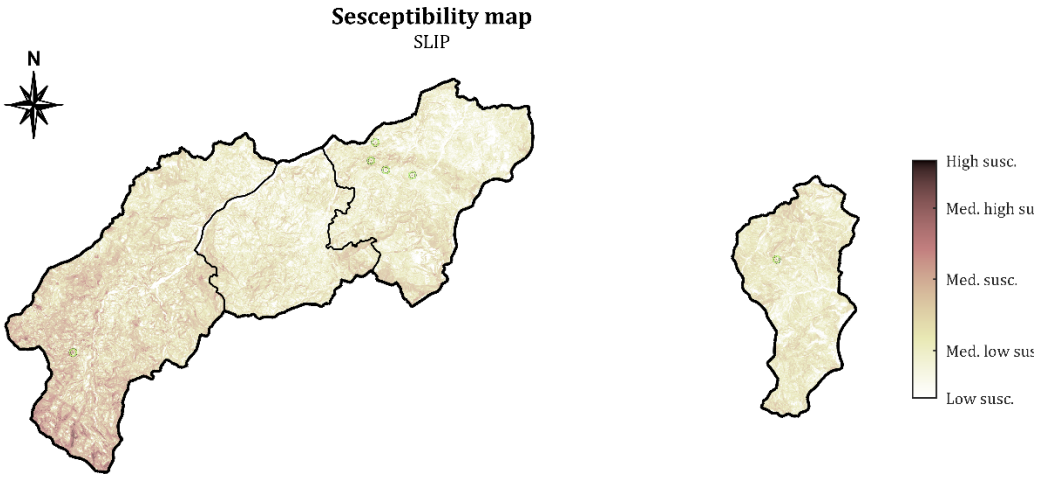

Figure V-36: Susceptibility map of the entire study area, obtained from the instability predictions of SLIP, during the event of November 1, 2010. Green and red polygons represent the stable and unstable polygons of the event.

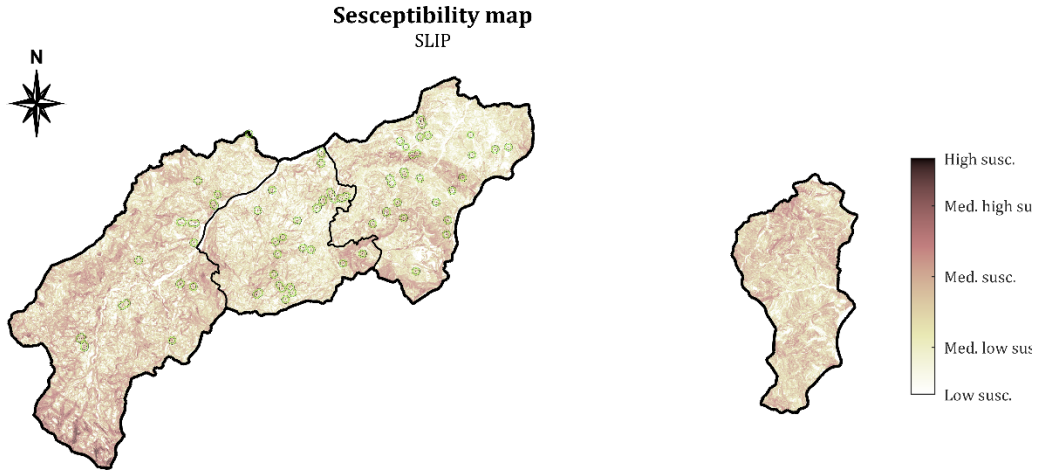

Figure V-37: Susceptibility map of the entire study area, obtained from the instability predictions of SLIP, during the event of April 5, 2013. Green and red polygons represent the stable and unstable polygons of the event.

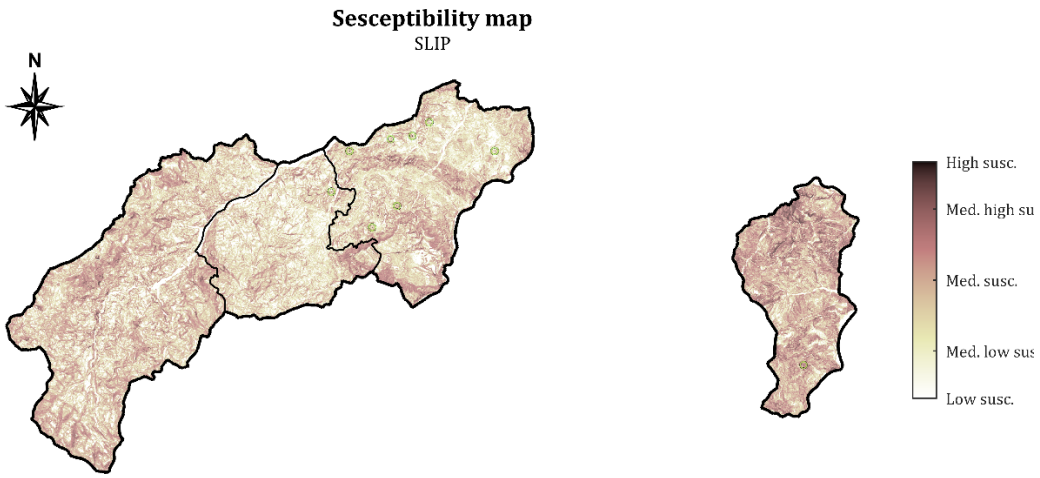

Figure V-38: Susceptibility map of the entire study area, obtained from the instability predictions of SLIP, during the event of March 5, 2014. Green and red polygons represent the stable and unstable polygons of the event.

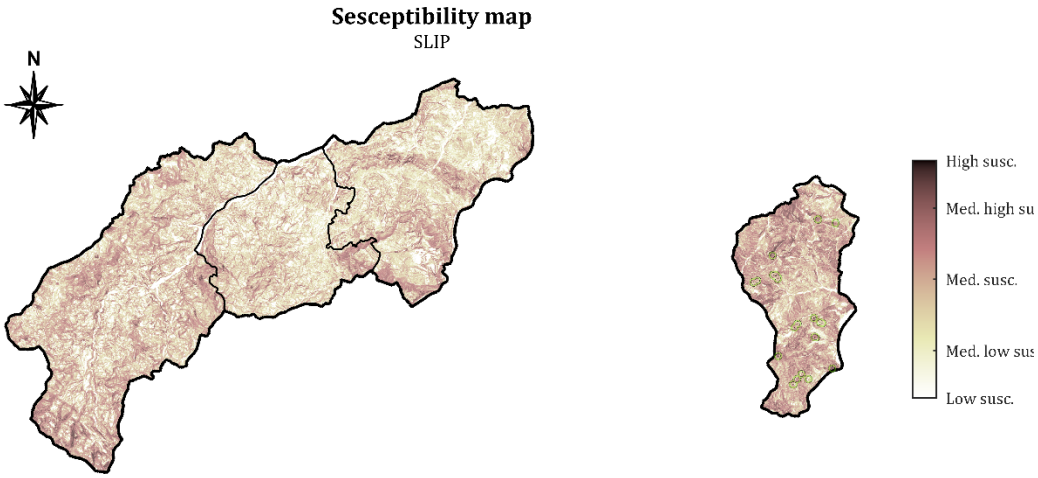

Figure V-39: Susceptibility map of the entire study area, obtained from the instability predictions of SLIP, during the event of May 17, 2023. Green and red polygons represent the stable and unstable polygons of the event.

5.5 The Application Of The H-SLIP Model

The final results presented in this chapter pertain to the H-SLIP model, applied to the seven events discussed in Section 5.1.2, which were also used for PIP-AI and SLIP. In particular, the ANN3 architecture of the PIP-AI model was combined with the results of the SLIP model (see Section 3.4). The percentage importance of each model was set to 50%, meaning the prediction values from both models have equal influence on the final prediction.

The primary motivation for opting for a hybrid analysis lies in maintaining physical control over the problem while enhancing it with the pattern recognition capabilities offered by AI. Although modelling a study area appropriately using a physical model might seem the optimal choice, one tends to forget that the number of parameters required to achieve this effectively is substantial and demands a high degree of precision. Conversely, relying solely on AI tools to address complex problems could be a double-edged sword. On one hand, AI provides an advanced interpretation of the patterns triggering landslides, but on the other hand, it might neglect the physical nature of the problem. This could result in misleading outcomes if the patterns of a new event deviate from those previously encountered by the model. In fact, this issue could be addressed using physically-based models, which however, as mentioned earlier, require a detailed parameter analysis of the study area (a challenging task for extensive regions such as Italy).

Without further elaboration, Figures V-40, V-41, V-42, V-43, V-44, V-45, and V-46, display the susceptibility maps obtained for the entire study area during the seven analysed events. As can be observed, the results are largely similar to those of the PIP-AI model but appear to show slight improvements in areas outside the stable and unstable polygons, where no data regarding the presence or absence of landslides are available. These improvements are considered plausible because, although certainty is lacking, it is difficult to believe that all the high susceptibility areas are those identified by the PIP-AI model. This assumption is based on the observation that such areas would likely have been reported, given their frequent location near road networks (Figure V-11).

Finally, an AUROC analysis was conducted. Specifically, the ROC curves of the pixels contained within the stable and unstable polygons during all seven events were compared (Figures V-47, V-48, V-49, and V-50). It can be observed that there is generally a substantial increase in the quality of predictions from SLIP to H-SLIP. Furthermore, the quality of predictions from PIP-AI and H-SLIP appears entirely comparable, with no significant decreases or increases relative to the PIP-AI model. When this observation is combined with the earlier discussion on the nature of these two types of models, it further supports the notion that adopting hybrid models such as H-SLIP is the most sensible choice. Additionally, it is worth noting that the SLIP model was intentionally calibrated in a coarse manner. A more detailed analysis with SLIP would likely further enhance the results achieved with H-SLIP, which are, however, already high in their current state.

To conclude, it is recommended to adopt a hybrid model such as H-SLIP to address, on one hand, the lack of detailed modelling and characterization (a challenging task for physically-based models) and, on the other hand, the lack of physical reality control inherent in AI models.

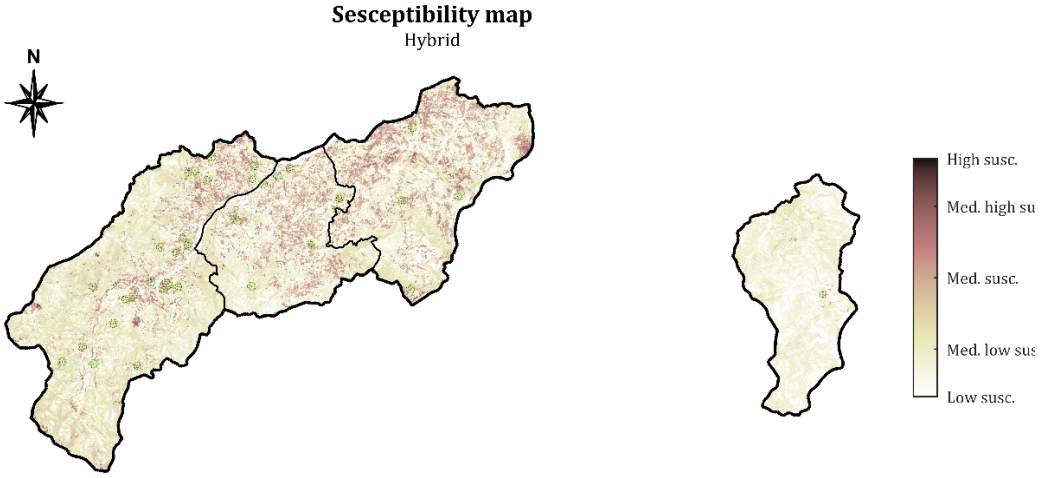

Figure V-40: Susceptibility map of the entire study area, obtained from the instability predictions of H-SLIP, during the event of November 1, 2000. Green and red polygons represent the stable and unstable polygons of the event.

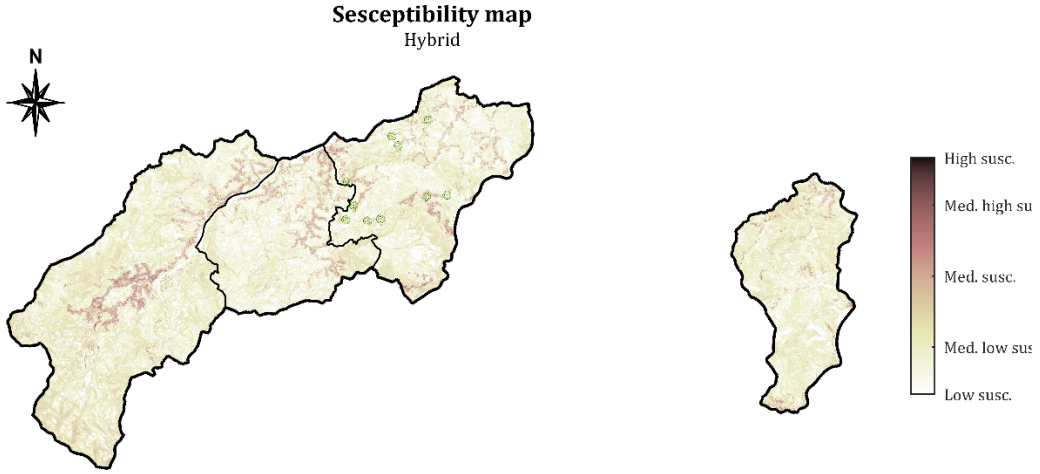

Figure V-41: Susceptibility map of the entire study area, obtained from the instability predictions of H-SLIP, during the event of March 1, 2004. Green and red polygons represent the stable and unstable polygons of the event.

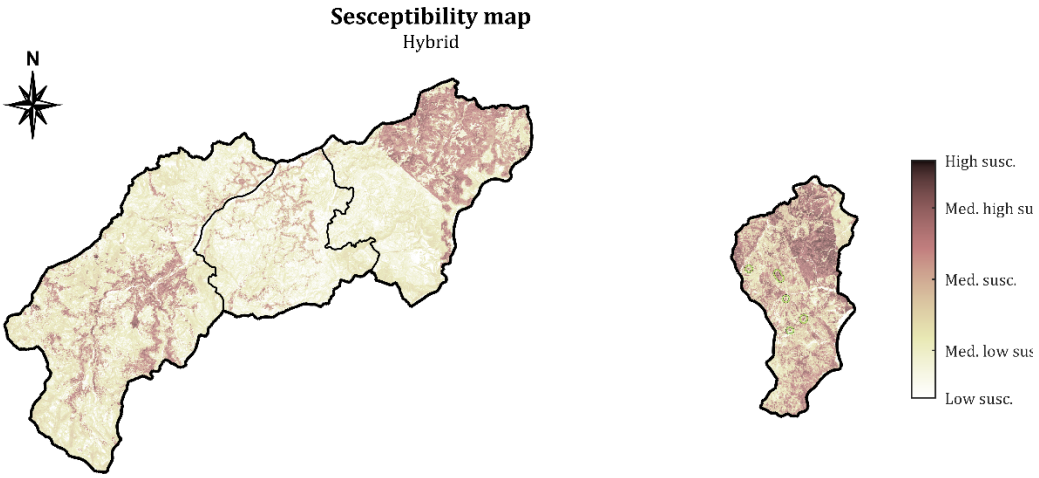

Figure V-42: Susceptibility map of the entire study area, obtained from the instability predictions of H-SLIP, during the event of April 11, 2005. Green and red polygons represent the stable and unstable polygons of the event.

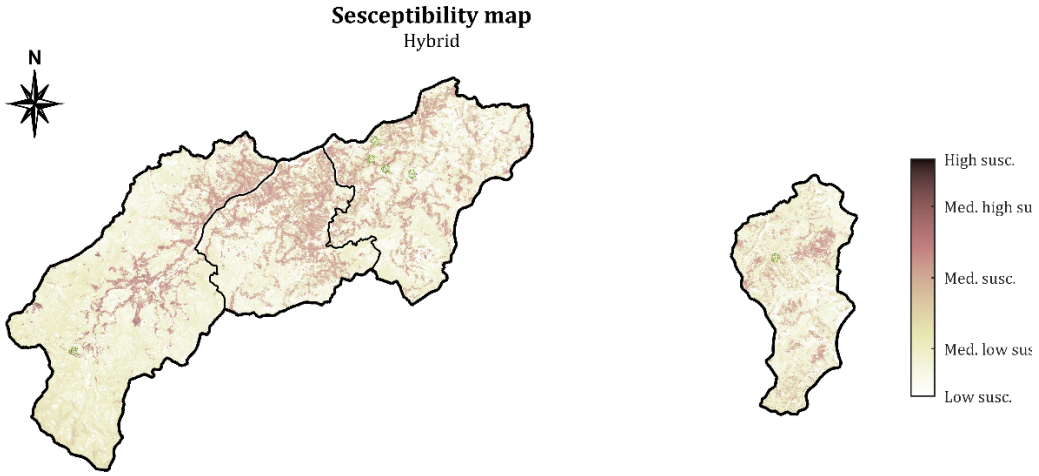

Figure V-43: Susceptibility map of the entire study area, obtained from the instability predictions of H-SLIP, during the event of November 1, 2010. Green and red polygons represent the stable and unstable polygons of the event.

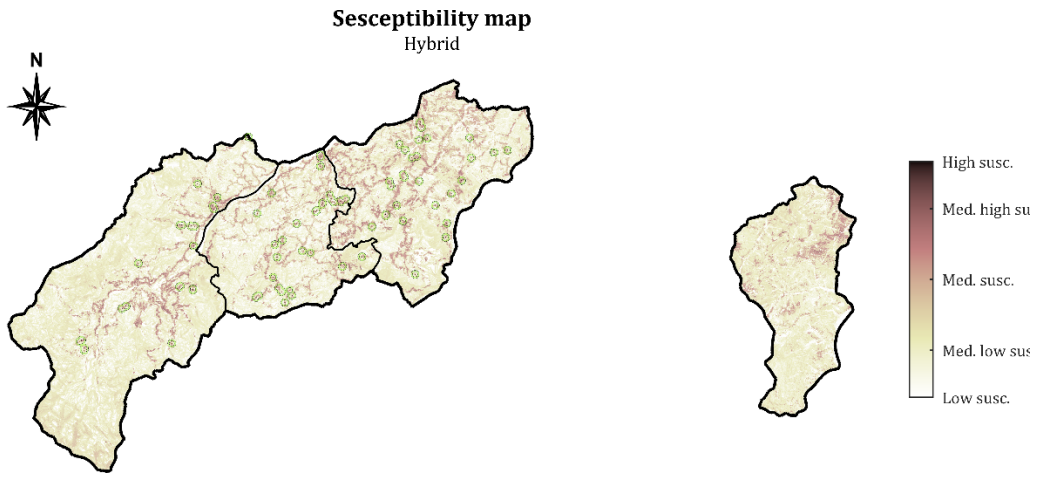

Figure V-44: Susceptibility map of the entire study area, obtained from the instability predictions of H-SLIP, during the event of April 5, 2013. Green and red polygons represent the stable and unstable polygons of the event.

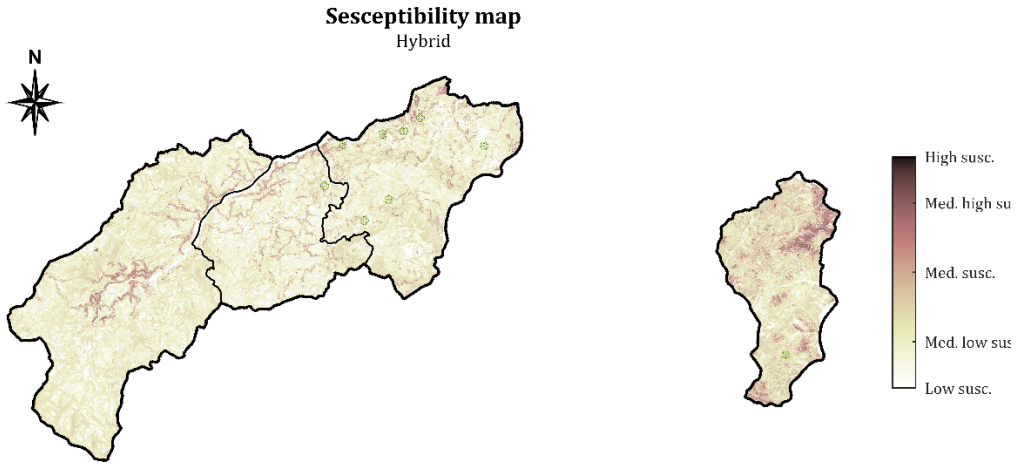

Figure V-45: Susceptibility map of the entire study area, obtained from the instability predictions of H-SLIP, during the event of March 5, 2014. Green and red polygons represent the stable and unstable polygons of the event.

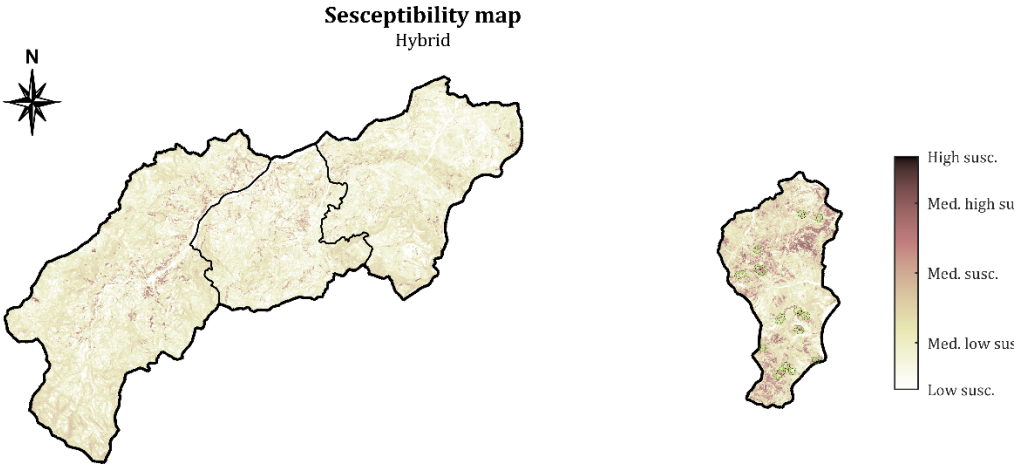

Figure V-46: Susceptibility map of the entire study area, obtained from the instability predictions of H-SLIP, during the event of May 17, 2023. Green and red polygons represent the stable and unstable polygons of the event.

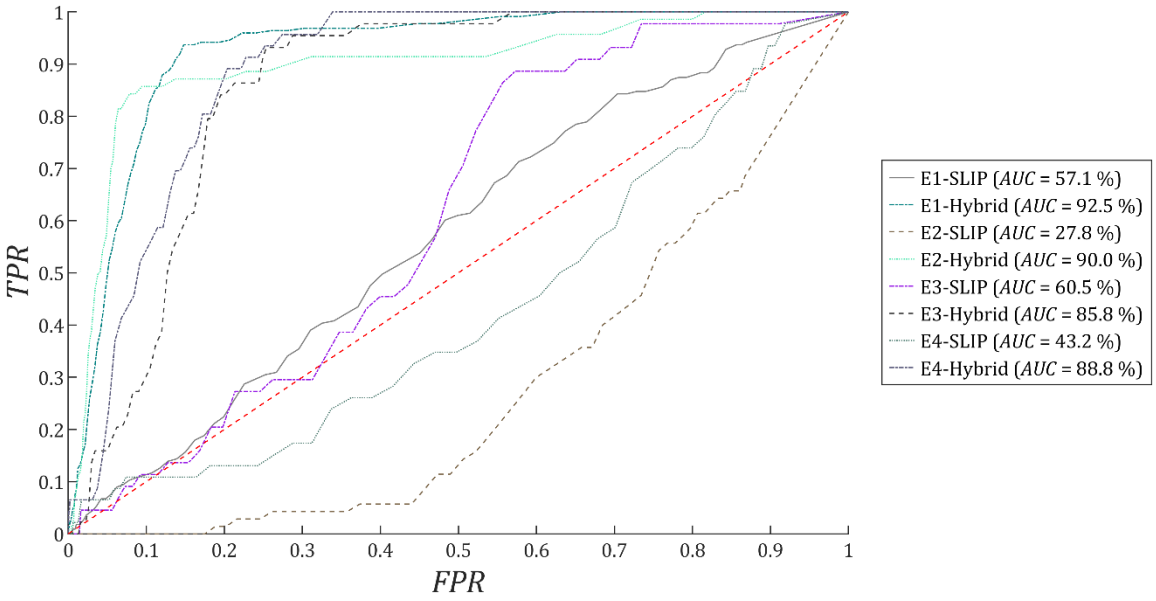

Figure V-47: Comparison of the AUROC curves between SLIP and H-SLIP models (part I). The curves are obtained with the pixels contained in the stable and unstable polygons of the events E1, E2, E3, and E4. E1 = November 1, 2000; E2 = March 1, 2004; E3 = April 11, 2005; E4 = November 1, 2010.

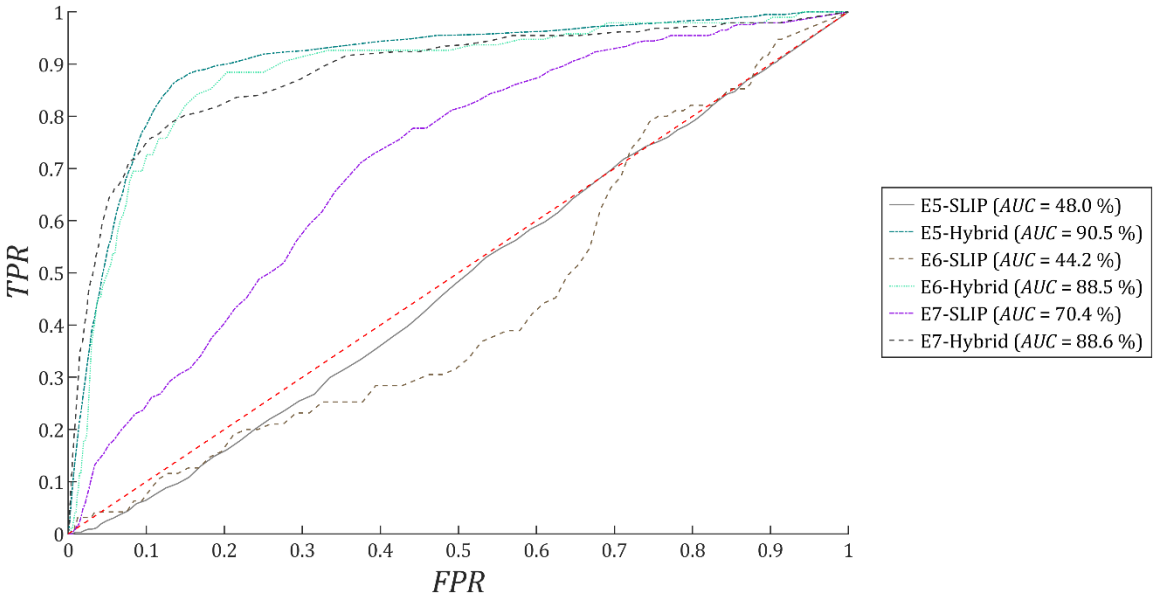

Figure V-48: Comparison of the AUROC curves between SLIP and H-SLIP models (part II). The curves are obtained with the pixels contained in the stable and unstable polygons of the events E5, E6, and E7. E5 = April 5, 2013; E6 = March 5, 2014; E7 = May 17, 2023.

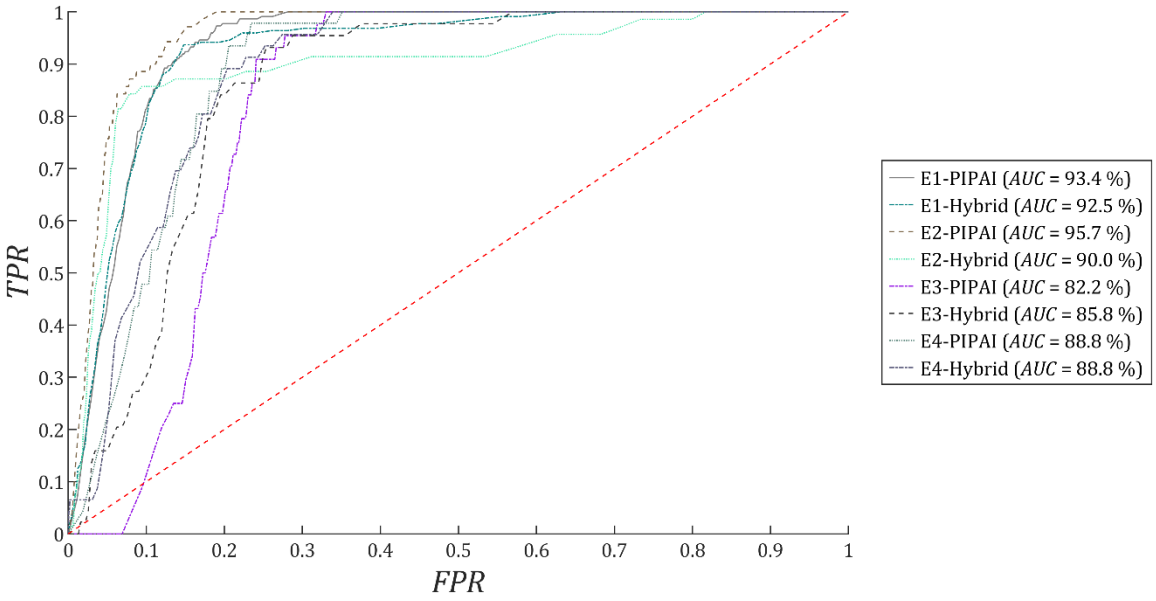

Figure V-49: Comparison of the AUROC curves between PIP-AI and H-SLIP models (part I). The curves are obtained with the pixels contained in the stable and unstable polygons of the events E1, E2, E3, and E4. E1 = November 1, 2000; E2 = March 1, 2004; E3 = April 11, 2005; E4 = November 1, 2010.

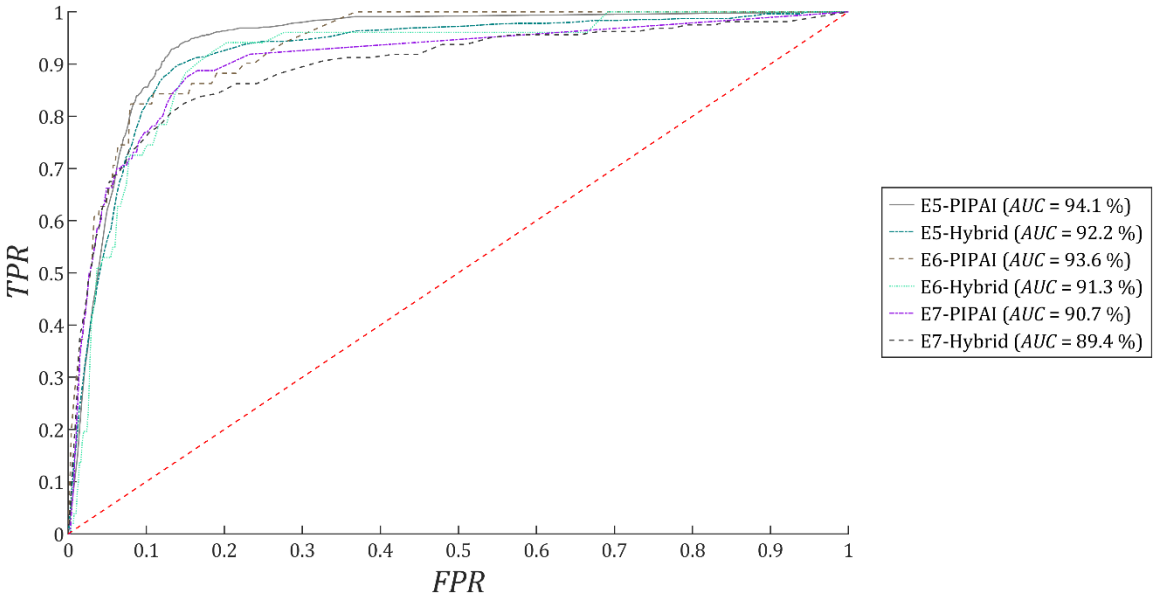

Figure V-50: Comparison of the AUROC curves between PIP-AI and H-SLIP models (part II). The curves are obtained with the pixels contained in the stable and unstable polygons of the events E5, E6, and E7. E5 = April 5, 2013; E6 = March 5, 2014; E7 = May 17, 2023.

VI EXTRA

6.1 LANDSLIDE EVOLUTION

Modelling landslide evolution involves significant challenges due to the complex physical, mechanical, and hydrological processes involved. Landslides are highly heterogeneous flows of disaggregated material, driven by mechanisms such as particle rolling, inter-grain friction, surface erosion, and variable gravitational forces along the slope. These phenomena operate across macroscopic and microscopic scales, making precise simulation difficult.

To address these complexities, simplified numerical models are often employed. Common approaches include Particle Finite Element Methods (PFEM) (L. Wang et al., 2019), Smoothed Particle Hydrodynamics (SPH) (Cui & Zhang, 2023; M. Yu et al., 2018), and the G2L method (Global height to Local depth) (X. Wang & Liu, 2021). Each offers distinct advantages, ranging from accurately simulating granular material behaviour to approximating fluid dynamics in landslide motion. Despite this, these approaches often require several parameters that may not be available. Moreover, when the landslides to be modelled are in particularly complex contexts, the analyses may require significant computational power as well as extended processing times, which might also involve multiple attempts. This is the reason why, in this section, a new simplified and efficient approach is proposed, hereinafter referred to as Geo Point Evolution (GPE).

Regardless of the chosen method, detailed terrain morphology, typically derived from DEMs, is essential to account for energy dissipation and the preferential flow direction, which is mainly dictated by gravitational potential gradients.

6.1.1 THE GEO POINT EVOLUTION (GPE) MODEL

The Geo Point Evolution model (GPE) is a simplified and efficient model to assess preferential landslide paths and their cinematic/dynamics aspects, particularly useful for large-scale applications such as early warning systems. This model estimates key outcomes, such as the potential interaction of landslides with infrastructure or landslide body mass and velocity at each time step of the path considered (Misiano et al., 2024).

6.1.1.1 Preferential paths

Regarding the preferential path, that is assumed to be followed by the moving landslide body, the fundamental principle relies on the critical assumption that the mass movement is

primarily governed by slope morphology. Therefore, two complementary approaches can be employed to trace the landslide trajectory:

- Point-by-Point Approach - the steepest path is calculated by identifying, at each point, the neighbouring DEM cell with the maximum negative gradient.
- Stepwise Gradient Descent - movements are discretized into elementary steps, and the steepest descent is computed iteratively until the minimum is reached.

However, both these methods rely on schematizing the landslide body as a single point, corresponding to its centre of mass. This simplification allows for efficient calculation but requires adjustments, such as snapping to DEM points at each step. An overview of the two possible approaches is given in Figure VI-1.

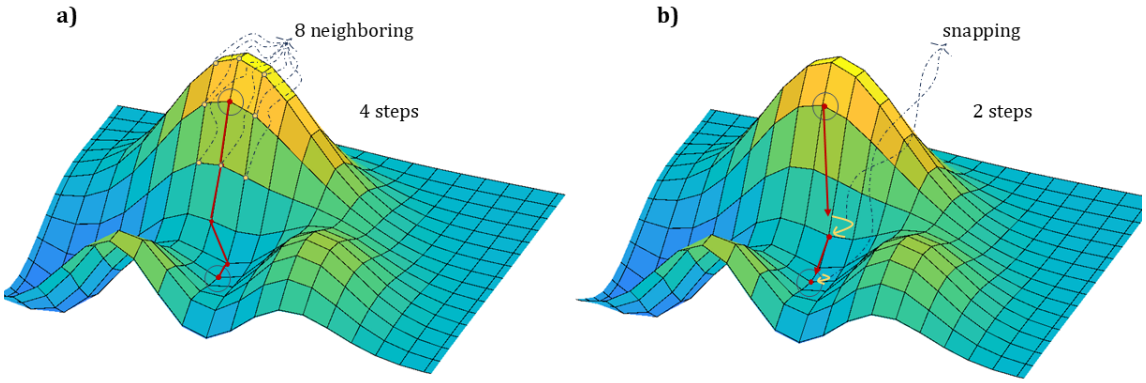

Figure VI-1: The two possible approaches in determining the preferential path of landslides, i.e., the point-by-point approach (a) and the stepwise gradient descent approach (b). With the point-by-point approach, each step of the path is characterized by a movement to one of the 8 neighbouring points, depending on the maximum negative slope. With the stepwise gradient descent approach, the steps of the path are unlinked from the DEM, therefore the movement to the next point follows the direction of the maximum gradient and must be subsequently snap to the nearest point of the DEM to continue, until the end of the path.

Regardless of the approach used, the preferential path represents the maximum possible evolution. The reason behind this is because the end point of the preferential path is the local minimum of the DEM, but the actual landslide path could be just a part of the preferential path assessed, because the actual deposit point depends on the equilibrium between the stabilizing and destabilizing forces, as will be discussed in the next sections. Moreover, if the stepwise gradient descent algorithm is chosen, a snapping procedure must be performed on each step (Figure VI-1b), to link the end of the current step to a point of the DEM, since the gradient can be assessed only over the DEM points.

When the DEM is sufficiently detailed, which means high resolution, the two approaches tend to give the same resulting preferential path, but the local minimum reached (which is the end of the path) may be too early and mainly dictated by the too high resolution, which would lead to stop the path in a wrong minimum. To avoid this behaviour it is recommended to use a DEM with a resolution in the range of 10-20 meters per cell, or to avoid the point-by-

point approach (which is more prone to this issue) and use instead the stepwise gradient descent, set with a default step size around 10 meters (which can vary depending on the gradient, evaluated in each step).

Finally, to apply the various equations and balances of the following sections, it is necessary to "rectify" the path, from a segmented three-dimensional line to a one-dimensional straight polyline, as illustrated in Figure VI-2.

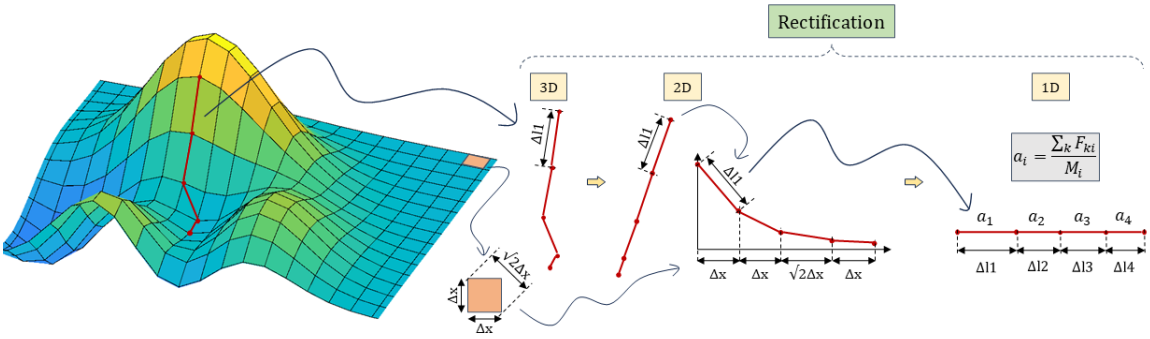

Figure VI-2: The "rectification" of a preferential landslide path with the point-by-point approach. First, the preferential path is taken from a 3D space and converted into a 2D space. The single steps can have a pre-fixed length, that can be one of the sides of the cell or its diagonal. After this, the path is converted from a 2D space and studied as a mono-dimensional problem.

6.1.1.2 Equations of motion and force balances

The motion of the landslide is modelled as uniformly accelerated, governed by Newton's second law, with the discretization of the path in steps that enables for a step-by-step update of the various parameters.

The equations account for a force balance, similarly to what was seen for the SLIP model (see Section 3.1.1.3). Thus, also in this case the equilibrium is between:

- destabilizing forces, i.e., the components of gravitational force along the sliding plane.
- stabilizing forces, represented by the basal friction acting between the soil mass and the slope surface.

Consequently, the resulting acceleration, which may change value at each step of the path (see Figure VI-2), can be calculated as:

$$a_i = \frac{T_{d_i} - T_{s_i}}{M_i} = \frac{T_{d_i} \cdot (1 - Fs_i^*)}{M_i} \tag{49}$$

where:

- T_{d_i} and T_{s_i} represent the destabilizing and stabilizing forces at the step i, respectively
- M_i is the mass of the moving landslide body at the step i
- Fs_i^* is the dynamic factor of safety at the step i

Regarding the dynamic factor of safety (Fs_i^*) of Equation 49, it should be noted that the first value (when $i = 1$) is the same coming from SLIP. Instead, during all the remaining steps, a simplified dynamic factor can be assessed, as shown in the following Equation 50. If no SLIP analysis is present as support, also in the first step it can be used the simplified factor, as shown below.

$$Fs_i^*(i > 1) = \frac{M_i \cdot g \cdot cos\,\beta_i \cdot tan\,\varphi_{ss_i}}{M_i \cdot g \cdot sin\,\beta_i} \tag{50}$$

$$Fs_i^* = \begin{cases} Fs_{SLIP}, & i = 1 \\ \dfrac{tan\,\varphi_{ss_i}}{tan\,\beta_i}, & i > 1 \;\; (i \geq 1\; if\; no\; SLIP) \end{cases} \tag{51}$$

where:

- φ_{ss_i} is the basal friction at the step i, between the soil mass that is sliding and the underlying soil, at the step i, which is equal to $\frac{2}{3} \cdot \varphi'$
- β_i is the slope angle at the step i

Using this definition, it becomes easily demonstrable that the formulation of the acceleration at any step can be expressed as:

$$a_i = \begin{cases} g \cdot sin\,\beta_i \cdot (1 - Fs_{SLIP}), & i = 1 \\ g \cdot sin\,\beta_i \cdot \left(1 - \dfrac{tan\,\varphi_{ss_i}}{tan\,\beta_i}\right), & i > 1 \;\; (i \geq 1\; if\; no\; SLIP) \end{cases} \tag{52}$$

By means of the acceleration assessed in Equation 52, it is possible to use the laws of the uniformly accelerated motion. In other words, it is possible to assess the initial and final speed in each step, because these steps have already a pre-established length and direction, evaluated as described in Section 6.1.1.1. Furthermore, if during a specific step the velocity reach a null value (before the final point of the pre-established path), that specific step is the last one and the end point of that step represent the deposit point of the current landslide.

6.1.1.3 Incorporation of eroded mass

During motion, the landslide mass may grow due to erosion of the underlying, erodible topsoil, above which the moving mass is sliding. This process is quantified using two key dynamic factors of safety: the top factor of safety (Fs_t) and the bottom factor of safety (Fs_b). The Fs_t represents the ratio between the stabilizing and destabilizing forces along the sliding surface, namely the surface which separates the moving mass from the underlying erodible soil. The Fs_b represents the ratio between the stabilizing and destabilizing forces along the surface that separates the bottom stable soil from the top erodible soil. An overview scheme of what was discussed above is shown in Figure VI-3.

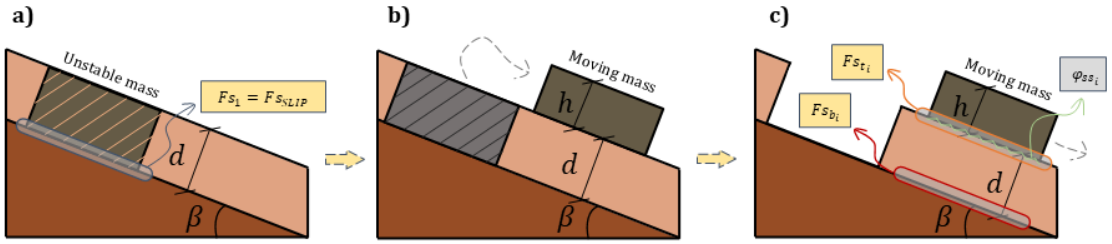

Figure VI-3: Scheme of the top and bottom dynamic factors of safety. First, the unstable mass, which is characterized by a factor of safety below the unity (from SLIP), detaches from the bottom, stable soil (a). Subsequently, the detached mass starts to slide above the top-erodible soil (b). Then, for each step of the path, two surfaces are delineated, i.e., the surface where Fsb is assessed, that separates the bottom, stable soil (dark brown layer) from the top-erodible soil (depth d), and the surface where Fst is assessed, that separates the moving mass (depth h) from the top-erodible soil (c).

The top and bottom dynamic factors of safety at the step i can be formulated by means of the Skempton laws (Skempton, 1954), manipulating the formulas of the effective stresses of Iverson (Iverson & Reid, 1992; Reid & Iverson, 1992), as follows:

$$Fs_{b_i} = \frac{c_{b_i}}{\gamma_{soil} \cdot (h_{i-1} + d) \cdot \sin\beta_i \cdot \cos\beta_i} + \frac{\left[(h_{i-1} + d) - B_D \cdot h_{i-1} \cdot (1 + A_D \cdot \tan\beta_i) + \frac{\gamma_w}{\gamma_{soil}} \cdot d\right] \cdot \tan\varphi_{ss_i}}{(h_{i-1} + d) \cdot \tan\beta_i} \tag{53}$$

$$Fs_{t_i} = \frac{c_{t_i}}{\gamma_{soil} \cdot h_{i-1} \cdot \sin\beta_i \cdot \cos\beta_i} + \frac{[1 - B_D \cdot (1 + A_D \cdot \tan\beta_i)] \cdot \tan\varphi_{ss_i}}{\tan\beta_i} \tag{54}$$

where:

- c_{b_i} and c_{t_i} are the cohesion of the bottom and top (erodible) soil, respectively
- h_{i-1} is the height of the moving mass from the previous step, because that mass, with that height, is now sliding over the new erodible soil
- d is the height of the top, erodible soil
- A_D and B_D are the Skempton parameters for the top-erodible soil
- γ_w and γ_{soil} are the specific weight of water and soil (specifically the moving mass, which is a mixture of soil and water, equal to γ_{sat} for simplicity), respectively.

To conclude, the formulation that allows to estimate which is the percentage of eroded depth is described as follows:

$$\Delta h_i = \frac{1 - Fs_{t_i}}{Fs_{b_i} - Fs_{t_i}} \cdot d \tag{55}$$

Thus, in each step it is possible to incorporate a certain percentage of erodible depth, which once summed, from the start of the current path, allows to estimate the final deposited volume of the triggered landslide.

6.2 A BIODEGRADABLE NET FOR VEGETATION'S GROWTH

When stabilizing a slope through naturalistic techniques, specifically when vegetation planting is intended to use because it would provide root reinforcement and enhanced evapotranspiration, it becomes necessary to ensure that such vegetation has the opportunity to grow without any interference.

To ensure this occurs in the best possible manner, protection networks are often indispensable. Commonly, these "anti-erosion" nets/meshes are constructed with plastic materials, which would pollute and contaminate the site where they are installed. Moreover, in some cases, they are expected to be removed after a specific period.

In recent years, two more sustainable alternatives have emerged. The first is represented by jute meshes, composed of natural textile fibres, which represent a less invasive environmental solution. An even more innovative approach involves biodegradable nets, which present two key benefits: (i) the complete disappearance of the net after a determined period of time, without requiring human intervention, and (ii) the eco-compatibility of the intervention, as once degraded by solar radiation, these networks would not pollute the site in any way, thus not releasing polluting substances once destroyed.

In this chapter, the modelling of an experimental prototype of such biodegradable networks will be presented. This net and its biodegradable polymer are currently under development by TENAX S.p.A., a leading company in the geosynthetics industry. In fact, a segment of this research was dedicated to establishing a partnership with a company investigating a field closely related to the primary research focus, i.e., vegetation-soil interaction and its landslide prevention applications. Consequently, a collaborative relationship was established with TENAX S.p.A., who contributed experimental test data and samples of the net, to facilitate the refinement of modelling and production methodologies.

6.2.1 EXPERIMENTAL STRAIN-CONTROLLED TESTS

The prototype of the biodegradable mesh used has two directions of load, the Machine (MD) and Transverse (TD) Directions, as all the geotextile membranes (Figure VI-4).

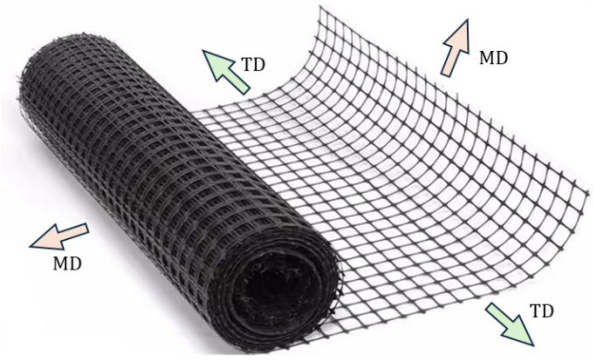

Figure VI-4: Scheme of the Machine and Transverse Directions for a geotextile mesh.

The traction tests were conducted on both these directions, for single strands and samples of the net. This means that four different types of tests were performed, namely the single strand along the MD direction (SSMD), the single strand along the TD direction (SSTD), the net sample along the MD direction (NSMD), and finally the net sample along the TD direction (NSTD). Regarding the number of strands of the net samples used, these were equal to 8 for both the directions, and the width and length of the sample was 10 x 10 centimetres. Instead, the number of repetitions per test type was set to 5 for SSMD, 4 for SSTD, 4 for NSMD, and 3 for NSTD, which means that five equal tests were performed for the single strand along MD, and equally for the others. The testing machine model used is the Zwick Roell 10kN Proline (SN: 728985), which can execute strain-controlled tests. The results of the SSMD, SSTD, NSMD, and NSTD tests are illustrated in Figure VI-5, VI-6, VI-7, and VI-8, respectively.

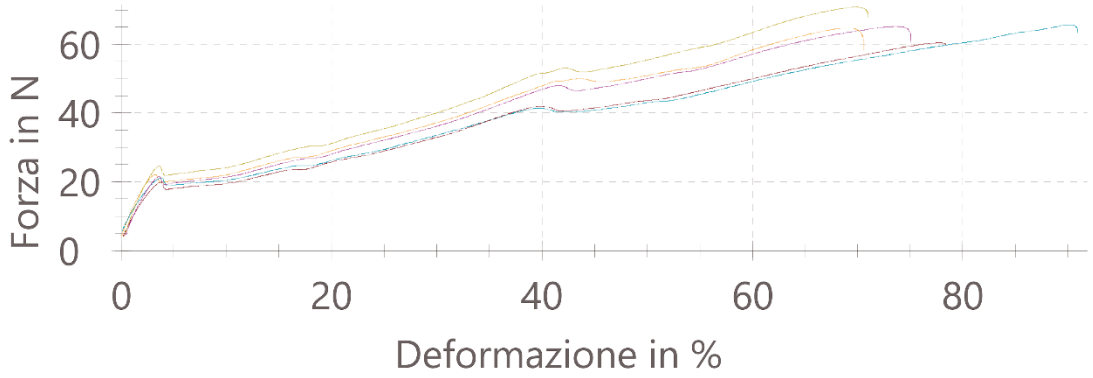

Figure VI-5: Results of the laboratory tests made on a single coil along the machine direction. The machine used is the Zwick Roell 10kN Proline. The test was repeated 5 times under equal conditions. Tests ended with the failure of the specimens.

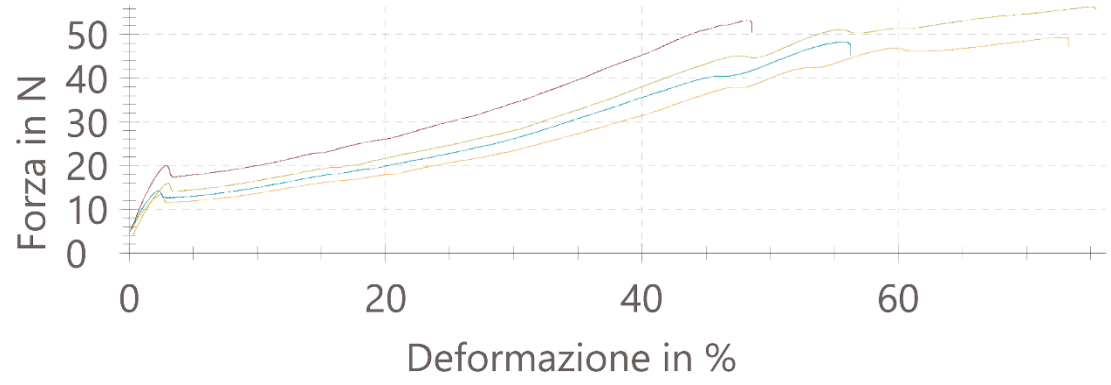

Figure VI-6: Results of the laboratory tests made on a single coil along the transverse direction. The machine used is the Zwick Roell 10kN Proline. The test was repeated 4 times under equal conditions. Tests ended with the failure of the specimens.

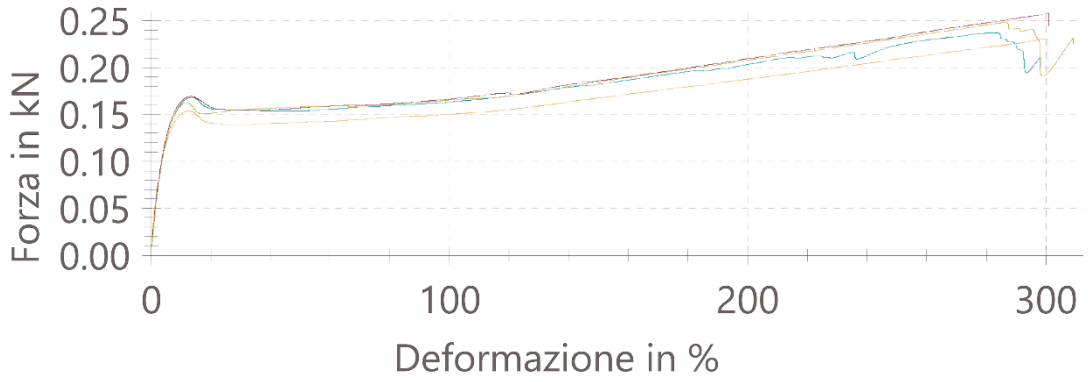

Figure VI-7: Results of the laboratory tests made on a sample of the net (10x10 centimetres, 8x8 strands) along the machine direction. The machine used is the Zwick Roell 10kN Proline. The test was repeated 4 times under equal conditions. Force values, on the y-axis must be read as the total force applied on 8 strands. Tests ended due to the reaching of the maximum strain by the laboratory machine.

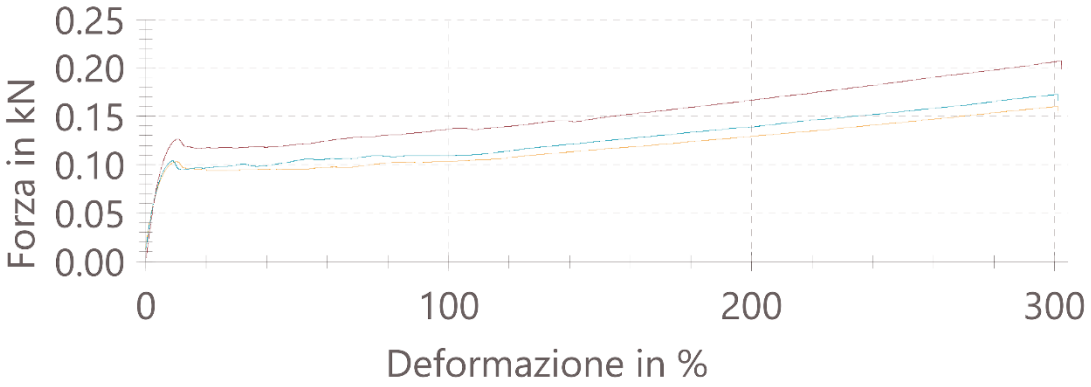

Figure VI-8: Results of the laboratory tests made on a sample of the net (10x10 centimetres, 8x8 strands) along the transverse direction. The machine used is the Zwick Roell 10kN Proline. The test was repeated 4 times under equal conditions. Force values, on the y-axis must be read as the total force applied on 8 strands. Tests ended due to the reaching of the maximum strain by the laboratory machine.

In order to compare the results, it is necessary to convert the forces of the NSMD and NSTD tests (Figure VI-7 and VI-8, respectively) from values referred to 8 strands (in [kN]), to values referred to a single strand (in [N]). This conversion can be made easily if it is assumed that the specimen grips are significantly more rigid than the sample under test, because it is sufficient to distribute the load equally across all the 8 strands. This hypothesis will be confirmed by the finite elements analyses made to re-create the laboratory test (the following Section 6.2.3).

It must be noted that the strands of the mesh sample tests (namely NSMD and NSTD) exhibited a very different behaviour when compared to the tests made on the single strands (namely SSMD and SSTD). Generally, the mesh demonstrates a reduced stiffness and more plasticity. This last consideration can be reinforced by the fact that the experimental evidence

indicates that the network remained intact even when the testing machine was extended to its maximum range of strain, as depicted in Figure VI-9.

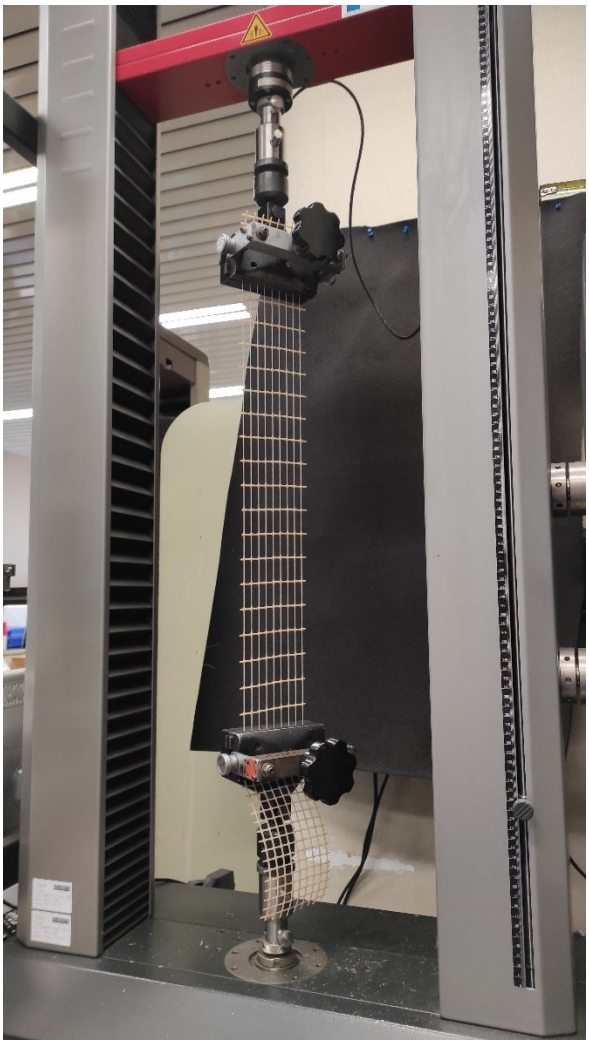

Figure VI-9: Picture of one of the tests made on the sample of the net along the machine direction (NSMD tests). As it can be noticed, these tests were terminated due to the reaching of the maximum range of strain allowed. The machine used is the Zwick Roell 10kN Proline

6.2.2 Main Hypotheses

The main assumptions and hypotheses adopted to modelling the problem are the following:

- the specimen grips are significantly stiffer than the specimen to test, therefore loads can be distributed equally across the strands used
- the necking does not occur as a localized phenomenon, but as documented by the technical staff conducting the tests, it appears that the reduction of cross-sectional area is a global phenomenon, especially in case of NSMD and NSTD test types
- the nodes of the mesh have the same mechanical properties of the strands along MD

- the areas of the various strands along each of the two directions are averaged and then, two mean circle areas are assigned to each strand of the model, depending on the direction
- the material is modelled as a strain-hardening elasto-plastic material, with the plastic phase that is modelled point by point, based on the average lines coming from the stress-strain curves of Figures VI-5, VI-6, VI-7, and VI-8.

Through these assumptions, it is possible to obtain a set of key values from the tests performed, Young's modulus included (also if, generally, the elastic phase of such material seems to be very limited), which are reported in the following Table VI-1 and Figure VI-10.

Test	Load 2% [N]	Load 5% [N]	1st peak [N]	1st peak ε [%]	E (2%) [MPa]
SSMD	17.159	19.886	21.826	3.52	360.788
SSTD	14.607	14.382	15.667	2.70	392.654
NSMD	8.750	15.375	20.375	12	183.978
NSTD	6.375	11.250	13.875	10	171.371

Table VI-1: Key mechanical values of the biodegradable material under test. These results are referred to a single strand, regardless of the type of test.

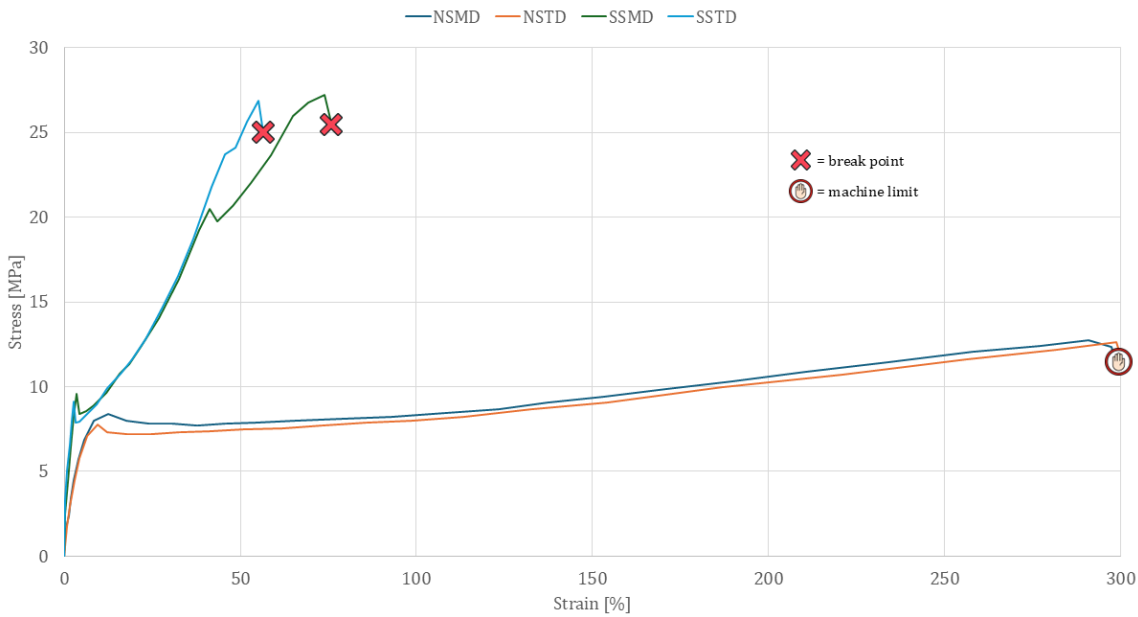

Figure VI-10: The averaged lines of the four types of tests, i.e., SSMD, SSTD, NSMD, and NSTD. These results are obtained averaging the curves of all the specimens tested, depending on the type of test. The resulting line is referred to a single strand, regardless of the type of test. The tests performed on the single strands (SSMD, SSTD) were terminated due to the breakage of the specimens, instead, the two tests on the mesh (NSMD, NSTD) were terminated due to the reaching of the maximum possible strain, therefore due to test machine limits. These results are expressed as engineering curves, therefore the reference area to obtain the stress is fixed and constant.

As it can be noticed with Figure VI-10, where the various curves represent the stress-strain behaviour referred to a single strand, the tests made on the samples of the mesh exhibit significantly higher ductility. Nevertheless, the MD and TD directions are almost identical if the two cases (single strands and net samples) are compared separately. The unique difference is for the final part of the curve with the single strands, where SSMD exhibited more ductility than SSTD. Generally, results suggest an absence of correlation between single strand tests and net sample tests.

6.2.3 Finite Elements Analyses

Because of the results obtained with the hypotheses of Section 6.2.2 and the curves of Figure VI-10, which in a common situation should be comparable, the finite elements analyses were aimed at re-creating the same conditions of the laboratory tests. The reason why the curves should have been comparable is because the material is the same, thus, if the adopted hypotheses are correct, the stress-strain curve must be the same, which would confirm that the mechanical properties are the same. Since finite elements analyses are based on the stress-strain curves for each finite element that defines the final geometric structure, it appears evident that there is already an immediate problem with the model configuration: which of the two curves should be used?

Just one curve should be used, but since there is no correspondence between single strands and mesh samples, the analyses are conducted separately. This means that, if it possible to re-create precisely the laboratory tests with two separate stress-strain curves, one to be used with the modelling of the strand and one with the modelling of the entire mesh, then there is a problem with the tests, to investigate.

Thus, six different models were created with the software Abaqus (by SIMULIA Corporation) (Dassault Systèmes, 2014). Three models were created to model the single strand, the other three were created for the mesh sample.

Regarding the tests on the single strands, the modelling was based on simple truss elements for the mono-dimensional analysis (Figure VI-11a), or linear tetrahedral elements (Figure VI-11c) and quadratic hexahedral elements (Figure VI-11b) for the three-dimensional analyses. An attempt was also performed with linear hexahedral elements, but the results were underestimated on the stress-strain curve, which means that under the same load, the elements have experienced more deformation (see the green line of Figure VI-12). This could be caused by the limited capacity of linear hex in describing localized deformations (as the strand would present at the extremities). However, the nodes at the left extremity of the strand are fixed along the three directions (pinned support), while the nodes at the right extremity are free to move only along the y-axis direction (roller support), to create the same conditions (constrains) of the real tests. The final force applied is equal to 60 kN, applied on the right end of the strand. To re-create the laboratory test, the final force was

reached incrementally, with 100 steps. The resulting stress-strain curves are shown in Figure VI-12 for all the type of models above-mentioned.

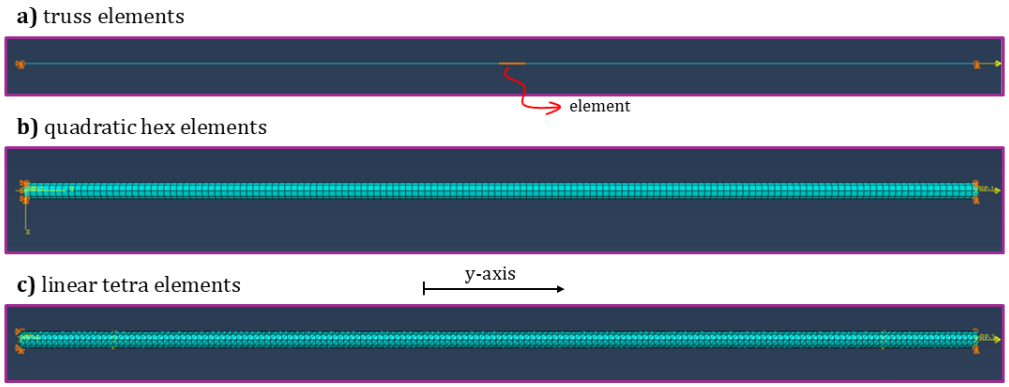

Figure VI-11: Screenshots of the single strand modelled in Abaqus with truss finite elements (a), quadratic hexahedral elements (b), and linear tetrahedral elements (c).

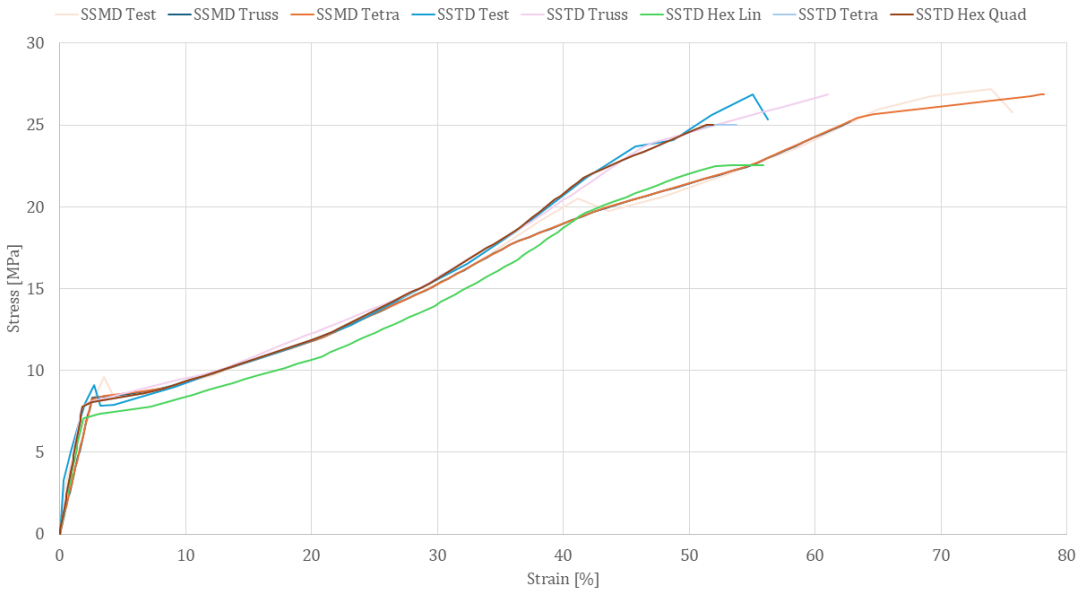

Figure VI-12: Stress-strain curves obtained by the various models, compared to the real experimental tests. The models were designed and run with Abaqus. The unique model that deviates from the expected behaviour is the single strand made with hexahedral linear elements (SSTD Hex Lin, in green).

Regarding the tests on the net samples, the modelling was based on simple beam elements for the two-dimensional analysis (Figure VI-13a), beams coupled with two plates at the extremities of the strands (with the intent to simulate the effect of the loading heads, see Figure VI-13b), or a mix of quadratic hexahedral elements and tetrahedral elements (Figure VI-13c) for the three-dimensional analyses. The nodes at the left extremities of the strands are fixed along the three directions (pinned support), while the nodes at the right extremities

are free to move only along the y-axis direction (roller support), to create the same conditions (constrains) of the real tests. The second structure, that is beams coupled with plates, was considered to demonstrate that the hypothesis of an equal distribution of the load between the various strands is corrected, because the loading heads have significantly greater stiffness compared to the strands (loading heads are made with steel), therefore, these rigid bodies would distribute the loads evenly among the strands. Instead, the third structure was used to prove that also considering the 3d effects of the problem (necking of strands), the result is consistent, also if the net is slightly stiffer (see green line of Figure VI-14). However, the final force applied is equal to 240 kN, applied on the right ends of the strands and distributed equally (except for the case with the 2d plate elements at the extremities, where the force was applied directly to the plates). To re-create the laboratory test, the final force was reached incrementally, with 100 steps. The resulting stress-strain curves are shown in Figure VI-14 for all the type of models above-mentioned.

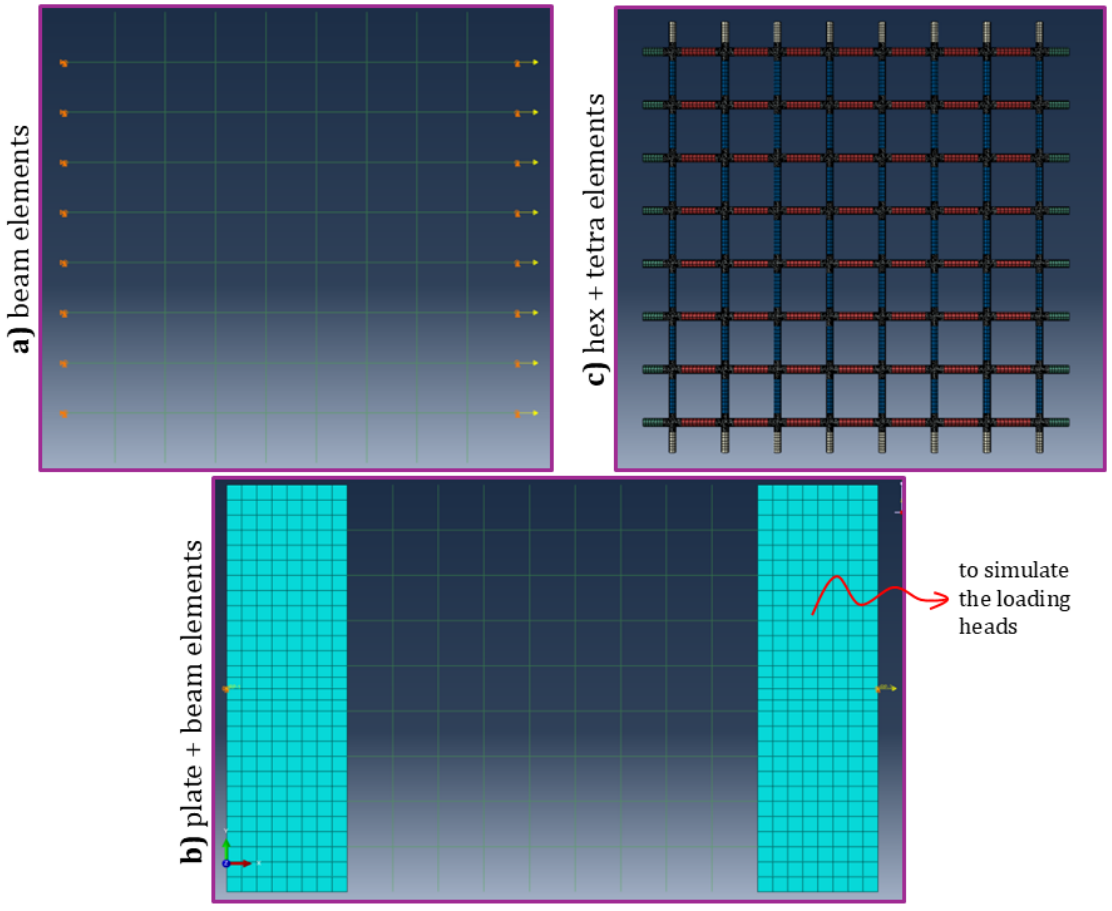

Figure VI-13: Screenshots of the net samples modelled in Abaqus with beam elements (a), plate (to simulate the loading heads) coupled with beam elements (b), and a mixture of hexahedral and tetrahedral elements (c).

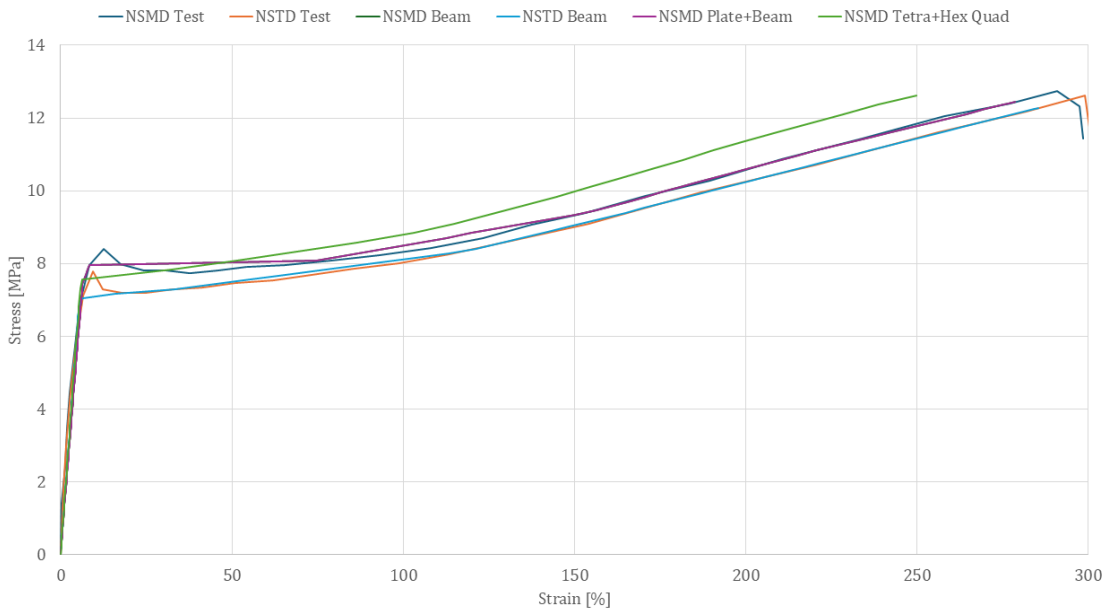

Figure VI-14: Stress-strain curves obtained by the various models, compared to the real experimental tests. The models were designed and run with Abaqus. The unique model that slightly deviates from the expected behaviour is the net sample with linear tetrahedral and quadratic hexahedral elements (NSMD Tetra+Hex Quad, in green).

Generally, results showed in both cases that it is possible to re-create the laboratory tests without any issues, because there is a good correspondence between the experimental stress-strain curves and the ones obtained from the finite element models, thus, the hypotheses and assumptions adopted in Section 6.2.2 are correct, but the single strands and net samples were studied as two separate materials. In fact, if the stress-strain experimental curve of the single strand is used with the models of Figure VI-13, there is no correspondence at all (these curves have been excluded to simplify the reading of the figures), but the net exhibits high stiffness.

6.2.4 Discussion About Laboratory Tests

Looking at the results obtained in Section 6.2.2 and 6.2.3, three possibilities emerge: (i) the nodes of the mesh have different mechanical properties; (ii) the curves obtained from SSMD and SSTD tests refers to a different material than the one of NSMD and NSTD tests; or, finally, (iii) the single strands were taken from net samples where the biodegradation process was triggered (possibly caused by suboptimal sample storage conditions or performance decline due to extended periods of inactivity). The reason why the last possibility was taken into account is because the behaviour of SSMD and SSTD tests appears to be very rigid and fragile, typical of degraded plastics. In fact, it should be noted that the performance was not better than NSMD and NSTD, because the maximum load, which would break the specimen, is assessed only for SSMD and SSTD. Instead, NSMD and NSTD reached the maximum possible strain, allowed by the test machine.

Consequently, it is suggested to perform again the tests described in Section 6.2.1 for future developments of this experimental work, paying close attention to the specimens selected for testing, which should have been preserved in the same manner and produced in the same batch. Furthermore, it is suggested to use a laboratory machine with a greater travel distance of the moving crosshead, which in case of the Zwick Roell 10kN Proline is equal to a maximum of 98 cm, from which approximately 10 cm for the specimen and about 25 cm for the accessories used to anchor the specimen to the moving plate (per side, thus approximately 50 cm) must be subtracted. In fact, if the length of the deformed specimen, which would be 40 cm (300% deformation), were added to that of the accessories, that is 50 cm, the resulting total length would be about 90 cm, close to the machine's maximum limit.

CONCLUSIONS

This study has comprehensively analysed various aspects of rainfall-induced shallow landslides and the role of vegetation in these phenomena. Initially, the literature on soil slips was examined in depth, providing an overview of significant past catastrophic events, state-of-the-art predictive models, and the challenges posed by the complex nature of shallow landslides. Subsequently, the coupling of vegetation with these phenomena was introduced step by step, beginning with evidence from the literature and then presenting various mechanical root-reinforcement models currently available.

The models adopted and developed for this study, i.e., SLIP, LEP-AI, PIP-AI, and H-SLIP, were then described in detail. This included a brief introduction of the platform X-SLIP, which is the result of continuous research and optimization conducted over several years. Following this, the primary results were presented based on a case study analysing several municipalities in the Italian provinces of Reggio Emilia and Parma, Emilia-Romagna, which were significantly affected by rainfall-induced shallow landslides over the past years. Furthermore, secondary experimental aspects were explored, such as the potential use of biodegradable anti-erosion nets that allow for the planting of different vegetative species as part of bioengineering interventions, as well as the kinematic and evolutionary aspects of shallow landslide phenomena, by means of the GPE model.

All of this is a natural (or perhaps unnatural) consequence of climate change, which has confronted us with new realities and demands requiring urgent action. Through this study, an effort was made to contribute meaningfully to scientific research and progress by raising critical questions and offering potential solutions.

GENERAL DISCUSSION

The initial premises of the LEP-AI model were to provide an efficient and rapid tool capable of acting as a filter to identify municipalities at higher risk of sallow landslides during rainfall events. Considering the processing speed offered by this type of model, once trained, it fully meets this requirement. For example, analysing 40 municipalities, including REs over the past 23 years in the provinces of Reggio Emilia and Parma, the LEP-AI model currently takes approximately 0.06 seconds, which is a remarkable result compared to existing models. This makes it a preferable alternative to rainfall-thresholds, commonly employed by civil

protection agencies, as LEP-AI enables deeper pattern recognition and incorporates additional variables into the analysis.

However, the current outcomes of LEP-AI reveal that its predictive quality is still insufficient for use in civil protection applications. This limitation appears to stem from incomplete datasets, which efforts to address with various techniques have so far proven inadequate. Nonetheless, the results are encouraging and suggest that further research in this direction is worthwhile due to the numerous advantages outlined in previous chapters.

Regarding the PIP-AI model, assuming the availability of a previous, perfectly functioning "filter," its results are highly acceptable and consistent. The model has demonstrated a stable architecture capable of delivering very good instability predictions for all pixels within stable and unstable polygons. Instead, the entire study area can be process in approximately 1.2 seconds, at a resolution of 15 x 15 meters. While these times are exceptional, scaling the model to larger areas including more than about 15 municipalities, while maintaining the same resolution, presents computational challenges due to the exponential growth in pixel volume and processing demands. For this reason, a lightweight model like LEP-AI remains necessary, whereas PIP-AI is better suited for detailed, pixel-by-pixel instability analyses.

An interesting observation regarding PIP-AI concerns the influence of vegetative species on the model's predictions. Certain species, such as Abies Alba, Quercus Ilex, and Quercus Robur, appear to increase the likelihood of instability when their probability of presence in a pixel rises, under equal conditions. This finding contradicts existing literature, which generally indicates a stabilizing effect from vegetation. However, PIP-AI also identifies species that behave as expected, i.e., reducing landslide probability as their presence increases, but these species do not rank among the most important in the feature importance analysis. Conversely, the aforementioned three species occupy the 5th, 8th, and 10th positions, respectively. Anyway, it should be noted that the methods employed to define feature importance (Feature Permutation) and feature influence (Partial Dependence Plots) are only two among many available. This discrepancy warrants further investigation in future studies.

Another consideration for PIP-AI concerns its performance outside the training and testing areas, which were instead the regions with higher confidence in pixel stability or instability. Specifically, results in the remaining study area suggest a general overestimation of high-susceptibility zones. This issue could be mitigated by adopting a hybrid approach, such as the H-SLIP model, which combines the strengths of physically-based and AI models. In H-SLIP, results within stable and unstable polygons remain nearly identical to those of PIP-AI, but outside these areas, susceptibility generally decreases, better reflecting reality. Additionally, since SLIP was used for the physically-based part, experimental aspects of the problem are better addressed. For instance, regarding vegetation, SLIP explicitly accounts for mechanical and hydraulic reinforcement through root cohesion and infiltration coefficients.

Finally, a few observations are offered on marginal aspects discussed in the Extra chapter. The GPE model is still in its embryonic stage but holds promise. While it incorporates numerous, often significant, simplifications, previous applications (not included in this study) have demonstrated its potential, such as during the February 2, 2014, landslide in Enna (Misiano et al., 2024). Regarding the biodegradable net, due to time constraints, further experimental analyses were not conducted. However, initial results suggest that the material's properties are highly time dependent. If the results obtained reflect a more recent production batch, determining the time window during which its performance meets a specific standard would suffice to decide on the most appropriate vegetative species for slope stabilization.

CHALLENGES AND FUTURE RESEARCH

Based on the previous considerations, the main challenges that remain open are:

- resolving the issue of incomplete landslide datasets for models such as LEP-AI
- numerically quantifying the vegetative contribution of different species to the final instability results, especially in the case of AI models, as with PIP-AI, it is only possible to estimate their qualitative behaviour
- studying the effects of vegetation in the post-trigger phase of landslides, particularly the potential interference (in favour of safety) of vegetation in the landslide path, with the possible early stopping of motion.

Future studies will therefore primarily focus on addressing the following points:

- improving the predictive quality of LEP-AI and developing a new system that minimizes the issues with current landslide datasets
- enhancing the interaction between physically-based models and AI models, potentially using Physics-Informed Neural Networks (PINNs) that integrate models such as SLIP into susceptibility assessment or that take into account the physical reality of the problem
- advancing techniques for interpreting AI models, both LEP-AI and PIP-AI, leading to progress in the field of eXplainable Artificial Intelligence (XAI)
- integrating new landslide inventories for training LEP-AI and PIP-AI models
- further investigating the results obtained regarding vegetative species from the PIP-AI model
- improving the GPE model, considering the effects of vegetation, particularly in forested areas
- enhancing the efficiency, both computational and data storage, of the X-SLIP platform.

APPENDICES

A – MACHINE LEARNING

The field of Machine Learning (ML) is characterized by a multitude of algorithms designed to learn specific behaviours from data. Indeed, there are various machine learning models, some of which will be briefly explored in the following sections.

Regardless the type of algorithm used, with supervised algorithms the crucial part of the problem is represented by the training dataset, which must be made of input features and the related output for each observation. The errors between the predictions of the model at the current state and the actual outputs are thus used to modify the internal parameters (such as weights and biases for neural networks), with an iterative procedure that is aimed at minimizing the errors between predicted and actual outputs.

A.1 – LOGISTIC REGRESSION (LR)

Logistic Regression (LR) is a statistical method widely used in machine learning for binary classification tasks (BLR), where the goal is to predict one of two possible outcomes. Unlike linear regression, which models a continuous output, logistic regression estimates the probability of a data point belonging to a specific class using the sigmoid function (see Equation 36 and 57).

Particularly, the sigmoid function transforms a linear combination of input features into a probability value, which ranges from 0 to 1:

$$z = \beta_0 + \beta_1 \cdot x_1 + \cdots + \beta_n \cdot x_n \tag{56}$$

$$Out = \frac{1}{1 + e^{-z}} \tag{57}$$

The algorithm uses maximum likelihood estimation (Myung, 2003) to optimize the parameters ($\beta_0, \beta_1, \ldots, \beta_n$) by minimizing the difference between predicted probabilities and actual class labels. Therefore, LR assumes a linear relationship between the input features and the log-odds of the outcome, making it interpretable and computationally efficient.

Despite its simplicity, LR remains a robust and interpretable choice for a wide variety of applications, especially when the relationship between the input features and the outcomes

is approximately linear. Additionally, LR can be used also as a multi classifier, by means of extensions such as multinomial and ordinal LR.

A.2 – Support Vector Machines (SVMs)

Support Vector Machines (SVM) represent one of the most popular machine learning algorithms, primarily used for classification and regression tasks. SVM operates by finding the optimal hyperplane that maximally separates data points of different classes (Figure 0-1), in a high-dimensional feature space. The algorithm identifies in this high-dimensional space which are the data points closest to a given hyperplane, which are critical in defining the decision boundary and are also known as support vectors.

Different forms of SVM can be built, depending on the type of input data and the correlation with outputs. However, in its simplest form, SVM aims to maximize the margin, i.e., the distance between the given hyperplane and the nearest data points for each class, ensuring a great generalization, which means that the model can well predict also unseen data. When data is non-linearly separable, SVM makes use of kernel functions, which transforms the input features into a higher-dimensional space where a linear separation is possible. For instance, a kernel function could be represented by the square of the input feature, which means that a certain input over an axis of the hyper-space (high-dimensional space) is transformed in its square instead of using its original value. Specifically, the most common kernel functions include the radial basis function, polynomial, and sigmoid kernels.

The mathematical formulation of SVM involves solving a convex optimization problem, with the intent to minimize misclassification while maximizing the margin. SVM is particularly effective in high-dimensional spaces and works well even with small datasets.

To conclude, the ability of SVM to handle complex, non-linear decision boundaries through kernel functions makes it versatile for a wide variety of applications.

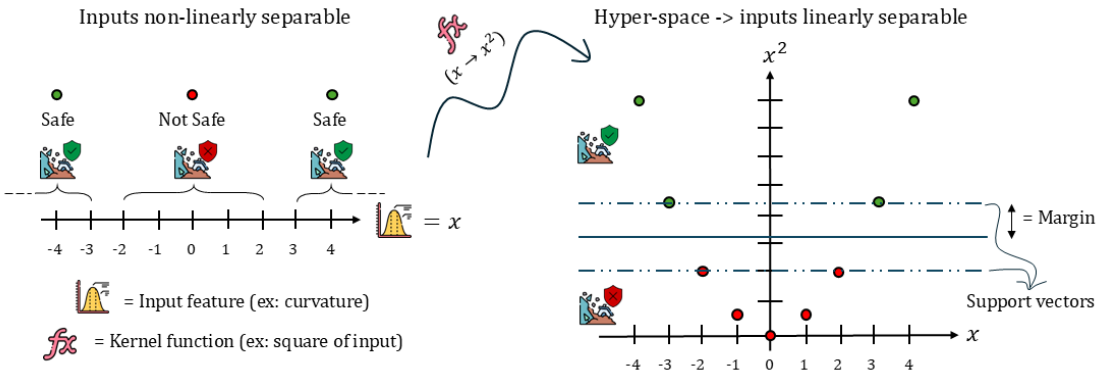

Figure 0-1: Illustrative scheme of the support vector machines' functioning. In this example a single feature is considered, i.e., the curvature. If the input is used in the normal space (that is the actual input values over a single axis) it is not possible to separate linearly the two outputs. Instead, if a kernel function is applied, which in this case is the square of the input, then it is possible to separate linearly the two outputs with a simple line, which in this instance is also horizontal. The margin is the distance between the support vector and the separating line.

A.3 – Decision-Tree Ensembles (AdaBoost, RF, etc.)

Decision-Tree Ensembles (DTE) are advanced machine learning methods that combine multiple decision trees, also referred to as "weak learners", to improve predictive accuracy and robustness. These methods are classified based on how the trees are trained and combined, primarily into two categories: bagging and boosting (Figure 0-2).

- bagging (bootstrap aggregating) - in bagging, decision trees are trained in parallel on different bootstrap samples of the training data. Each tree independently predicts the outcome, and the final output is determined by aggregating their predictions, typically through majority voting for classification tasks or averaging for regression. Algorithms such as Random Forests (RF) leverage this approach, improving stability and reducing overfitting by decorrelating individual trees through feature randomness.
- boosting - in boosting, decision trees are trained sequentially, with each tree correcting the errors of its predecessor. The input data is weighted, emphasizing misclassified instances, and subsequent trees focus on these harder-to-predict cases. The final output is a weighted combination of all trees. Popular algorithms such as XGBoost and AdaBoost use this approach to create highly accurate models by minimizing error iteratively.

To conclude, DTEs are powerful tools in machine learning, combining the simplicity of individual decision trees with the improved accuracy and generalization of ensemble methods. They can be applied in a very wide range of domains, such as classification, regression, and feature ranking.

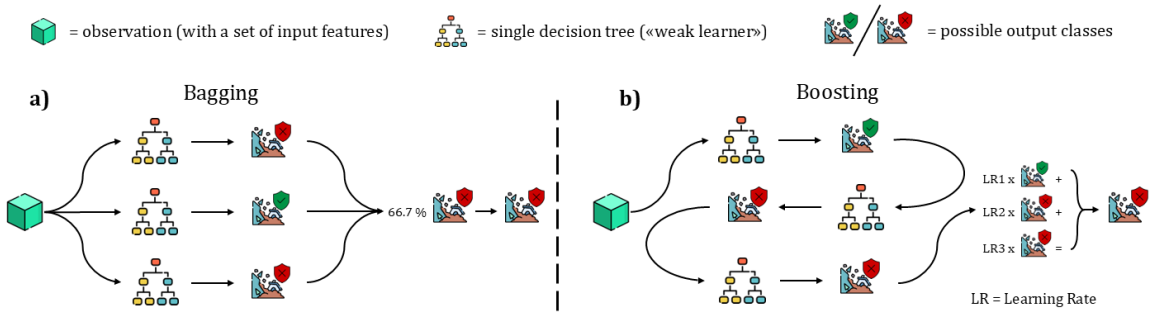

Figure 0-2: Illustrative scheme of the two main decision-tree ensemble types: bagging (a) and boosting (b). With the bagging techniques (a), the single weak learners (which are independent and different) give a separate output. The final output is commonly assigned through the vote of majority between all the outputs given by the different trees. With the boosting techniques (b), the single weak learners are dependent on the previous one. The result is a sort of chain of trees (weak learners), which are put sequentially. Since each tree tries to correct the errors made by the previous, the final tree is the more stable. Anyway, the output is the linear combination of the learning rates of each tree and their single (and partial) results.

A.4 – Artificial Neural Networks (ANNs): The Multi-Layer Perceptron (MLP)

To delve deeper into Artificial Neural Networks (ANN), it is necessary to first introduce the concept of Deep Learning (DL). DL is a subset of ML, and generally of artificial intelligence, which enables models to learn directly from raw data, reducing the need for manual feature engineering. Unlike traditional ML algorithms, which require users to predefine inputs and structure datasets meticulously, DL models automatically extract relevant features and identify complex patterns during training. This adaptability comes with specific requirements, such as larger datasets to prevent overfitting and achieve effective generalization. Among DL architectures, Multi-Layer Perceptron (MLP) networks are one of the former and widely used, particularly for modelling complex, non-linear problems.

MLPs, also referred to as fully connected feedforward neural networks, are structured in layers: an input layer, one or more hidden layers, and an output layer. Each layer comprises computational units called neurons (or nodes). Neurons in each layer are fully connected to those in adjacent layers, forming a unidirectional flow of information. A neuron operates by computing a weighted sum of its input values, adding a bias term, and applying an activation function to introduce non-linearity. The resulting value serves as the input for the neurons of the subsequent layer.

Training a MLP involves adjusting the network's weights and biases through a process called backpropagation of errors, which minimizes the difference between predicted and actual outputs. This difference is also referred to as loss. Different types of loss exist, but the main type, commonly adopted for ANNs, is the cross-entropy loss (see Equation 40 and 41).

Backpropagation relies on reducing the loss through some optimization algorithms, such as Stochastic Gradient Descent (SGD) or advanced variants, which can be Adam or L-BFGS, to iteratively update parameters. Moreover, some regularization techniques, including L1 (lasso) and L2 (ridge), are often employed to penalize large parameter values, reducing the risk of overfitting, which is a common issue of this type of architecture. Other key hyperparameters include the number of layers, neurons per layer, activation functions, learning rate (not necessary with L-BFGS), and dropout.

MLPs can be particularly effective in a wide range of applications, because they can model intricate relationships between inputs and outputs. However, their performance depends on the quality and quantity of training data, as well as careful selection of regularization and optimization strategies.

To conclude, the combination of flexibility, scalability, and accuracy makes MLPs a popular choice for addressing complex classification and regression problems in geosciences and beyond. A schematic view of the MLP functioning is given in Figure 0-3, which summarizes the key aspects of this type of architecture and emphasizes the role of the loss during the training of the model.

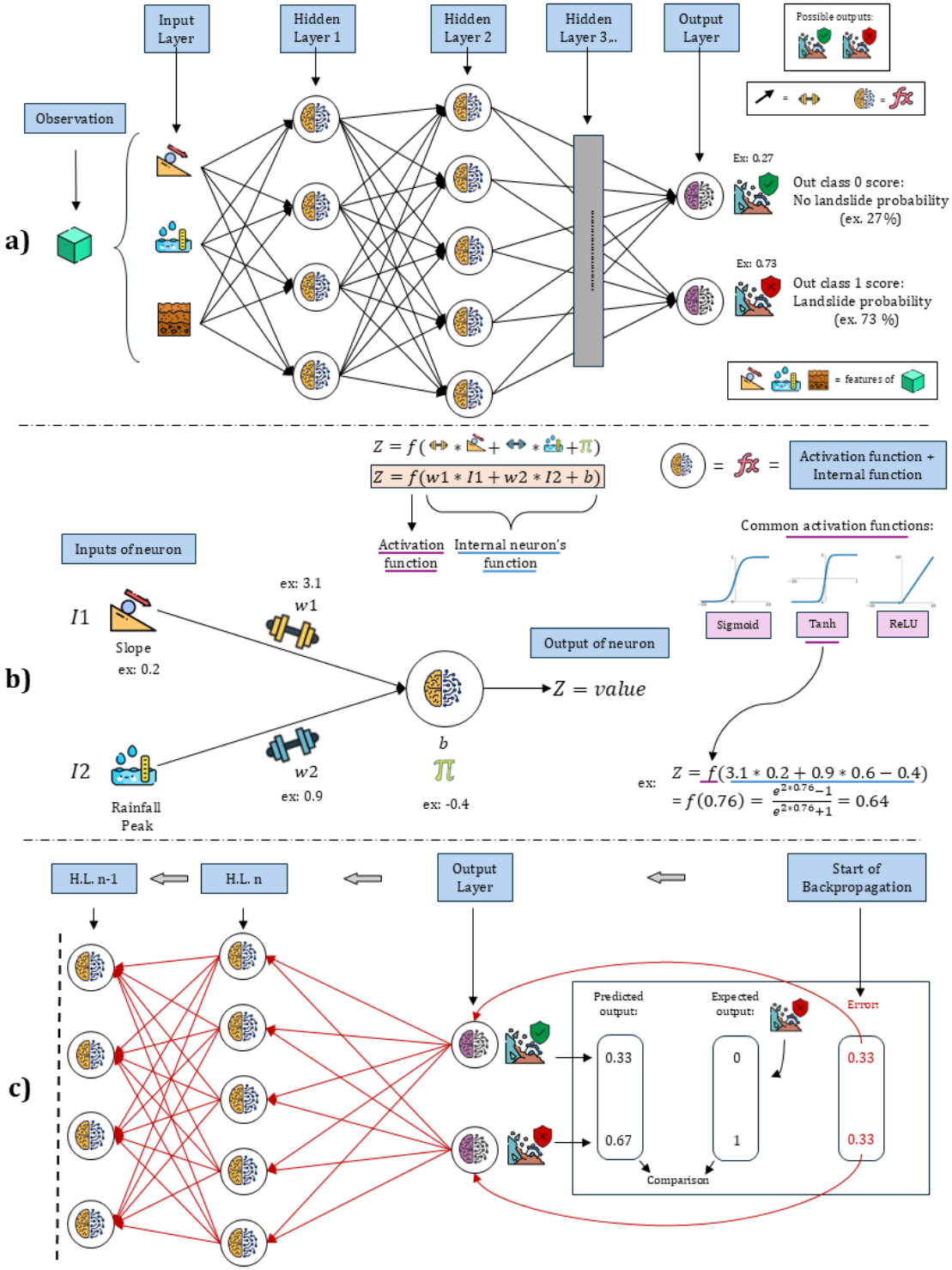

Figure 0-3: Illustrative scheme of the multi-layer perceptron functioning: a) overview of the structure, which in this case has three input features, multiple hidden layers, and two final neurons ('landslide' and 'no landslide' probabilities); b) detail of the functioning of a single neuron, which receives just two inputs and passes the values through both the internal and activation functions, returning the output value; c) detail of the functioning of the backpropagation, based on the errors obtained from the comparison between predicted and expected outputs.

A.5 – KOLMOGOROV-ARNOLD NETWORKS (KANS)

Kolmogorov–Arnold Networks (KAN) are a special and quite recent class of neural networks, based on the theoretical results of Kolmogorov's superposition theorem (Arnold, 1963, 1999; Braun & Griebel, 2009), which states that any multivariate continuous function can be represented as a finite sum of univariate functions. In KANs, this theorem is applied to build neural networks where a set of univariate hidden neurons computes intermediate functions (with a free law), which are then combined from the first to the output layer, in order to approximate complex, multi-dimensional patterns.

Unlike a traditional neural network, which relies on layered architectures with interconnected neurons, a KAN emphasizes the use of fewer hidden neurons by decomposing the input-output relationship into simpler components. This is possible by means of a special activation function inside each neuron, namely the B-spline. The B-spline has the property of being shape-flexible, meaning that the function is not predefined but can be modelled, and thus the final shape of the function depends on some parameters. In other words, unlike classical ANNs, where activation functions are predetermined (e.g., ReLU, Sigmoid etc.), in KANs, the activation functions of neurons depend on the data used for training and the backpropagation process, which can adjust the parameters of each neuron's polylines. This approach reduces the complexity of the network while maintaining its approximation power. In fact, a KAN is particularly suitable for applications where the underlying relationships between variables can be decomposed into simpler, independent functions, making them an efficient choice for certain regression and function approximation tasks.

Despite this, KANs are generally less used in practice when compared to architectures such as MLP, primarily due to the computational cost of implementing the transformations. However, recent advancements and optimization are increasing their applicability.

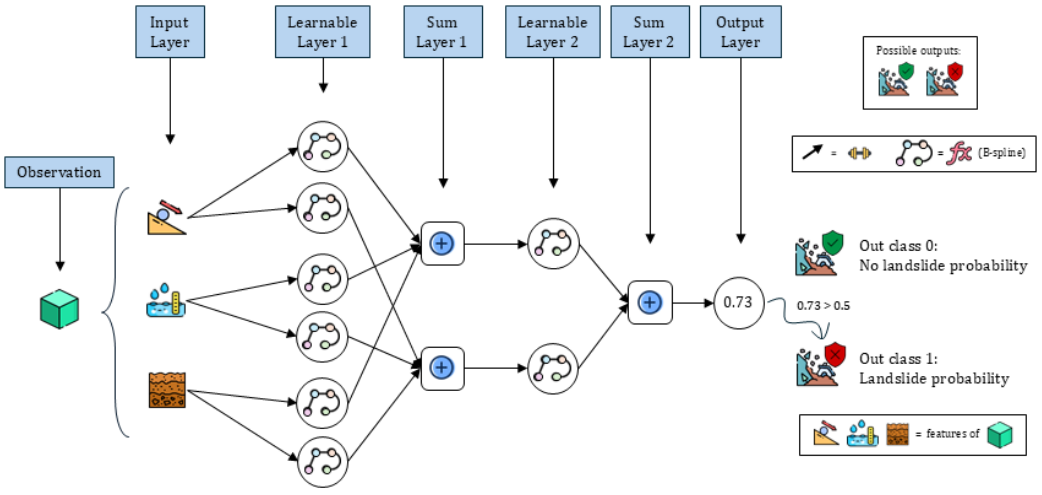

Figure 0-4: Illustrative scheme of the Kormogolov-Arnold network. In contrast with multi-layer perceptrons, in this case there are learnable layers (with functions that have a free form) and summing layers. At the end of the process, it is possible to represent the output with a specific function (sum and concatenation of simple functions).

A.6 – eXplainable Artificial Intelligence (XAI)

eXplainable Artificial Intelligence (XAI) focuses on making ML models more interpretable and transparent by providing insights into how inputs influence outputs. Some of the widely used XAI techniques can be Feature Permutation, Partial Dependence Plots (PDP), and the introduction of random features, which all together may help in elucidating the relationships between input features and model predictions.

Feature Permutation evaluates the importance of a feature by measuring the impact of randomizing its values on the model's performance. In other words, by permuting one feature at a time and observing the change in metrics such as accuracy or loss, this method quantifies the feature's contribution to the model. For instance, the more the loss increase after permuting a specific feature, the more that feature is important. Therefore, a significant performance drop indicates a highly influential feature. This technique is computationally efficient and applicable to any machine learning model, offering a straightforward way to rank feature importance.

On the other hand, PDPs allow to visualize the marginal effect of a feature on the model's predictions by averaging over the values obtained with a specific value. Thus, for each unique value of a feature, all the outcomes of the observations with that value are averaged and it is possible to create a graph of the influence of a single feature (and its values) on the final output. For instance, a PDP might show how increasing slope angle affects landslide susceptibility while holding other feature values constant.

Finally, introducing a random feature among the existing features of a dataset may give useful insights into the behaviour of the model. For instance, if the introduction of the random feature is combined with the Feature Permutation technique, then it is possible to know which are the features that are less important than the random feature and exclude them from the dataset, in order to reduce the non-sense information and improve the quality of the model (in addition to reduce the computational cost).

Together, Feature Permutation, PDPs, and random feature represent some of the indispensable tools that help in understanding and interpreting complex machine learning models, which are oftentimes seen as "black box" models.

The integration of XAI into ML models is considered by the author of this work the beginning of a new era and a paradigm shift in the scientific community. Traditionally, problems have been approached by starting with evidence, proposing hypotheses, and developing models based on those hypotheses, subsequently confirming or refuting the proposed solution. However, with machine learning, this paradigm may evolve, because it will no longer be our task to formulate hypotheses as a starting point for building a model; instead, our role will be to investigate the possible causes and contributing factors that led to the generation of a specific model. In other words, the process will reverse, since we will derive hypotheses from results rather than starting with hypotheses to reach conclusions

B – Relevant Hydraulic and Vegetation Indices

Some relevant indices, commonly used to train artificial intelligence models, are the Topographic Wetness Index (TWI), the Hydrological Response Unit (HRU), the Normalized Difference Vegetation Index (NDVI), the Shannon Wiener Index (SWI), the Enhanced Vegetation Index (EVI), and the Soil-Adjusted Vegetation Index (SAVI).

B.1 – TWI

The TWI is a useful index which quantifies, within a certain area, where the water could be accumulated. In other words, it quantifies how much water is accumulated inside a certain cell of a given DEM map.

To obtain a map containing the TWI values for each cell, a necessary preliminary step consists of defining the upstream contributing area. The upstream contributing area is a map that defines the water flow routing and direction. By means of techniques such as the D8 flow routing (O'Callaghan & Mark, 1984), or similar, the processing of the various pixels is the same and starts from the DEM map. Basically, the uppermost points of the DEM exhibit null values (no water accumulation), while the lower points demonstrate high values. This signifies that null pixels do not receive water from the points situated above them, whereas pixels with substantial values collect water from an extensive area positioned above them.

Before applying the flow algorithm, it is necessary to fill the possible gaps and voids of the DEM, through a smoothing process. After that, the mechanism of the D8 flow routing is illustrated in Figure 0-5, which demonstrates that each pixel of the DEM has 8 cells in which it can discharge water, depending on the slope. Therefore, once the flow direction of a given pixel is assessed, the next pixel would receive the value of the pixel above it, which must be summed to the intrinsic value of the pixel (that is the unit). Following this process, each pixel is represented by an integer number, corresponding to the number of the pixels that are above it and discharged water to the current pixel.

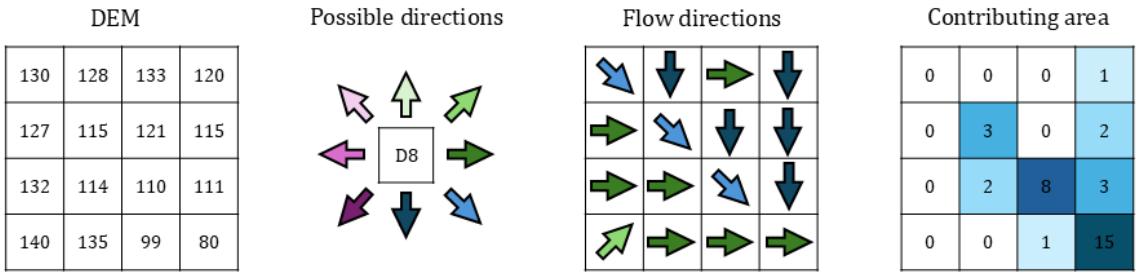

Figure 0-5: Scheme of the D8 flow routing process. The cells that do not receive water but just discharge it contains a null value in the contributing area map. Instead, the cell with the highest value receives the water from all the pixels above it (15 pixels), in this specific case.

Once the contributing area had been defined, it is possible to assess the value of the TWI for each cell of the map, using the following expression:

$$TWI = ln\frac{UCA}{tan\,\beta} \tag{58}$$

where:

- UCA is the value of the upslope (upstream) contributing area for a given pixel
- β is the value of the slope for the same given pixel

B.2 – HRU

The HRU is a useful index which quantifies, within a certain area, some units that are supposed to respond equally to rainfall, from a hydrological point of view. In other words, based on a process of classification of different maps, the pixels of these maps are grouped into classes and the possible combinations of these classes represent a HRU.

The properties that are commonly used for the definition of the HRUs are the slope, soil class, and land use maps. Soil classes and land uses are already grouped into classes, which can be further grouped into less classes (for instance, with the approach seen in Table III-2 and III-5). Instead, the slope values need to be classified based on ranges, which are upon the decision of the user. Generally, from 5 to 10 ranges of slope are sufficient, and it is suggested to take the thresholds for the classes from quantile values.

An example of the process to create HRUs is given in Figure 0-6.

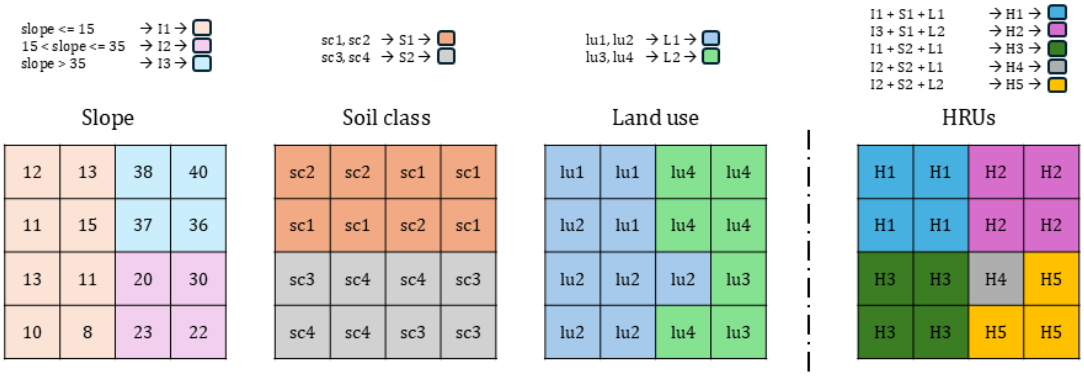

Figure 0-6: Scheme of the HRU's creation, based on slope, soil, and land use macro-classes. Specifically, in this example slope classes were created based on some ranges (on the top), which lead to the creation of I1, I2, and I3 classes; soil raw classes (sc1, sc2, sc3, sc4) were grouped into two main macro-classes, S1 and S2; land use were also grouped started from the raw classes (lu1, lu2, lu3, lu4) into two main classes, L1 and L2. The result is that 5 different combinations of macro-classes are possible, as shown on the right side of the figure.

B.3 – NDVI

The NDVI is a useful index which quantifies, within a certain area, the amount of green that is related to vegetation, i.e., the greenness and the density of the vegetation. In fact, healthy vegetation has a characteristic spectral reflectance curve, which can be assessed by calculating the difference between two bands: the visible red and near-infrared. To estimates

this index in each cell of the map, it is necessary to have a satellite image. Generally, since the amount of "green" vary, depending on the period of the year, this is index is dynamic, which means that changes according to the season considered. In fact, it is commonly assessed 4 times per year, namely with 4 satellite images taken in the middle of each season. However, the NDVI values can range from -1 (no vegetation) to 1 (healthy vegetation).

The formulation of the NDVI is quite straightforward and it is the following:

$$NDVI = \frac{NIR - Red}{NIR + Red} \tag{59}$$

where:

- NIR is the amount of light reflected in the near-infrared electromagnetic spectrum
- Red is the amount of light reflected in the red range of the electromagnetic spectrum

B.4 – SWI, EVI, AND SAVI

The SWI is a useful index which generally quantifies, within a certain area, the diversity. When applied for vegetation purposes, the SWI can quantify the vegetation diversity and structural complexity within terrestrial ecosystems. In these cases, this index would integrate two fundamental components: species richness and species evenness. Thus, the SWI can mathematically capture both the number of unique plant species present and their relative abundance, generating a dimensionless value that increases with greater species diversity and more uniform species distribution (Agbelade et al., 2017; Hashemi et al., 2013; Song et al., 2016). Higher index values typically indicate more complex vegetative systems, which are commonly correlated to enhanced mechanical properties and reduced erosion potential.

The EVI can be described as an optimized NDVI, which means that is based on the same principles but with additional terms, as can be seen from Equation 60. While NDVI demonstrates high sensitivity to chlorophyll concentration, EVI provides superior responsiveness to canopy structural variations. Moreover, EVI captures more nuanced vegetation attributes, including leaf area index (LAI), canopy morphology, plant physiognomy, and architectural complexity (Z. Jiang et al., 2008; Waring et al., 2006). However, EVI values can range from 0 (unhealthy vegetation) to 1 (healthy vegetation).

$$EVI = G \cdot \frac{NIR - Red}{NIR + C1 \cdot Red - C2 \cdot Blue + L} \tag{60}$$

where:

- NIR is the amount of light reflected in the near-infrared electromagnetic spectrum
- Red is the amount of light reflected in the red range of the electromagnetic spectrum
- G is a gain factor, which commonly is equal to 2.5 or 2.4
- $Blue$ is the amount of light reflected in the blue range of the electromagnetic spectrum

- $C1$ and $C2$ are the coefficients of the aerosol resistance term (blue band correction for aerosol influences in the red band), which commonly are 6 and 7.5 respectively
- L is the canopy background adjustment (typically equal to 1), which addresses non-linear, differential NIR and Red radiant transfer through a canopy

Finally, the SAVI is also another optimized NDVI, which minimize the effects of soil reflectance. In fact, soil reflectance may distort NDVI, especially in areas with sparse vegetation. The range of the possible values for SAVI ranges from 0 (unhealthy vegetation) to 1 (healthy vegetation). The formulation of the SAVI index is the following:

$$SAVI = \frac{(NIR - Red) \cdot (1 + L)}{NIR + Red + L} \tag{61}$$

where:

- NIR is the amount of light reflected in the near-infrared electromagnetic spectrum
- Red is the amount of light reflected in the red range of the electromagnetic spectrum
- L is the canopy background adjustment, which in case of moderate vegetation density is commonly set to 0.5 and serves to address non-linear, differential NIR and Red radiant transfer through a canopy

C – Fiber Bundle Model (FBM)

The Fiber Bundle Model (FBM) is a theoretical framework introduced in a basic form during the early 20th century (Peirce, 1926) and subsequently refined with a more robust and comprehensive formulation (Pollen & Simon, 2005), as it is known today. FBM is generally used to study the mechanical behaviour and failure dynamics of materials that can be schematized as a group of multiple individual fibres.

Consequently, when applied to the problem of soil coupled with vegetation roots, the FBM provides a simplified yet powerful approach to analyse the contribution of root systems to slope stability. In this context, the roots can be conceptualized as a bundle of fibres embedded in the soil, where each fibre represents a single root (or a group). These fibres collectively contribute to the shear strength of the soil-root matrix, enhancing its stability against shallow landslides.

The main assumption of the FBM is that each fibre has a specific breaking threshold, which depends on its material properties and the surrounding soil conditions. Sometimes, these breaking thresholds can be assigned to each fibre by means of a Weibull distribution. Anyway, thresholds are not the same for all the fibres contained in the bundle and this means that as external stresses (e.g., soil shear stress) increase, some fibres may fail individually and progressively. Thus, at each step, the remaining fibres (which are still intact) redistribute the load and continue to support this system, until a critical stress level is reached, leading to

complete failure. The above-discussed behaviour can capture the progressive weakening of root-reinforced soil, offering insights into how roots may mitigate slope failure. In fact, the main advantage of FBM consist of accounting for variability in root properties, such as diameter, length, and tensile strength, which influence the maximum final load of the bundle and the failure sequence of fibres. Additionally, the interaction between roots and soil, including factors such as cohesion and friction, can be integrated into the modelling, with the aim to provide a more realistic representation of root reinforcement.

Since the contribution of vegetation is commonly expressed as an additional cohesive term (root cohesion c_r), which is then added to the classical limit equilibrium equations used in slope stability analysis, the collective action of the root system assessed with the FBM is also quantified in terms of a single term, that is the root cohesion.

FBM is particularly valuable for evaluating the role of different vegetation species in slope stabilization, as it allows for comparisons of root strength and failure dynamics under various scenarios, simplifying complex interactions into manageable computations.

Following the development and the success of the FBM, several techniques based on the same principles emerged, specifically designed for applications to soil and root-related problems. Among these, one of the most well-known is the Root Bundle Model (RBM), first introduced in the 2010s (Schwarz, Cohen, et al., 2010; Schwarz, Lehmann, et al., 2010).

An overview of the FBM and RBM functioning, including main formulation, is given in Section 2.2 of Chapter II, with Equations 5, 6, 7, 8, 9, and 10.

D – Scripts Of The X-SLIP Platform

The development and fine-tuning of the X-SLIP platform required several years of work, involving constant implementations, corrections, and refinements. Presenting in this section all the platform's scripts (at the current stage of progress) as plain text is considered neither constructive nor practical. For this reason, the entire platform with all its scripts and functions, conceived and developed during this extensive effort, have been compiled and structured within a GitHub project, available at the following links:

- https://github.com/SalvatoreMisia/M-SLIP.git
- https://github.com/SalvatoreMisia/M-SLIP/tree/b7997ce (updated version at the time of thesis submission)

BIBLIOGRAPHY

Abdi, E., Majnounian, B., Genet, M., & Rahimi, H. (2010). Quantifying the effects of root reinforcement of Persian Ironwood (Parrotia persica) on slope stability; a case study: Hillslope of Hyrcanian forests, northern Iran. *Ecological Engineering*, *36*(10). https://doi.org/10.1016/j.ecoleng.2010.06.020

Abdollahi, M., Vahedifard, F., & Tracy, F. T. (2023). Post-Wildfire Stability of Unsaturated Hillslopes Against Rainfall-Triggered Landslides. *Earth's Future*, *11*(3). https://doi.org/10.1029/2022EF003213

Abe, K., & Ziemer, R. R. (1991). Effect of Tree Roots on Shallow-Seated Landslides 1. *USDA Forest Service Gen. Tech. Rep.*

Abeysiriwardana, H. D., & Gomes, P. I. A. (2022). Integrating vegetation indices and geo-environmental factors in GIS-based landslide-susceptibility mapping: using logistic regression. *Journal of Mountain Science*, *19*(2). https://doi.org/10.1007/s11629-021-6988-8

Abiodun, O. I., Jantan, A., Omolara, A. E., Dada, K. V., Mohamed, N. A. E., & Arshad, H. (2018). State-of-the-art in artificial neural network applications: A survey. In *Heliyon* (Vol. 4, Issue 11). https://doi.org/10.1016/j.heliyon.2018.e00938

Achu, A. L., Aju, C. D., Di Napoli, M., Prakash, P., Gopinath, G., Shaji, E., & Chandra, V. (2023). Machine-learning based landslide susceptibility modelling with emphasis on uncertainty analysis. *Geoscience Frontiers*, *14*(6). https://doi.org/10.1016/j.gsf.2023.101657

Adhikari, A. R., Gautam, M. R., Yu, Z., Imada, S., & Acharya, K. (2013). Estimation of root cohesion for desert shrub species in the Lower Colorado riparian ecosystem and its potential for streambank stabilization. *Ecological Engineering*, *51*. https://doi.org/10.1016/j.ecoleng.2012.12.005

Agbelade, A. D., Onyekwelu, J. C., & Oyun, M. B. (2017). Tree Species Richness, Diversity, and Vegetation Index for Federal Capital Territory, Abuja, Nigeria. *International Journal of Forestry Research*, *2017*. https://doi.org/10.1155/2017/4549756

Ahmed, A. A., Sayed, S., Abdoulhalik, A., Moutari, S., & Oyedele, L. (2024). Applications of machine learning to water resources management: A review of present status and future opportunities. In *Journal of Cleaner Production* (Vol. 441). https://doi.org/10.1016/j.jclepro.2024.140715

Ali, F. (2010). Use of vegetation for slope protection: Root mechanical properties of some tropical plants. *International Journal of Physical Sciences*, *5*(5).

Altmann, A., Toloşi, L., Sander, O., & Lengauer, T. (2010). Permutation importance: A corrected feature importance measure. *Bioinformatics*, *26*(10). https://doi.org/10.1093/bioinformatics/btq134

Alvioli, M., Guzzetti, F., & Rossi, M. (2014). Scaling properties of rainfall induced landslides predicted by a physically based model. *Geomorphology*, *213*. https://doi.org/10.1016/j.geomorph.2013.12.039

Alvioli, M., Melillo, M., Guzzetti, F., Rossi, M., Palazzi, E., von Hardenberg, J., Brunetti, M. T., & Peruccacci, S. (2018). Implications of climate change on landslide hazard in Central Italy. *Science of the Total Environment*, *630*. https://doi.org/10.1016/j.scitotenv.2018.02.315

Alzubaidi, L., Zhang, J., Humaidi, A. J., Al-Dujaili, A., Duan, Y., Al-Shamma, O., Santamaría, J., Fadhel, M. A., Al-Amidie, M., & Farhan, L. (2021). Review of deep learning: concepts, CNN architectures, challenges, applications, future directions. *Journal of Big Data*, *8*(1). https://doi.org/10.1186/s40537-021-00444-8

Andreu, V., Khuder, H., Mickovski, S. B., Spanos, I. A., Norris, J. E., Dorren, L., Nicoll, B. C., Achim, A., Rubio, J. L., Jouneau, L., & Berger, F. (2008). Ecotechnological solutions for unstable slopes: Ground bio-and eco-engineering techniques and strategies. In *Slope Stability and Erosion Control: Ecotechnological Solutions*. https://doi.org/10.1007/978-1-4020-6676-4_7

Anstead, L., & Boar, R. R. (2010). Willow Spiling: Review of Streambank Stabilisation Projects in the UK. *Freshwater Reviews*, *3*(1). https://doi.org/10.1608/frj-3.1.2

Arnold, V. (1963). *Representation of continuous functions of three variables by the superposition of continuous functions of two variables*. https://doi.org/10.1090/trans2/028/05

Arnold, V. (1999). From Hilbert's superposition problem to dynamical systems. In *The Arnoldfest*. https://doi.org/10.1090/fic/024/01

Arnone, E., Caracciolo, D., Noto, L. V., Preti, F., & Bras, R. L. (2016). Modeling the hydrological and mechanical effect of roots on shallow landslides. *Water Resources Research*, *52*(11). https://doi.org/10.1002/2015WR018227

Asada, H., & Minagawa, T. (2023). Impact of Vegetation Differences on Shallow Landslides: A Case Study in Aso, Japan. *Water (Switzerland)*, *15*(18). https://doi.org/10.3390/w15183193

Azarafza, M., Azarafza, M., Akgün, H., Atkinson, P. M., & Derakhshani, R. (2021). Deep learning-based landslide susceptibility mapping. *Scientific Reports*, *11*(1). https://doi.org/10.1038/s41598-021-03585-1

Bainbridge, R., Lim, M., Dunning, S., Winter, M. G., Diaz-Moreno, A., Martin, J., Torun, H., Sparkes, B., Khan, M. W., & Jin, N. (2022). Detection and forecasting of shallow landslides: lessons from a natural laboratory. *Geomatics, Natural Hazards and Risk*, *13*(1). https://doi.org/10.1080/19475705.2022.2041108

Bardi, F., Raspini, F., Frodella, W., Lombardi, L., Nocentini, M., Gigli, G., Morelli, S., Corsini, A., & Casagli, N. (2017). Monitoring the rapid-moving reactivation of earth flows by means of GB-InSAR: The April 2013 Capriglio Landslide (Northern Appennines, Italy). *Remote Sensing*, *9*(2). https://doi.org/10.3390/rs9020165

Basher, L. R. (2013). Erosion Processes and Their Control in New Zealand. *Ecosystem Services in New Zealand: Conditions and Trends*.

Bathurst, J. C., Bovolo, C. I., & Cisneros, F. (2010). Modelling the effect of forest cover on shallow landslides at the river basin scale. *Ecological Engineering*, *36*(3). https://doi.org/10.1016/j.ecoleng.2009.05.001

Baum, R. L., & Godt, J. W. (2010). Early warning of rainfall-induced shallow landslides and debris flows in the USA. *Landslides*, *7*(3). https://doi.org/10.1007/s10346-009-0177-0

Bayer, B., Simoni, A., Schmidt, D., & Bertello, L. (2017). Using advanced InSAR techniques to monitor landslide deformations induced by tunneling in the Northern Apennines, Italy. *Engineering Geology*, *226*. https://doi.org/10.1016/j.enggeo.2017.03.026

BC Ministry of Forests. (2002, November 21). *Forest and Range Practices Act*. King's Printer, Victoria, British Columbia, Canada. https://www.bclaws.gov.bc.ca/civix/document/id/complete/statreg/02069_01

Berahmand, K., Daneshfar, F., Salehi, E. S., Li, Y., & Xu, Y. (2024). Autoencoders and their applications in machine learning: a survey. *Artificial Intelligence Review*, *57*(2). https://doi.org/10.1007/s10462-023-10662-6

Berti, M., Martina, M. L. V., Franceschini, S., Pignone, S., Simoni, A., & Pizziolo, M. (2012). Probabilistic rainfall thresholds for landslide occurrence using a Bayesian approach. *Journal of Geophysical Research: Earth Surface*, *117*(4). https://doi.org/10.1029/2012JF002367

Bertolini, G., Guida, M., & Pizziolo, M. (2005). Landslides in Emilia-Romagna region (Italy): Strategies for hazard assessment and risk management. *Landslides*, *2*(4). https://doi.org/10.1007/s10346-005-0020-1

Bischetti, G. B., Chiaradia, E. A., Epis, T., & Morlotti, E. (2009). Root cohesion of forest species in the Italian Alps. *Plant and Soil*, *324*(1). https://doi.org/10.1007/s11104-009-9941-0

Bischetti, G. B., Chiaradia, E. A., Simonato, T., Speziali, B., Vitali, B., Vullo, P., & Zocco, A. (2005). Root strength and root area ratio of forest species in lombardy (Northern Italy). *Plant and Soil*, *278*(1–2). https://doi.org/10.1007/s11104-005-0605-4

Bischetti, G. B., De Cesare, G., Mickovski, S. B., Rauch, H. P., Schwarz, M., & Stangl, R. (2021). Design and temporal issues in Soil Bioengineering structures for the stabilisation of shallow soil movements. *Ecological Engineering*, *169*. https://doi.org/10.1016/j.ecoleng.2021.106309

Bishop, A. W. (1955). The use of the slip circle in the stability analysis of slopes. *Geotechnique*, *5*(1). https://doi.org/10.1680/geot.1955.5.1.7

Bishop, A. W., & Morgenstern, N. (1960). Stability coefficients for earth slopes. *Geotechnique*, *10*(4). https://doi.org/10.1680/geot.1960.10.4.129

Bogaard, T., & Greco, R. (2018). Invited perspectives: Hydrological perspectives on precipitation intensity-duration thresholds for landslide initiation: Proposing hydro-meteorological thresholds. In *Natural Hazards and Earth System Sciences* (Vol. 18, Issue 1). https://doi.org/10.5194/nhess-18-31-2018

Bordoloi, S., & Ng, C. W. W. (2020). The effects of vegetation traits and their stability functions in bio-engineered slopes: A perspective review. In *Engineering Geology* (Vol. 275). https://doi.org/10.1016/j.enggeo.2020.105742

Borga, M., Dalla Fontana, G., Da Ros, D., & Marchi, L. (1998). Shallow landslide hazard assessment using a physically based model and digital elevation data. *Environmental Geology*, *35*(2–3). https://doi.org/10.1007/s002540050295

Bouma, J. (1981). Soil morphology and preferential flow along macropores. *Agricultural Water Management*, *3*(4). https://doi.org/10.1016/0378-3774(81)90009-3

Bouma, J. (1991). Influence of soil macroporosity on environmental quality. *Advances in Agronomy*, *46*(C). https://doi.org/10.1016/S0065-2113(08)60577-5

Bouma, J., & Dekker, L. W. (1978). A case study on infiltration into dry clay soil I. Morphological observations. *Geoderma*, *20*(1). https://doi.org/10.1016/0016-7061(78)90047-2

Bradley, A. P. (1997). The use of the area under the ROC curve in the evaluation of machine learning algorithms. *Pattern Recognition*, *30*(7). https://doi.org/10.1016/S0031-3203(96)00142-2

Brath, A., Casagli, N., Marani, M., Mercogliano, P., & Motta, R. (2023). *Rapporto della Commissione tecnico-scientifica istituita con deliberazione della Giunta Regionale n. 984/2023 e determinazione dirigenziale 14641/2023, al fine di analizzare gli eventi meteorologici estremi del mese di maggio 2023*.

Braun, J., & Griebel, M. (2009). On a constructive proof of Kolmogorov's superposition theorem. *Constructive Approximation*, *30*(3). https://doi.org/10.1007/s00365-009-9054-2

Breiman, L. (2001). Random forests. *Machine Learning*, *45*(1). https://doi.org/10.1023/A:1010933404324

Bruijnzeel, L. A. (2004). Hydrological functions of tropical forests: Not seeing the soil for the trees? *Agriculture, Ecosystems and Environment*, *104*(1). https://doi.org/10.1016/j.agee.2004.01.015

Brunetti, M. T., Peruccacci, S., Rossi, M., Luciani, S., Valigi, D., & Guzzetti, F. (2010). Rainfall thresholds for the possible occurrence of landslides in Italy. *Natural Hazards and Earth System Science*, *10*(3). https://doi.org/10.5194/nhess-10-447-2010

Budimir, M. E. A., Atkinson, P. M., & Lewis, H. G. (2015). A systematic review of landslide probability mapping using logistic regression. In *Landslides* (Vol. 12, Issue 3). https://doi.org/10.1007/s10346-014-0550-5

Bui, D. T., Shahabi, H., Omidvar, E., Shirzadi, A., Geertsema, M., Clague, J. J., Khosravi, K., Pradhan, B., Pham, B. T., Chapi, K., Barati, Z., Bin Ahmad, B., Rahmani, H., Gróf, G., & Lee, S. (2019). Shallow landslide prediction using a novel hybrid functional machine learning algorithm. *Remote Sensing*, *11*(8). https://doi.org/10.3390/rs11080931

Burrows, K., Marc, O., & Andermann, C. (2023). Retrieval of Monsoon Landslide Timings With Sentinel-1 Reveals the Effects of Earthquakes and Extreme Rainfall. *Geophysical Research Letters*, *50*(16). https://doi.org/10.1029/2023GL104720

Burt, T., Boardman, J., Foster, I., & Howden, N. (2016). More rain, less soil: Long-term changes in rainfall intensity with climate change. *Earth Surface Processes and Landforms*, *41*(4). https://doi.org/10.1002/esp.3868

Burylo, M., Hudek, C., & Rey, F. (2011). Soil reinforcement by the roots of six dominant species on eroded mountainous marly slopes (Southern Alps, France). *Catena*, *84*(1–2). https://doi.org/10.1016/j.catena.2010.09.007

Butler, K. T., Davies, D. W., Cartwright, H., Isayev, O., & Walsh, A. (2018). Machine learning for molecular and materials science. In *Nature* (Vol. 559, Issue 7715). https://doi.org/10.1038/s41586-018-0337-2

Cannon, S. H., & DeGraff, J. (2009). The increasing wildfire and post-fire debris-flow threat in western USA, and implications for consequences of climate change. *Landslides - Disaster Risk Reduction*. https://doi.org/10.1007/978-3-540-69970-5_9

Cardinali, M., Galli, M., Guzzetti, F., Ardizzone, F., Reichenbach, P., & Bartoccini, P. (2006). Rainfall induced landslides in December 2004 in south-western Umbria, central Italy: Types, extent, damage and risk assessment. *Natural Hazards and Earth System Science*, *6*(2). https://doi.org/10.5194/nhess-6-237-2006

Casadei, M., Dietrich, W. E., & Miller, N. L. (2003). Testing a model for predicting the timing and location of shallow landslide initiation in soil-mantled landscapes. *Earth Surface Processes and Landforms*, *28*(9). https://doi.org/10.1002/esp.470

Cazzuffi, D., Gioffrè, D., & Cardile, G. (2016). Environmental aspects in geosynthetic-soil reinforcement structures: The role of vegetation. *GA 2016 - 6th Asian Regional Conference on Geosynthetics: Geosynthetics for Infrastructure Development, Proceedings*.

Cecconi, M., Pane, V., Napoli, P., & Cattoni, E. (2012). Deep roots planting for surface slope protection. *Electronic Journal of Geotechnical Engineering*, *17 U*.

Chang, J. C., & Slaymaker, O. (2002). Frequency and spatial distribution of landslides in a mountainous drainage basin: Western Foothills, Taiwan. *Catena*, *46*(4). https://doi.org/10.1016/S0341-8162(01)00157-6

Chang, K. T., Merghadi, A., Yunus, A. P., Pham, B. T., & Dou, J. (2019). Evaluating scale effects of topographic variables in landslide susceptibility models using GIS-based machine learning techniques. *Scientific Reports*, *9*(1). https://doi.org/10.1038/s41598-019-48773-2

Chen, L., Peng, L., & Yang, L. (2024). Improving Landslide Prediction: Innovative Modeling and Evaluation of Landslide Scenario with Knowledge Graph Embedding. *Remote Sensing*, *16*(1). https://doi.org/10.3390/rs16010145

Chen, W., Fan, L., Li, C., & Pham, B. T. (2020). Spatial prediction of landslides using hybrid integration of artificial intelligence algorithms with frequency ratio and index of entropy in Nanzheng county, China. *Applied Sciences (Switzerland)*, *10*(1). https://doi.org/10.3390/app10010029

Chen, W., Wang, Q., Hesthaven, J. S., & Zhang, C. (2021). Physics-informed machine learning for reduced-order modeling of nonlinear problems. *Journal of Computational Physics*, *446*. https://doi.org/10.1016/j.jcp.2021.110666

Chen, Z., Wang, Z., Xi, H., Yang, Z., Zou, L., Zhou, Z., & Zhou, C. (2016). Recent advances in high slope reinforcement in China: Case studies. *Journal of Rock Mechanics and Geotechnical Engineering*, *8*(6). https://doi.org/10.1016/j.jrmge.2016.11.001

Cheng, L., Cord-Ruwisch, R., & Shahin, M. A. (2013). Cementation of sand soil by microbially induced calcite precipitation at various degrees of saturation. *Canadian Geotechnical Journal*, *50*(1). https://doi.org/10.1139/cgj-2012-0023

Choi, K. Y., & Cheung, R. W. M. (2013). Landslide disaster prevention and mitigation through works in Hong Kong. *Journal of Rock Mechanics and Geotechnical Engineering*, *5*(5). https://doi.org/10.1016/j.jrmge.2013.07.007

Chung, M. C., Tan, C. H., & Chen, C. H. (2017). Local rainfall thresholds for forecasting landslide occurrence: Taipingshan landslide triggered by Typhoon Saola. *Landslides*, *14*(1). https://doi.org/10.1007/s10346-016-0698-2

Cignetti, M., Godone, D., Notti, D., Giordan, D., Bertolo, D., Calò, F., Reale, D., Verde, S., & Fornaro, G. (2023). State of activity classification of deep-seated gravitational slope deformation at regional scale based on Sentinel-1 data. *Landslides*, *20*(12). https://doi.org/10.1007/s10346-023-02114-7

Claessens, L., Knapen, A., Kitutu, M. G., Poesen, J., & Deckers, J. A. (2007). Modelling landslide hazard, soil redistribution and sediment yield of landslides on the Ugandan footslopes of Mount Elgon. *Geomorphology*, *90*(1–2). https://doi.org/10.1016/j.geomorph.2007.01.007

Claessens, L., Schoorl, J. M., & Veldkamp, A. (2007). Modelling the location of shallow landslides and their effects on landscape dynamics in large watersheds: An application for Northern New Zealand. *Geomorphology*, *87*(1–2). https://doi.org/10.1016/j.geomorph.2006.06.039

Cohen, D., Lehmann, P., & Or, D. (2009). Fiber bundle model for multiscale modeling of hydromechanical triggering of shallow landslides. *Water Resources Research*, *45*(10). https://doi.org/10.1029/2009WR007889

Cohen, D., & Schwarz, M. (2017). Tree-root control of shallow landslides. *Earth Surface Dynamics*, *5*(3). https://doi.org/10.5194/esurf-5-451-2017

Collison, A. J. C. (2001). The distribution and strength of riparian tree roots in relation to riverbank reinforcement. *Hydrological Processes*, *15*(1). https://doi.org/10.1002/hyp.152

Comino, E., & Druetta, A. (2009). In situ shear tests of soil samples with grass roots in alpine environment. *American Journal of Environmental Sciences*, *5*(4). https://doi.org/10.3844/ajessp.2009.474.485

Comino, E., Marengo, P., & Rolli, V. (2010). Root reinforcement effect of different grass species: A comparison between experimental and models results. *Soil and Tillage Research*, *110*(1). https://doi.org/10.1016/j.still.2010.06.006

Copernicus. (n.d.). Retrieved 23 October 2024, from https://dataspace.copernicus.eu/

Corominas, J., van Westen, C., Frattini, P., Cascini, L., Malet, J. P., Fotopoulou, S., Catani, F., Van Den Eeckhaut, M., Mavrouli, O., Agliardi, F., Pitilakis, K., Winter, M. G., Pastor, M., Ferlisi, S., Tofani, V., Hervás, J., & Smith, J. T. (2014). Recommendations for the quantitative analysis of landslide risk. *Bulletin of Engineering Geology and the Environment*, *73*(2). https://doi.org/10.1007/s10064-013-0538-8

Cronkite-Ratcliff, C., Schmidt, K. M., & Wirion, C. (2022). Comparing Root Cohesion Estimates from Three Models at a Shallow Landslide in the Oregon Coast Range. *GeoHazards*, *3*(3). https://doi.org/10.3390/geohazards3030022

Cross, S. S., Harrison, R. F., & Kennedy, R. L. (1995). Introduction to neural networks. *The Lancet*, *346*(8982). https://doi.org/10.1016/S0140-6736(95)91746-2

Crosta, G. (1998). Regionalization of rainfall thresholds: An aid to landslide hazard evaluation. *Environmental Geology*, *35*(2–3). https://doi.org/10.1007/s002540050300

Crovelli, R. A. (2000). Probability models for estimation of number and costs of landslides. In *US Geological Survey*.

Crozier, M. J. (2005). Multiple-occurrence regional landslide events in New Zealand: Hazard management issues. *Landslides*, *2*(4). https://doi.org/10.1007/s10346-005-0019-7

Crozier, M. J. (2010). Deciphering the effect of climate change on landslide activity: A review. In *Geomorphology* (Vol. 124, Issues 3–4). https://doi.org/10.1016/j.geomorph.2010.04.009

Cruden, D. M., & Varnes, D. J. (1996). Landslide types and processes. *Special Report - National Research Council, Transportation Research Board*, *247*.

Cui, B., & Zhang, L. (2023). Application of Smoothed Particle Hydrodynamics (SPH) for the Simulation of Flow-Like Landslides on 3D Terrains. *CMES - Computer Modeling in Engineering and Sciences*, *135*(1). https://doi.org/10.32604/cmes.2022.022309

Dai, F. C., Lee, C. F., & Ngai, Y. Y. (2002). Landslide risk assessment and management: An overview. *Engineering Geology*, *64*(1). https://doi.org/10.1016/S0013-7952(01)00093-X

Danjon, F., Fourcaud, T., & Bert, D. (2005). Root architecture and wind-firmness of mature Pinus pinaster. *New Phytologist*, *168*(2). https://doi.org/10.1111/j.1469-8137.2005.01497.x

Dassault Systèmes. (2014). ABAQUS 6.14 Getting Started with Abaqus: Interactive Edition. *ABAQUS 6.14 Getting Started*.

De Baets, S., Poesen, J., Reubens, B., Wemans, K., De Baerdemaeker, J., & Muys, B. (2008). Root tensile strength and root distribution of typical Mediterranean plant species and their contribution to soil shear strength. *Plant and Soil*, *305*(1–2). https://doi.org/10.1007/s11104-008-9553-0

De Baets, S., Torri, D., Poesen, J., Salvador, M. P., & Meersmans, J. (2008). Modelling increased soil cohesion due to roots with EUROSEM. *Earth Surface Processes and Landforms*, *33*(13). https://doi.org/10.1002/esp.1647

Degen, D., Caviedes Voullième, D., Buiter, S., Hendricks Franssen, H. J., Vereecken, H., González-Nicolás, A., & Wellmann, F. (2023). Perspectives of physics-based machine learning strategies for geoscientific applications governed by partial differential equations. In *Geoscientific Model Development* (Vol. 16, Issue 24). https://doi.org/10.5194/gmd-16-7375-2023

Delsigne, F., Lahousse, P., Flez, C., & Guiter, G. (2001). Le Riou Bourdoux : un 'monstre' alpin sous haute surveillance. *Revue Forestière Française*, *5*. https://doi.org/10.4267/2042/5269

Depicker, A., Jacobs, L., Mboga, N., Smets, B., Van Rompaey, A., Lennert, M., Wolff, E., Kervyn, F., Michellier, C., Dewitte, O., & Govers, G. (2021). Historical dynamics of landslide risk from population and forest-cover changes in the Kivu Rift. *Nature Sustainability*, *4*(11). https://doi.org/10.1038/s41893-021-00757-9

Dext3r. (n.d.). Retrieved 23 October 2024, from https://simc.arpae.it/dext3r/

Dhakal, A. S., & Sidle, R. C. (2003). Long-term modelling of landslides for different forest management practices. *Earth Surface Processes and Landforms*, *28*(8). https://doi.org/10.1002/esp.499

Di Napoli, M., Di Martire, D., Bausilio, G., Calcaterra, D., Confuorto, P., Firpo, M., Pepe, G., & Cevasco, A. (2021). Rainfall-induced shallow landslide detachment, transit and runout susceptibility mapping by integrating machine learning techniques and gis-based approaches. *Water (Switzerland)*, *13*(4). https://doi.org/10.3390/w13040488

DiBiagio, A., Capobianco, V., Oen, A., & Tallaksen, L. M. (2024). State-of-the-art: parametrization of hydrological and mechanical reinforcement effects of vegetation in slope stability models for shallow landslides. *Landslides*. https://doi.org/10.1007/s10346-024-02300-1

Dietrich, W. E., Bellugi, D., & Real de Asua, R. (2011). *Validation of the Shallow Landslide Model, SHALSTAB, for forest management*. https://doi.org/10.1029/ws002p0195

Docker, B. B., & Hubble, T. C. T. (2008). Quantifying root-reinforcement of river bank soils by four Australian tree species. *Geomorphology*, *100*(3–4). https://doi.org/10.1016/j.geomorph.2008.01.009

Dou, J., Paudel, U., Oguchi, T., Uchiyama, S., & Hayakawa, Y. S. (2015). Shallow and deep-seated landslide differentiation using support vector machines: A case study of the chuetsu area, Japan. *Terrestrial, Atmospheric and Oceanic Sciences*, *29*(2). https://doi.org/10.3319/TAO.2014.12.02.07(EOSI)

Dowling, C. A., & Santi, P. M. (2014). Debris flows and their toll on human life: A global analysis of debris-flow fatalities from 1950 to 2011. *Natural Hazards*, *71*(1). https://doi.org/10.1007/s11069-013-0907-4

Draebing, D., Gebhard, T., & Pheiffer, M. (2023). Geology and vegetation control landsliding on forest-managed slopes in scarplands. *Earth Surface Dynamics*, *11*(1). https://doi.org/10.5194/esurf-11-71-2023

Dupuy, L., Fourcaud, T., & Stokes, A. (2005). A numerical investigation into the influence of soil type and root architecture on tree anchorage. *Plant and Soil*, *278*(1–2). https://doi.org/10.1007/s11104-005-7577-2

Dyson, A. P., Tolooiyan, A., & Griffiths, D. V. (2023). Numerical Modelling Techniques for Stability Analysis of Slopes Reinforced with Shallow Roots. *Geotechnics*, *3*(2). https://doi.org/10.3390/geotechnics3020016

EarthExplorer. (n.d.). Retrieved 23 October 2024, from https://earthexplorer.usgs.gov/

EcoDataCube. (n.d.). Retrieved 23 October 2024, from https://ecodatacube.eu/

Engwirda, D. (2024). *INPOLY: A fast points-in-polygon test*. Github. https://github.com/dengwirda/inpoly

Esmaiili, M., Abdi, E., Nieber, J. L., Jafary, M., & Majnounian, B. (2021). How roots of Picea abies and Fraxinus excelsior plantations contribute to soil strength and slope stability: Evidence from a study case in the Hyrcanian Forest, Iran. *Soil Research*, *59*(3). https://doi.org/10.1071/SR20083

Fan, C. C., & Chen, Y. W. (2010). The effect of root architecture on the shearing resistance of root-permeated soils. *Ecological Engineering*, *36*(6). https://doi.org/10.1016/j.ecoleng.2010.03.003

Fell, R., Ho, K. K. S., Lacasse, S., & Leroi, E. (2020). A framework for landslide risk assessment and management. In *Landslide Risk Management*. https://doi.org/10.1201/9781439833711-4

Feng, D., Chen, F., & Xu, W. (2013). Efficient leave-one-out strategy for supervised feature selection. *Tsinghua Science and Technology*, *18*(6). https://doi.org/10.1109/tst.2013.6678908

Fernandez, M. A. (2017). Adoption of erosion management practices in New Zealand. *Land Use Policy*, *63*. https://doi.org/10.1016/j.landusepol.2017.01.040

Ferrario, M. F., & Livio, F. (2024). Rapid Mapping of Landslides Induced by Heavy Rainfall in the Emilia-Romagna (Italy) Region in May 2023. *Remote Sensing*, *16*(1). https://doi.org/10.3390/rs16010122

Flach, P. A., & Kull, M. (2015). Precision-Recall-Gain curves: PR analysis done right. *Advances in Neural Information Processing Systems*, *2015-January*.

Fleming, R. W., & Taylor, F. A. (1980). ESTIMATING THE COSTS OF LANDSLIDE DAMAGE IN THE UNITED STATES. *Geological Survey Circular (United States)*, *832*.

Forbes, K., Broadhead, J., Bischetti, G. B., Brardinoni, F., Dykes, A., Gray, D., Lmaizumi, F., Kuriakose, S. L., Osman, N., Petley, D., Stokes, A., Verbist, B., & Wu, L. H. (2013). The role of trees and forests in the prevention of landslides and rehabilitation of landslide-affected areas in Asia Second edition. *Forests and Landslides*.

Formetta, G., Capparelli, G., & Versace, P. (2016). Evaluating performance of simplified physically based models for shallow landslide susceptibility. *Hydrology and Earth System Sciences*, *20*(11). https://doi.org/10.5194/hess-20-4585-2016

Frattini, P., Crosta, G., & Sosio, R. (2009). Approaches for defining thresholds and return periods for rainfall-triggered shallow landslides. *Hydrological Processes*, *23*(10). https://doi.org/10.1002/hyp.7269

Fredlund, D. G., Morgenstern, N. R., & Widger, R. A. (1978). SHEAR STRENGTH OF UNSATURATED SOILS. *Canadian Geotechnical Journal*, *15*(3). https://doi.org/10.1139/t78-029

Fredlund, D. G., & Rahardjo, H. (1993). Soil Mechanics for Unsaturated Soils. In *Soil Mechanics for Unsaturated Soils*. https://doi.org/10.1002/9780470172759

Fredlund, D. G., Xing, A., Fredlund, M. D., & Barbour, S. L. (1996). The relationship of the unsaturated soil shear strength to the soil-water characteristic curve. *Canadian Geotechnical Journal*, *33*(3). https://doi.org/10.1139/t96-065

Freund, Y. (2009). *A more robust boosting algorithm*.

Friedman, J., Hastie, T., & Tibshirani, R. (2000). Additive logistic regression: A statistical view of boosting. In *Annals of Statistics* (Vol. 28, Issue 2). https://doi.org/10.1214/aos/1016218223

Froude, M. J., & Petley, D. N. (2018). Global fatal landslide occurrence from 2004 to 2016. *Natural Hazards and Earth System Sciences*, *18*(8). https://doi.org/10.5194/nhess-18-2161-2018

Fusco, F., Abbate, A., Calcaterra, D., De Vita, P., Guerriero, L., Longoni, L., & Papini, M. (2023). SUSCEPTIBILITY MAPPING OF SHALLOW LANDSLIDES INDUCING DEBRIS FLOWS: A COMPARISON OF PHYSICS-BASED APPROACHES. *Italian Journal of Engineering Geology and Environment*, *Special Issue 1*. https://doi.org/10.4408/IJEGE.2023-01.S-09

Fusco, F., De Vita, P., Mirus, B. B., Baum, R. L., Allocca, V., Tufano, R., Clemente, E. Di, & Calcaterra, D. (2019). Physically based estimation of rainfall thresholds triggering shallow landslides in volcanic slopes of Southern Italy. *Water (Switzerland)*, *11*(9). https://doi.org/10.3390/w11091915

Galve, J. P., Cevasco, A., Brandolini, P., Piacentini, D., Azañón, J. M., Notti, D., & Soldati, M. (2016). Cost-based analysis of mitigation measures for shallow-landslide risk reduction strategies. *Engineering Geology*, *213*. https://doi.org/10.1016/j.enggeo.2016.09.002

Gao, L., Wang, X., Johnson, B. A., Tian, Q., Wang, Y., Verrelst, J., Mu, X., & Gu, X. (2020). Remote sensing algorithms for estimation of fractional vegetation cover using pure vegetation index values: A review. In *ISPRS Journal of Photogrammetry and Remote Sensing* (Vol. 159). https://doi.org/10.1016/j.isprsjprs.2019.11.018

García-Ruiz, J. M., Beguería, S., Arnáez, J., Sanjuán, Y., Lana-Renault, N., Gómez-Villar, A., Álvarez-Martínez, J., & Coba-Pérez, P. (2017). Deforestation induces shallow landsliding in the montane and subalpine belts of the Urbión Mountains, Iberian Range, Northern Spain. *Geomorphology*, *296*. https://doi.org/10.1016/j.geomorph.2017.08.016

Gardner, M. W., & Dorling, S. R. (1998). Artificial neural networks (the multilayer perceptron) - a review of applications in the atmospheric sciences. *Atmospheric Environment*, *32*(14–15). https://doi.org/10.1016/S1352-2310(97)00447-0

Gariano, S. L., Brunetti, M. T., Iovine, G., Melillo, M., Peruccacci, S., Terranova, O., Vennari, C., & Guzzetti, F. (2015). Calibration and validation of rainfall thresholds for shallow landslide forecasting in Sicily, southern Italy. *Geomorphology*, *228*. https://doi.org/10.1016/j.geomorph.2014.10.019

Gariano, S. L., & Guzzetti, F. (2016). Landslides in a changing climate. In *Earth-Science Reviews* (Vol. 162). https://doi.org/10.1016/j.earscirev.2016.08.011

Gatto, M. P. A., Lentini, V., Montrasio, L., & Castelli, F. (2023a). A simplified semi-quantitative procedure based on the SLIP model for landslide risk assessment: the case study of

Gioiosa Marea (Sicily, Italy). *Landslides*, *20*(7). https://doi.org/10.1007/s10346-023-02040-8

Gatto, M. P. A., Lentini, V., Montrasio, L., & Castelli, F. (2023b). Rainfall-induced shallow landslides triggered after vegetation removed because of fires: G-XSLIP application to Gioiosa Marea (Sicily, Italy). *E3S Web of Conferences*, *415*. https://doi.org/10.1051/e3sconf/202341504005

Gatto, M. P. A., Misiano, S., & Montrasio, L. (2022). On the Use of MATLAB to Import and Manipulate Geographic Data: A Tool for Landslide Susceptibility Assessment. *Geographies*, *2*(2). https://doi.org/10.3390/geographies2020022

Gatto, M. P. A., & Montrasio, L. (2023). X-SLIP: A SLIP-based multi-approach algorithm to predict the spatial–temporal triggering of rainfall-induced shallow landslides over large areas. *Computers and Geotechnics*, *154*. https://doi.org/10.1016/j.compgeo.2022.105175

Geertsema, M., Highland, L., & Vaugeouis, L. (2009). Environmental impact of landslides. *Landslides - Disaster Risk Reduction*. https://doi.org/10.1007/978-3-540-69970-5_31

Genet, M., Kokutse, N., Stokes, A., Fourcaud, T., Cai, X., Ji, J., & Mickovski, S. (2008). Root reinforcement in plantations of Cryptomeria japonica D. Don: effect of tree age and stand structure on slope stability. *Forest Ecology and Management*, *256*(8). https://doi.org/10.1016/j.foreco.2008.05.050

Genet, M., Stokes, A., Salin, F., Mickovski, S. B., Fourcaud, T., Dumail, J. F., & Van Beek, R. (2005). The influence of cellulose content on tensile strength in tree roots. *Plant and Soil*, *278*(1–2). https://doi.org/10.1007/s11104-005-8768-6

Geologia, suoli e sismica - Regione Emilia-Romagna - Ambiente. (n.d.). Retrieved 22 October 2024, from https://ambiente.regione.emilia-romagna.it/it/geologia

Geoportale della Lombardia. (n.d.). Retrieved 22 October 2024, from https://www.geoportale.regione.lombardia.it/

Geoportale Nazionale. (n.d.). Retrieved 22 October 2024, from https://gn.mase.gov.it/portale/home

Geoportale Regione Emilia-Romagna. (n.d.). Retrieved 22 October 2024, from https://geoportale.regione.emilia-romagna.it/

Geoportale Regione Liguria. (n.d.). Retrieved 22 October 2024, from https://geoportal.regione.liguria.it/

Geoscopio. (n.d.). Retrieved 22 October 2024, from https://www.regione.toscana.it/-/geoscopio

Ghestem, M., Cao, K., Ma, W., Rowe, N., Leclerc, R., Gadenne, C., & Stokes, A. (2014). A framework for identifying plant species to be used as 'ecological engineers' for fixing soil on unstable slopes. *PLoS ONE*, *9*(8). https://doi.org/10.1371/journal.pone.0095876

Ghestem, M., Veylon, G., Bernard, A., Vanel, Q., & Stokes, A. (2014). Influence of plant root system morphology and architectural traits on soil shear resistance. *Plant and Soil*, *377*(1–2). https://doi.org/10.1007/s11104-012-1572-1

Gidon, J. S., & Sahoo, S. (2020). Rainfall-Induced Slope Failures and Use of Bamboo as a Remedial Measure: A Review. In *Indian Geotechnical Journal* (Vol. 50, Issue 5). https://doi.org/10.1007/s40098-020-00409-3

Glade, T. (2003). Landslide occurrence as a response to land use change: A review of evidence from New Zealand. *Catena*, *51*(3–4). https://doi.org/10.1016/S0341-8162(02)00170-4

GloH2O. (n.d.). Retrieved 23 October 2024, from https://www.gloh2o.org/

Gomi, T., Sidle, R. C., Miyata, S., Kosugi, K., & Onda, Y. (2008). Dynamic runoff connectivity of overland flow on steep forested hillslopes: Scale effects and runoff transfer. *Water Resources Research*, *44*(8). https://doi.org/10.1029/2007WR005894

Gonzalez-Ollauri, A., & Mickovski, S. B. (2017). Plant-soil reinforcement response under different soil hydrological regimes. *Geoderma*, *285*. https://doi.org/10.1016/j.geoderma.2016.10.002

GPM. (n.d.). Retrieved 23 October 2024, from https://gpm.nasa.gov/

Gray, D. H., & Megahan, W. F. (1981). Forest vegetation removal and slope stability in the Idaho batholith. *U.S. Department of Agriculture, Forest Service, Research Paper*, *INT-271*. https://doi.org/10.5962/bhl.title.68699

Gray, D. H., & Ohashi, H. (1983). Mechanics of fiber reinforcement in sand. *Journal of Geotechnical Engineering*, *109*(3). https://doi.org/10.1061/(ASCE)0733-9410(1983)109:3(335)

Greenway, D. R. (1987). Vegetation and slope stability. *Slope Stability*, 187–230.

Greenwell, B. M. (2017). pdp: An R package for constructing partial dependence plots. *R Journal*, *9*(1). https://doi.org/10.32614/rj-2017-016

Greenwood, J. R. (2006). SLIP4EX - A program for routine slope stability analysis to include the effects of vegetation, reinforcement and hydrological changes. *Geotechnical and Geological Engineering*, *24*(3). https://doi.org/10.1007/s10706-005-4156-5

Greenwood, J. R., Norris, J. E., & Wint, J. (2004). Assessing the contribution of vegetation to slope stability. *Proceedings of the Institution of Civil Engineers: Geotechnical Engineering*, *157*(4). https://doi.org/10.1680/geng.2004.157.4.199

Greenwood, J. R., Norris, J. E., & Wint, J. (2007). Discussion: Assessing the contribution of vegetation to slope stability. In *Proceedings of the Institution of Civil Engineers: Geotechnical Engineering* (Vol. 160, Issue 1). https://doi.org/10.1680/geng.2007.160.1.51

Guhathakurta, P., Sreejith, O. P., & Menon, P. A. (2011). Impact of climate change on extreme rainfall events and flood risk in India. *Journal of Earth System Science*, *120*(3). https://doi.org/10.1007/s12040-011-0082-5

Gunning, D., Stefik, M., Choi, J., Miller, T., Stumpf, S., & Yang, G. Z. (2019). XAI-Explainable artificial intelligence. *Science Robotics*, *4*(37). https://doi.org/10.1126/scirobotics.aay7120

Guo, Z., Tian, B., Li, G., Huang, D., Zeng, T., He, J., & Song, D. (2023). Landslide susceptibility mapping in the Loess Plateau of northwest China using three data-driven techniques-a case study from middle Yellow River catchment. *Frontiers in Earth Science*, *10*. https://doi.org/10.3389/feart.2022.1033085

Guthrie, R. H. (2002). The effects of logging on frequency and distribution of landslides in three watersheds on Vancouver Island, British Columbia. *Geomorphology*, *43*(3–4). https://doi.org/10.1016/S0169-555X(01)00138-6

Guzzetti, F. (2000). Landslide fatalities and the evaluation of landslide risk in Italy. *Engineering Geology*, *58*(2). https://doi.org/10.1016/S0013-7952(00)00047-8

Guzzetti, F., Gariano, S. L., Peruccacci, S., Brunetti, M. T., Marchesini, I., Rossi, M., & Melillo, M. (2020). Geographical landslide early warning systems. In *Earth-Science Reviews* (Vol. 200). https://doi.org/10.1016/j.earscirev.2019.102973

Guzzetti, F., Peruccacci, S., Rossi, M., & Stark, C. P. (2007). Rainfall thresholds for the initiation of landslides in central and southern Europe. *Meteorology and Atmospheric Physics*, *98*(3–4). https://doi.org/10.1007/s00703-007-0262-7

Guzzetti, F., Stark, C. P., & Salvati, P. (2005). Evaluation of flood and landslide risk to the population of Italy. *Environmental Management*, *36*(1). https://doi.org/10.1007/s00267-003-0257-1

H. Gray, D., & T. Leiser, A. (1982). *Biotechnical slope protection and erosion control* (1st Edition). Van Nostrand. http://worldcat.org/isbn/0442212224

Hales, T. C., Ford, C. R., Hwang, T., Vose, J. M., & Band, L. E. (2009). Topographic and ecologic controls on root reinforcement. *Journal of Geophysical Research: Earth Surface*, *114*(3). https://doi.org/10.1029/2008JF001168

Hallegatte, S., Rozenberg, J., Rentschler, J., Nicolas, C., & Fox, C. (2019). Strengthening New Infrastructure Assets: A Cost-Benefit Analysis. In *Strengthening New Infrastructure Assets: A Cost-Benefit Analysis*. https://doi.org/10.1596/1813-9450-8896

Hancox, G. T. ., & Wright, K. . (2005). *Analysis of landsliding caused by the 15-17 February 2004 rainstorm in the Wanganui-Manawatu hill country, southern North Island, New Zealand*. Institute of Geological & Nuclear Sciences.

Hao, L., A., R., Van Westen, C., K. S., S., Ranjan Martha, T., Jaiswal, P., & G. McAdoo, B. (2020). Constructing a complete landslide inventory dataset for the 2018 monsoon disaster in Kerala, India, for land use change analysis. *Earth System Science Data*, *12*(4). https://doi.org/10.5194/essd-12-2899-2020

Hasegawa, S., Dahal, R. K., Nishimura, T., Nonomura, A., & Yamanaka, M. (2009). DEM-Based analysis of earthquake-induced shallow landslide susceptibility. *Geotechnical and Geological Engineering*, *27*(3). https://doi.org/10.1007/s10706-008-9242-z

Hashemi, S. A., Fallah Chai, M. M., & Bayat, S. (2013). An analysis of vegetation indices in relation to tree species diversity using by satellite data in the northern forests of Iran. *Arabian Journal of Geosciences*, *6*(9). https://doi.org/10.1007/s12517-012-0576-8

He, L., Wu, X., He, Z., Xue, D., Luo, F., Bai, W., Kang, G., Chen, X., & Zhang, Y. (2023). Susceptibility Assessment of Landslides in the Loess Plateau Based on Machine Learning Models: A Case Study of Xining City. *Sustainability*, *15*(20). https://doi.org/10.3390/su152014761

He, S., Wang, J., & Liu, S. (2020). Rainfall event-duration thresholds for landslide occurrences in China. *Water (Switzerland)*, *12*(2). https://doi.org/10.3390/w12020494

Hewlett, J. D., & Hibbert, A. R. (1967). Factors affecting the response of small watersheds to precipitation in humid areas. *Forest Hydrology*. https://doi.org/10.1177/0309133309338118

Himiyama, Y. (1998). Land use/cover changes in Japan: From the past to the future. *Hydrological Processes*, *12*(13–14). https://doi.org/10.1002/(sici)1099-1085(19981030)12:13/14<1995::aid-hyp714>3.0.co;2-c

Hong, H. (2023). Assessing landslide susceptibility based on hybrid Best-first decision tree with ensemble learning model. *Ecological Indicators*, *147*. https://doi.org/10.1016/j.ecolind.2023.109968

Hu, X. song, Brierley, G., Zhu, H. li, Li, G. rong, Fu, J. tao, Mao, X. qing, Yu, Q. qin, & Qiao, N. (2013). An exploratory analysis of vegetation strategies to reduce shallow landslide activity on loess hillslopes, Northeast Qinghai-Tibet Plateau, China. *Journal of Mountain Science*, *10*(4). https://doi.org/10.1007/s11629-013-2584-x

Huang, F., Chen, J., Liu, W., Huang, J., Hong, H., & Chen, W. (2022). Regional rainfall-induced landslide hazard warning based on landslide susceptibility mapping and a critical rainfall threshold. *Geomorphology*, *408*. https://doi.org/10.1016/j.geomorph.2022.108236

Hughes, A. O. (2016). Riparian management and stream bank erosion in New Zealand. In *New Zealand Journal of Marine and Freshwater Research* (Vol. 50, Issue 2). https://doi.org/10.1080/00288330.2015.1116449

Hungr, O., Leroueil, S., & Picarelli, L. (2014). The Varnes classification of landslide types, an update. In *Landslides* (Vol. 11, Issue 2). https://doi.org/10.1007/s10346-013-0436-y

Imaizumi, F., & Sidle, R. C. (2012). Effect of forest harvesting on hydrogeomorphic processes in steep terrain of central Japan. *Geomorphology*, *169–170*. https://doi.org/10.1016/j.geomorph.2012.04.017

Imaizumi, F., Sidle, R. C., & Kamei, R. (2008). Effects of forest harvesting on the occurrence of landslides and debris flows in steep terrain of central Japan. *Earth Surface Processes and Landforms*, *33*(6). https://doi.org/10.1002/esp.1574

Ioffe, S., & Szegedy, C. (2015). Batch normalization: Accelerating deep network training by reducing internal covariate shift. *32nd International Conference on Machine Learning, ICML 2015*, *1*.

ISPRA. (n.d.). Retrieved 22 October 2024, from https://idrogeo.isprambiente.it/app/iffi

ISPRA. (2023). *Quadro di sintesi dissesto frane Emilia-Romagna, Italia (aggiornamento 19/05/2023)* .

Iverson, R. M. (1997). The physics of debris flows. *Reviews of Geophysics*, *35*(3). https://doi.org/10.1029/97RG00426

Iverson, R. M., & Reid, M. E. (1992). Gravity-driven groundwater flow and slope failure potential: 1. Elastic Effective-Stress Model. *Water Resources Research*, *28*(3). https://doi.org/10.1029/91WR02694

Jakob, M. (2000). The impacts of logging on landslide activity at Clayoquot Sound, British Columbia. *Catena*, *38*(4). https://doi.org/10.1016/S0341-8162(99)00078-8

Jakob, M. (2022). Landslides in a changing climate. *Landslide Hazards, Risks, and Disasters*, 505–579. https://doi.org/10.1016/B978-0-12-818464-6.00003-2

Jakob, M., & Owen, T. (2021). Projected effects of climate change on shallow landslides, North Shore Mountains, Vancouver, Canada. *Geomorphology*, *393*. https://doi.org/10.1016/j.geomorph.2021.107921

Jayawickreme, D. H., Van Dam, R. L., & Hyndman, D. W. (2010). Hydrological consequences of land-cover change: Quantifying the influence of plants on soil moisture with time-lapse electrical resistivity. *Geophysics*, *75*(4). https://doi.org/10.1190/1.3464760

Jemec Auflič, M., Bezak, N., Šegina, E., Frantar, P., Gariano, S. L., Medved, A., & Peternel, T. (2023). Climate change increases the number of landslides at the juncture of the Alpine, Pannonian and Mediterranean regions. *Scientific Reports*, *13*(1). https://doi.org/10.1038/s41598-023-50314-x

Ji, J., Mao, Z., Qu, W., & Zhang, Z. (2020). Energy-based fibre bundle model algorithms to predict soil reinforcement by roots. *Plant and Soil*, *446*(1–2). https://doi.org/10.1007/s11104-019-04327-z

Jiang, H., Zou, Q., Zhou, B., Jiang, Y., Cui, J., Yao, H., & Zhou, W. (2023). Estimation of Shallow Landslide Susceptibility Incorporating the Impacts of Vegetation on Slope Stability. *International Journal of Disaster Risk Science*, *14*(4). https://doi.org/10.1007/s13753-023-00507-9

Jiang, Z., Huete, A. R., Didan, K., & Miura, T. (2008). Development of a two-band enhanced vegetation index without a blue band. *Remote Sensing of Environment*, *112*(10). https://doi.org/10.1016/j.rse.2008.06.006

Jirasek, F., & Hasse, H. (2023). Combining Machine Learning with Physical Knowledge in Thermodynamic Modeling of Fluid Mixtures. In *Annual Review of Chemical and Biomolecular Engineering* (Vol. 14). https://doi.org/10.1146/annurev-chembioeng-092220-025342

Jones, J. N., Boulton, S. J., Bennett, G. L., Stokes, M., & Whitworth, M. R. Z. (2021). Temporal Variations in Landslide Distributions Following Extreme Events: Implications for Landslide Susceptibility Modeling. *Journal of Geophysical Research: Earth Surface*, *126*(7). https://doi.org/10.1029/2021JF006067

Jorner, K., Brinck, T., Norrby, P. O., & Buttar, D. (2021). Machine learning meets mechanistic modelling for accurate prediction of experimental activation energies. *Chemical Science*, *12*(3). https://doi.org/10.1039/d0sc04896h

Kadavi, P. R., Lee, C. W., & Lee, S. (2018). Application of ensemble-based machine learning models to landslide susceptibility mapping. *Remote Sensing*, *10*(8). https://doi.org/10.3390/rs10081252

Kaggle. (n.d.). Retrieved 22 October 2024, from https://www.kaggle.com/

Kalhor, A. (2020). An introduction to artificial neural networks. In *Hardware Architectures for Deep Learning*. https://doi.org/10.1049/PBCS055E_ch1

Kalsnes, B., & Capobianco, V. (2022). Use of Vegetation for Landslide Risk Mitigation. In *Springer Climate*. https://doi.org/10.1007/978-3-030-86211-4_10

Kamchoom, V., & Leung, A. K. (2018). Hydro-mechanical reinforcements of live poles to slope stability. *Soils and Foundations*, *58*(6). https://doi.org/10.1016/j.sandf.2018.08.003

Kawagoe, S., Kazama, S., & Sarukkalige, P. R. (2010). Probabilistic modelling of rainfall induced landslide hazard assessment. *Hydrology and Earth System Sciences*, *14*(6). https://doi.org/10.5194/hess-14-1047-2010

Kepner, J., Kipf, A., Engwirda, D., Vembar, N., Jones, M., Milechin, L., Gadepally, V., Hill, C., Kraska, T., Arcand, W., Bestor, D., Bergeron, W., Byun, C., Hubbell, M., Houle, M., Kirby, A., Klein, A., Mullen, J., Prout, A., … Michaleas, P. (2020). Fast Mapping onto Census Blocks. *2020 IEEE High Performance Extreme Computing Conference, HPEC 2020*. https://doi.org/10.1109/HPEC43674.2020.9286157

Khan, I. U., Afzal, S., & Lee, J. W. (2022). Human activity recognition via hybrid deep learning based model. *Sensors*, *22*(1). https://doi.org/10.3390/s22010323

Kikuchi, T., Sakita, K., Nishiyama, S., & Takahashi, K. (2023). Landslide susceptibility mapping using automatically constructed CNN architectures with pre-slide topographic DEM of deep-seated catastrophic landslides caused by Typhoon Talas. *Natural Hazards*, *117*(1). https://doi.org/10.1007/s11069-023-05862-w

Kim, H. G., Lee, D. K., & Park, C. (2018). Assessing the cost of damage and effect of adaptation to landslides considering climate change. *Sustainability (Switzerland)*, *10*(5). https://doi.org/10.3390/su10051628

Kim, Y. J., Kotwal, A. R., Cho, B. Y., Wilde, J., & You, B. H. (2019). Geosynthetic reinforced steep slopes: Current technology in the United States. In *Applied Sciences (Switzerland)* (Vol. 9, Issue 10). https://doi.org/10.3390/app9102008

Kokutse, N. K., Temgoua, A. G. T., & Kavazović, Z. (2016). Slope stability and vegetation: Conceptual and numerical investigation of mechanical effects. *Ecological Engineering*, *86*. https://doi.org/10.1016/j.ecoleng.2015.11.005

Kraft, B., Jung, M., Körner, M., Koirala, S., & Reichstein, M. (2022). Towards hybrid modeling of the global hydrological cycle. *Hydrology and Earth System Sciences*, *26*(6). https://doi.org/10.5194/hess-26-1579-2022

Kun, F., Raischel, F., Hidalgo, R. C., & Herrmann, H. J. (2006). Extensions of fibre bundle models. *Lecture Notes in Physics*, *705*. https://doi.org/10.1007/3-540-35375-5_3

Lavell, A., Oppenheimer, M., Diop, C., Hess, J., Lempert, R., Li, J., Muir-Wood, R., Myeong, S., Moser, S., Takeuchi, K., Cardona, O. D., Hallegatte, S., Lemos, M., Little, C., Lotsch, A., & Weber, E. (2012). Climate change: New dimensions in disaster risk, exposure, vulnerability, and resilience. In *Managing the Risks of Extreme Events and Disasters to Advance Climate Change Adaptation: Special Report of the Intergovernmental Panel on Climate Change* (Vol. 9781107025066). https://doi.org/10.1017/CBO9781139177245.004

Law, Y. K., Lee, C. K. F., Pang, C. C., Hau, B. C. H., & Wu, J. (2023). Vegetation regeneration on natural terrain landslides in Hong Kong: Direct seeding of native species as a restoration tool. *Land Degradation and Development*, *34*(3). https://doi.org/10.1002/ldr.4492

Lawrence, J. (2024, February 27). *ITALY: LANDSLIDE, FLOOD MANAGEMENT AND PREVENTION*. International Trade Administration. https://www.trade.gov/market-intelligence/italy-landslide-flood-management-and-prevention

Lee, C. T., Huang, C. C., Lee, J. F., Pan, K. L., Lin, M. L., & Dong, J. J. (2008a). Statistical approach to earthquake-induced landslide susceptibility. *Engineering Geology*, *100*(1–2). https://doi.org/10.1016/j.enggeo.2008.03.004

Lee, C. T., Huang, C. C., Lee, J. F., Pan, K. L., Lin, M. L., & Dong, J. J. (2008b). Statistical approach to storm event-induced landslides susceptibility. *Natural Hazards and Earth System Science*, *8*(4). https://doi.org/10.5194/nhess-8-941-2008

Lee, J. T., Chu, M. Y., Lin, Y. S., Kung, K. N., Lin, W. C., & Lee, M. J. (2020). Root traits and biomechanical properties of three tropical pioneer tree species for forest restoration in landslide areas. *Forests*, *11*(2). https://doi.org/10.3390/f11020179

Lehmann, P., von Ruette, J., & Or, D. (2019). Deforestation Effects on Rainfall-Induced Shallow Landslides: Remote Sensing and Physically-Based Modelling. *Water Resources Research*, *55*(11). https://doi.org/10.1029/2019WR025233

Leung, F. T. Y., Yan, W. M., Hau, B. C. H., & Tham, L. G. (2015). Root systems of native shrubs and trees in Hong Kong and their effects on enhancing slope stability. *Catena*, *125*. https://doi.org/10.1016/j.catena.2014.10.018

Lewandowska, J., Tran Ngoc, T. D., Vauclin, M., & Bertin, H. (2008). Water Drainage in Double-Porosity Soils: Experiments and Micro–Macro Modeling. *Journal of Geotechnical and Geoenvironmental Engineering*, *134*(2). https://doi.org/10.1061/(asce)1090-0241(2008)134:2(231)

Li, L., Lan, H., Guo, C., Zhang, Y., Li, Q., & Wu, Y. (2017). A modified frequency ratio method for landslide susceptibility assessment. *Landslides*, *14*(2). https://doi.org/10.1007/s10346-016-0771-x

Li, S., Wang, Z., & Stutz, H. H. (2023). State-of-the-art review on plant-based solutions for soil improvement. In *Biogeotechnics* (Vol. 1, Issue 3). https://doi.org/10.1016/j.bgtech.2023.100035

Li, X., Cheng, J. L., & Yu, D. H. (2023). A methodological framework of landslide quantitative risk assessment in areas with incomplete historical landslide information. *Journal of Mountain Science*, *20*(9). https://doi.org/10.1007/s11629-023-7950-8

Li, X., & Zhang, L. M. (2009). Characterization of dual-structure pore-size distribution of soil. *Canadian Geotechnical Journal*, *46*(2). https://doi.org/10.1139/T08-110

Li, Y., & Duan, W. (2024). Decoding vegetation's role in landslide susceptibility mapping: An integrated review of techniques and future directions. In *Biogeotechnics* (Vol. 2, Issue 1). https://doi.org/10.1016/j.bgtech.2023.100056

Liu, J., Chen, Z., Kanungo, D. P., Song, Z., Bai, Y., Wang, Y., Li, D., & Qian, W. (2019). Topsoil reinforcement of sandy slope for preventing erosion using water-based polyurethane soil stabilizer. *Engineering Geology*, *252*. https://doi.org/10.1016/j.enggeo.2019.03.003

Liu, X., Lan, H., Li, L., & Cui, P. (2022). An ecological indicator system for shallow landslide analysis. *Catena*, *214*. https://doi.org/10.1016/j.catena.2022.106211

Liu, Z., Gilbert, G., Cepeda, J. M., Lysdahl, A. O. K., Piciullo, L., Hefre, H., & Lacasse, S. (2021). Modelling of shallow landslides with machine learning algorithms. *Geoscience Frontiers*, *12*(1). https://doi.org/10.1016/j.gsf.2020.04.014

Lombardo, L., & Mai, P. M. (2018). Presenting logistic regression-based landslide susceptibility results. *Engineering Geology*, *244*. https://doi.org/10.1016/j.enggeo.2018.07.019

Lopez Saez, J., Corona, C., Stoffel, M., Schoeneich, P., & Berger, F. (2012). Probability maps of landslide reactivation derived from tree-ring records: Pra Bellon landslide, southern French Alps. *Geomorphology*, *138*(1). https://doi.org/10.1016/j.geomorph.2011.08.034

Lu, L., Meng, X., Mao, Z., & Karniadakis, G. E. (2021). DeepXDE: A deep learning library for solving differential equations. *SIAM Review*, *63*(1). https://doi.org/10.1137/19M1274067

Luo, H. Y., Zhang, L. M., Zhang, L. L., He, J., & Yin, K. S. (2023). Vulnerability of buildings to landslides: The state of the art and future needs. In *Earth-Science Reviews* (Vol. 238). https://doi.org/10.1016/j.earscirev.2023.104329

Luo, X., Lin, F., Chen, Y., Zhu, S., Xu, Z., Huo, Z., Yu, M., & Peng, J. (2019). Coupling logistic model tree and random subspace to predict the landslide susceptibility areas with considering the uncertainty of environmental features. *Scientific Reports*, *9*(1). https://doi.org/10.1038/s41598-019-51941-z

Lusiana, N., Shinohara, Y., & Imaizumi, F. (2024). Quantifying effects of changes in forest age distribution on the landslide frequency in Japan. *Natural Hazards*, *120*(9), 8551–8570. https://doi.org/10.1007/s11069-024-06537-w

Ma, Z., Mei, G., & Piccialli, F. (2021). Machine learning for landslides prevention: a survey. In *Neural Computing and Applications* (Vol. 33, Issue 17). https://doi.org/10.1007/s00521-020-05529-8

Mango, L. M., Melesse, A. M., McClain, M. E., Gann, D., & Setegn, S. G. (2011). Land use and climate change impacts on the hydrology of the upper Mara River Basin, Kenya: Results of a modeling study to support better resource management. *Hydrology and Earth System Sciences*, *15*(7). https://doi.org/10.5194/hess-15-2245-2011

Mantero, G., Morresi, D., Marzano, R., Motta, R., Mladenoff, D. J., & Garbarino, M. (2020). The influence of land abandonment on forest disturbance regimes: a global review. In *Landscape Ecology* (Vol. 35, Issue 12). https://doi.org/10.1007/s10980-020-01147-w

Mao, Z., Jagtap, A. D., & Karniadakis, G. E. (2020). Physics-informed neural networks for high-speed flows. *Computer Methods in Applied Mechanics and Engineering*, *360*. https://doi.org/10.1016/j.cma.2019.112789

Mao, Z., Jourdan, C., Bonis, M. L., Pailler, F., Rey, H., Saint-André, L., & Stokes, A. (2013). Modelling root demography in heterogeneous mountain forests and applications for slope stability analysis. *Plant and Soil*, *363*(1–2). https://doi.org/10.1007/s11104-012-1324-2

Marc, O., Behling, R., Andermann, C., Turowski, J. M., Illien, L., Roessner, S., & Hovius, N. (2019). Long-term erosion of the Nepal Himalayas by bedrock landsliding: The role of monsoons, earthquakes and giant landslides. *Earth Surface Dynamics*, *7*(1). https://doi.org/10.5194/esurf-7-107-2019

Marden, M., & Rowan, D. (2015). The effect of land use on slope failure and sediment generation in the Coromandel region of New Zealand following a major storm in 1995. *New Zealand Journal of Forestry Science*, *45*(1). https://doi.org/10.1186/s40490-015-0036-9

Marden, M., Rowan, D., & Phillips, C. (2005). Stabilising characteristics of New Zealand indigenous riparian colonising plants. *Plant and Soil*, *278*(1–2). https://doi.org/10.1007/s11104-004-7598-2

Marinelli, A., Medici, C., Rosi, A., Tofani, V., Bianchini, S., & Casagli, N. (2022). Shallow Landslides and Rockfalls Velocity Assessment at Regional Scale: A Methodology Based on a Morphometric Approach. *Geosciences (Switzerland)*, *12*(4). https://doi.org/10.3390/geosciences12040177

Martel, J.-L., Brissette, F. P., Lucas-Picher, P., Troin, M., & Arsenault, R. (2021). Climate Change and Rainfall Intensity–Duration–Frequency Curves: Overview of Science and Guidelines for Adaptation. *Journal of Hydrologic Engineering*, *26*(10). https://doi.org/10.1061/(asce)he.1943-5584.0002122

Martelloni, G., Segoni, S., Fanti, R., & Catani, F. (2012). Rainfall thresholds for the forecasting of landslide occurrence at regional scale. *Landslides*, *9*(4). https://doi.org/10.1007/s10346-011-0308-2

Martin, R. P. (2001). Landscaping and bio-engineering of slopes in Hong Kong. *Geotechnical Engineering Meeting Society'S Needs, Vols 1 and 2, Proceedings*, *1990*.

Masi, E. B., Segoni, S., & Tofani, V. (2021). Root reinforcement in slope stability models: A review. In *Geosciences (Switzerland)* (Vol. 11, Issue 5). https://doi.org/10.3390/geosciences11050212

MathWorks Inc. (2024a). *Ensemble of bagged decision trees*. https://mathworks.com/help/stats/treebagger.html

MathWorks Inc. (2024b). *Fit ensemble of learners for classification*. https://mathworks.com/help/stats/fitcensemble.html

MathWorks Inc. (2024c). *Receiver operating characteristic (ROC) curve or other performance curve for classifier output*. https://it.mathworks.com/help/stats/perfcurve.html#bunsogv-OPTROCPT

MathWorks Inc. (2024d). *Train support vector machine (SVM) classifier for one-class and binary classification*. https://mathworks.com/help/stats/fitcsvm.html

Md.Sharafat, C., Md.Naimur, R., Md.Sujon, S., Md.Abu, S., Mahmud, K. H., & Hafsa, B. (2024). GIS-based landslide susceptibility mapping using logistic regression, random forest and decision and regression tree models in Chattogram District, Bangladesh. *Heliyon*, *10*(1). https://doi.org/10.1016/j.heliyon.2023.e23424

Medina, V., Hürlimann, M., Guo, Z., Lloret, A., & Vaunat, J. (2021). Fast physically-based model for rainfall-induced landslide susceptibility assessment at regional scale. *Catena*, *201*. https://doi.org/10.1016/j.catena.2021.105213

Meijer, G. J. (2021). A generic form of fibre bundle models for root reinforcement of soil. *Plant and Soil*, *468*(1–2). https://doi.org/10.1007/s11104-021-05039-z

Meijer, G. J., Knappett, J. A., Bengough, A. G., Bull, D. J., Liang, T., & Muir Wood, D. (2022). DRAM: A three-dimensional analytical model for the mobilisation of root reinforcement in direct shear conditions. *Ecological Engineering*, *179*. https://doi.org/10.1016/j.ecoleng.2022.106621

Melillo, M., Brunetti, M. T., Peruccacci, S., Gariano, S. L., Roccati, A., & Guzzetti, F. (2018). A tool for the automatic calculation of rainfall thresholds for landslide occurrence. *Environmental Modelling and Software*, *105*. https://doi.org/10.1016/j.envsoft.2018.03.024

Meng, Z. jiang, Ma, P. hui, & Peng, J. bing. (2021). Characteristics of loess landslides triggered by different factors in the Chinese Loess Plateau. *Journal of Mountain Science*, *18*(12). https://doi.org/10.1007/s11629-021-6880-6

Merceron, A., & Tato, A. (2020). An Introduction to Neural Networks. *Proceedings of the 13th International Conference on Educational Data Mining, EDM 2020*. https://doi.org/10.4135/9781446288061.n11

Merghadi, A., Yunus, A. P., Dou, J., Whiteley, J., ThaiPham, B., Bui, D. T., Avtar, R., & Abderrahmane, B. (2020). Machine learning methods for landslide susceptibility studies: A comparative overview of algorithm performance. In *Earth-Science Reviews* (Vol. 207). https://doi.org/10.1016/j.earscirev.2020.103225

Mickovski, S. B., & Thomson, C. S. (2017). Developing a framework for the sustainability assessment of eco-engineering measures. *Ecological Engineering*, *109*. https://doi.org/10.1016/j.ecoleng.2017.10.004

Mickovski, S. B., & van Beek, L. P. H. (2009). Root morphology and effects on soil reinforcement and slope stability of young vetiver (Vetiveria zizanioides) plants grown in semi-arid climate. *Plant and Soil*, *324*(1). https://doi.org/10.1007/s11104-009-0130-y

Miles, D. W. R., & Swanson, F. J. (1986). Vegetation composition on recent landslides in the Cascade Mountains of western Oregon. *Canadian Journal of Forest Research*, *16*(4). https://doi.org/10.1139/x86-132

Misiano, S., Antonio Gatto, M. P., & Montrasio, L. (2024). A SLIP-based post-failure model to predict the propagation of soil slips and their interaction with infrastructures. *Procedia Structural Integrity*, *62*, 576–584. https://doi.org/10.1016/j.prostr.2024.09.081

Misiano, S., Gatto, M. P. A., & Montrasio, L. (2023). Predicting the Soil Slip Triggering Through the SLIP Model and ML Approaches Including Vegetation. *Springer Series in Geomechanics and Geoengineering*. https://doi.org/10.1007/978-3-031-34761-0_85

Miyata, S., Kosugi, K., Gomi, T., & Mizuyama, T. (2009). Effects of forest floor coverage on overland flow and soil erosion on hillslopes in Japanese cypress plantation forests. *Water Resources Research*, *45*(6). https://doi.org/10.1029/2008WR007270

Mohamed, W. N. A. W., Osman, N., & Abdullah, R. (2023). A review of bioengineering techniques for slope stability in Malaysia. In *International Journal of Environmental Science and Technology* (Vol. 20, Issue 3). https://doi.org/10.1007/s13762-022-04235-3

Montavon, G. (2020). Introduction to Neural Networks. In *Lecture Notes in Physics* (Vol. 968). https://doi.org/10.1007/978-3-030-40245-7_4

Montgomery, D. R., & Dietrich, W. E. (1994). A physically based model for the topographic control on shallow landsliding. *Water Resources Research*, *30*(4). https://doi.org/10.1029/93WR02979

Montgomery, D. R., Schmidt, K. M., Greenberg, H. M., & Dietrich, W. E. (2000). Forest clearing and regional landsliding. *Geology*, *28*(4). https://doi.org/10.1130/0091-7613(2000)28<311:FCARL>2.0.CO;2

Montrasio, L. (2000). Stability analysis of soil slip. In C.A. Brebbia (Ed.), *International Conference Risk* (pp. 357–366). WIT Press. https://doi.org/10.2495/RISK000331

Montrasio, L., Gatto, M. P. A., & Miodini, C. (2023). The role of plants in the prevention of soil-slip: the G-SLIP model and its application on territorial scale through G-XSLIP platform. *Landslides*, *20*(6). https://doi.org/10.1007/s10346-023-02031-9

Montrasio, L., Terrone, A., & Morandi, M. C. (2015). Modeling the shallow landslides occurred in Tizzano Val Parma in April 2013. In *Engineering Geology for Society and Territory - Volume 2: Landslide Processes*. https://doi.org/10.1007/978-3-319-09057-3_285

Montrasio, L., & Valentino, R. (2007). Experimental analysis and modelling of shallow landslides. *Landslides*, *4*(3). https://doi.org/10.1007/s10346-007-0082-3

Montrasio, L., & Valentino, R. (2008a). A model for triggering mechanisms of shallow landslides. *Natural Hazards and Earth System Science*, *8*(5). https://doi.org/10.5194/nhess-8-1149-2008

Montrasio, L., & Valentino, R. (2008b). A simplified model for the evaluation of the degree of saturation in slope stability analysis of shallow soils. *Unsaturated Soils: Advances in Geo-Engineering - Proceedings of the 1st European Conference on Unsaturated Soils, E-UNSAT 2008*. https://doi.org/10.1201/9780203884430.ch129

Montrasio, L., & Valentino, R. (2016a). Modelling Rainfall-induced Shallow Landslides at Different Scales Using SLIP - Part i. *Procedia Engineering*, *158*. https://doi.org/10.1016/j.proeng.2016.08.475

Montrasio, L., & Valentino, R. (2016b). Modelling Rainfall-induced Shallow Landslides at Different Scales Using SLIP - Part II. *Procedia Engineering*, *158*. https://doi.org/10.1016/j.proeng.2016.08.476

Montrasio, L., Valentino, R., Corina, A., Rossi, L., & Rudari, R. (2014). A prototype system for space–time assessment of rainfall-induced shallow landslides in Italy. *Natural Hazards*, *74*(2). https://doi.org/10.1007/s11069-014-1239-8

Montrasio, L., Valentino, R., & Losi, G. L. (2009). Rainfall-induced shallow landslides: A model for the triggering mechanism of some case studies in Northern Italy. *Landslides*, *6*(3). https://doi.org/10.1007/s10346-009-0154-7

Montrasio, L., Valentino, R., & Losi, G. L. (2011). Towards a real-time susceptibility assessment of rainfall-induced shallow landslides on a regional scale. *Natural Hazards and Earth System Science*, *11*(7). https://doi.org/10.5194/nhess-11-1927-2011

Montrasio, L., Valentino, R., & Losi, G. L. (2012). Shallow landslides triggered by rainfalls: Modeling of some case histories in the Reggiano Apennine (Emilia Romagna Region, Northern Italy). *Natural Hazards*, *60*(3). https://doi.org/10.1007/s11069-011-9906-5

Montrasio, L., Valentino, R., Losi, G. L., Corina, A., Rossi, L., & Rudari, R. (2013). Space-time hazard assessment of rainfall-induced shallow landslides. *Landslide Science and Practice: Global Environmental Change*, *4*. https://doi.org/10.1007/978-3-642-31337-0_37

Montrasio, L., Valentino, R., & Meisina, C. (2018). Soil Saturation and Stability Analysis of a Test Site Slope Using the Shallow Landslide Instability Prediction (SLIP) Model. *Geotechnical and Geological Engineering*, *36*(4). https://doi.org/10.1007/s10706-018-0465-3

Montrasio, L., Valentino, R., & Quintavalla, C. (2010). Estimation of the Degree of Saturation of Shallow Soils from Satellite Observations to Model Soil Slips Occurred in Emilia

Romagna Region of Northern Italy. *International Journal of Geosciences*, *01*(02). https://doi.org/10.4236/ijg.2010.12008

Moraci, N., Mandaglio, M. C., Gioffrè, D., & Pitasi, A. (2017). Debris flow susceptibility zoning: An approach applied to a study area. *Rivista Italiana Di Geotecnica*, *51*(2). https://doi.org/10.19199/2017.2.0557-1405.047

Mosca, E., Szigeti, F., Tragianni, S., Gallagher, D., & Groh, G. (2022). SHAP-Based Explanation Methods: A Review for NLP Interpretability. *Proceedings - International Conference on Computational Linguistics, COLING*, *29*(1).

Mountrakis, G., Im, J., & Ogole, C. (2011). Support vector machines in remote sensing: A review. In *ISPRS Journal of Photogrammetry and Remote Sensing* (Vol. 66, Issue 3). https://doi.org/10.1016/j.isprsjprs.2010.11.001

Murgia, I., Giadrossich, F., Mao, Z., Cohen, D., Capra, G. F., & Schwarz, M. (2022). Modeling shallow landslides and root reinforcement: A review. *Ecological Engineering*, *181*. https://doi.org/10.1016/j.ecoleng.2022.106671

Myung, I. J. (2003). Tutorial on maximum likelihood estimation. *Journal of Mathematical Psychology*, *47*(1). https://doi.org/10.1016/S0022-2496(02)00028-7

Nagarajan, R., Roy, A., Vinod Kumar, R., Mukherjee, A., & Khire, M. V. (2000). Landslide hazard susceptibility mapping based on terrain and climatic factors for tropical monsoon regions. *Bulletin of Engineering Geology and the Environment*, *58*(4). https://doi.org/10.1007/s100649900032

Nasa. (n.d.). Retrieved 22 October 2024, from https://gpm.nasa.gov/landslides/projects.html

Nasta, P., Palladino, M., Ursino, N., Saracino, A., Sommella, A., & Romano, N. (2017). Assessing long-term impact of land-use change on hydrological ecosystem functions in a Mediterranean upland agro-forestry catchment. *Science of the Total Environment*, *605–606*. https://doi.org/10.1016/j.scitotenv.2017.06.008

Nefeslioglu, H. A., Gokceoglu, C., & Sonmez, H. (2008). An assessment on the use of logistic regression and artificial neural networks with different sampling strategies for the preparation of landslide susceptibility maps. *Engineering Geology*, *97*(3–4). https://doi.org/10.1016/j.enggeo.2008.01.004

Ng, C. W. W., & Zhan, L. T. (2007). Comparative study of rainfall infiltration into a bare and a grassed unsaturated expansive soil slope. *Soils and Foundations*, *47*(2). https://doi.org/10.3208/sandf.47.207

Ng, S. L., Chu, L. M., Li, L., & Qin, J. (2011). Performance assessment of slope greening techniques in Hong Kong. *Asian Geographer*, *28*(2). https://doi.org/10.1080/10225706.2011.623424

Nguyen, B. Q. V., Song, C. H., & Kim, Y. T. (2022). A Hybrid Physical and Machine Learning Model for Assessing Landslide Spatial Probability Caused by Raising of Ground Water Table and Earthquake in Atsuma, Japan — Case Study. *KSCE Journal of Civil Engineering*, *26*(8). https://doi.org/10.1007/s12205-022-1656-2

Nguyen, V. V., Pham, B. T., Vu, B. T., Prakash, I., Jha, S., Shahabi, H., Shirzadi, A., Ba, D. N., Kumar, R., Chatterjee, J. M., & Bui, D. T. (2019). Hybrid machine learning approaches for landslide susceptibility modeling. *Forests*, *10*(2). https://doi.org/10.3390/f10020157

Nhu, V. H., Shirzadi, A., Shahabi, H., Singh, S. K., Al-Ansari, N., Clague, J. J., Jaafari, A., Chen, W., Miraki, S., Dou, J., Luu, C., Górski, K., Pham, B. T., Nguyen, H. D., & Ahmad, B. Bin. (2020). Shallow landslide susceptibility mapping: A comparison between logistic model tree, logistic regression, naïve bayes tree, artificial neural network, and support vector machine algorithms. *International Journal of Environmental Research and Public Health*, *17*(8). https://doi.org/10.3390/ijerph17082749

Ni, J. J., Leung, A. K., Ng, C. W. W., & Shao, W. (2018). Modelling hydro-mechanical reinforcements of plants to slope stability. *Computers and Geotechnics*, *95*. https://doi.org/10.1016/j.compgeo.2017.09.001

Nilaweera, N. S., & Nutalaya, P. (1999). Role of tree roots in slope stabilisation. *Bulletin of Engineering Geology and the Environment*, *57*(4). https://doi.org/10.1007/s100640050056

Niraj, K. C., Singh, A., & Shukla, D. P. (2023). Effect of the Normalized Difference Vegetation Index (NDVI) on GIS-Enabled Bivariate and Multivariate Statistical Models for Landslide Susceptibility Mapping. *Journal of the Indian Society of Remote Sensing*, *51*(8). https://doi.org/10.1007/s12524-023-01738-5

Nocentini, N., Rosi, A., Segoni, S., & Fanti, R. (2023). Towards landslide space-time forecasting through machine learning: the influence of rainfall parameters and model setting. *Frontiers in Earth Science*, *11*. https://doi.org/10.3389/feart.2023.1152130

Norris, J. E. (2005). Root reinforcement by hawthorn and oak roots on a highway cut-slope in Southern England. *Plant and Soil*, *278*(1–2). https://doi.org/10.1007/s11104-005-1301-0

Notti, D., Cignetti, M., Godone, D., & Giordan, D. (2023). Semi-automatic mapping of shallow landslides using free Sentinel-2 images and Google Earth Engine. *Natural Hazards and Earth System Sciences*, *23*(7). https://doi.org/10.5194/nhess-23-2625-2023

Numata, I., Khand, K., Kjaersgaard, J., Cochrane, M. A., & Silva, S. S. (2021). Forest evapotranspiration dynamics over a fragmented forest landscape under drought in southwestern Amazonia. *Agricultural and Forest Meteorology*, *306*. https://doi.org/10.1016/j.agrformet.2021.108446

Nurtjahjaningtyas, I., Wicaksono, L. A., & Shofi, A. M. R. (2023). Modeling Geocells as Slope Reinforcement Using the Limit Equilibrium Method. *IOP Conference Series: Earth and Environmental Science*, *1249*(1). https://doi.org/10.1088/1755-1315/1249/1/012007

O., F., O., P., N., B., & Etiegni, L. (2012). Effects of Deforestation on Water Resources: Integrating Science and Community Perspectives in the Sondu-Miriu River Basin, Kenya. In *New Advances and Contributions to Forestry Research*. https://doi.org/10.5772/34373

Oakley, N. S., Lancaster, J. T., Kaplan, M. L., & Ralph, F. M. (2017). Synoptic conditions associated with cool season post-fire debris flows in the Transverse Ranges of southern California. *Natural Hazards*, *88*(1). https://doi.org/10.1007/s11069-017-2867-6

O'Callaghan, J. F., & Mark, D. M. (1984). The extraction of drainage networks from digital elevation data. *Computer Vision, Graphics, & Image Processing*, *28*(3). https://doi.org/10.1016/S0734-189X(84)80011-0

Okada, Y., Cai, F., & Kurokawa, U. (2023). Changes in Slope Stability over the Growth and Decay of Japanese Cedar Tree Roots. *Forests*, *14*(2). https://doi.org/10.3390/f14020256

Oliveira, S. C., Zêzere, J. L., Lajas, S., & Melo, R. (2017). Combination of statistical and physically based methods to assess shallow slide susceptibility at the basin scale. *Natural Hazards and Earth System Sciences*, *17*(7). https://doi.org/10.5194/nhess-17-1091-2017

OpenDataER. (n.d.). Retrieved 22 October 2024, from https://dati.emilia-romagna.it/dataset

OpenLandMap. (n.d.). Retrieved 23 October 2024, from https://openlandmap.org/

Operstein, V., & Frydman, S. (2000). The influence of vegetation on soil strength. *Ground Improvement*, *4*(2). https://doi.org/10.1680/grim.2000.4.2.81

Ota, I. (2010). Forest law and policy developments in Japan. *Forest Policy and Forest Economics Department of Forest Sciences.*, *1*. https://doi.org/10.3929/ethz-a-006396456

Otter, D. W., Medina, J. R., & Kalita, J. K. (2021). A Survey of the Usages of Deep Learning for Natural Language Processing. *IEEE Transactions on Neural Networks and Learning Systems*, *32*(2). https://doi.org/10.1109/TNNLS.2020.2979670

Pack, R. T. (1998). The SINMAP Approach to Terrain Stability Mapping. *8th Congress of the International Association of Engineering Geology*.

Papathoma-Koehle, M., & Glade, T. (2013). The role of vegetation cover change in landslide hazard and risk. In *The Role of Ecosystems in Disaster Risk Reduction*.

Parise, M., & Cannon, S. H. (2012). Wildfire impacts on the processes that generate debris flows in burned watersheds. *Natural Hazards*, *61*(1). https://doi.org/10.1007/s11069-011-9769-9

Patil, U. D., Shelton, A. J., & Aquino, E. (2021). Bioengineering solution to prevent rainfall-induced slope failures in tropical soil. *Land*, *10*(3). https://doi.org/10.3390/land10030299

Pavan, V., Nanni, S., Mallegni, R., & Nucciotti, C. (2021). *Rapporto IdroMeteoClima Emilia-Romagna*.

Peirce, F. T. (1926). 32—X.—Tensile Tests for Cotton Yarns v.—"The Weakest Link" Theorems on the Strength of Long and of Composite Specimens. *Journal of the Textile Institute Transactions*, *17*(7). https://doi.org/10.1080/19447027.1926.10599953

Peng, C. Y. J., Lee, K. L., & Ingersoll, G. M. (2002). An introduction to logistic regression analysis and reporting. *Journal of Educational Research*, *96*(1). https://doi.org/10.1080/00220670209598786

Peng, J., Wang, S., Wang, Q., Zhuang, J., Huang, W., Zhu, X., Leng, Y., & Ma, P. (2019). Distribution and genetic types of loess landslides in China. *Journal of Asian Earth Sciences*, *170*. https://doi.org/10.1016/j.jseaes.2018.11.015

Peruccacci, S., Brunetti, M. T., Gariano, S. L., Melillo, M., Rossi, M., & Guzzetti, F. (2017). Rainfall thresholds for possible landslide occurrence in Italy. *Geomorphology*, *290*. https://doi.org/10.1016/j.geomorph.2017.03.031

Peruccacci, S., Gariano, S. L., Melillo, M., Solimano, M., Guzzetti, F., & Brunetti, M. T. (2023a). The ITAlian rainfall-induced LandslIdes CAtalogue, an extensive and accurate spatio-temporal catalogue of rainfall-induced landslides in Italy. *Earth System Science Data*, *15*(7). https://doi.org/10.5194/essd-15-2863-2023

Peruccacci, S., Gariano, S. L., Melillo, M., Solimano, M., Guzzetti, F., & Brunetti, M. T. (2023b). The ITAlian rainfall-induced LandslIdes CAtalogue, an extensive and accurate spatio-

temporal catalogue of rainfall-induced landslides in Italy. *Earth System Science Data*, *15*(7). https://doi.org/10.5194/essd-15-2863-2023

Pham, B. T., Shirzadi, A., Shahabi, H., Omidvar, E., Singh, S. K., Sahana, M., Asl, D. T., Ahmad, B. Bin, Quoc, N. K., & Lee, S. (2019). Landslide susceptibility assessment by novel hybrid machine learning algorithms. *Sustainability (Switzerland)*, *11*(16). https://doi.org/10.3390/su11164386

Phillips, C., Hales, T., Smith, H., & Basher, L. (2021). Shallow landslides and vegetation at the catchment scale: A perspective. *Ecological Engineering*, *173*. https://doi.org/10.1016/j.ecoleng.2021.106436

Phillips, C., & Marden, M. (2005). Use of Plants for Ground Bioengineering and Erosion & Sediment Control in New Zealand. *Landcare Research*, *February 2015*.

Phillips, C., & Marden, M. (2012). Reforestation Schemes to Manage Regional Landslide Risk. In *Landslide Hazard and Risk*. https://doi.org/10.1002/9780470012659.ch18

Phillips, C., Marden, M., & Basher, L. (2015). Forests and erosion protection-getting to the root of the matter. *New Zealand Journal of Forestry*, *60*(2).

Piciullo, L., Gariano, S. L., Melillo, M., Brunetti, M. T., Peruccacci, S., Guzzetti, F., & Calvello, M. (2017). Definition and performance of a threshold-based regional early warning model for rainfall-induced landslides. *Landslides*, *14*(3). https://doi.org/10.1007/s10346-016-0750-2

Pizziolo, M., Del Maschio, L., Gozza, G., & Pignone, S. (2008). Determinazione di Soglie Pluviometriche per l'Innesco di Frane in Emilia-Romagna. *Il Geologo Dell'Emilia-Romagna*. https://www.geologiemiliaromagna.it/rivista/2008-29_Pizziolo.pdf

Pollen, N., & Simon, A. (2005). Estimating the mechanical effects of riparian vegetation on stream bank stability using a fiber bundle model. *Water Resources Research*, *41*(7). https://doi.org/10.1029/2004WR003801

Polster, D. F. (2003). Soil Bioengineering for Slope Stabilization and Site Restoration. *Mining and the Environment III*, *3*.

Pourghasemi, H. R., Teimoori Yansari, Z., Panagos, P., & Pradhan, B. (2018). Analysis and evaluation of landslide susceptibility: a review on articles published during 2005–2016 (periods of 2005–2012 and 2013–2016). In *Arabian Journal of Geosciences* (Vol. 11, Issue 9). https://doi.org/10.1007/s12517-018-3531-5

Pradhan, S., Hansen, A., & Chakrabarti, B. K. (2010). Failure processes in elastic fiber bundles. *Reviews of Modern Physics*, *82*(1). https://doi.org/10.1103/RevModPhys.82.499

Preti, F., & Giadrossich, F. (2009). Root reinforcement and slope bioengineering stabilization by Spanish Broom (Spartium junceum L.). *Hydrology and Earth System Sciences*, *13*(9). https://doi.org/10.5194/hess-13-1713-2009

Protezione Civile Nazionale. (2016, July 28). *Il Sistema di allertamento nazionale*. Dipartimento Della Protezione Civile, Governo Italiano. https://www.protezionecivile.gov.it/it/approfondimento/il-sistema-di-allertamento-nazionale/

Puglisi, C., Campolo, D., Falconi, L., Leoni, G., & Lumaca, S. (2013). Landslide hazard assessment project in the Messina municipality area (Sicily, Italy). *Landslide Science and Practice: Risk Assessment, Management and Mitigation*, *6*. https://doi.org/10.1007/978-3-642-31319-6_49

Punetha, P., Samanta, M., & Sarkar, S. (2019). Bioengineering as an effective and ecofriendly soil slope stabilization method: A review. In *Advances in Natural and Technological Hazards Research* (Vol. 50). https://doi.org/10.1007/978-3-319-77377-3_10

Qi, X., Mendes, J., Bainbridge, R., Dunning, S., Winter, M., & Lim, M. (2023). Real-time shallow landslide hazard assessment on a regional scale. *EarthArXiv*. https://doi.org/https://doi.org/10.31223/X50M10

Quanto costa all'Italia la crisi climatica? (2021, August). *Greenpeace*.

Rai, R., & Sahu, C. K. (2020). Driven by Data or Derived through Physics? A Review of Hybrid Physics Guided Machine Learning Techniques with Cyber-Physical System (CPS) Focus. In *IEEE Access* (Vol. 8). https://doi.org/10.1109/ACCESS.2020.2987324

Raia, S., Alvioli, M., Rossi, M., Baum, R. L., Godt, J. W., & Guzzetti, F. (2014). Improving predictive power of physically based rainfall-induced shallow landslide models: A probabilistic approach. *Geoscientific Model Development*, *7*(2). https://doi.org/10.5194/gmd-7-495-2014

Raimondi, L., Pepe, G., Firpo, M., Calcaterra, D., & Cevasco, A. (2023). An open-source and QGIS-integrated physically based model for Spatial Prediction of Rainfall-Induced Shallow Landslides (SPRIn-SL). *Environmental Modelling and Software*, *160*. https://doi.org/10.1016/j.envsoft.2022.105587

Raissi, M., Perdikaris, P., & Karniadakis, G. E. (2019). Physics-informed neural networks: A deep learning framework for solving forward and inverse problems involving nonlinear partial differential equations. *Journal of Computational Physics*, *378*. https://doi.org/10.1016/j.jcp.2018.10.045

Rauch, H. P., von der Thannen, M., Raymond, P., Mira, E., & Evette, A. (2022). Ecological challenges* for the use of soil and water bioengineering techniques in river and coastal

engineering projects. *Ecological Engineering*, *176*. https://doi.org/10.1016/j.ecoleng.2021.106539

Regione Autonoma della Sardegna. (2018). Soglie Pluviometriche. In *Regione Sardegna*. Regione Sardegna. https://www.regione.sardegna.it/documenti/1_386_20180807131413.pdf

Reichenbach, P., Rossi, M., Malamud, B. D., Mihir, M., & Guzzetti, F. (2018). A review of statistically-based landslide susceptibility models. In *Earth-Science Reviews* (Vol. 180). https://doi.org/10.1016/j.earscirev.2018.03.001

Reid, M. E., & Iverson, R. M. (1992). Gravity-driven groundwater flow and slope failure potential: 2. Effects of slope morphology, material properties, and hydraulic heterogeneity. *Water Resources Research*, *28*(3). https://doi.org/10.1029/91WR02695

Ren, D., & Leslie, L. M. (2020). Climate warming enhancement of catastrophic southern California debris flows. *Scientific Reports*, *10*(1). https://doi.org/10.1038/s41598-020-67511-7

Rengers, F. K., McGuire, L. A., Oakley, N. S., Kean, J. W., Staley, D. M., & Tang, H. (2020). Landslides after wildfire: initiation, magnitude, and mobility. *Landslides*, *17*(11). https://doi.org/10.1007/s10346-020-01506-3

Rickenmann, D. (1999). Empirical relationships for debris flows. *Natural Hazards*, *19*(1). https://doi.org/10.1023/A:1008064220727

Rickli, C., & Graf, F. (2009). Effects of forests on shallow landslides - Case studies in Switzerland. *Forest Snow and Landscape Research*, *82*(1).

Rmer, W. (2013). Environmental Change and Geomorphic Response in Humid Tropical Mountains. In *Environmental Change and Sustainability*. https://doi.org/10.5772/53395

Robichaud, P. R., Lewis, S. A., Wagenbrenner, J. W., Ashmun, L. E., & Brown, R. E. (2013). Post-fire mulching for runoff and erosion mitigation. Part I: Effectiveness at reducing hillslope erosion rates. *Catena*, *105*. https://doi.org/10.1016/j.catena.2012.11.015

Robichaud, P. R., Wagenbrenner, J. W., Lewis, S. A., Ashmun, L. E., Brown, R. E., & Wohlgemuth, P. M. (2013). Post-fire mulching for runoff and erosion mitigation Part II: Effectiveness in reducing runoff and sediment yields from small catchments. *Catena*, *105*. https://doi.org/10.1016/j.catena.2012.11.016

Robison, E. G., Hydrologist, F., Mills, K. A., Paul, J., & Skaugset, A. (1999). Storm Impacts and Landslides of 1996: Final Report Oregon Department of Forestry Forest Practices Monitoring Program. *Oregon Department of Forestry*.

Roder, G., Ruljigaljig, T., Lin, C. W., & Tarolli, P. (2016). Natural hazards knowledge and risk perception of Wujie indigenous community in Taiwan. *Natural Hazards*, *81*(1). https://doi.org/10.1007/s11069-015-2100-4

Roering, J. J., Schmidt, K. M., Stock, J. D., Dietrich, W. E., & Montgomery, D. R. (2003). Shallow landsliding, root reinforcement, and the spatial distribution of trees in the Oregon Coast Range. *Canadian Geotechnical Journal*, *40*(2). https://doi.org/10.1139/t02-113

Rosi, A., Peternel, T., Jemec-Auflič, M., Komac, M., Segoni, S., & Casagli, N. (2016). Rainfall thresholds for rainfall-induced landslides in Slovenia. *Landslides*, *13*(6). https://doi.org/10.1007/s10346-016-0733-3

Rossi, G., Catani, F., Leoni, L., Segoni, S., & Tofani, V. (2013). HIRESSS: A physically based slope stability simulator for HPC applications. *Natural Hazards and Earth System Science*, *13*(1). https://doi.org/10.5194/nhess-13-151-2013

Rossi, L. M. W., Rapidel, B., Roupsard, O., Villatoro-sánchez, M., Mao, Z., Nespoulous, J., Perez, J., Prieto, I., Roumet, C., Metselaar, K., Schoorl, J. M., Claessens, L., & Stokes, A. (2017). Sensitivity of the landslide model LAPSUS_LS to vegetation and soil parameters. *Ecological Engineering*, *109*. https://doi.org/10.1016/j.ecoleng.2017.08.010

Rossi, M., Witt, A., Guzzetti, F., Malamud, B. D., & Peruccacci, S. (2010). Analysis of historical landslide time series in the Emilia-Romagna region, northern Italy. *Earth Surface Processes and Landforms*, *35*(10). https://doi.org/10.1002/esp.1858

Saito, H., Murakami, W., Daimaru, H., & Oguchi, T. (2017). Effect of forest clear-cutting on landslide occurrences: Analysis of rainfall thresholds at Mt. Ichifusa, Japan. *Geomorphology*, *276*. https://doi.org/10.1016/j.geomorph.2016.09.024

Saito, H., Nakayama, D., & Matsuyama, H. (2010). Relationship between the initiation of a shallow landslide and rainfall intensity-duration thresholds in Japan. *Geomorphology*, *118*(1–2). https://doi.org/10.1016/j.geomorph.2009.12.016

Sakals, M. E., Innes, J. L., Wilford, D. J., Sidle, R. C., & Grant, G. E. (2006). The role of forests in reducing hydrogeomorphic hazards. *Forest Snow and Landscape Research*, *80*(1).

Sakals, M. E., & Sidle, R. C. (2004). A spatial and temporal model of root cohesion in forest soils. *Canadian Journal of Forest Research*, *34*(4). https://doi.org/10.1139/x03-268

Salemi, L. F., Groppo, J. D., Trevisan, R., Bicci Seghesi, G., de Moraes, J. M., de Barros Ferraz, S. F., & Martinelli, L. A. (2012). Hydrological consequences of land-use change from forest to pasture in the Atlantic rain forest region. *Ambiente e Agua*, *7*(3). https://doi.org/10.4136/1980-993X

Salimi, K., & Ghazavi, M. (2021). Soil reinforcement and slope stabilisation using recycled waste plastic sheets. *Geomechanics and Geoengineering*, *16*(6). https://doi.org/10.1080/17486025.2019.1683620

Salvatici, T., Tofani, V., Rossi, G., D'Ambrosio, M., Tacconi Stefanelli, C., Benedetta Masi, E., Rosi, A., Pazzi, V., Vannocci, P., Petrolo, M., Catani, F., Ratto, S., Stevenin, H., & Casagli, N. (2018). Application of a physically based model to forecast shallow landslides at a regional scale. *Natural Hazards and Earth System Sciences*, *18*(7). https://doi.org/10.5194/nhess-18-1919-2018

Samaniego, E., Anitescu, C., Goswami, S., Nguyen-Thanh, V. M., Guo, H., Hamdia, K., Zhuang, X., & Rabczuk, T. (2020). An energy approach to the solution of partial differential equations in computational mechanics via machine learning: Concepts, implementation and applications. *Computer Methods in Applied Mechanics and Engineering*, *362*. https://doi.org/10.1016/j.cma.2019.112790

Sarker, I. H. (2021). Machine Learning: Algorithms, Real-World Applications and Research Directions. In *SN Computer Science* (Vol. 2, Issue 3). https://doi.org/10.1007/s42979-021-00592-x

Satchell, D. (2018). *Trees for steep slopes*. http://www.nzffa.org.nz/farm-forestry-model/why-farm-forestry/trees-for erosion-controlsoil-conservation/report-trees-for-steep-slopes/

Sato, T., Katsuki, Y., & Shuin, Y. (2023). Evaluation of influences of forest cover change on landslides by comparing rainfall-induced landslides in Japanese artificial forests with different ages. *Scientific Reports*, *13*(1). https://doi.org/10.1038/s41598-023-41539-x

Schapire, R. E. (1999). A brief introduction to boosting. *IJCAI International Joint Conference on Artificial Intelligence*, *2*.

Scheidl, C., Heiser, M., Kamper, S., Thaler, T., Klebinder, K., Nagl, F., Lechner, V., Markart, G., Rammer, W., & Seidl, R. (2020). The influence of climate change and canopy disturbances on landslide susceptibility in headwater catchments. *Science of the Total Environment*, *742*. https://doi.org/10.1016/j.scitotenv.2020.140588

Schilirò, L., Esposito, C., & Scarascia Mugnozza, G. (2015). Evaluation of shallow landslide-triggering scenarios through a physically based approach: An example of application in the southern Messina area (northeastern Sicily, Italy). *Natural Hazards and Earth System Sciences*, *15*(9). https://doi.org/10.5194/nhess-15-2091-2015

Schilirò, L., Montrasio, L., & Scarascia Mugnozza, G. (2016). Prediction of shallow landslide occurrence: Validation of a physically-based approach through a real case study.

Science of the Total Environment, *569–570*. https://doi.org/10.1016/j.scitotenv.2016.06.124

Schmaltz, E. M., Steger, S., & Glade, T. (2017). The influence of forest cover on landslide occurrence explored with spatio-temporal information. *Geomorphology*, *290*. https://doi.org/10.1016/j.geomorph.2017.04.024

Schmid, I., & Kazda, M. (2001). Vertical distribution and radial growth of coarse roots in pure and mixed stands of Fagus sylvatica and Picea abies. *Canadian Journal of Forest Research*, *31*(3). https://doi.org/10.1139/cjfr-31-3-539

Schmidt, J., Turek, G., Clark, M. P., Uddstrom, M., & Dymond, J. R. (2008). Probabilistic forecasting of shallow, rainfall-triggered landslides using real-time numerical weather predictions. *Natural Hazards and Earth System Science*, *8*(2). https://doi.org/10.5194/nhess-8-349-2008

Schmidt, K. M., Roering, J. J., Stock, J. D., Dietrich, W. E., Montgomery, D. R., & Schaub, T. (2001). The variability of root cohesion as an influence on shallow landslide susceptibility in the Oregon Coast Range. *Canadian Geotechnical Journal*, *38*(5). https://doi.org/10.1139/cgj-38-5-995

Schwarz, M., Cohen, D., & Or, D. (2010). Root-soil mechanical interactions during pullout and failure of root bundles. *Journal of Geophysical Research: Earth Surface*, *115*(4). https://doi.org/10.1029/2009JF001603

Schwarz, M., Giadrossich, F., & Cohen, D. (2013). Modeling root reinforcement using a root-failure Weibull survival function. *Hydrology and Earth System Sciences*, *17*(11). https://doi.org/10.5194/hess-17-4367-2013

Schwarz, M., Lehmann, P., & Or, D. (2010). Quantifying lateral root reinforcement in steep slopes - from a bundle of roots to tree stands. *Earth Surface Processes and Landforms*, *35*(3). https://doi.org/10.1002/esp.1927

Schwarz, M., Preti, F., Giadrossich, F., Lehmann, P., & Or, D. (2010). Quantifying the role of vegetation in slope stability: A case study in Tuscany (Italy). *Ecological Engineering*, *36*(3). https://doi.org/10.1016/j.ecoleng.2009.06.014

Schwendtner, B., Papathoma-Köhle, M., & Glade, T. (2013). Risk evolution: How can changes in the built environment influence the potential loss of natural hazards. *Natural Hazards and Earth System Sciences*, *13*(9). https://doi.org/10.5194/nhess-13-2195-2013

Segoni, S., Lagomarsino, D., Fanti, R., Moretti, S., & Casagli, N. (2015). Integration of rainfall thresholds and susceptibility maps in the Emilia Romagna (Italy) regional-scale

landslide warning system. *Landslides*, *12*(4). https://doi.org/10.1007/s10346-014-0502-0

Segoni, S., Piciullo, L., & Gariano, S. L. (2018). A review of the recent literature on rainfall thresholds for landslide occurrence. In *Landslides* (Vol. 15, Issue 8). https://doi.org/10.1007/s10346-018-0966-4

Segoni, S., Rosi, A., Fanti, R., Gallucci, A., Monni, A., & Casagli, N. (2018). A regional-scale landslide warning system based on 20 years of operational experience. *Water (Switzerland)*, *10*(10). https://doi.org/10.3390/w10101297

Shang, K., Yao, Y., Di, Z., Jia, K., Zhang, X., Fisher, J. B., Chen, J., Guo, X., Yang, J., Yu, R., Xie, Z., Liu, L., Ning, J., & Zhang, L. (2023). Coupling physical constraints with machine learning for satellite-derived evapotranspiration of the Tibetan Plateau. *Remote Sensing of Environment*, *289*. https://doi.org/10.1016/j.rse.2023.113519

Sharma, P., Chung, W. T., Akoush, B., & Ihme, M. (2023). A Review of Physics-Informed Machine Learning in Fluid Mechanics. In *Energies* (Vol. 16, Issue 5). https://doi.org/10.3390/en16052343

Shinohara, Y., & Kume, T. (2022). Changes in the factors contributing to the reduction of landslide fatalities between 1945 and 2019 in Japan. *Science of the Total Environment*, *827*. https://doi.org/10.1016/j.scitotenv.2022.154392

Shou, K. J., & Chen, J. (2021). On the rainfall induced deep-seated and shallow landslide hazard in Taiwan. *Engineering Geology*, *288*. https://doi.org/10.1016/j.enggeo.2021.106156

Sibson, R. (1981). A Brief Description of Natural Neighbour Interpolation. In *Interpreting multivariate data*.

Sidle, R. C., & Swanston, D. N. (1982). Analysis of a small debris slide in coastal Alaska. *Canadian Geotechnical Journal*, *19*(2). https://doi.org/10.1139/t82-018

Sidle, R. C., Ziegler, A. D., Negishi, J. N., Nik, A. R., Siew, R., & Turkelboom, F. (2006). Erosion processes in steep terrain - Truths, myths, and uncertainties related to forest management in Southeast Asia. *Forest Ecology and Management*, *224*(1–2). https://doi.org/10.1016/j.foreco.2005.12.019

Simpson Nyambane, O., & Kinyua Mwea, S. (2011). Root tensile strength of 3 typical plant species and their contribution to soil shear strength; a case study: Sasumua Backslope, Nyandarua District, Kenya. In *Journal of Civil Engineering Research and Practice* (Vol. 8, Issue 1).

Skempton, A. W. (1954). The pore-pressure coefficients a and b. *Geotechnique*, *4*(4). https://doi.org/10.1680/geot.1954.4.4.143

Smith, M. J., Black, J. D., Lindsay, F. M., & Mickovski, S. B. (2015). Soil nailing the green way: Sustainable stabilisation of a failing slope using innovative soil nail head design to give a fully vegetated green slope finish. *Geotechnical Engineering for Infrastructure and Development - Proceedings of the XVI European Conference on Soil Mechanics and Geotechnical Engineering, ECSMGE 2015*, *4*.

Soglie Pluviometriche, Politecnico di Torino (2004). http://www.idrologia.polito.it/didattica/PIT/2015_2016/4.Mitigazione/Non_Strutturali/Provvedimenti_Documenti/soglie_pluviometrichev2.pdf

SoilGrids. (n.d.). Retrieved 23 October 2024, from https://soilgrids.org/

Song, Q., Wang, B., Wang, J., & Niu, X. (2016). Endangered and endemic species increase forest conservation values of species diversity based on the Shannon-Wiener index. *IForest*, *9*(JUNE2016). https://doi.org/10.3832/ifor1373-008

Spiekermann, R. I., McColl, S., Fuller, I., Dymond, J., Burkitt, L., & Smith, H. G. (2021). Quantifying the influence of individual trees on slope stability at landscape scale. *Journal of Environmental Management*, *286*. https://doi.org/10.1016/j.jenvman.2021.112194

Spiekermann, R. I., van Zadelhoff, F., Schindler, J., Smith, H., Phillips, C., & Schwarz, M. (2023). Comparing physical and statistical landslide susceptibility models at the scale of individual trees. *Geomorphology*, *440*. https://doi.org/10.1016/j.geomorph.2023.108870

Stevens, V., Stead, D., & Millard, T. (2006). The Role of Root Reinforcement in Slope Stability: A Review. *Sea to Sky 2006: The 59th Canadian Geotechnical Conference, and the 7th Joint CGS/IAH-CNC Groundwater Specialty Conference, October 1-4, Vancouver, BC, Canada*.

Stokes, A., Atger, C., Bengough, A. G., Fourcaud, T., & Sidle, R. C. (2009). Desirable Plant root traits for protecting natural and engineered slopes against landslides. In *Plant and Soil* (Vol. 324, Issue 1). https://doi.org/10.1007/s11104-009-0159-y

Stokes, A., Douglas, G. B., Fourcaud, T., Giadrossich, F., Gillies, C., Hubble, T., Kim, J. H., Loades, K. W., Mao, Z., McIvor, I. R., Mickovski, S. B., Mitchell, S., Osman, N., Phillips, C., Poesen, J., Polster, D., Preti, F., Raymond, P., Rey, F., … Walker, L. R. (2014). Ecological mitigation of hillslope instability: Ten key issues facing researchers and practitioners. In *Plant and Soil* (Vol. 377, Issues 1–2). https://doi.org/10.1007/s11104-014-2044-6

Stokes, A., Norris, J. E., Van Beek, L. P. H., Bogaard, T., Cammeraat, E., Mickovski, S. B., Jenner, A., Di Iorio, A., & Fourcaud, T. (2008). How vegetation reinforces soil on slopes. In *Slope*

Stability and Erosion Control: Ecotechnological Solutions. https://doi.org/10.1007/978-1-4020-6676-4_4

Stokes, A., Sotir, R., Chen, W., & Ghestem, M. (2010). Soil bio- and eco-engineering in China: past experience and future priorities. In *Ecological Engineering* (Vol. 36, Issue 3). https://doi.org/10.1016/j.ecoleng.2009.07.008

Stone, M. (1974). Cross-Validatory Choice and Assessment of Statistical Predictions. *Journal of the Royal Statistical Society Series B: Statistical Methodology*, *36*(2). https://doi.org/10.1111/j.2517-6161.1974.tb00994.x

Stoppiglia, H., Dreyfus, G., Dubois, R., & Oussar, Y. (2003). Ranking a random feature for variable and feature selection. *Journal of Machine Learning Research*, *3*.

Strauch, R., Istanbulluoglu, E., Siddhartha Nudurupati, S., Bandaragoda, C., Gasparini, N. M., & Tucker, G. E. (2018). A hydroclimatological approach to predicting regional landslide probability using Landlab. *Earth Surface Dynamics*, *6*(1). https://doi.org/10.5194/esurf-6-49-2018

Sun, L., Gao, H., Pan, S., & Wang, J. X. (2020). Surrogate modeling for fluid flows based on physics-constrained deep learning without simulation data. *Computer Methods in Applied Mechanics and Engineering*, *361*. https://doi.org/10.1016/j.cma.2019.112732

Svozil, D., Kvasnička, V., & Pospíchal, J. (1997). Introduction to multi-layer feed-forward neural networks. *Chemometrics and Intelligent Laboratory Systems*, *39*(1). https://doi.org/10.1016/S0169-7439(97)00061-0

Sze, V., Chen, Y. H., Yang, T. J., & Emer, J. S. (2017). Efficient Processing of Deep Neural Networks: A Tutorial and Survey. In *Proceedings of the IEEE* (Vol. 105, Issue 12). https://doi.org/10.1109/JPROC.2017.2761740

Tarolli, P., Pijl, A., Cucchiaro, S., & Wei, W. (2021). Slope instabilities in steep cultivation systems: Process classification and opportunities from remote sensing. *Land Degradation and Development*, *32*(3). https://doi.org/10.1002/ldr.3798

Tarquini, S., Isola I., Favalli, M., Battistini, A., & Dotta, G. (2023). *TINITALY, a digital elevation model of Italy with a 10 meters cell size (Version 1.1). Istituto Nazionale di Geofisica e Vulcanologia (INGV).* https://doi.org/10.13127/tinitaly/1.1

Terwilliger, V. J., & Waldron, L. J. (1990). Assessing the contribution of roots to the strength of undisturbed, slip prone soils. *Catena*, *17*(2). https://doi.org/10.1016/0341-8162(90)90005-X

Terzaghi, K. (1943). Theoretical Soil Mechanics. In *Theoretical Soil Mechanics*. https://doi.org/10.1002/9780470172766

Thomas, R. E., & Pollen-Bankhead, N. (2010). Modeling root-reinforcement with a fiber-bundle model and Monte Carlo simulation. *Ecological Engineering*, *36*(1). https://doi.org/10.1016/j.ecoleng.2009.09.008

Tian, X., Zhang, M., Yang, C., & Ma, J. (2021). FusionNDVI: A Computational Fusion Approach for High-Resolution Normalized Difference Vegetation Index. *IEEE Transactions on Geoscience and Remote Sensing*, *59*(6). https://doi.org/10.1109/TGRS.2020.3014698

Tien Bui, D., Tuan, T. A., Klempe, H., Pradhan, B., & Revhaug, I. (2016). Spatial prediction models for shallow landslide hazards: a comparative assessment of the efficacy of support vector machines, artificial neural networks, kernel logistic regression, and logistic model tree. *Landslides*, *13*(2). https://doi.org/10.1007/s10346-015-0557-6

Tiranti, D., & Ronchi, C. (2023). Climate Change Impacts on Shallow Landslide Events and on the Performance of the Regional Shallow Landslide Early Warning System of Piemonte (Northwestern Italy). *GeoHazards*, *4*(4). https://doi.org/10.3390/geohazards4040027

Trezzini, F., Giannella, G., & Guida, T. (2013). Landslide and flood: Economic and social impacts in Italy. *Landslide Science and Practice: Social and Economic Impact and Policies*, *7*. https://doi.org/10.1007/978-3-642-31313-4_22

Trigila, A., Iadanza, C., Bussettini, M., & Lastoria, B. (2018). Dissesto idrogeologico in Italia: pericolosità e indicatori di rischio - Edizione 2018. In *ISPRA, Rapporti 287/2018*.

Trigila, A., Iadanza, C., Lastoria, B., Bussettini, M., & Barbano, A. (2021). *Dissesto idrogeologico in Italia: pericolosità e indicatori di rischio - Edizione 2021*.

Tu, H. M., & Chen, H. M. (2020). From deforestation to afforestation: Effect of slopeland use policies on land use/cover change in Taiwan. *Land Use Policy*, *99*. https://doi.org/10.1016/j.landusepol.2020.105038

Tu, H., Moura, S., Wang, Y., & Fang, H. (2023). Integrating physics-based modeling with machine learning for lithium-ion batteries. *Applied Energy*, *329*. https://doi.org/10.1016/j.apenergy.2022.120289

Turner, A. K. (2018). Social and environmental impacts of landslides. In *Innovative Infrastructure Solutions* (Vol. 3, Issue 1). https://doi.org/10.1007/s41062-018-0175-y

UNDRR, & CRED. (2020). The human cost of disasters: an overview of the last 20 years (2000-2019). In *Centre for Research on the Epidemiology of Disasters*.

USGS. (n.d.). Retrieved 22 October 2024, from https://www.usgs.gov/programs/landslide-hazards/data

Van Zadelhoff, F. B., Albaba, A., Cohen, D., Phillips, C., Schaefli, B., Dorren, L., & Schwarz, M. (2022). Introducing SlideforMAP: a probabilistic finite slope approach for modelling shallow-landslide probability in forested situations. *Natural Hazards and Earth System Sciences*, *22*(8). https://doi.org/10.5194/nhess-22-2611-2022

Vanacker, V., Vanderschaeghe, M., Govers, G., Willems, E., Poesen, J., Deckers, J., & De Bievre, B. (2003). Linking hydrological, infinite slope stability and land-use change models through GIS for assessing the impact of deforestation on slope stability in high Andean watersheds. *Geomorphology*, *52*(3–4). https://doi.org/10.1016/S0169-555X(02)00263-5

Vanapalli, S. K., Fredlund, D. G., Pufahl, D. E., & Clifton, A. W. (1996). Model for the prediction of shear strength with respect to soil suction. *Canadian Geotechnical Journal*, *33*(3). https://doi.org/10.1139/t96-060

Varnes, D. (1978). Slope Movement Types and Processes. *Special Report*, *176*.

Vennari, C., Gariano, S. L., Antronico, L., Brunetti, M. T., Iovine, G., Peruccacci, S., Terranova, O., & Guzzetti, F. (2014). Rainfall thresholds for shallow landslide occurrence in Calabria, southern Italy. *Natural Hazards and Earth System Sciences*, *14*(2). https://doi.org/10.5194/nhess-14-317-2014

Vieira, B. C., Fernandes, N. F., & Filho, O. A. (2010). Shallow landslide prediction in the Serra do Mar, São Paulo, Brazil. *Natural Hazards and Earth System Science*, *10*(9). https://doi.org/10.5194/nhess-10-1829-2010

von Ruette, J., Lehmann, P., Fan, L., Bickel, S., Or, D., & Anonymous. (2017). STEP-TRAMM; a modeling interface for simulating localized rainfall induced shallow landslides and debris flow runout pathways. *Geophysical Research Abstracts*, *19*.

Von Ruette, J., Lehmann, P., & Or, D. (2018). Quantifying deforestation effects on rainfall induced shallow landslides and debris flows pathways. In *Geophysical Research Abstracts* (Vol. 20).

Von Ruette, J., Papritz, A., Lehmann, P., Rickli, C., & Or, D. (2011). Spatial statistical modeling of shallow landslides-Validating predictions for different landslide inventories and rainfall events. *Geomorphology*, *133*(1–2). https://doi.org/10.1016/j.geomorph.2011.06.010

Waldron, L. J. (1977). The Shear Resistance of Root-Permeated Homogeneous and Stratified Soil. *Soil Science Society of America Journal*, *41*(5). https://doi.org/10.2136/sssaj1977.03615995004100050005x

Waldron, L. J., & Dakessian, S. (1981). Soil reinforcement by roots: Calculation of increased soil shear resistance from root properties. *Soil Science*, *132*(6). https://doi.org/10.1097/00010694-198112000-00007

Walford, L. A., & Zon, R. (1942). Conservation of Renewable Natural Resources: Some Fundamental Aspects of the Problem. *Copeia*, *1942*(1). https://doi.org/10.2307/1437968

Wang, H. B., Zhou, B., Wu, S. R., Shi, J. S., & Li, B. (2011). Characteristic analysis of large-scale loess landslides: A case study in Baoji City of Loess Plateau of Northwest China. *Natural Hazards and Earth System Science*, *11*(7). https://doi.org/10.5194/nhess-11-1829-2011

Wang, H., Zhang, L., Luo, H., He, J., & Cheung, R. W. M. (2021). AI-powered landslide susceptibility assessment in Hong Kong. *Engineering Geology*, *288*. https://doi.org/10.1016/j.enggeo.2021.106103

Wang, L., Zhang, X., & Tinti, S. (2019). Shallow landslides modeling using a particle finite element model with emphasis on landslide evolution. *Earth Surface Dynamics Discussions*, *May*.

Wang, S., Fu, B., Piao, S., Lü, Y., Ciais, P., Feng, X., & Wang, Y. (2016). Reduced sediment transport in the Yellow River due to anthropogenic changes. *Nature Geoscience*, *9*(1). https://doi.org/10.1038/ngeo2602

Wang, X., & Liu, Q. (2021). Modeling shallow geological flows on steep terrains using a specific differential transformation. *Acta Mechanica*, *232*(6). https://doi.org/10.1007/s00707-021-02944-3

Wang, X., Ma, C., Wang, Y., Wang, Y., Li, T., Dai, Z., & Li, M. (2020). Effect of root architecture on rainfall threshold for slope stability: variabilities in saturated hydraulic conductivity and strength of root-soil composite. *Landslides*, *17*(8). https://doi.org/10.1007/s10346-020-01422-6

Wang, Y., Brandt, M., Zhao, M., Tong, X., Xing, K., Xue, F., Kang, M., Wang, L., Jiang, Y., & Fensholt, R. (2018). Major forest increase on the Loess Plateau, China (2001–2016). *Land Degradation and Development*, *29*(11). https://doi.org/10.1002/ldr.3174

Waring, R. H., Coops, N. C., Fan, W., & Nightingale, J. M. (2006). MODIS enhanced vegetation index predicts tree species richness across forested ecoregions in the contiguous U.S.A. *Remote Sensing of Environment*, *103*(2). https://doi.org/10.1016/j.rse.2006.05.007

Wei, H., Zhao, W., & Wang, H. (2021). Effects of vegetation restoration on soil erosion on the loess plateau: A case study in the ansai watershed. *International Journal of*

Environmental Research and Public Health, *18*(12). https://doi.org/10.3390/ijerph18126266

Williams, C. K. I. (2021). The Effect of Class Imbalance on Precision-Recall Curves. In *Neural Computation* (Vol. 33, Issue 4). https://doi.org/10.1162/neco_a_01362

Wohlgemuth, P. M., Hubbert, K. R., Beyers, J. L., & Weise, D. R. (2007). Evaluating the effectiveness of Burned Area Emergency Response (BAER) efforts after the 2003 wildfires, Southern California. *Report - University of California Water Resources Center*, *109*.

Wold, S. (1978). Cross-Validatory Estimation of the Number of Components in Factor and Principal Components Models. *Technometrics*, *20*(4). https://doi.org/10.1080/00401706.1978.10489693

Woldesenbet, T. A., Elagib, N. A., Ribbe, L., & Heinrich, J. (2017). Hydrological responses to land use/cover changes in the source region of the Upper Blue Nile Basin, Ethiopia. *Science of the Total Environment*, *575*. https://doi.org/10.1016/j.scitotenv.2016.09.124

World Bank Group. (n.d.). Retrieved 22 October 2024, from https://datacatalog.worldbank.org/search/dataset/0037584

World Landslides Forum: Each year, landslides cause damage to 6 billion Euros. (2023). In *ISPRA*. ISPRA.

Wu, H., Yao, C., Li, C., Miao, M., Zhong, Y., Lu, Y., & Liu, T. (2020). Review of application and innovation of geotextiles in geotechnical engineering. In *Materials* (Vol. 13, Issue 7). https://doi.org/10.3390/MA13071774

Wu, T. H. (1976). *Investigation of Landslides on Prince of Wale Island, Alaska*.

Wu, T. H. (1984). EFFECT OF VEGETATION ON SLOPE STABILITY. *Transportation Research Record*. https://doi.org/10.1016/0148-9062(85)92272-7

Wu, T. H. (1994a). Slope stabilization using vegetation. *Geotechnical Engineering: Emerging Trends in Design and Practice*.

Wu, T. H. (1994b). Slope stabilization using vegetation. *Geotechnical Engineering: Emerging Trends in Design and Practice*. https://doi.org/10.1016/0148-9062(95)90187-a

Wu, T. H., McKinnell, W. P., & Swanston, D. N. (1979). Strength of tree roots and landslides on Price of Wales Island, Alaska. *Can Geotech J*, *16*(1). https://doi.org/10.1139/t79-003

Wu, T. H., & Swanston, D. N. (1980). Risk of landslides in shallow soils and its relation to clearcutting in southeastern Alaska. *Forest Science*, *26*(3). https://doi.org/10.1093/forestscience/26.3.495

Wu, W., & Sidle, R. C. (1995). A Distributed Slope Stability Model for Steep Forested Basins. *Water Resources Research*, *31*(8). https://doi.org/10.1029/95WR01136

WU, Y.-H., NAKAKITA, E., & KUNITOMO, M. (2020). FUTURE CHANGE OF RAINFALL-TRIGGERED LANDSLIDE RISK USING NHRCM05 BASED ON CRITICAL LINE METHOD. *Journal of Japan Society of Civil Engineers, Ser. B1 (Hydraulic Engineering)*, *76*(2). https://doi.org/10.2208/jscejhe.76.2_i_67

Xiao, T., Zhang, L. M., Cheung, R. W. M., & Lacasse, S. (2022). Predicting spatio-temporal man-made slope failures induced by rainfall in Hong Kong using machine learning techniques. *Geotechnique*, *73*(9). https://doi.org/10.1680/jgeot.21.00160

Xie, W., Li, X., Jian, W., Yang, Y., Liu, H., Robledo, L. F., & Nie, W. (2021). A novel hybrid method for landslide susceptibility mapping-based geodetector and machine learning cluster: A case of Xiaojin County, China. *ISPRS International Journal of Geo-Information*, *10*(2). https://doi.org/10.3390/ijgi10020093

Xu, H., He, X., Shan, F., Niu, G., & Sheng, D. (2023). Machine Learning in the Stochastic Analysis of Slope Stability: A State-of-the-Art Review. In *Modelling* (Vol. 4, Issue 4, pp. 426–453). Multidisciplinary Digital Publishing Institute (MDPI). https://doi.org/10.3390/modelling4040025

Xu, X. Z., Guo, W. Z., Liu, Y. K., Ma, J. Z., Wang, W. L., Zhang, H. W., & Gao, H. (2017). Landslides on the Loess Plateau of China: a latest statistics together with a close look. *Natural Hazards*, *86*(3). https://doi.org/10.1007/s11069-016-2738-6

Xu, Y., Kohtz, S., Boakye, J., Gardoni, P., & Wang, P. (2023). Physics-informed machine learning for reliability and systems safety applications: State of the art and challenges. *Reliability Engineering and System Safety*, *230*. https://doi.org/10.1016/j.ress.2022.108900

Xu, Y., Luo, L., Guo, W., Jin, Z., Tian, P., & Wang, W. (2024). Revegetation Changes Main Erosion Type on the Gully–Slope on the Chinese Loess Plateau Under Extreme Rainfall: Reducing Gully Erosion and Promoting Shallow Landslides. *Water Resources Research*, *60*(3). https://doi.org/10.1029/2023WR036307

Yamase, K., Todo, C., Torii, N., Tanikawa, T., Yamamoto, T., Ikeno, H., Ohashi, M., Dannoura, M., & Hirano, Y. (2021). Dynamics of soil reinforcement by roots in a regenerating coppice stand of Quercus serrata and effects on slope stability. *Ecological Engineering*, *162*. https://doi.org/10.1016/j.ecoleng.2021.106169

Yang, L., Cui, Y., Xu, C., & Ma, S. (2024). Application of coupling physics–based model TRIGRS with random forest in rainfall-induced landslide-susceptibility assessment. *Landslides*. https://doi.org/10.1007/s10346-024-02276-y

Yu, M., Huang, Y., Deng, W., & Cheng, H. (2018). Forecasting landslide mobility using an SPH model and ring shear strength tests: A case study. *Natural Hazards and Earth System Sciences*, *18*(12). https://doi.org/10.5194/nhess-18-3343-2018

Yu, Y., Si, X., Hu, C., & Zhang, J. (2019). A review of recurrent neural networks: Lstm cells and network architectures. In *Neural Computation* (Vol. 31, Issue 7). https://doi.org/10.1162/neco_a_01199

Zenodo. (n.d.). Retrieved 22 October 2024, from https://zenodo.org/

Zhan, T. L. T., Ng, C. W. W., & Fredlund, D. G. (2007). Field study of rainfall infiltration into a grassed unsaturated expansive soil slope. *Canadian Geotechnical Journal*, *44*(4). https://doi.org/10.1139/T07-001

Zhang, G., Wang, L., & Wang, Y. (2017). Pile reinforcement mechanism of soil slopes. *Acta Geotechnica*, *12*(5). https://doi.org/10.1007/s11440-017-0543-3

Zhang, H., Ma, J., Chen, C., & Tian, X. (2020). NDVI-Net: A fusion network for generating high-resolution normalized difference vegetation index in remote sensing. *ISPRS Journal of Photogrammetry and Remote Sensing*, *168*. https://doi.org/10.1016/j.isprsjprs.2020.08.010

Zhang, J., Qiu, H., Tang, B., Yang, D., Liu, Y., Liu, Z., Ye, B., Zhou, W., & Zhu, Y. (2022). Accelerating Effect of Vegetation on the Instability of Rainfall-Induced Shallow Landslides. *Remote Sensing*, *14*(22). https://doi.org/10.3390/rs14225743

Zhang, T., Li, Y., Wang, T., Wang, H., Chen, T., Sun, Z., Luo, D., Li, C., & Han, L. (2022). Evaluation of different machine learning models and novel deep learning-based algorithm for landslide susceptibility mapping. *Geoscience Letters*, *9*(1). https://doi.org/10.1186/s40562-022-00236-9

Zhang, Z., & Sabuncu, M. R. (2018). Generalized cross entropy loss for training deep neural networks with noisy labels. *Advances in Neural Information Processing Systems*, *2018-December*.

Zhao, B., Dai, Q., Han, D., Dai, H., Mao, J., & Zhuo, L. (2019). Probabilistic thresholds for landslides warning by integrating soil moisture conditions with rainfall thresholds. *Journal of Hydrology*, *574*. https://doi.org/10.1016/j.jhydrol.2019.04.062

Zhou, X., Wen, H., Zhang, Y., Xu, J., & Zhang, W. (2021). Landslide susceptibility mapping using hybrid random forest with GeoDetector and RFE for factor optimization. *Geoscience Frontiers*, *12*(5). https://doi.org/10.1016/j.gsf.2021.101211

Zhuang, J., Peng, J., Wang, G., Javed, I., Wang, Y., & Li, W. (2018). Distribution and characteristics of landslide in Loess Plateau: A case study in Shaanxi province. *Engineering Geology*, *236*. https://doi.org/10.1016/j.enggeo.2017.03.001

Ziemer, R. R. (1981a). Roots and stability of forested slopes. *Erosion and Sediment Transport in Pacific Rim Steeplands. Proc. Christchurch Symposium, January 1981*.

Ziemer, R. R. (1981b). The role of vegetation in the stability of forested slopes. *Proc. Int. XVII IUFRO World Congress*.

Zon, R. (1935). Shelterbelts - Futile dream or workable plan. In *Science* (Vol. 81, Issue 2104). https://doi.org/10.1126/science.81.2104.391

Zon, R., Cooper, W. S., Pearson, G. A., Shantz, H. L., Douglass, A. E., Abbot, C. G., Sears, P. B., Huntington, E., Cooke, M. L., Dana, S. T., Eisenhower, M. S., & McGown, J. F. (2017). *Conservation of Renewable Natural Resources* (W. S. Cooper, Ed.; Reprint 2016). University of Pennsylvania Press, Inc. https://doi.org/10.2307/j.ctv4rfr5m

La borsa di dottorato è stata cofinanziata con risorse del
Programma Operativo Nazionale Ricerca e Innovazione 2014-2020, risorse FSE REACT-EU
Azione IV.4 “Dottorati e contratti di ricerca su tematiche dell’innovazione”
e Azione IV.5 “Dottorati su tematiche Green”